GNSS Channel Characterization and Enhanced Weak Signal Processing

(URL: http://www.geomatics.ucalgary.ca/graduatetheses)

by

Shashank Satyanarayana

September 2011

UNIVERSITY OF CALGARY

GNSS CHANNEL CHARACTERIZATION AND ENHANCED WEAK SIGNAL

PROCESSING

by

Shashank Satyanarayana

A THESIS

SUBMITTED TO THE FACULTY OF GRADUATE STUDIES

IN PARTIAL FULFILMENT OF THE REQUIREMENTS FOR THE

DEGREE OF DOCTOR OF PHILOSOPHY

DEPARTMENT OF GEOMATICS ENGINEERING

CALGARY, ALBERTA

September, 2011

Abstract

Indoor positioning has gained increasing importance and attention over the past decade due to its numerous applications. Requirements for E911 Phase 2 for services like Public Safety Answering Points (PSAPs) which was mandated by the Federal Communications Commission (FCC) have further increased the demand for better GPS receiver performance under indoor conditions. This has led to new challenges where proper understanding of the signal propagation characteristics becomes a vital part for an efficient design of high sensitivity receivers. This research work focuses on the characterization of GNSS weak signals in several harsh environments and the development of high sensitivity acquisition and tracking algorithms.

A reference-rover processing architecture for weak signal measurement and processing is considered for the characterization process. The adopted characterization methodology is analyzed in terms of accuracy and reliability using both software and hardware simulations with the final goal of measuring real GPS signals as weak as -165 dBm with a predefined level of accuracy. Using the developed methodology, the amplitude characterization of real GPS signals in several harsh environments such as urban, sub-urban, foliage and indoor scenarios is then performed. The empirical distributions of signal amplitudes received in harsh environments are compared against standard parametric models. It is shown that, in most situations, a composite model is capable of capturing both slow and fast fading effects where the fast fading component is modelled using a Rician or Nakagami-m distribution and the slow fading components using a Log-Normal or Gamma distribution.

Temporal, spectral and spatial characteristics of indoor GPS signals are further analyzed as part of the signal characterization process. Second order statistics such as average fade durations, level crossing rate and mean fade distances are extracted and empirical curves are compared against standard parametric models. Following the characterization analysis, a model for the spectra of slow and fast fading components was obtained. Utilizing the characterization results, a simulation scheme is proposed for the simulation of indoor GNSS signals. It is shown that the first and second order statistics of the simulated data are in good agreement with the empirical data.

Enhanced signal processing techniques are then proposed for GPS weak signal acquisition and tracking for standalone receivers. A new detection scheme for weak signal acquisition based on the Generalized Likelihood Ratio Test (GLRT) is proposed and its performance is evaluated using simulations and compared against existing techniques. The results showed improvements with respect to existing techniques. Finally, a new tracking architecture is proposed for tracking weak GPS signals. The proposed technique is effective in terms of maintaining frequency lock with accurate Doppler estimates in several indoor dynamic conditions.

Acknowledgement

Dedicated to my parents

Thank you for all the support and encouragement

Table of Contents

List of Tables

List of Figures and Illustrations

xvii

xviii

List of Abbreviations

Abbreviations		Description
ACF	:	Autocorrelation Function
AFD	:	Average Fade Duration
AGPS	:	Assisted Global positioning System
AWGN	:	Additive White Gaussian Noise
BER	:	Bit Error Rate
BPB	:	Baseband Processing Block
BPSK	:	Binary Phase Shift Keying
CC	:	Central Chi-square
CCIT	:	Calgary Centre for Innovative Technology
CDF	:	Cumulative Density Function
CDMA	:	Code Division Multiple Access
CIR	:	Channel Impulse Response
CR	:	Conference Room
CRLB	:	Cramer-Rao Lower Bound
DA	:	Data Aided
DLL	:	Delay Lock Loop
DNC	:	Differentially Non-coherent
FCC	:	Federal Communications Commission
FFT	:	Fast Fourier Transform
FT	:	Fourier Transform
GLRT	:	Generalized Likelihood Ratio Test
GNSS	:	Global Navigation Satellite System
GPS	:	Global Positioning System
GTD	:	Geometrical Theory of Diffraction
IF	:	Intermediate Frequency
IFFT	:	Inverse Fast Fourier Transform
KDE	:	Kernel Density Estimation
KV	:	Known variance
LCR	:	Level Crossing Rate
LMS	:	Land Mobile Satellite
LNA	:	Low Noise Amplifier
LOS	:	Line of Sight
MC	:	Monte Carlo
MCS	:	Master Control Station
ME	:	McEwan Hall
MFD	:	Mean Fade Distance
ML	:	Maximum Likelihood
MML	:	Modified ML
MSE	:	Mean Square Error
NC	:	Non-coherent

NCBP	:	Non-coherent Block Processing
NCC	:	Non-Central Chi-square
NCF	:	Non-Central Fisher
NCO	:	Numerically Controlled Oscillator
NDA	:	Non Data Aided
NL	:	Navigation Laboratory
NLOS	:	Non-Line of Sight
NI	:	National Instruments
PDF	:	Probability Density Function
PG	:	Processing Gain
PRN	:	Pseudo-Random Noise
PDP	:	Power Delay Profile
PSD	:	Power Spectral Density
RF	:	Radio Frequency
RLN	:	Rice/Log-Normal
RHCP	:	Right Hand Circularly Polarized
ROC	:	Receiver Operating Characteristics
RR	:	Reference-Rover
SA	:	Satellite Availability
SD	:	Squaring Detector
SNR	:	Signal to Noise Ratio
UC	:	Uncorrelated
UKV	:	Unknown variance
UTD	:	Uniform Theory of Diffraction
WH	:	Wooden House
WSS	:	Wide Sense Stationary

List of Symbols

Symbol		Definition
T_{chip}	:	Chip period [s]
T_b	:	Data bit period [s]
f_c	:	Carrier frequency [Hz]
f_D	:	Doppler frequency [Hz]
λ	:	Wavelength of carrier wave [m]
f_s	:	Sampling frequency [Hz]
T_s	:	Sampling period [s]
τ	:	Time delay [s]
T_c	:	Coherent integration time [s]
T	:	Total integration time [s]
d	:	Navigation data bits
c	:	PRN code
η	:	Additive white Gaussian noise
r	:	GNSS signal at output of communication channel
y	:	Received GNSS signal
z	:	Received signal envelope
$\tilde{w}$	:	Complex correlator output
a	:	Attenuation factor
p	:	Path loss component
s	:	Shadow fading component
ρ		Mean shadow level with respect to outdoor scenario
R	:	Correlation function
N_0	:	Thermal noise power spectral density
F	:	Noise factor of the system
C_t	:	Transmitted carrier power
C	:	Received carrier power
I	:	In-phase component
Q	:	Quadrature phase component
μ	:	Mean
σ	:	Standard deviation
α	:	Signal to noise ratio
$\Re\{\cdot\}$	:	Real part of a value
M	:	Number of correlator outputs
A		Signal amplitude
$H(\cdot)$	:	Filter transfer function

P_t	:	Satellite transmit power
P_r	:	Received signal power
G_t	:	Transmitter antenna gain
G_r	:	Receiver antenna gain
k_b	:	Boltzmann constant
T_0	:	Reference noise temperature
T_{sys}	:	System noise temperature
T_{ant}	:	Antenna noise temperature
R_x	:	Autocorrelation function
S_x	:	Power spectral density
L_Z	:	Level crossing rate
f_{3dB}	:	3 dB filter cut-off frequency

Chapter One: **INTRODUCTION AND OVERVIEW**

In recent years, Global Navigation Satellite System (GNSS) receiver technology is gaining increasing importance due to its ability of providing three dimensional positioning information of the user in any weather condition, anywhere and at any time on the earth under Line of Sight (LOS) conditions. Ever since the Selective Availability feature of the Global Positioning System (GPS) was removed, there have been innumerable applications of GPS in the commercial market. The use of GPS in commercial aircraft, fleet management and vehicle navigation are amongst several successful applications. Outstanding performance of GPS in outdoor scenarios is luring people across the globe to extend its application in signal degraded environments such as urban canyons, forest canopies and indoors. The introduction of new satellite systems such as Galileo, GLONASS, Compass and the modernization of GPS have further revolutionized the receiver market, pushing the need to provide accurate and precise position, location and navigation information to the user. GNSSs cover a wide range of applications from military to a diverse range of unanticipated civilian needs. For example, apart from military and marine, GNSSs are extensively used in agriculture, sports equipment, land vehicles, fire fighting, mobile phones, pet tracking and many more. However, with the traditional receiver technologies, applications of GNSS are limited to open sky conditions where the received signal strength from any satellite in view is moderately high. However, requirements for E911 Phase 2 (Wireless 911 Services 2010), which were mandated by the Federal Communications Commission (FCC) and location-based services have increased the demand for better GNSS receiver

performance under harsh environments such as urban canyons, indoor environments and beneath forest canopies. This has led to new challenges in GNSS receiver design. Thus, proper understanding of the signal propagation characteristics and the development of new receiver algorithms under such harsh environmental conditions becomes vital to meet the expected level of performance criteria.

1.1 Background

GNSS signal propagation in environments like downtowns/urban canyons, indoors and forest canopies is a complex phenomenon wherein the Radio Frequency (RF) wave experiences many of the physical effects such as reflection, diffraction, attenuation and scattering before reaching the receiver antenna. Due to these effects, the receiver antenna sees the superposition of multiple copies of the transmitted signal wherein each signal would have experienced different attenuations, delays and phase shifts while travelling from the transmitter to the receiver. Superposition of multiple signal waveforms with different delays and phase shifts can result either in amplification of the signal (constructive manner) or in attenuation of the signal (destructive manner). In addition, if the receiver is in motion (such as driving through a city core), it will also experience the phenomenon called Doppler spread in which direct and reflected signals will have different Doppler values depending on the receiver speed and direction. These physical phenomena result in what is known as fading. Fading is a phenomenon wherein multiple signals sum up together causing time-varying attenuation/amplification of the signal power (Rappaport 2001).

The most common and unavoidable problems in GNSS signal processing under harsh environments are the excess signal attenuation and fading. The nominal received signal power of GPS signals is around -128.5 dBm (GPS ICD 2010) which approximately corresponds to a Carrier-to-Noise density power ratio (C/N_0) of 38 dB-Hz. With the effect of fading and/or signal blockage from surrounding materials such as buildings, trees, etc. an attenuation of up to tens of dB (Klukas et al. 2003) can be observed in an indoor scenario significantly degrading the receiver performance. Attenuation increases as the number of obstacles between the satellite and the receiver antenna increases. Thus, to summarize, GNSS receiver algorithms should be designed to compensate for the instantaneous fluctuations in the signal power level as well as for the mean signal attenuation.

1.2 Literature review

The following subsections summarize previous efforts made towards the characterization of a Land Mobile Satellite (LMS) communication channel and the signal processing algorithms developed to overcome the effect of the communication channel on the transmitted signals. Initially, a brief overview of channel characterization methodologies is explained. Narrowband characterization of GNSS signals and their limitations are discussed next. Finally, existing approaches, algorithms and their limitations for GNSS weak signal processing are summarized.

1.2.1 Characterization and modeling of GNSS weak signals

Modeling approaches introduced in the literature for the characterization of the LMS channel can be broadly classified into three groups: *Empirical models, Deterministic or*

Physical models and *Statistical models* (Fontan et al. 1997, Ibnkahla 2004). Statistical models can be further classified as Single and Mixture models (Abdi et al. 2003). In addition, various combinations of Deterministic and Statistical models are also available in the literature (Fontan et al. 1997).

Empirical models are the most widespread approaches which use information like environmental conditions, elevation angle of the satellite and frequency of the transmitted signal to scale their parameters. Typical empirical models are listed in (Fontan et al. 1997, Rappaport 2001).

Deterministic or Physical models provide high prediction accuracies of the signal variations, however, these models require a huge amount of information regarding the local environment. Typically, deterministic models are based on the combination of Geometrical Theory of Diffraction (GTD)/Uniform Theory of Diffraction (UTD), rough surface theory and scattering theories (Fontan et al. 1997). Since GNSS satellites provide worldwide coverage, it becomes very difficult to characterize a vast area of scenarios through deterministic models.

Statistical models are less computationally intensive than deterministic models and are more phenomenological than the empirical models (Ibnkahla 2004). Here, well known standard distributions are assumed based on the type of scenario in which the receiver is operating. For example, the dependent parameters can be the types of reflectors (results in specular or diffused signal), the presence or absence of LOS components (for example, it could results in either Rayleigh or Rice distribution), receiver dynamics and signal blocking elements (presence or absence of shadowing) etc. Once the distribution is chosen, parameters for that distribution are obtained empirically based on field

experiments. Advantages of the statistical models are their flexibility and efficient system performance predictions for a wide range of signal characteristics and scenarios.

Parameters for statistical characterization of the multipath channel vary depending on whether the channel is *narrowband* or *wideband*. Narrowband channels are those channels in which the delay spread (time between multipath rays) are considerably smaller than the symbol duration, approximately less than one tenth of a chip, (Ibnkahla 2004). Here, one code chip is referred to as a symbol. In such scenarios, it can be modeled that all multipath signals arrive at the receiver antenna nearly at the same time with different amplitude and phase characteristics. This scenario leads to what is commonly known as *flat fading* or *frequency non-selective* fading (Rappaport 2001). On the other hand in a wideband channel, the delay spread is considerably higher than the symbol period and thus the bandwidth of the channel is smaller than the bandwidth of the transmitted signal. This results in what is known as *frequency selective* fading channel (Rappaport 2001). Typically, narrowband channels are characterized by their first order statistics such as signals envelop Probability Density Function (PDF) and Cumulative Density Function (CDF) as well as by second order statistics such as Average Fade Duration (AFD) and Level Crossing Rate (LCR). On the other hand, wideband channels are characterized by Power Delay Profile (PDP), channel Coherence Bandwidth (BW_{coh}), channel Coherence Time (T_{coh}) and Doppler spectrum.

1.2.1.1 Limitations

Various existing statistical models discussed in the previous sections are derived based on several assumptions. In general, the suitability of a specific statistical model depends on

the assumptions made on factors such as dynamics of the transmitter and receiver, type of scenario (example: LOS, NLOS, urban, semi-urban, rural, etc.), propagation medium and their characteristics (example: tropospheric effects, ionospheric effects, clouds, rain, etc.). The GNSS communication channel is a typical LMS channel in which transmitter and receiver are in continuous motion. Therefore, it becomes necessary to validate the existing statistical models with respect to the different GNSS signal propagation scenarios. The following paragraph summarizes the previous efforts made towards characterizing GPS communication channels and their limitations.

In a previous attempt to determine the characteristics of indoor GPS signals, Islam et al (2007) tried to analyze the propagation effect based on pseudolites which are capable of transmitting high power signals in the L1 band. However, this type of approach does not guarantee that the measured fading phenomena translate directly on the much weaker GPS L1 signal. In addition, it does not consider the effect of ionosphere and troposphere. It has been shown that the distribution of the signal amplitude fits the Nakagami model (Lakhzouri et al. 2005). Also, authors have tried to measure the second order statistics of the signal in a typical office environment (Lakhzouri et al. 2005b). However, the data analysis was limited to few scenarios and based on short measurements. None of the mentioned works provide insight into the fading characteristics in terms of second order statistics of the signal. An extensive research has been done in the past to measure and model the channel impulse response (CIR) in urban, semi-urban, rural and indoor environments using channel sounding techniques (Steingass & Lehner 2003, Fontán et al. 2004, Steingass & Lehner 2004, Lehner & Steingass 2005, Steingass & Lehner 2006, Steingass & Lehner 2007, Steingass & Lehner 2008, Steingass et al. 2009, Schubert et al.

2009). In these research works, high power satellite-like signals were transmitted using a Zeppelin NT airship at an altitude between 1500 and 4000 m. Over 60 different datasets were collected in various environments and later analyzed using high resolution techniques to obtain the CIR of the channel. A recent study has shown promising results in characterizing indoor GPS signals using a channel sounder (Jost & Wang 2009). This type of characterization is very helpful in analyzing the time dispersive nature of the environment. But the above work lacks of information on the second order and spatial characteristics of the channel. In (Mitelman et al. 2006), signal power levels were measured in many challenging environments such as shopping malls, elevators and underground plazas, but the information on second order statistics of the signals was only marginally determined. Therefore, this research work aims at extensively characterizing the first and second order statistics of GPS signals under harsh environments

1.2.2 GNSS Weak signals processing

As already mentioned, any GNSS receiver operating under harsh conditions such as indoors has to combat two phenomena, fading and excess attenuation. Fading results in an instantaneous variation of the signal strength due to the constructive and destructive nature of multipath. Excess attenuation makes the noise component dominate impairing the estimation of any synchronization parameters such as carrier frequency, carrier phase and code delay. This section reviews the existing signal processing algorithms used in weak GNSS signal processing.

In the past, several efforts have been made for improving the sensitivity (ability to reliably track signals with reduced strength) of a GNSS receiver. Existing efforts can be broadly classified into the following categories.

- Network assisted GNSS (example AGPS) (Brown & Olson 2005)

- Sensor aided GNSS (Petovello et al. 2008)

- Tracking loop optimization and advanced signal processing/estimation techniques (Borio & Lachapelle 2009, Psiaki & Jung 2002)

- Block processing/Open loop architectures (Uijt de Haag 1999, Yang & Han 2007)

- Advanced architectures (Parkinson & Spilker 1996, Lashley & Bevly 2009, Lashley & Bevly 2007)

GNSS receivers operating in network assisted mode can receive information about visible satellites, precise time and orbital information. This greatly helps the acquisition of satellite signals improving the Time To First Fix (TTFF) (Brown & Olson 2005). In some situations, a GNSS receiver operating in weak signal environments can send the raw data along with approximate time of reception to a remote server that can process the raw samples and send back the position information.

Sensor assisted GNSS receivers utilize self contained sensors such as Inertial Measurement Unit (IMU) to aid velocity (in term of Doppler observations) and position information to maintain continuous operations. Extensive research have been done to integrate inertial units in tight/ultra tight mode (Petovello et al. 2008) to increase tracking performance in weak signal environments

Efforts have been made towards the optimization of tracking loop parameters in order to extend the tracking sensitivity of the GNSS receivers in weak signal environments. Various signal processing algorithms have been proposed to extend the phase estimation over multiple data bit periods so that extended integration can be performed in order to reduce the effect of noise (Borio & Lachapelle 2009, Kazemi 2008). Advanced estimation techniques have been used in order to overcome the effect of noise (Psiaki & Jung 2002).

Open loop tracking architecture utilizes block processing algorithms such as Fast Fourier Transform (FFT) in order to increase the signal detectability (Uijt de Haag 1999, Anyaegbu 2006, Yang & Han 2007). Block processing of GNSS signals involves buffering of data samples and then applying suitable signal processing algorithms to extract useful information from the incoming signal samples. As compared to sequential techniques there is no feedback from the previously estimated parameters. Generally in GNSS, the length of a data block is defined as an integer multiple of the signal code period. Block processing improves signal observability as compared to sequential processing.

Advanced receiver architectures such as vector tracking methods combine the tasks of signal tracking and position/velocity estimation into a single estimation algorithm. The advantages of vector tracking methods as highlighted in (Lashley & Bevly 2009) are the increased tracking sensitivity, ability to bridge small signal outages, rapid signal reacquisition and improved immunity against interference and jamming.

1.2.2.1 Limitations

One of the main objectives of this research work is to enhance the sensitivity of a GNSS receiver when working in standalone mode without any external aid or assistance. Therefore the limitations discussed here are with respect to a receiver operating in standalone mode. In Psiaki & Jung (2002), an extended Kalman filter was used to track weak GPS signals. Through simulations, it was shown that the proposed algorithm was capable of tracking weak signals with a C/N_0 of 15 dB-Hz. However, results using real GPS data under fading conditions are marginally reported. A memory based non-coherent architecture for estimating the carrier phase and frequency over multiple data period is explored in (Borio & Lachapelle 2009, Borio et al. 2009, Borio et al. 2009). It is shown that the proposed algorithm is capable of tracking weak signals with C/N_0 of 14.5 dB-Hz. Here, attenuated static real GPS data, indoor static data and dynamic data under urban environments (foliage) are considered to show the effectiveness of the proposed algorithm. In (Yang & Han 2007), a block processing architecture based on bit estimation and removal technique has been considered. However, the analysis of the algorithm was limited to signals that were simulated with a C/N_0 of 19 dB-Hz. It should be noted that the analysis or results for weak signal tracking under dynamic indoor scenarios have been marginally considered or reported in the existing literature.

GPS weak signals processing under fading conditions has been marginally considered. For this reason, this research work is also aiming at developing new signal processing algorithms that can handle fading and weak signal-to-noise ratio scenarios at the same time.

1.3 Objectives and contributions

With the knowledge of the existing literature, this research work aims at characterizing the GNSS propagation channel in harsh environments such as indoors, under foliage and in urban canyons. Specific focus is given to the GPS L1 signal. The knowledge gained during the characterization process can then be used for improving sensitivity of a standalone receiver. The main objectives of this research work are as follows:

1. **Study of various signal propagation models**: The main focus is on the identification of statistical models capable of describing the signal propagation characteristics under various GNSS scenarios. Several single, composite and mixture models have been identified and their applicability to GNSS signal propagation highlighted.

2. **Identification/development of signal characterization methodologies**: A methodology for characterizing GPS signals with power levels as low as -165 dBm is presented. A block processing approach has been adopted to characterize GPS weak signals. Towards this, a comprehensive analysis of a Modified Maximum Likelihood (MML) C/N_0 estimation technique is at first provided. Based on the theoretical properties of the MML C/N_0 estimator, the minimum coherent integration time required for achieving a predefined level of accuracy is quantified. The extended analysis of the C/N_0 estimator provides a means to determine the processing parameters for characterizing real GNSS weak signals. These values are then used for the temporal and spatial characterization of GPS signals in harsh environments.

3. **Characterization of first and second order statistics of GPS signals**: The received signal amplitude is characterized in different environments such as urban, semi-urban, under foliage and indoors. More emphasis is given to the indoor propagation channel.

Empirically obtained amplitude distributions are compared against standard single and composite parametric models. Second order statistics of the incoming signal envelopes such as AFD, LCR, and Mean Fade Distance (MFD) are characterized in several indoor scenarios. Temporal/spectral/spatial characterizations of GPS signals are determined using single and multiple antennas. Several experimental strategies based on a rotation table and instrumented cart are discussed for the effective characterization of GPS signals. In addition, analysis in terms of simultaneous satellite availability and signal fading characteristics under difficult conditions are performed. The characterization results are used in the development of a simulation model capable of simulating indoor GNSS signals that can be further used for building sophisticated software/hardware GNSS simulators.

4. **Design and development of new weak signal processing algorithms:** A new detection scheme for weak signal acquisition based on the Generalized Likelihood Ratio Test (GLRT) under the presence of data bit modulation is proposed. The proposed scheme is designed to provide an improved signal detection probability as compared to existing detection schemes under the presence of data bit modulation. Performance of the new detection scheme is evaluated using simulations and compared against existing techniques. Finally, a new architecture for tracking weak GPS signals is described. Performance of the proposed tracking scheme is evaluated using both software and hardware simulations. The effectiveness of the proposed algorithm is also shown by tracking GPS weak signals in several indoor environments under dynamic conditions, where the signal power levels falls below 10 dB-Hz on several occasions. The proposed tracking technique is designed to quickly recover

from deep fade conditions and to provide accurate Doppler estimates in signal degraded environments

1.4 Thesis outline

The structure of this thesis is summarized in the following paragraphs.

Chapter 2 reviews the theoretical background relative to the signal propagation in a typical LMS channel. In this chapter, a brief overview of the GPS communication channel is presented highlighting different signal propagation mechanisms and models describing the received signals. Overviews of several channel parameters for capturing the statistics of a communication channel are also described.

Chapter 3 describes in detail the methodology used for the characterization of GPS signals in harsh environments. Several strategies for the characterization of GPS signals are discussed. A feasible/repeatable strategy based on a reference-rover configuration is described for the characterization of real GPS weak signal. This includes the description of the hardware setup, system calibration and signal recovery methodology. The accuracy and reliability of the adopted methodology is validated using software and hardware simulations. A methodology for estimating weak signal power is discussed and the reliability of the considered C/N_0 estimator is analyzed.

Chapter 4 provides a detailed analysis on the first order statistics of signals received in various scenarios such as urban, semi-urban, foliage and indoors. Empirical distributions are compared against the standard parametric models discussed in Chapter 2. Statistics such as mean shadow levels and satellite availability statistics are also provided.

Chapter 5 provides a detailed analysis on the second order statistics of the received signal envelop under several indoor scenarios. Empirical values of AFD, LCR and MFD for different indoor scenarios are compared against standard parametric models. Temporal, spectral and spatial statistics of the received GNSS signal such as autocorrelation function (ACF), power spectral density (PSD) and decorrelation distances have been characterized. Finally, a simulation scheme for simulating indoor GNSS signals based on the empirical results is described.

Chapter 6 describes the enhanced signal processing techniques for acquisition and tracking of weak GNSS signals in stand alone conditions. A new signal detection scheme in the presence of data bit modulation is proposed. Also, a hybrid non-coherent and block processing architecture is proposed for tracking weak GNSS signals. Simulations and real data analysis are used to validate the effectiveness of the proposed techniques.

Chapter 7: Conclusions are provided along with suggestions for future work.

Chapter Two: **CHANNEL CHARACTERIZATION- STATE OF THE ART**

This chapter briefly reviews the RF wave propagation mechanism in a typical LMS communication channel. At first, an overview of the GPS signal and its characteristics is provided along with a description of different propagation scenarios. Various signal propagation mechanisms and their impact on the transmitted signal are briefly discussed followed by a generic model for the received signal. Deterministic and stochastic descriptions of the propagation channel are provided highlighting various channel parameters. Finally, a concise review of existing statistical models used for predicting the first and second order statistics of the received signal envelope is provided.

2.1 Overview of the GPS

Global Positioning System (GPS) is a space based radio navigation system consisting of three major segments (Parkinson & Spilker 1996): *space segment, control segment and user segment*. The space segment consists of a satellite constellation which transmits ranging signals down to the Earth. The control segment consists of ground based control stations for monitoring the satellites and their transmitted signals. Finally the user segment consists of all the GPS civil and military users that employ GPS receivers capable of performing navigation and timing related functions. Following paragraphs provide a brief description of each individual segment.

The **space segment** has a standard configuration of 24 satellites distributed among six Earth-centered orbital planes with four satellites per plane (Kaplan & Hegarty 2006). The six orbital planes are equally spaced with 60° separation around the equator with an inclination of 55°. Each GPS satellite revolves around the Earth in nearly circular orbits

at an altitude of about 20200 km with an orbital period of 11 hours, 58 minutes (one half of a sidereal day). Currently, GPS has a constellation of 32 satellites with maximum of up to 6 satellites per orbital plane as shown in Figure 2-1.
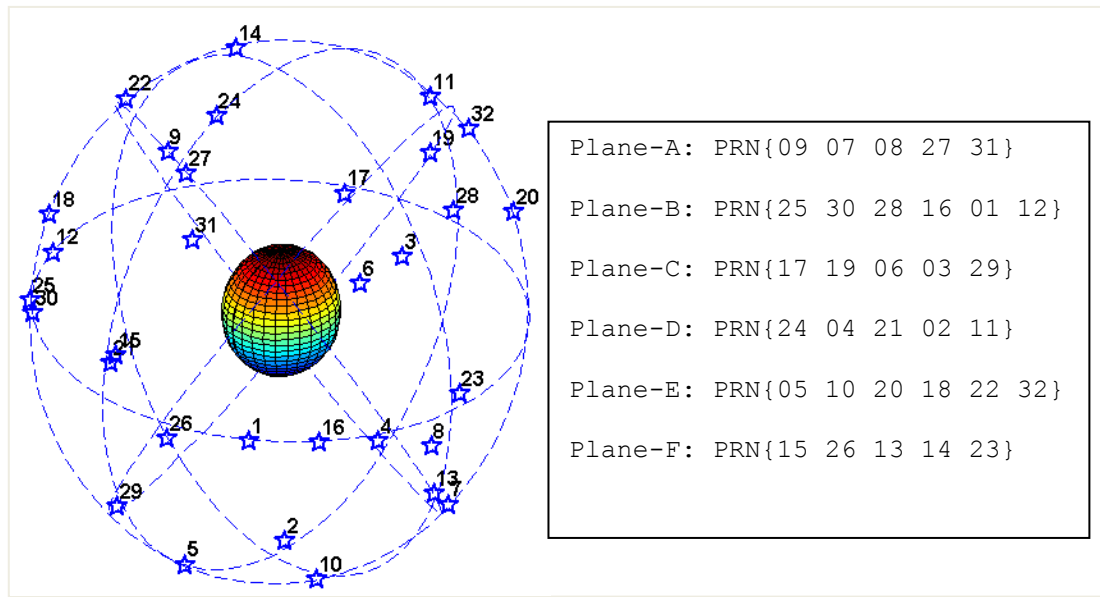
Figure 2-1: GPS satellite constellation with six orbital planes (A-F) with each having a maximum of six satellites per orbit as on 21-Oct-2010.

The **control segment** consists of several ground monitoring stations which are distributed around the world. Ground stations are responsible for monitoring and controlling the satellite constellation. The GPS control segment consists of one Master Control Station (MCS), six monitor stations and four large ground antenna stations. Each monitor station tracks the navigation signals and then sends data to the MCS. The MCS is responsible for determining any necessary updates required to maintain precise navigation. Updates generated by the MCS are uploaded to the satellites in an S-band telemetric channel via the ground antennas.

The **user segment** consists of all the civilian and military users that employ a GPS receiver unit capable of identifying (acquiring) each visible satellite and extracting the

necessary ranging and satellite position information by continuously tracking the satellite signal. Once the ranging and satellite position information is extracted for a minimum of four satellites, the receiver unit computes position, velocity and timing information.

2.2 Transmitted GPS signal structure

Since the date of development, six classes (groups) of GPS satellites have been launched: Block I/II/IIA/IIR/IIR-M/IIF. Current GPS satellites belong to the group of Block IIA/IIR/ IIR-M/IIF. The most advanced class of GPS satellites called Block III are yet to be launched. Signals transmitted by the most recent family of GPS satellites (Block IIF) are listed below (Kaplan & Hegarty 2006):

- L1 centered at 1575.42 MHz. One civilian signal (C/A code, Coarse Acquisition) and two military (restricted) signals (P(Y) code and M-code) are transmitted at this frequency

- L2 centered at 1227.6 MHz. One civilian signal (L2C code) and two military (restricted) signals (P(Y) code and M-code) are transmitted at this frequency

- L5 centered at 1176.45 MHz. L5 is a civilian signal meant for safety of life applications. L5 signals have improved signal structure for enhanced performance, higher transmission power compared to L1 and L2 signals and higher processing gain.

GPS satellites use spread spectrum technique to transmit navigation data. More specifically, Direct Sequence Code Division Multiple Access (DS-CDMA) technique has been adopted. In DS-CDMA technique, data bits are multiplied with a Pseudo-Random Noise (PRN) code whose frequency is much higher than the actual data rate. PRN codes

can take values in the set {-1, +1} and each constant element of the sequence of period

T_{chip} is called chip. The process of multiplying the data bits with a high frequency PRN

code is known as *spreading* as it spreads the bandwidth of the original signal by a factor

of T_b/T_{chip} where T_b is the data bit period. The ratio T_b/T_{chip} is also known as the

Processing Gain (PG) of the system (Haykin 2001). Finally, the spread signal is

modulated using a high frequency RF carrier wave before transmission. DS-CDMA

techniques have many advantages over other modulation techniques such as:

- Multiple access capability. Many satellites can transmit their signal at the same time, all sharing the same frequency band with minimal access interference (cross correlation)

- Reasonable level of tolerance to intentional and unintentional jamming. Due to a high processing gain, CDMA techniques are more resilient against interference than other modulation techniques

- Capability to compute the time of travel of the signal. This is possibly one of the most important advantages as it serves the fundamental goal of GPS by providing the required ranging capability. The time of travel when multiplied by the speed of light provides the range between user and satellite, thus allowing the user to triangulate the signal coming from other satellites to compute its position.

In this research work, GPS L1 C/A signals are extensively considered for signal

characterization and development of weak signal processing algorithms under harsh

environments. Thus, the GPS L1 C/A signal structure and its characteristics are discussed

in this section.

The modulation scheme of a GPS L1 C/A signal is shown in Figure 2-2. The transmitted signal from i^{th} satellite can be written as

$$x(t) = \sqrt{2C_{t,i}}\, d_i(t) c_i(t) \cos\left(2\pi f_c t\right) \tag{2.1}$$

where

- $C_{t,i}$ is the transmitted carrier power

- $d_i(t)$ is the navigation data bits at 50 Hz rate. Navigation data contains information regarding GPS time, satellite clock and orbital parameters, satellite health status

- $c_i(t)$ is the PRN code at a chipping frequency of 1.023 MHz $(1/T_{chip})$ with a code length of 1023 chips. Therefore, the GPS L1 C/A code repeats every 1 ms and there are 20 repetitions of the code for each data bit period

- f_c is the center frequency of signal that is Binary Phase Shift Keying (BPSK) modulated by a carrier wave at 1575.42 MHz

The data bit sequence, $d_i(t)$, and code sequence, $c_i(t)$, can be written as follows (Haykin 2001)

$$
\begin{aligned}
d_i(t) &= \sum_{n=-\infty}^{\infty} d_i[n] g_{T_b}(t - nT_b) \\
c_i(t) &= \sum_{n=-\infty}^{\infty} c_i[n] g_{T_{chip}}(t - nT_{chip})
\end{aligned} \tag{2.2}
$$

where $d_i[n]$ and $c_i[n]$ are the sequence of data symbols and code symbols which take bipolar values, ± 1. $g_T(t)$ is a rectangular pulse given by

$$g_T(t) = \begin{cases} 1 & 0 < t < T; \ T \in \left[T_b, T_{chip}\right] \\ 0 & elsewhere \end{cases} \tag{2.3}$$
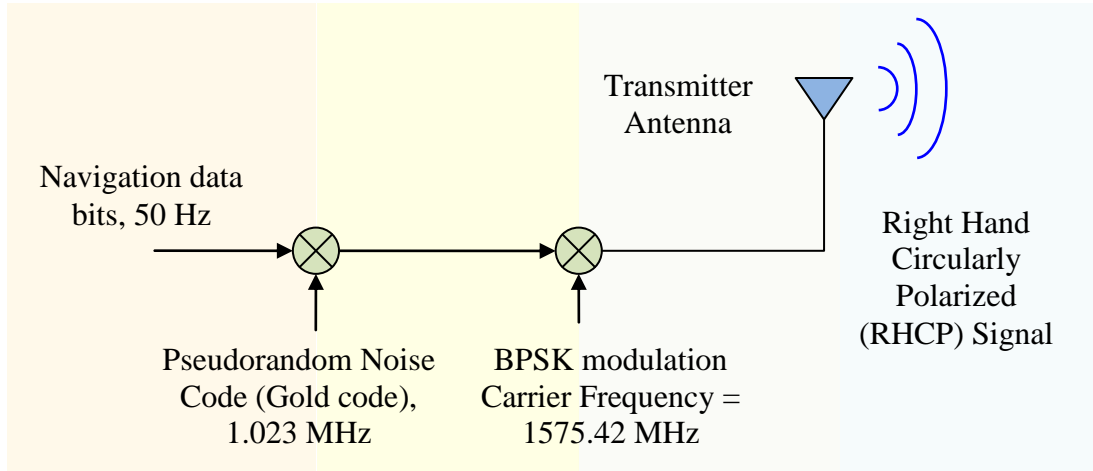
Figure 2-2: GPS L1 C/A signal transmitter architecture. 50 Hz navigation data are multiplied with a pseudorandom code (Gold code) and then BPSK modulated before transmission.

Each satellite uses a unique binary PRN, $c_i[n]$, from the family of Gold codes which carries the ranging information. Gold codes are generated by modulo-2 addition (exclusive or-ing) of two maximal length sequences (m-sequence) (Kaplan & Hegarty 2006). Gold codes are preferred over m-sequences because of its improved cross correlation properties. The normalized autocorrelation and cross-correlation of Gold codes can take four and three values, respectively (Misra & Enge 2001):

$$R_{c_i c_i} = \left\{ 1, -\frac{1}{1023}, \frac{63}{1023}, -\frac{65}{1023} \right\}$$

$$R_{c_i c_j} = \left\{ -\frac{1}{1023}, \frac{63}{1023}, -\frac{65}{1023} \right\} \tag{2.4}$$

where c_i represents the PRN code for the ith satellite and R is the correlation function expressed as

$$R_{c_i c_j}(k) = \frac{1}{N_c} \sum_{n=1}^{N_c} c_i[n]\left(c_j[n-k] \mod N_c\right). \tag{2.5}$$

In Figure 2-3(a), the blue curve shows the autocorrelation function for PRN01 whereas the red curve represents the cross-correlation between PRN01 and PRN02. Figure 2-3(b) shows the magnitude spectrum of the GPS L1 C/A signal highlighting its spectral occupation.
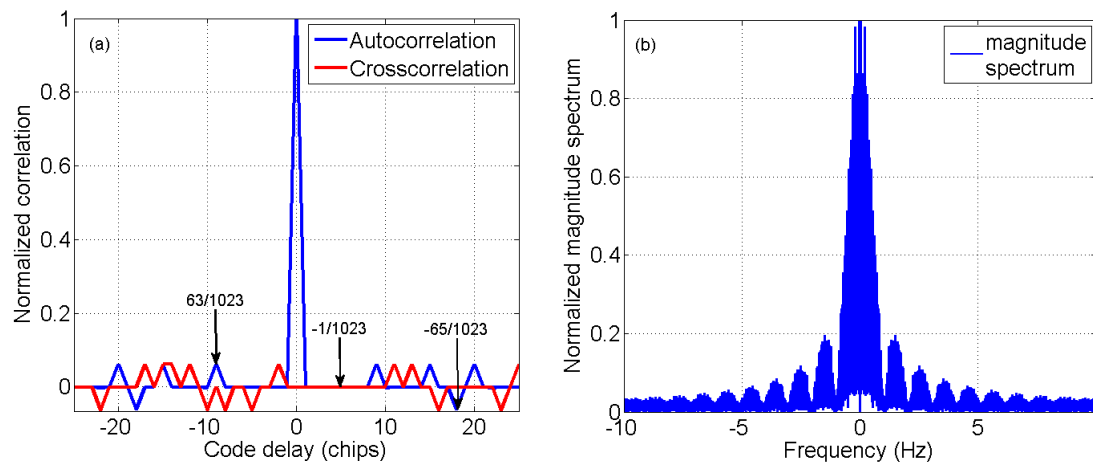
Figure 2-3: (a) Autocorrelation function for PRN01 (blue) and cross-correlation between PRN01 and PRN02 (red). (b) normalized magnitude spectrum of the GPS L1 C/A signal.

Finally, the transmitted GPS L1 C/A signal is band limited to 20.46 MHz for spurious transmission prevention. GPS L1 C/A signal transmit power levels are set to guarantee a minimum received power level of −158.5 dBW for a user equipment employing a 0 dBic antenna (GPS ICD 2010). The GPS signals are Right Hand Circularly Polarized (RHCP) and characterized by an axial ratio or ellipticity of no worse than 1.2 dB within an angle of 14.3° from bore sight (Spilker 1996).

2.3 Signal propagation mechanism

In a typical GNSS scenario, signals transmitted from any satellite experience Doppler shift due to the relative motion between satellite and receiver. Also, signals may follow multiple propagation paths before reaching the receiver antenna. In such a scenario, the receiver recovers multiple replicas of the same signal with different parameters based on the geometry of the reflectors. The multiple signals that are reflected, refracted, scattered or diffracted from different sources sum up together causing time-varying attenuation or amplification of the signal power leading to a phenomenon called fading (Rappaport 2001). In urban areas, satellite signals are also blocked by buildings and trees (shadowing), which further deteriorate the received signal power.

In a typical wireless communication channel, noise sources can be divided into two groups: multiplicative and additive (Saunders 2007). Multiplicative noise comes from various physical phenomena such as reflection, diffraction, shadowing etc. encountered by the transmitted signal before reaching the receiver antenna. Additive noise comes from different sources such as thermal agitation within the receiver, atmospheric effects, cosmic radiation and interference from other transmitters and other electrical appliances. Following subsections provide a brief summary of various noise and interference sources and their implications on the received GPS signal.

2.3.1 Free space propagation

In free space, the transmitted radio wave radiated from a point in any given direction will propagate outwards from that point at the speed of light. As the wave propagates in space, the intensity of the electromagnetic wave reduces. The deterministic relationship

between the transmitted power and received power at a distance l meters away is given by the Friis formula (Misra & Enge 2001) as

$$P_r = P_t G_t G_r \left(\frac{\lambda}{4\pi l} \right)^2 L \tag{2.6}$$

where P_t is the transmitter power, G_t and G_r are the gains of transmitter and receiver antenna respectively, λ is the wavelength of the carrier wave, l is the distance between the satellite and the receiver, and L accounts for any other losses in the chain such as rain, cloud, antenna misalignment etc. Thus, the free space propagation loss is defined by

$$FSL = 10 \log_{10} \left(\frac{\lambda}{4\pi l} \right)^2 \quad dB.$$

In case of GPS, *FSL* varies approximately between 182 to 186 dB. Considering *FSL* and other additional mismatch and processing losses, the nominal assured received signal power near the Earth surface is approximately -158.5 dBW (Kaplan & Hegarty 2006).

2.3.2 Shadow fading

The path loss model discussed in the Section 2.3.1 is capable of accurately predicting the propagation loss for a given transmitter-receiver antenna separation. However, in practice, clutter sources such as buildings and trees in the LOS path result in variations of the nominal power predicted by the path loss model. The phenomena in which the LOS signals are blocked by the natural or man-made structures such as mountains, buildings and trees resulting in power level variations are known as shadow fading (or slow fading). As pointed out in (Watson 2005), variations due to shadowing depends on the homogeneousness of the propagation medium. For example, signal variations indoors

depend on the characteristics of the materials used to build the roof tops. Structures with large electrical wiring, ventilators, duct pipes, fasteners etc. result in larger power variations as compared to plain wooden rooftops.

2.3.3 Reflection and Refraction

Reflection and refraction are two physical phenomena that can affect the propagation of an electromagnetic wave impinging on a medium having different electrical properties. In the first case (reflection), the wave partially gets reflected back to the medium from which it was originated. In the second case (refraction), the wave gets partially transmitted into the second medium (Rappaport 2001) as shown in Figure 2-4. The incident, reflected and transmitted electric filed intensities are related to each other through the Fresnel reflection coefficient which in turn depends on the properties of the medium, angle of incidence, wavelength and polarization of the electromagnetic wave (Rappaport 2001). There exists a special occasion in which a vertically (parallel) polarized signal impinging at a specific angle known as *Brewster angle* is completely transmitted though the second medium without being reflected back to the first medium. GPS signals indoors change their polarization due to various reflecting materials. In the GPS L1 C/A case, the transmitted RHCP signal can be decomposed into two orthogonal fields, horizontal and vertical to study the reflection properties.
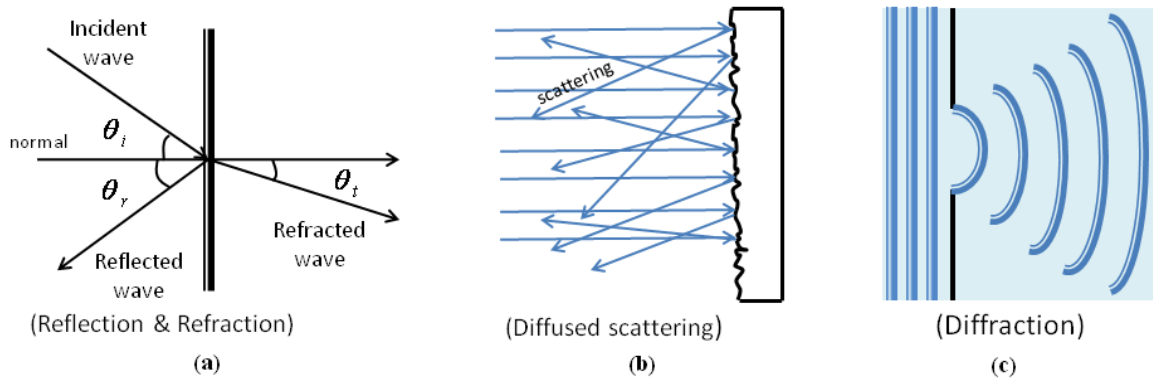
Figure 2-4: Signal propagation phenomena (a) reflection and refraction (b) diffused scattering and (c) diffraction.

2.3.4 Diffraction

Apparent bending of the waves around sharp obstacles is known as diffraction. If there exists an obstacle with sharp irregularities along the transmission path, secondary waves are generated which spread through space. This is also known as knife edge diffraction (Saunders & Aragón-Zavala 2007). The area behind the obstructions is referred to as shadowed region. A typical example of diffraction in the context of GNSS is the bending of the waves around the corners of a building in urban scenarios. The knife edge diffraction is explained by the *Huygens principle*, which states that each point on a propagating wave acts as a secondary source and can create a new wave-front that propagates into the shadow area of the obstacle as shown in Figure 2-4 (Saunders & Aragón-Zavala 2007).

2.3.5 Diffused scattering

Reflections from rough surfaces results in what is known as diffused scattering. Diffused scattering occurs when wave travels though a medium with small obstacles whose sizes are comparable to the wavelength of the wave (Saunders & Aragón-Zavala 2007).

Diffused scattering causes the impinging signal power to be reradiated in different directions with varying phase, power, and polarization as shown in Figure 2-4. Diffused scattering is highly unpredictable because of the nature of its source.

Based on the various signal propagation phenomena described in this section and their impact on the received GPS signal, fading can be broadly classified into three different subgroups namely (Saunders & Aragón-Zavala 2007):

- **Large scale fading** (also known as very slow variations, path loss) which is mainly due to the change in the distance between the transmitter and receiver;

- **Medium-scale fading** (also known as shadowing, long term variations, slow fading) which is mainly due to the momentary blockage of the LOS signal by trees, mountains, building, etc.;

- **Small scale fading** (also known as multipath fading, short term variations, fast fading) which is mainly due to the constructive and destructive nature of the multiple signals arriving at the antenna due to reflection, diffraction, refraction and scattering.

2.3.6 Thermal noise

The major source of additive noise in a GPS receiver is the thermal noise also known as Johnson-Nyquist Noise. Thermal noise is a random white process generated by thermal agitation of electrons in an electronic device and is proportional to the absolute temperature of the conductor. The thermal noise power spectral density is given by (Haykin 2001)

$$N_0 = k_b T_{sys} \quad \text{(W/Hz)} \tag{2.7}$$

where k_b is the Boltzmann constant $\left(1.3806504 \times 10^{-23} \ J/K\right)$ and T_{sys} is the system noise temperature given by $T_{sys} = T_{ant} + (F-1)T_0$ where T_{ant} is the antenna noise temperature, F is the receiver noise factor and T_0 is the reference noise temperature $(\approx 290 K^0)$. T_{ant} depends on the antenna gain pattern and the impinging noise power . In general, GPS antennas are assumed to have an antenna noise temperature of $130^0 K$ (Langley 1997). The receiver noise factor, F , is the cumulative effect of all electronic components present in the RF down conversion stage of the receiver and in given by the Friis formula (Haykin 2001)

$$F = F_1 + \frac{F_2 - 1}{G_1} + \frac{F_3 - 1}{G_1 G_2} + ... + \frac{F_N - 1}{G_1 G_2 ... G_{N-1}} \qquad (2.8)$$

where F_i and G_i represents the noise factor and gain of each component in the down conversion stage.

2.3.7 Doppler effects

Since GPS satellites are non-geostationary, there always exists a relative motion between the satellites and the user on the Earth surface. Thus, GPS communication channel is a typical LMS channel in which the transmitter is in continuous motion with respect to a static or dynamic receiver on the Earth surface. This non-linear relative motion between transmitter and receiver introduces a continuously varying Doppler shift on the transmitted frequency. The relationship between Doppler frequency and relative velocity between user and satellite can be expressed as (Kaplan & Hegarty 2006)

$$f_D = f_T \frac{\left(\vec{v}_{user} - \vec{v}_{sat}\right)\vec{u}}{c_L} \qquad (2.9)$$

where f_D is the Doppler frequency, f_T is the transmitted frequency, $\vec{v}_{user}$ and $\vec{v}_{sat}$ are the vectors representing the user and satellite velocity respectively, $\vec{u}$ is the unit vector pointing from user to the satellite and c_L is the speed of light. Since the relative velocities are different for different satellites, the Doppler frequency associated with a particular satellite is different from any other satellite. For GPS signals, the Doppler frequency can be in the range of ± 4 kHz (Kaplan & Hegarty 2006).

2.4 Received signal model

An overview of the transmitted GPS signal was provided in Section 2.2. Various natural and man-made noise sources that affect the transmitted GPS signals before reaching the receiver antenna were briefly discussed in Section 2.3. This section derives a generalized model for the received signal. Let the transmitted signal from any GPS satellite before entering the communication channel be represented as (Stüber 2002)

$$x(t) = \Re\{\tilde{x}(t)\exp(j2\pi f_c t)\} \tag{2.10}$$

where $\tilde{x}(t) = \sqrt{2C_t}d(t)c(t)$. Then, the received signal can be written as

$$y(t) = r(t) + \eta(t) \tag{2.11}$$

where $r(t)$ is the useful signal at the output of the channel and $\eta(t)$ is the additive white Gaussian noise (AWGN). Figure 2-5 shows the block diagram of a typical wireless communication channel. The useful signal at the output of the channel, $r(t)$, can be further expressed as:

$$r(t) = \Re\left\{\sum_{k=0}^{K(t)} a'_k(t)\tilde{x}\big(t - \tau_k(t)\big)\exp\Big[j2\pi\big(f_c + f_{D,k}(t)\big)\big(t - \tau_k(t)\big)\Big]\right\} \tag{2.12}$$

where $a'_k(t)$, $\tau_k(t)$ and $f_{D,k}(t)$ are the time varying attenuation factor, time delay and Doppler frequency variations associated with the kth multipath component and $K(t)$ is the total number of propagation paths present at time t. Here the attenuation factor $a'_k(t)$ encapsulate the effects of path loss, shadowing and scattering and thus can be further expanded as (Saunders & Aragón-Zavala 2007)

$$a'_k(t) = p(t)s_k(t)a_k(t) \tag{2.13}$$

where $p(t)$ is the path loss component, $s_k(t)$ is the shadow fading component and $a_k(t)$ is attenuation factor associated with the k-th reflected wave. Now, Eq. (2.12) can be rewritten as

$$r(t) = \Re\{\tilde{r}(t)\exp(j2\pi f_c t)\} \tag{2.14}$$

where $\tilde{r}(t)$ is the complex baseband equivalent of the received signal at the output of the channel and is given by

$$\tilde{r}(t) = \sum_{k=0}^{K(t)} a'_k(t)\tilde{x}(t-\tau_k(t))\exp(j\phi_k(t)) \tag{2.15}$$

and

$$\phi_k(t) = 2\pi\left[f_{D,k}(t)t - (f_c + f_{D,k}(t))\tau_k(t)\right]. \tag{2.16}$$
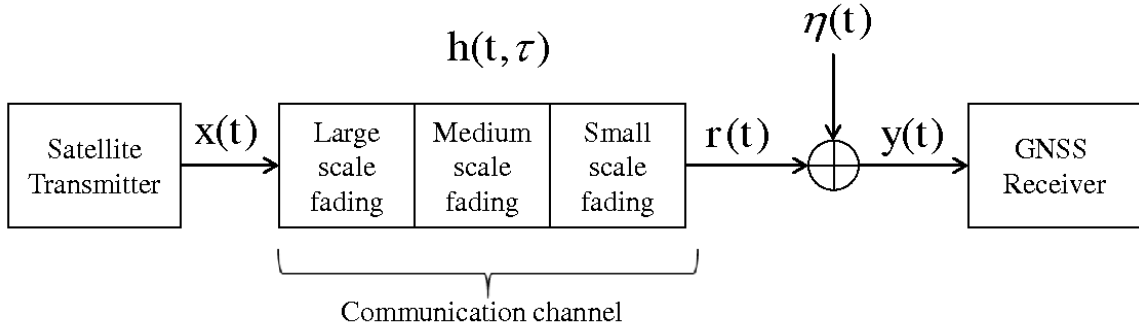
Figure 2-5: Signal propagation model: the communication channel is modeled as a time-varying linear process acting on the transmitted signal.

From Eq. (2.15), the signal at the receiver can be written as the output of a linear time-variant filter with a baseband impulse response given by (Haykin 2001)

$$\tilde{r}(t) = 0.5 \int_{-\infty}^{\infty} h(t,\tau)\tilde{x}(t-\tau)d\tau \qquad (2.17)$$

where $h(t,\tau)$ is the complex baseband impulse response given by

$$h(t,\tau) = \sum_{k=0}^{K(t)} a'_k(t)\delta\big(\tau - \tau_k(t)\big)\exp\big(j\phi_k(t)\big). \qquad (2.18)$$

Here, $h(t,\tau)$ is interpreted as response of the channel at time t due to an impulse applied at time $t-\tau$. $\delta(\cdot)$ is the Dirac delta function. The noise component, $\eta(t)$, at the input of the receiver has a constant double sided PSD $S_\eta(f) = N_0/2$ and can be represented as

$$\eta(t) = \Re\big[\tilde{\eta}(t)\exp\big(j2\pi f_c t\big)\big] \qquad (2.19)$$

where $\tilde{\eta}(t) = \eta_I(t) + j\eta_Q(t)$ is the equivalent complex baseband noise process whose power spectral density is given by $S_{\eta_I}(f) = S_{\eta_Q}(f) = N_0$ (Haykin 2001). Thus, from (2.10) to (2.19) it follows that the received complex baseband signal at the antenna input can be modelled as

$$\tilde{y}(t) = \tilde{r}(t) + \tilde{\eta}(t)$$

$$= \underbrace{\sum_{k=0}^{K(t)} a_k'(t)\tilde{x}(t - \tau_k(t))\exp(j\phi_k(t))}_{\text{LOS signal + multipath}} + \underbrace{\tilde{\eta}(t)}_{\text{AWGN}} \qquad (2.20)$$

2.5 Channel classification

From Section 2.4, it is clear that the channel output can be viewed as the output of a linear time-variant filter with impulse response $h(t,\tau)$. The channel can be considered deterministic if the impulse response is known at each time instant, t, and for all delays, τ. However in practice, the complete knowledge of the channel is seldom available. In such cases, each variable of the channel impulse response is known only in a statistical sense. Thus, the channel parameters are described through their PDF. The stochastic description of the channel enables one to simulate the impulse response at different time instants which can be used for the evaluation of different receiver algorithms. Following subsections provide an overview of deterministic and stochastic characterization of the channel. A brief description of the channel parameters such as coherence time and coherence bandwidth is also provided.

2.5.1 Deterministic and stochastic functions

A communication channel can be viewed as a linear time-variant filter with $x(t)$ and $r(t)$ as input and output, respectively. Thus, there exist four different functions that can relate the input signal and its spectrum to the output signal and its spectrum. The descriptions of these four functions are summarized below (Stüber 2002, Saunders & Aragón-Zavala 2007):

- Input delay spread function, $h(t,\tau)$, relates the output of the channel to the input of the channel in the time domain. $h(t,\tau)$ describes the delay and power associated with each reflected signal in a multipath environment.

- Time-variant transfer function, $T(f,t)$, is obtained by taking the Fourier Transform (FT) of $h(t,\tau)$ with respect to the delay, τ. This function relates the output spectrum to the input signal in time domain. $T(f,t)$ describes the spectral response of the communication channel.

- Delay-Doppler spread function, $S(\tau,v)$, is obtained by taking the FT of $h(t,\tau)$ with respect to t where v is the Doppler frequency. This function provides a measure of both delay and Doppler spread simultaneously.

- Output Doppler spread function, $H(f,v)$, is obtained as the FT of $T(f,t)$ with respect to t or as the FT of $S(\tau,v)$ with respect to τ. This function relates the output signal spectrum to the input signal spectrum.

Deterministic channel functions and their relationships are as shown in Figure 2-6(a). Stochastic description of the channel functions are given in terms of their autocorrelation function as follows (Stüber 2002, Ibnkahla 2004).

$$
\begin{aligned}
R_h(t,t';\tau,\tau') &= E\left[h(t,\tau)h^*(t',\tau')\right] \\
R_T(f,f';t,t') &= E\left[T(f,t)T^*(f',t')\right] \\
R_S(\tau,\tau';v,v') &= E\left[S(\tau,v)S^*(\tau',v')\right] \\
R_H(f,f';v,v') &= E\left[H(f,v)H^*(f',v')\right]
\end{aligned}
\qquad (2.21)
$$
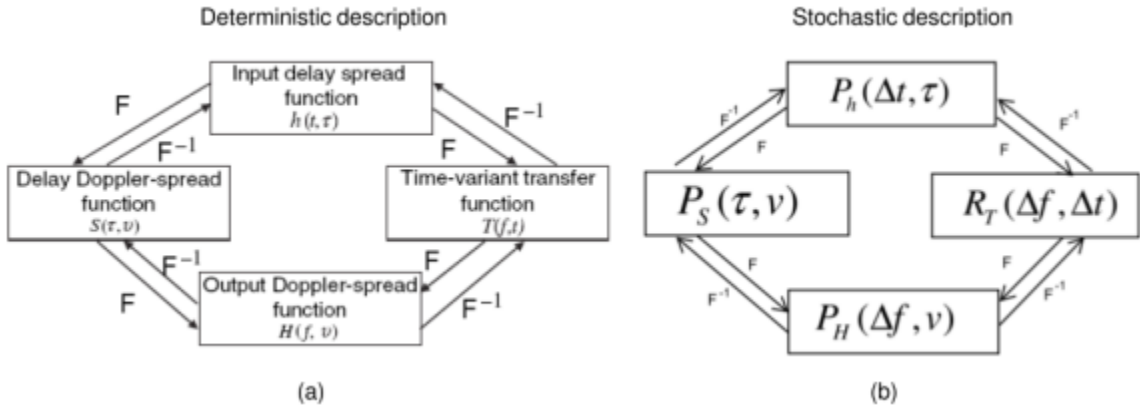
Figure 2-6: (a) Deterministic channel functions and their interrelationship. (b) Stochastic functions of a WSSUC channel.

The autocorrelation functions given in (2.21) can be further simplified by assuming the random process to be Wide Sense Stationary (WSS) and the scatterers to be uncorrelated (UC). The autocorrelation functions of such a Wide Sense Stationary uncorrelated (WSSUC) channel is given by (Stüber 2002)

$$
\begin{aligned}
R_h(t, t + \Delta t; \tau, \tau') &= \delta(\tau - \tau') P_h(\Delta t, \tau) \\
R_T(f, f + \Delta f; t, t + \Delta t) &= R_T(\Delta f, \Delta t) \\
R_S(\tau, \tau'; v, v') &= \delta(\tau - \tau') \delta(v - v') P_S(\tau, v) \\
R_H(f + \Delta f; v, v') &= \delta(v - v') P_H(\Delta f, v)
\end{aligned}
\tag{2.22}
$$

where $P_h(\Delta t, \tau)$ is known as the delay cross-power spectrum, $R_T(\Delta f, \Delta t)$ is the spaced time spaced frequency correlation function, $P_S(\tau, v)$ is the scattering function, and $P_H(\Delta f, v)$ is the Doppler cross-power spectral density (Ibnkahla 2004). Stochastic functions and their relationships for a WSSUC channel are as shown in Figure 2-6(b)

The Power Delay Profile (PDP) also known as delay power spectral density is defined as $P_h(\tau) = P_h(0, \tau)$. It describes the average received power as a function of the multipath delay parameter, τ. Assuming ergodicity, the PDP can be computed from the measured

values of the impulse response $h(t,\tau)$ as $P(\tau) = E_t \left[\left| h(t,\tau) \right|^2 \right]$ (Ibnkahla 2004). The mean

time delay (μ_τ) and rms delay spread (σ_τ) can be defined as

$$\mu_\tau = \frac{\int_0^\infty \tau P_h(\tau) d\tau}{\int_0^\infty P_h(\tau) d\tau} \; ; \; \sigma_\tau = \sqrt{\frac{\int_0^\infty (\tau - \mu_\tau)^2 P_h(\tau) d\tau}{\int_0^\infty P_h(\tau) d\tau}} \; . \tag{2.23}$$

In a similar way, the Doppler power spectral density can be defined as $P_H(v) = P_H(0,v)$.

This function can be used to measure the *average Doppler shift* and *Doppler spread* of

the channel.

The function $R_T(\Delta f, \Delta t)$ can be used to determine the *coherence time* and the *coherence*

bandwidth of the propagation channel. The function $R_T(\Delta f) = R_T(\Delta f, 0)$ is defined as the

spaced frequency correlation function and the coherence bandwidth is defined as the

smallest value of Δf for which the correlation function $R_T(\Delta f)$ is equal to some

predefines correlation coefficient such as 0.37 or 0.5 (Stüber 2002). The coherence

bandwidth provides a measure of the frequency interval in which all the spectral

components of the transmitted signal pass through a channel with equal gain and linear

phase (Rappaport 2001). Within this bandwidth, any two frequency components will have

a strong amplitude correlation. Hence, any two frequency components separated by an

interval equal or greater than the coherence bandwidth are affected differently by the

channel. Since $P_h(\tau)$ and $R_H(\Delta f)$ are related through the FT, the inverse of the rms

delay spread is proportional to the coherence bandwidth of the channel.

In a similar way, the spaced time correlation function, $R_T(\Delta t) = R_T(0, \Delta t)$, is used to define the coherence time of the channel. The coherence time can be interpreted as the time period during which the channel impulse response remains invariant *or* the time duration over which two received signals have potential strong amplitude correlation (Rappaport 2001). The coherence time characterizes the time varying nature of a frequency dispersive channel. Since $P_H(v)$ and $R_H(\Delta t)$ are related through the FT, inverse of the Doppler spread is proportional to the coherence time of the channel.

2.5.2 Types of small scale fading

From Section 2.5.1, it is clear that there exist two different independent phenomena affecting the received signal namely, the time and frequency dispersion. Time dispersion refers to the range of values over which the transmitted signal is spread over time. Frequency dispersion refers to the range of frequencies over which the signal spectrum is spread. In practice, these two independent processes lead to four different types of fading, namely (Ibnkahla 2004):

- **Frequency non-selective fading**: the coherence bandwidth of the channel is higher than the transmitted signal bandwidth. Since the transmitted bandwidth is narrow as compared to the channel bandwidth, this type of channels is also known as *narrowband* channels or *flat fading* channels.

- **Frequency selective fading**: the coherence bandwidth of the channel is smaller than the transmitted signal bandwidth. Since the transmitted bandwidth is wide as compared to the channel bandwidth, this type of channels is also known as

wideband channels. Here, the different spectral components of the transmitted signals are affected by different channel gain and phase response.

- **Time non-selective fading**: the coherence time of the channel is greater than the transmitted symbol period. This type of channels is also known as *slow fading* channel. The term *slow fading* here, should not be confused with the slow fading caused by the shadowing process. Since the coherence time is greater than one symbol duration, the energy of the signal is preserved during the coherent integration performed during the correlation process in GNSS signal processing.

- **Time selective fading**: the coherence time of the channel is smaller than the transmitted symbol period. This type of channels is also known as *fast fading* channel.

In practice, real communication channels are both time and frequency dispersive. This means that the channel in reality can be a combination of narrowband or wideband with fast/slow fading. Earlier studies show that the rms delay spread of GNSS signals in suburban environments and indoors is less than one tenth of a GPS L1 C/A PRN code chip (Jost & Wang 2009, Steingass & Lehner 2007), i.e. $\sigma_\tau << T_{chip}$. Based on the classifications described above, it can be safely assumed that the GPS signals under such environments experience a frequency non-selective fading and its channel can be categorized as a narrowband. The narrowband channel hypothesis implies that $x(t - \tau_k(t)) \approx x(t - \tau'(t)) \forall k$. Thus, Eq. (2.15) can be further simplified as

$$\tilde{r}(t) = \tilde{x}\big(t - \tau'(t)\big) \sum_{k=0}^{K(t)} a_k'(t) \exp\big(j\phi_k(t)\big)$$

$$= \tilde{x}\big(t - \tau'(t)\big) h(t) \qquad\qquad (2.24)$$

$$= \tilde{x}(t) * \big[h(t)\delta(\tau - \tau'(t)) \big]$$

If $\tilde{x}(t) = 1$, then the output of the channel completely characterizes the impulse response of the channel, $h(t)$. In general, narrowband channels are characterized based on first and second order statics of the received signal envelope. In the following section, a brief summary of various narrowband fading models is provided.

2.6 Narrowband fading models

This section provides an overview of various existing statistical models used to describe the effect of the communication channel on the transmitted signal. As mentioned earlier, the first and second order statistics are used to capture the fading effects. More specifically, the first order statistics refer to the distribution of the incoming signal envelope and second order statistics refer to its temporal/spectral characteristics such as ACF, PSD, LCR and AFD (Ibnkahla 2004).

2.6.1 First order statistics

As explained earlier, the received signal at the ground terminal is affected by all three kinds of fading phenomena: large scale, medium scale and small scale fading. In general, the PDF of the received signal amplitude depends on the nature of the environment and their dynamics. For example, a homogenous medium may result in a stationary fading process, whereas, significant change in the propagation medium (non-homogenous) may result in a nonstationary fading process. For example, an antenna mounted on a moving car in an urban environment experiences nonstationary fading phenomena wherein the

GNSS signals are momentarily blocked by buildings causing significant power variations. Based on the nature of the process, existing statistical models that describe the PDF of the received signal amplitude can be classified into three groups namely; *single, composite* and *mixture* models (Abdi et al. 2003). Single models describe the behaviour of the channel with a single distribution. For example, effects due to multipath scattering alone are well described by well known distributions such as Rayleigh, Rice, Nakagami-m, Weibull, Hoyt, Beckmann, etc (Simon 2004). Shadowing effect can be described by Log-Normal distribution. When a channel experiences both multipath scattering and shadowing, the net effect can be described by a single composite distribution which accounts for both multipath scattering and shadowing effect. Mixture models are weighted combinations (where the weights are time varying) of single/composite models. In the following paragraphs, a brief overview of various existing single/composite/mixture models is described.

2.6.1.1 Single state models

Neglecting the effect of shadowing and path loss, from Eq. (2.24), the received signal due to multipath scattering alone can be written as

$$\tilde{r}(t) = \sum_{k=0}^{K(t)} a_k(t) \exp\left(j\phi_k(t) \right) \qquad (2.25)$$

where it is assumed that $\tilde{x}(t) = 1$. Then the envelope of the received signal is given by $z(t) = \left|\tilde{r}(t)\right|$. Traditionally, in narrowband fading scenarios, the random variable $z(t)$ is modeled using standard distributions such as Rayleigh, Rice and Nakagami-m (Hashemi 1993). In a sufficiently scatter rich environment, under the presence of a strong LOS

component, inphase component, $\tilde{r}_I(t)$, and quadrature phase component, $\tilde{r}_Q(t)$, can be

modeled as $\tilde{r}_I(t) = \mathcal{N}(a_0 \cos(\theta_0(t)), \sigma_u^2)$ and $\tilde{r}_Q(t) = \mathcal{N}(a_0 \sin(\theta_0(t)), \sigma_u^2)$ respectively,

where a_0 and $\theta_0(t)$ are the amplitude and phase variations associated with the LOS

component (Stüber 2002) and σ_u^2 is the variance representing the scattered power. Under

such scenarios, the envelope of the received signal is modeled using the Rice distribution

given by (Stüber 2002)

$$f_Z(z) = \frac{z}{\sigma_u^2} \exp\left\{ \frac{-\left(z^2 + a_0^2\right)}{2\sigma_u^2} \right\} I_0\left(\frac{a_0 z}{\sigma_u^2} \right), \qquad z \geq 0 \qquad (2.26)$$

where $I_0(\cdot)$ is the modified Bessel function of the first kind and zero order. The Rice

Factor K is defined as the ratio of the LOS signal power to the scattered power as

$K = a_0^2 / (2\sigma_u^2)$. A high value of K indicates the presence of a strong LOS component. It

should be noted that under the absence of a LOS component, i.e. when $K = a_0 = 0$, Eq.

(2.26) reduces to a standard Rayleigh model.

A more realistic model for the received signal envelope known as Nakagami-m

distribution was proposed by Nakagami (Hashemi 1993). This distribution was selected

to fit the empirical data better than standard distributions such as Rayleigh and Rice. The

Nakagami-m distribution takes in to account the fact that different signal rays can have

unequal power levels. The Clarks Rayleigh model assumes equal power levels. It should

be noted that the Rayleigh distribution is a special case of the Nakagami-m distribution.

The Weibull distribution is yet another mathematical description of a probability model

for characterizing amplitude fading in a multipath environment. The Weibull distribution

does not have a theoretical justification for its utilization in channel modelling (Hashemi 1993) but it contains Rayleigh as a special case.

On the other hand, shadowing occurs when transmitted signals are blocked by geographical features like mountains, buildings and trees as the receiver moves from one place to another. This results in slow variations of the mean signal power levels. This local mean can be modeled as a random variable due to the shadow variations that are caused by geographical obstructions between satellite and receiver. This variation is traditionally modeled using a Log-Normal distribution (Stüber 2002):

$$f_S(s) = \frac{20/\ln(10)}{\sqrt{2\pi}\sigma_s s} \exp\left\{-\frac{(20\log_{10}(s)-\mu_s)^2}{2\sigma_s^2}\right\}, \quad s \geq 0 \qquad (2.27)$$

where μ_s and σ_s^2 are the mean and variance of the Log-Normal process respectively. In (Coulson et al. 1998, Griffiths & McGeehan 1982), it has been shown that the Generalized Gamma model can be used to describe shadowing variations as well. Similar results were observed in (Abdi & Kaveh 1999). The advantage of using the gamma distribution over the Log-Normal one is its mathematical tractability. More specifically, closed form expressions can be obtained for composite models involving both multipath and shadow fading. The Generalized Gamma distribution has the form

$$f_Z(z) \propto z^\alpha \exp(-z^\beta) \qquad (2.28)$$

where the parameter α models the severity of the fast fading component whereas β accounts for the severity of shadow fading. The Generalized Gamma distribution has received an increased attention during past few years due to the fact that it not only

contains a wide class of distributions such as Weibull, Nakagami-m, Gamma and others but it also properly describes combined fast fading and shadowing effects.

2.6.1.2 Composite models

Composite envelope fading models describe both shadowing and multipath phenomena using a single distribution. Suzuki (1977) showed that the received signal envelope in an urban environment could be represented as the product of the multipath faded envelope and shadow fading. The rationale behind Suzuki model is that, the envelope of the main wave arriving at a cluster of buildings represents a random variable which is subjected to the influence of propagation phenomena such as reflection, diffraction, etc. Upon arriving at the cluster, it undergoes local scattering which results in several sub-paths reaching the receiver roughly at the same time with different carrier phases. According to Suzuki, the received signal can be modeled as

$$\tilde{r}(t) = s(t)\tilde{u}(t) \tag{2.29}$$

where the shadow fading component $s(t)$ is modelled as a Log-Normal process and the multipath fading component $\tilde{u}(t)$ is modelled as a Rayleigh process independent from $s(t)$. In that case, the distribution of the received signal envelope $z(t) = |\tilde{r}(t)|$ can be determined using the relationship

$$
\begin{aligned}
f_Z(z) &= \int_0^\infty \frac{1}{|\xi|} f_{S\xi}\left(\frac{z}{\xi}, \xi\right) d\xi \\
&= \int_0^\infty \frac{1}{|\xi|} f_S\left(\frac{z}{\xi}\right) f_\xi(\xi) d\xi
\end{aligned}
\tag{2.30}
$$

where $\xi = |\tilde{u}(t)|$, $f_\xi(\cdot)$ and $f_S(\cdot)$ are the PDFs of multipath fading envelope and shadow fading envelope, respectively.

Loo (1985) introduced an additive combination of Rayleigh and Log-Normal distributed random phasors in which shadowing affects only the LOS component, while the scattered components are not shadowed. The resulting signal can be represented as (Loo 1985)

$$\tilde{r}(t) = s(t)\exp(j\theta_0(t)) + \tilde{u}(t) \tag{2.31}$$

where $s(t)$ is modelled as a Log-Normal process and $\tilde{u}(t)$ is modelled as Rayleigh process and independent from $s(t)$. In that case, the resulting distribution of signal envelope is given by

$$f_Z(z) = \int_0^\infty f_S(z-\xi) f_\xi(\xi)d\xi \tag{2.32}$$

.

Loo model was further modified (Corazza & Vatalaro 1994) assuming that shadowing may affect both the LOS component and the scattered components and a more general form of the Suzuki model was proposed considering the LOS component where $\tilde{u}(t)$ in (2.29) is modelled as a Rice process.

Vatalaro (1995) further divided the diffuse component in two independent components in which the first component is modeled as a shadowed Rice process and the second component is modeled using an unshadowed Rayleigh process. The model is thus (Vatalaro 1995)

$$\tilde{r}(t) = s(t)\tilde{u}_1(t) + \tilde{u}_2(t). \tag{2.33}$$

where $\tilde{u}_1(t)$ and $\tilde{u}_2(t)$ are Rice and Raleigh process respectively. Hwang et al (1997) proposed a new model involving direct and diffused components affected by independent shadow process as

$$\tilde{r}(t) = s_1(t)\exp(j\theta_0(t)) + s_2(t)\tilde{u}(t).$$ (2.34)

Several other composite models proposed in the literature are listed in (Abdi et al. 2003). Another class of composite models based on double scattering has been recently proposed in the literature (Ye & Satorius 2003). The rationale behind this process is that the satellite signal passes through ionosphere before reaching the Earth surface. Thus, ionosphere scatters the signal which can be modelled as Rice or Nakagami-m. Further, when the wave arrives at the Earth surface, due to local scattering, the wave gets further dispersed which can be modelled using Rayleigh or Rice distributions. Since these two phenomena are independent of each other, the overall process can be modelled using a double Rice distribution (product of two independent Rice processes).

2.6.1.3 Mixture models

Mixture models are used to describe the envelope statistics under non-stationary channel conditions. Mixture models are in general, a combination of single and/or composite models, such that different PDFs are used to describe the envelope characteristics under different conditions in a non-stationary channel. Mixture models use the received signal power to distinguish between channel states. For example a two state GOOD/BAD model proposed by (Lutz et al. 1991) is as shown in Figure 2-7. In such a case the overall distribution is given by

$$f_{overall}(m) = p_{Good}f_{Good}(m) + p_{Bad}f_{Bad}(m)$$ (2.35)

where p_{Good} and p_{Bad} are the probability of the channel being in the GOOD (with LOS and moderate multipath) and BAD (partially blocked, large scale shadowing) state. f_{Good} and f_{Bad} are the PDFs under GOOD and BAD state, respectively. In practice, the transition between GOOD and bad state are modeled using a first order discrete time Markov chain. Parameters for each state and state transitions are computed based on the measurements under different environments and elevation angles of the satellite. List of other mixture models proposed in the literature can be found in (Abdi et al. 2003, Ibnkahla 2004).
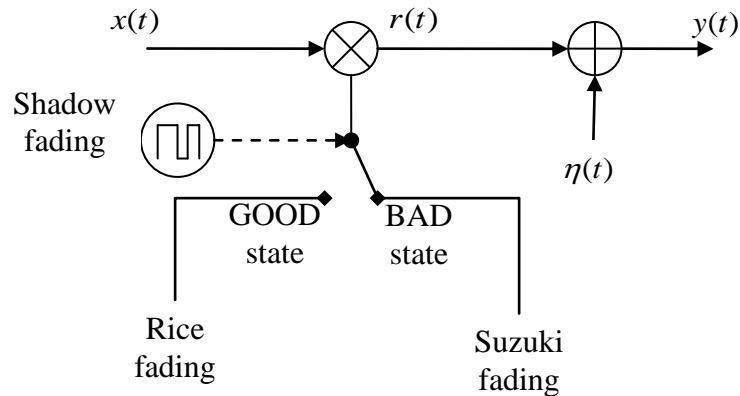
Figure 2-7: Lutz dynamic mixture model of a LMS channel.

2.6.2 Second order statistics

Second order characterization involves the extraction of information on the temporal behaviour of the received signal envelope. First order statistics such as PDF can only capture the dynamic range of the signal envelope but it fails to convey information on its temporal behaviour. This means that the PDF of the signal amplitude does not convey any information on how fast or slow the signal is varying with respect to time. Thus, it becomes crucial to characterize second order statistics of the fading process.

ACF is the most commonly used function to characterize a fading process. ACF provides a measure of channel coherence time. Assuming the fading process to be wide sense stationary, the ACF can be obtained using Eq. (2.22) as $R_T(0, \Delta t)$. Standard expressions of the ACF and PSD for the Rayleigh and Rice process can be found in (Stüber 2002).

LCR, L_Z, defines the average rate (times/second) at which signal envelope crosses a specific threshold Z upwards (or equivalently downwards) (Stüber 2002).
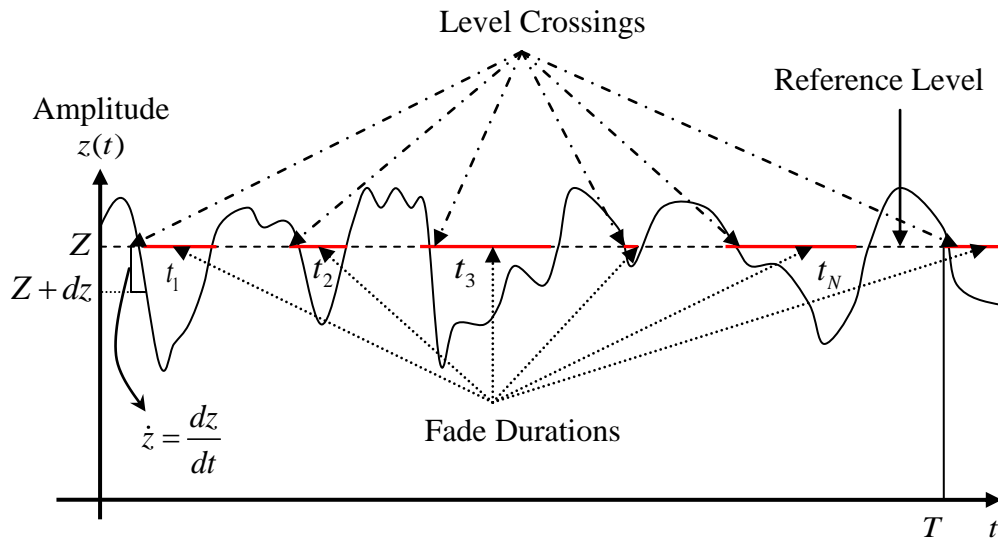
Figure 2-8: Graphical representation of LCR and AFD.

The computation of L_Z requires the knowledge of the joint distribution, $f(z, \dot{z})$, of the signal envelope, z, and its derivative $\dot{z}$. A generalized expression of LCR involving the joint distribution $f(z, \dot{z})$ can be written as follows (Stüber 2002)

$$L_Z = \int_0^\infty \dot{z} f(Z, \dot{z}) d\dot{z}. \tag{2.36}$$

In practice, the random variables z and $\dot{z}$ are assumed to be independent. Thus $f(z, \dot{z})$ can be expressed as product of two independent PDFs, $f(z)$ and $f(\dot{z})$.

Average fade duration (AFD) is defined as the average time that the signal envelope stays below a specific threshold level Z. Let t_i denote the time duration that the signal envelope stays below the threshold level Z in its ith crossing over a time interval T as shown in Figure 2-8. Assuming $z(t)$ stationary and ergodic and for T sufficiently large, the cumulative density function (CDF) of the signal can be written as (Stüber 2002)

$$F_Z(z) = p\big(z(t) < Z\big) \approx \frac{1}{T} \sum_i t_i . \tag{2.37}$$

Thus, the average fade duration can be written as

$$T_Z = \frac{1}{L_Z T} \sum_{i=1}^{L_Z T} t_i \approx \frac{p\big(z(t) < Z\big)}{L_Z} = \frac{F_Z(z)}{L_Z} \tag{2.38}$$

Standard expressions of LCR and AFD for standard fading models can be found in (Stüber 2002).

2.7 Summary

In this chapter, a brief description of the GPS signals structure and its characteristics were provided. Various signal propagation mechanisms and their impact on the transmitted GPS signals were discussed. It was highlighted that the GPS signals are affected by all three types of fading namely large scale, medium scale and small scale. Sub classifications of small scale fading were further discussed and in particular, the pertinence of narrowband fading channels with respect to GPS scenario was highlighted. An overview of various existing first and second order statistical models used to describe narrowband fading phenomena was provided. In the following chapters, the applicability and usefulness of various existing statistical models are analyzed and validated in the context of GPS scenarios using real signals.

Chapter Three: **CHANNEL CHARACTERIZATION METHODOLOGY AND WEAK SIGNAL POWER ESTIMATION**

Channel characterization is the art of analyzing the behaviour of a wireless propagation medium through experiments. Here, the communication channel is treated as a black box with an unknown transfer function. The output of the channel is analyzed using predefined input signals such rectangular pulses with fixed widths and/or sinusoids at pre-defined frequency to determine the channel input-output relationship (Jost & Wang 2009, Steingass & Lehner 2003). More specifically, as discussed in the previous chapter, the signals transmitted by the satellites experience a time varying fading phenomena before reaching the receiver antenna. In this research work, the signals transmitted by real GPS satellites are used to analyze the behaviour of the GNSS communication channel. In the current and subsequent chapters, the GPS communication channel has been characterized using real signals and various theoretical models of a typical LMS channel have been considered and analyzed in light of the experiment findings.

In this chapter, a brief overview of the adopted GNSS signal characterization approach is provided along with a detailed description of the signal measurement and characterization methodology adopted in this research work. Finally, the accuracy and reliability of the adopted methodology is validated using software and hardware simulations. Towards this, a detailed methodology to accurately measure real GPS signals as weak as -165 dBm with a predefined level of accuracy is presented.

3.1 Characterization approaches

Measuring real GPS signals in harsh environments such as indoors is itself a challenge due to the low signal strength and other impairments. This is due to the fact that the signals transmitted by any GPS satellite travel a long distance (20200 km) before reaching the receiver antenna resulting in high level of free space propagation loss. In addition, factors such as excess attenuation caused by walls, roofs and multipath results in deep signal fading which makes measuring GPS signals even harder. Thus, the accurate measurement of real GPS signals is difficult and challenging in such harsh environments.

In any standard GPS receiver, the incoming signal is correlated with a local replica of itself. The PRN code and carrier are removed to bring the signal to baseband and de-spread the signal spectrum. Later the demodulated signal is coherently integrated to raise the signal power above the noise floor. Long coherent integration provides sufficient processing gain in order to separate the useful signal from the background noise. However, long coherent integrations are limited by two main factors namely *data modulation* and *synchronization errors*.

In the case of GPS L1 C/A signals, navigation data symbols can introduce an 180° phase shift every 20 ms on the BPSK modulated carrier. Thus, coherent integration beyond 20 ms may result in destructive signal power accumulation. Integration beyond 20 ms is not possible without the *a priori* knowledge of the data bits. On the other hand, frequency and code phase mismatch between the incoming and local replica signal will result in synchronization losses. Major factors which result in frequency mismatch during long coherent integrations are the receiver clock drift, motion induced Doppler and multipath

induced phase errors. In order to overcome these limitations, several approaches have been adopted in the past to increase the processing gain and accurately characterize the GPS communication channel. Existing GPS characterization methods can be broadly classified into three groups:

- **High sensitivity receiver approach:** a high sensitivity standalone/assisted GPS receiver is used to measure weak GPS signals (Blunck et al. 2009). Commercially available off-the-shelf high sensitivity receivers capable of tracking weak signals of the order of -160 dBm are used to make measurements in various harsh environments. One of the disadvantages of this type of approach is that only the measurements provided by the commercial receiver are available for any kind of analysis. The commercial receiver is often used as a black box and its measurements are highly dependent on the synchronization algorithms implemented. Also, the measurements obtained from high sensitivity receivers are very noisy which might influence the results of the channel characterization.

- **Pseudolites and/or channel sounding approach:** In this approach, pseudolites (pseudo-satellite broadcasting GPS-like signals) are used with a very high gain transmitter in to overcome the high level of attenuation caused by external walls and rooftops (Islam et al. 2008). Here GPS-like transmitters are placed outside the building either on a fixed pole, crane (Paonni et al. 2008) or helicopter (Teuber et al. 2008). Again, based on this configuration, two synchronized receivers can be used to get the measurements, one directly from the transmitter and the other from an indoor receiver. Here, the receiver has a fairly good knowledge about the time and type of the signal waveform that is being transmitted which helps in characterizing most of

the signal parameters. One of the disadvantages is that the signal variations due to ionosphere and troposphere are ignored.

- **Reference–rover approach:** The third option is to get measurements from a pair of receivers that are synchronized to very high accuracy levels (Peterson et al. 1997). Here, the first receiver (reference) is placed in an open sky environment and the second receiver (rover) is placed in a harsh environment. The measurements such as Doppler frequency and navigation data bits obtained from the outdoor receiver can be effectively used to enable long coherent integration of signals from the rover receivers. This procedure is exploited in many of the previous research works that aim at characterizing real GPS signals (Peterson et al. 1997, Lakhzouri et al. 2005)

In this research work, the receiver-rover approach has been adopted: one receiver is used to collect outdoor GPS L1 C/A data and one or more receivers are used to collect real GPS signals under signal degraded environments. Further details of the test setups and the characterization approach are explained in the subsequent sections.

3.2 Measurement setup

The experimental test setup for collecting real GPS signals simultaneously requires the presence of multiple RF front-ends. Data collections have been made possible using two different National Instruments signal analyzers (National Instruments 2006) that provide simultaneous and synchronous IF data. The two signal analyzers are composed as follows:

- **NI-1**, a platform consisting of three RF down converters (PXI-5600) along with three high speed digitizers (PXI-5142) on a PXI-1065 chassis. NI-1 is able to

acquire signals in three different bandwidths with a sampling frequency up to 25 MHz, I/Q sampling

- **NI-2**, a platform consisting of two RF down converters (PXI-5600) along with two high speed digitizers (PXI-5622) on a PXI-1075 chassis. NI-2 has similar processing characteristics as that of the NI-1 system.

Figure 3-1 shows a sample test setup involving the two NI signal analyzers. The channels of each signal analyzer can be driven by the same clock and can be configured to provide synchronous sampling. The possibility of having dataset synchronously sampled allows several processing opportunity such as joint processing of several data channels. This also includes aiding (down to the sample level) from a reference channel.

Figure 3-1: Two National Instruments signal analyzers each having multiple RF down converters and digitizers.

In the most complex data collection considered in this thesis, the two NI systems were used simultaneously as shown in Figure 3-2. In this case, the two NI systems were driven by the same clock. The first channel of each platform is used to collect data from an antenna placed outdoors in open-sky conditions. Up to three antennas can be used to collect data in signal degraded environments.
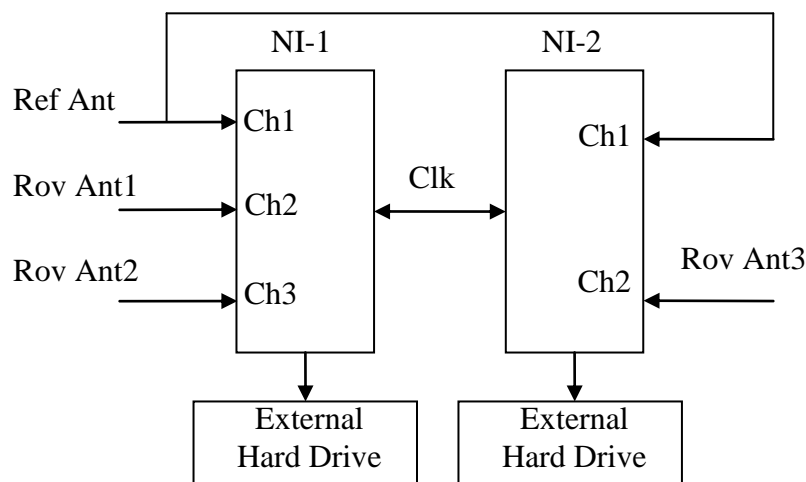
Figure 3-2: Data collection setup using two National Instruments platforms.

Each channel incorporates a super heterodyne architecture wherein the incoming RF signal is down converted to IF before further processing. More specifically, the signal received by the antenna is passed through a Low Noise Amplifier (LNA) and a bandpass filter before the mixer stages. The LNA limits the noise figure of the system and the bandpass filter removes any out of band (or image frequency) spurious components entering the mixer stage. The signal is then down converted to IF in multiple stages in order to provide improved image frequency rejection performance. The NI RF down converters have an IF bandwidth of 20 MHz centered around 15 MHz. The down-converted IF signal is then digitized by the NI digitizers at very high sampling rates. Then, the sampled signal is digitally down converted (complex down conversion) and re-

sampled to produce the desired IF and sampling rate. Finally, the digitized samples are stored on an external hard drive and later post processed using software receivers. Thus, the digitized samples obtained in this way can be represented as:

$$\tilde{y}_{IF}[i] = \sqrt{\frac{C_t}{2}} \sum_{k=0}^{K_T[i]} a'_k[i] d\left[iT_s - \tau_k[i]\right] c\left[iT_s - \tau_k[i]\right] \exp\left(j\phi_k[i]\right) + \tilde{\eta}_{IF}[i] \qquad (3.1)$$

where $\tilde{y}_{IF}[i]$ are the digitized IF samples and $\tilde{\eta}_{IF}[i]$ is the noise sequence obtained by down converting and digitizing $\eta(t)$ as

$$\tilde{\eta}_{IF}[i] = \frac{1}{2} \Re\left\{\tilde{\eta}[i] \exp(-j2\pi f_{IF} iT_s)\right\} \qquad (3.2)$$

The frequency domain representation of $\tilde{y}_{IF}[i]$ is shown in Figure 3-3. Here, an ideal low pass filter with cut-off frequency $B_{IF} = f_s / 2$ is assumed, where f_s represents the sampling frequency. Thus, under the assumption of $f_s = 2B_{IF}$, the noise power at the output of the digitizer is given by

$$\sigma_{\eta_I,IF}^2 = \sigma_{\eta_Q,IF}^2 = \int_{-B_{IF}}^{+B_{IF}} \frac{N_0}{4} df = \frac{N_0}{4} f_s = \frac{N_0}{4T_s} \qquad (3.3)$$
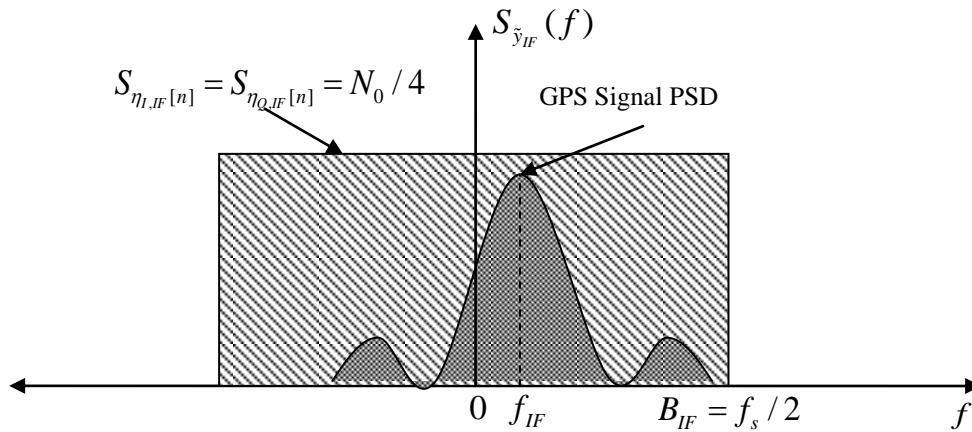
Figure 3-3: PSD of GPS signal and noise component at the output of the digitizer.

3.3 Reference-rover processing

In order to speed-up and facilitate the data processing and analysis, the PLAN group software receiver, GSNRx-rr™ has been used in this research work. GSNRx-rr™ is an enhanced version of the standard GSNRx™ (Petovello et al. 2009) software receiver and allows the joint processing of several sample sources. More specifically, the modified software GSNRx-rr™ accepts several input files where:

- the first input file is supposed to contain raw samples from a reference antenna containing clear-sky data

- the additional input files contain samples from rover antennas for example in indoor environments.

A configuration text file defines the settings for GSNRx-rr™ and contains information such as

- reference and rover data file paths

- number of rover channels

- code phase and Doppler frequency uncertainty grid

- rover coherent integration time.

GSNRx-rr™ is used jointly with the NI data acquisition system. Thus, data simultaneously collected using the NI systems are affected by the same clock errors that are removed by the differential processing performed by GSNRx-rr™. This allows the removal of common errors affecting reference and rover signals. Reference-rover processing using GSNRx-rr™ is accomplished as follows. The incoming digitized samples from the reference channel are continuously tracked by correlating it with a

locally generated replica as shown in Figure 3-4. The correlation process involves the generation of local complex carrier and code matching the phase and delay of the incoming C/A signal. The locally generated and incoming signals are multiplied and integrated over the integration time, T_c. The correlator outputs are further processed by the Baseband Processing Block (BPB). BPB includes carrier and code discriminators, loop filters and Numerically Controlled Oscillators (NCO). At the end of each T_c second, BPB updates the local NCOs with new values of code and carrier phase and/or frequency values. Thus, BPB is responsible for maintaining the code and carrier synchronization between the incoming reference signal and its locally generated replica. GSNRx-rr™ evaluates the complex correlators of the rover signals specified in a Doppler/code delay grid as shown in Figure 3-4. The centre point of the correlator grid corresponds to the Doppler frequency and code delay estimated from the reference channel. In this way, GSNRx-rr™ effectively operates in a differential mode where the parameters of the rover channels are determined with respect to the reference values.

The navigation bits estimated from the reference channel are used to wipe off the data modulation effect on the complex correlator outputs of the rover channels. Finally, rover Doppler frequency and code delay estimates are generated by interpolating the complex correlators evaluated by the rover channels and finding the position of the correlation maximum in the correlator search space. Complex correlator outputs along with pseudorange and carrier phase measurements for both reference and rover channels are stored onto a text file. These text files are further processed using post processing software developed in Matlab to extract the fading characteristics.
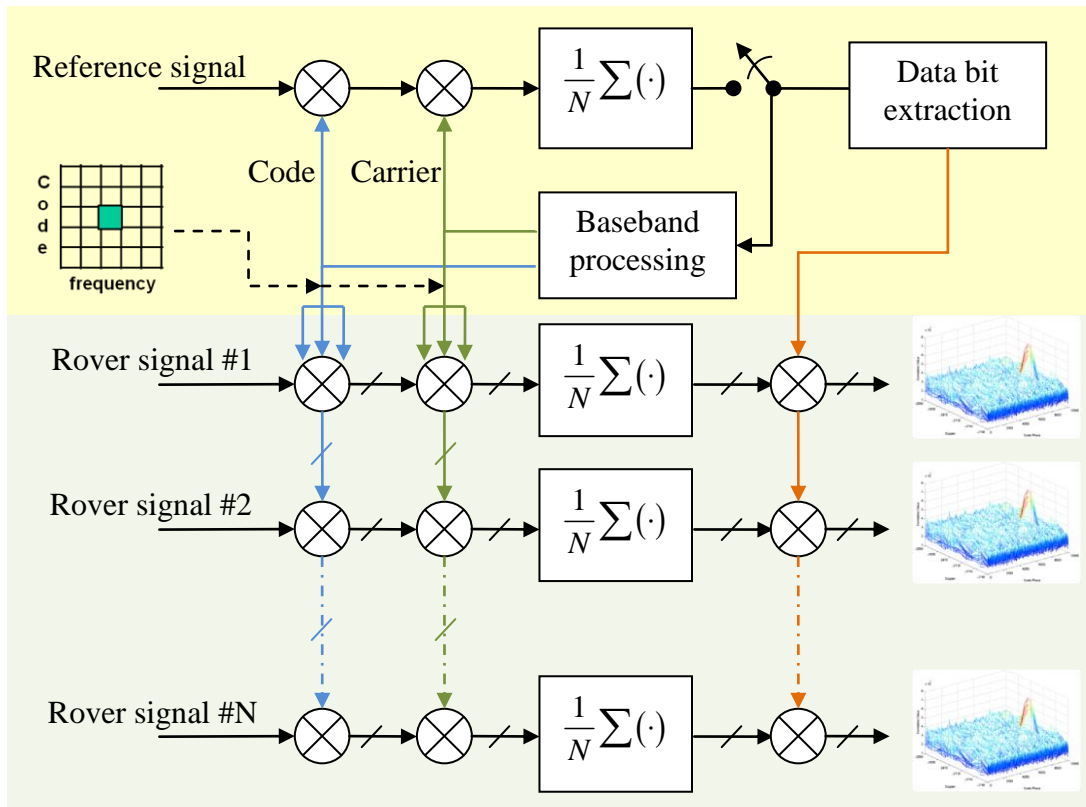
Figure 3-4: Reference-rover signal processing architecture adopted in GSNRx-rr[TM].

Under the assumption of perfect frequency synchronization (due to RR processing strategy), it is possible to show that the complex correlator outputs can be expressed as (Kaplan & Hegarty 2006)

$$\tilde{w} = \sqrt{\frac{C_t}{2}} \sum_{k=0}^{K_T} a_k' R(\Delta\tau_k) \exp\{j(\Delta\theta_k)\} + \tilde{\eta}' \tag{3.4}$$

where

- $R(\cdot)$ is the normalized autocorrelation function of the GPS L1 C/A code

- a_k', $\Delta\tau_k$ and $\Delta\theta_k$ are the attenuation factor, code delay and carrier phase difference between the locally generated signal and the kth multipath signal over the integration time T_c

- $\tilde{\eta}' = \eta_I' + j\eta_Q'$, where η_I' and η_Q' are two independent Gaussian noise processes with zero mean and variance $\sigma^2 = N_0 / (4T_c)$.

In Eq. (3.4), it is assumed that the multipath parameters are constant over the integration interval T_c. Correlator outputs given by Eq. (3.4) can be further expressed as

$$\tilde{w} = \sqrt{\frac{C_t}{2}}\,\beta\exp\left(j\varphi\right) + \tilde{\eta}' \tag{3.5}$$

where $\beta\exp\left(j\varphi\right) = \sum_{k=0}^{K_T} a_k' R(\Delta\tau_k)\exp\left\{j\left(\Delta\theta_k\right)\right\}$. Here, β represents the net attenuation factor and φ represents the net phase difference between the incoming signal and the local replica. Thus, the correlator outputs can be modelled as

$$\tilde{w} \sim \mathcal{CN}\left(\sqrt{\frac{C}{2}}\exp\left\{j\varphi\right\}, \frac{N_0}{4T_c}\right) \tag{3.6}$$

where $C = C_t\beta^2$ is the received carrier power and $\mathcal{CN}(a,b)$ denotes a complex Gaussian process with mean a and variance b. The correlator outputs of the rover signals obtained using RR processing are further processed to extract the fading parameters of the GPS communication channel. In the following section, a brief summary of various channel parameters considered in this work are summarized.

3.4 Characterization parameters

In Chapter 2, an overview of various fading phenomena and the corresponding parameters that characterize them was presented. The applicability of the narrowband fading hypothesis for a typical GNSS scenario was also highlighted. An effective

procedure for measuring and processing GNSS weak signals was presented in Section 3.1 to 3.3. In this section, additional channel parameters that characterise a typical GNSS weak signal scenario are summarized:

- **Absolute carrier power levels**: Determining the absolute carrier power levels of weak signals is of fundamental importance to determine the requirements of a GNSS receiver operating under harsh environment. These are necessary for the design of signal processing algorithms and hardware platforms that can reliably operate under weak signal conditions,

- **Mean shadow levels**: The RR processing strategy adopted in this work enables to determine the mean signal attenuation levels with respect to an outdoor scenario. These measurements provide an indication of the level of attenuation that can be experienced by a GNSS receiver under various scenarios compared to nominal outdoor GNSS conditions.

- **Satellite availability statistics**: User position computation in single point positioning, requires a minimum of four satellites (Kaplan & Hegarty 2006). Thus, it becomes critical to statistically analyze the total number of available satellites corresponding to a specific scenario. A signal from a specific satellite is declared available if its power level is above a fixed threshold corresponding to the receiver sensitivity. Thus, satellite availability statistics is used to determine how many signals are available for a fixed value of receiver sensitivity in a specific scenario and for a specific percentage of time. Due to the fading process, the signal power fluctuates and it can fall below the receiver sensitivity. Thus, the signal is not continuously available and the percentage of time of signal availability has to be determined.

- **Slow and fast fading components**: As described in the previous chapter, slow (due to shadowing) and fast (due to multipath scattering) fading affects the received signal in different scales. It is of interest to determine the contribution of these individual phenomena on the received signal power. Here, the range of signal power variations due to shadow fading and multipath fading are analyzed.

- **Distributions of the signal envelope**: Here, the first order statistics of the slow and fast fading components are extracted and analyzed. More specifically, the empirical PDFs of the slow and fast fading components are compared against some of the standard parametric distributions described in Chapter 2. The MSE criterion is adopted to determine the best fit among the considered parametric models. These parameters are later used in a simulation model for the generation of GNSS signals under harsh conditions.

- **Temporal/spectral characteristics**: The characterization of temporal/spectral characteristics of the received signal helps in understanding and developing new GNSS weak signal processing algorithms. These statistics provide useful information on the channel coherence time which is essential for determining the optimum coherent and non-coherent integrations times under weak signal conditions. Here, the second order statistics such as ACF, PSD, LCR and AFD are extracted from the empirical data. Later, the empirical results are compared against the standard theoretical models and the corresponding model parameters are extracted.

- **Spatial characteristics**: The statistics described above are obtained as a function of time and provides an indication of how long a static user has to wait before the signal will be out of a fade or how often a signal is affected by a fade. In a similar way, it is

possible to define statistics as a function of space. For example, for the spatial case, important metrics are the spatial correlation, average fade distance and level crossing rate with respect to the traveled distance. These statistics provide information about the distance a user has to travel in order to get a GPS signal out of a fade assuming temporal variations negligible.

It can be observed from the above listed parameters that the estimation of absolute power levels plays an important role in the accuracy of the characterization process. This is due to the fact that the remaining channel parameters are directly or indirectly derived from the estimated carrier powers. Thus, the accuracy of estimated carrier powers determines the effectiveness of the whole characterization process and the derived results. Therefore, the problem of determining the absolute carrier power levels of weak GPS signals under harsh environments is initially considered. A comprehensive theoretical analysis of the carrier power estimation technique adopted in this work is also provided.

3.5 Carrier power estimation

Absolute carrier power levels provide a measure of the incoming signal power independently from the test setup by considering the effect of the noise figure of the system. Absolute carrier power levels of the incoming signal can be computed from the estimated C/N_0 values and the noise figure of the measurement setup as (van Diggelen 2009)

$$\hat{C}_r[dBm] = \frac{\hat{C}}{N_0}[dBHz] + N_0[dBm/Hz] - NF[dB] \qquad (3.7)$$

where $\hat{C}_r$ is the estimated carrier power accounting for the receiver noise figure and NF is the noise figure of the receiver expressed in decibels. Thus, from Eq. (3.7), it is clear that the accuracy of estimated carrier power is determined by the accuracies of the estimated C/N_0. In turn, the accuracy of C/N_0 estimation algorithms depends on the true C/N_0 of the signal (high C/N_0 values are "simpler" to estimate) and the synchronization errors committed by the receivers. In the case of GPS L1 C/A signals, the nominal carrier power received in an outdoor scenario is around -128.5 dBm (GPS ICD 2010). Considering only thermal noise, the nominal C/N_0 is given as -128.5 - (-174) = 45.5 dB-Hz. In practice, various factors such as rain, cloud, receiver noise figure and correlation losses reduce the nominal C/N_0 by another 4-6 dB (Kaplan & Hegarty 2006). Also, in harsh environments such as indoors, GPS signals are further attenuated by 25-40 dB (Satyanarayana et al. 2010, van Diggelen 2009) due to multipath and shadowing. Thus, C/N_0 estimation algorithms are expected to operate under weak signal scenarios with input C/N_0 as low as 5-10 dB-Hz.

The problem of C/N_0 (or by extension Signal to Noise Ratio (SNR)) estimation has been extensively studied in the literature. A comprehensive analysis of various SNR estimators can be found in (Pauluzzi & Beaulieu 2000, Groves 2005). In (Pauluzzi & Beaulieu 2000), a performance comparison of several SNR estimation algorithms is presented for Data Aided (DA) and Non Data Aided (NDA) cases. It is shown that under the assumption of known data bits, the Maximum Likelihood (ML) SNR estimator outperforms every other estimator considered for the analysis. However, the theoretical analysis on the distribution of the SNR estimates is only marginally addressed. In

(Groves 2005), a theoretical analysis of several C/N_0 estimation algorithms in the context of GNSS is presented. However, the analysis is limited to the NDA case which may not be adequate for the accurate characterization of GNSS weak signals. A detailed analytical characterization of ML SNR estimator for a Quadrature Phase Shift Keying modulated signal under the hypothesis of known data bits is provided in (Cioni et al. 2005). Here, perfect phase synchronization between incoming and local replica signals is assumed, which may not be always true under weak signal conditions. Also, the entire analysis is presented in linear units whereas most practical applications operate using a logarithmic scale.

In general, C/N_0 or SNR values are expressed using decibel units, namely dB-Hz and dB, respectively. As it can be readily found, the performance of most weak signal processing algorithms is characterized as a function of C/N_0 or SNR expressed in decibels (Borio & Lachapelle 2009). Also, high sensitivity GPS receiver manufacturers specify the sensitivity of their receivers in decibel units (e.g. -160 dBm). However, in the literature SNR estimators are derived and analyzed in linear units (Pauluzzi & Beaulieu 2000, Cioni et al. 2005). The performance analysis carried out in linear units may not exactly map to the decibel domain due to the non-linear nature of the logarithmic transformation. In addition, most of the existing literature adopts the variance as a performance metric to compare different SNR estimators. However, error bounds and the associated confidence interval of any particular SNR estimator cannot, in general, be determined from the variance alone. This is due to the fact that the PDF of the SNR is asymmetrical with respect to its expected value.

Thus, due to the lack of sufficient statistical analysis of the carrier power estimators in the logarithmic domain, this chapter aims at providing a comprehensive theoretical analysis of the modified ML SNR estimator described in (Pauluzzi & Beaulieu 2000, Kaplan & Hegarty 2006) along with quantifying the minimum coherent integration time required to achieve a predetermined level of accuracy. Bias and error bounds associated with the considered SNR estimator have been quantified in the decibel scale. The theoretical results have been validated using Monte Carlo (MC) simulations and experiments based on a Spirent GSS 7700 hardware GPS signal simulator (Spirent 2008).

3.5.1 ML SNR estimation

In general, the post-correlation SNR, α, at the output of the correlator is given by (Borio 2008)

$$\alpha = \frac{E^2[\tilde{w}]}{Var[\Re(\tilde{w})]} = \frac{C}{2\sigma^2} = \frac{C}{2}\frac{4T_c}{N_0} = 2\frac{C}{N_0}T_c. \tag{3.8}$$

In practice, a GNSS receiver estimates the post-correlation SNR using a vector of correlator outputs and later converts it into C/N_0 estimates using Eq. (3.8). Let $\tilde{\mathbf{w}} = (\tilde{w}_1, \tilde{w}_2 \cdots \tilde{w}_M)$ represents a vector of M consecutive complex correlator outputs observed over T seconds where $M = T/T_c$. Under slow fading scenarios (e.g. static receivers), it can be assumed that multipath parameters are slowly varying over time such that values of β and φ can be assumed to be almost constant over T seconds. The ML C/N_0 estimator determines the SNR of the incoming signal using the observation vector $\tilde{\mathbf{w}}$ and later converts the SNR estimates into C/N_0 values using Eq. (3.8) . Considering Eq. (3.6), the PDF of the correlator outputs can be written as (Kay 1993)

$$f\left(\tilde{w};C,\sigma^2\right)=\frac{1}{\left(2\pi\sigma^2\right)^M}\exp\left(-\frac{1}{2\sigma^2}\sum_{m=1}^{M}\left|\tilde{w}_m-\sqrt{\frac{C}{2}}\exp\left(j\varphi\right)\right|^2\right). \tag{3.9}$$

The carrier power, C, and noise variance, σ^2, can be estimated by equating the partial derivatives of the log likelihood function $\left(\ln f(\tilde{w};C,\sigma^2)\right)$ with respect to C and σ^2 to zero (Kay 1993). The ratio of estimated carrier power, $\hat{C}$, and noise variance, $\hat{\sigma}^2$, determines the SNR at the correlator output. Thus, the ML SNR estimate is given by (Pauluzzi & Beaulieu 2000, Muthuraman & Borio 2010)

$$\hat{\alpha}=\frac{\hat{C}}{2\hat{\sigma}^2}=\frac{\left|\frac{1}{M}\sum_{m=1}^{M}\tilde{w}_m\right|^2}{\frac{1}{2M}\sum_{m=1}^{M}\left|\tilde{w}_m\right|^2-\left|\frac{1}{M}\sum_{m=1}^{M}\tilde{w}_m\right|^2} \tag{3.10}$$

where $\hat{\alpha}$ represents the ML SNR estimates in linear units (ratio). The numerator and denominator in Eq. (3.10) represent the estimate of carrier power and noise power, respectively. This form of estimator is traditionally known as the MLE-DA estimator (Pauluzzi & Beaulieu 2000) where DA stands for Data Aided. The ML estimate of the SNR values in logarithmic units (decibel scale) can be obtained using the invariance property of the ML technique as $\hat{\alpha}_{dB}=10\log\left(\hat{\alpha}\right)$ (Kay 1993).

In (Pauluzzi & Beaulieu 2000), it is shown that the MLE-DA given by Eq. (3.10) is a biased SNR estimator. In order to further improve the MLE-DA estimator accuracy, a modified structure as described in (Kaplan & Hegarty 2006) is considered. Figure 3-5 shows the modified structure of the MLE-DA SNR estimator where the noise variance is estimated using a non-existing PRN code based method. $\tilde{w}_{ext}=I_{ext}+jQ_{ext}$ represents the

complex correlator outputs obtained by correlating the incoming signals with a non-existing PRN code (not being transmitted by any GPS satellite). Thus, the correlator outputs obtained in this way can be modelled using Eq. (3.6) with a zero mean. Now, the noise variance of the correlator output can be estimated using $\tilde{w}_{ext}$ as

$$
\begin{aligned}
\hat{\sigma}^2 &= \frac{1}{2(M-1)} \sum_{i=1}^{M} \left| \tilde{w}_{ext,i} - \frac{1}{M} \sum_{k=1}^{M} \tilde{w}_{ext,k} \right|^2 \\
&= \frac{1}{2(M-1)} \sum_{i=1}^{M} \left[\left(I_{ext,i} - \bar{I}_{ext} \right)^2 + \left(Q_{ext,i} - \bar{Q}_{ext} \right)^2 \right]
\end{aligned}
\tag{3.11}
$$

where $\bar{I}_{ext}$ and $\bar{Q}_{ext}$ are the sample means of inphase and quadrature phase values. The mean component has been removed in order to account for any residual signal component. The noise variances values estimated in this way are nearly unbiased resulting in improved SNR estimates (Groves 2005).
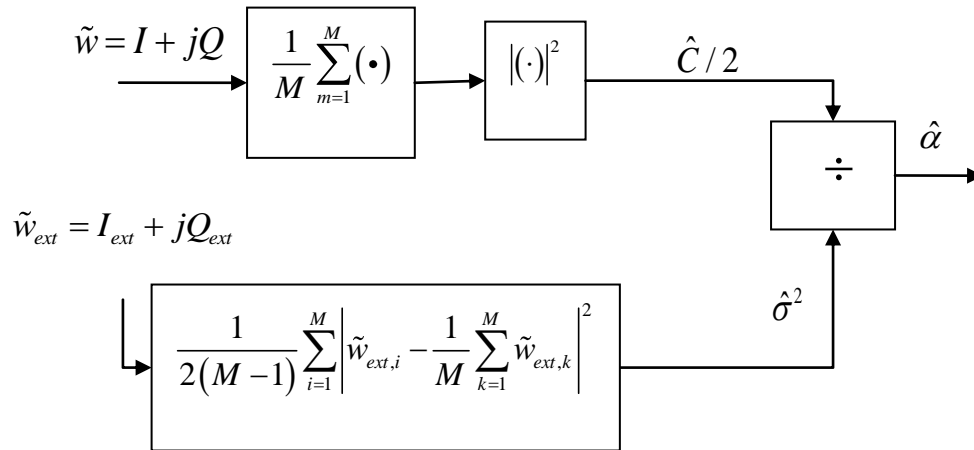
Figure 3-5: Structure of the MML for SNR estimation. The variance of the noise is computed externally using the correlator outputs determined from a non-existing PRN code.

In this way, a new SNR estimator is obtained as

$$\hat{\alpha} = \frac{\left(\left|\frac{1}{M}\sum_{m=1}^{M}\tilde{w}_m\right|\right)^2}{\frac{1}{2(M-1)}\sum_{i=1}^{M}\left|\tilde{w}_{ext,i} - \frac{1}{M}\sum_{k=1}^{M}\tilde{w}_{ext,k}\right|^2}.$$ (3.12)

This modified estimator is referred to as the Modified ML (MML). As evident from Eq. (3.12), the MML estimator coherently integrates the correlator outputs containing a signal component over the entire observation window of T seconds, the total integration time. The following section provides a detailed analytical characterization of the MML estimator.

3.5.2 Analytical characterization

The MML estimator given by Eq. (3.12) can be viewed as the ratio of two independent chi-square distributed random variables. The independence is due to the quasi-orthogonality of the codes used for the computation of the correlator outputs. Thus, it is possible to show that the numerator is distributed according to a Non-Central Chi-square (NCC) distribution as (Simon 2002)

$$num(\hat{\alpha}) \sim \frac{\sigma^2}{M}\chi_2^2(M\alpha)$$ (3.13)

where $num(\hat{\alpha})$ is the numerator of the MML estimator, α is the true value of the SNR and $\chi_{v_n}^2(\lambda_n)$ denotes the NCC distribution with v_n degrees of freedom and non-centrality parameter λ_n. Similarly, the denominator can be modelled as a Central Chi-square (CC) distributed random variable with $2(M-1)$ degrees of freedom as

$$den(\hat{\alpha}) \sim \frac{\sigma^2}{2(M-1)}\chi_{2(M-1)}^2$$ (3.14)

where $den(\hat{\alpha})$ is the denominator of the MML estimator and $\chi^2_{v_d}$ is the CC distribution

with v_d degrees of freedom. Thus, the ratio of these two quantities is distributed

according to a Non-Central Fisher (NCF) distribution as (Cioni et al. 2005, Papoulis

1991)

$$f_{\hat{A}}(\hat{\alpha}) = \frac{\dfrac{\sigma^2}{M} 2 \dfrac{\chi_2^2(M\alpha)}{2}}{\dfrac{\sigma^2}{2(M-1)} 2(M-1) \dfrac{\chi^2_{2(M-1)}}{2(M-1)}} = \frac{2}{M} F\left(2, 2(M-1), M\alpha\right) \qquad (3.15)$$

where $f_{\hat{A}}(\hat{\alpha})$ is the PDF of $\hat{\alpha}$, $F(v_n, v_d, \lambda_n)$ is the NCF distribution with parameters

v_n, v_d and λ_n as the input parameters. Thus, from the statistics of the non-central F

distribution, the mean and variance of the MML estimator are given by (Kay 1998)

$$E[\hat{\alpha}] = \frac{(M-1)(M\alpha + 2)}{M(M-2)} \approx \alpha + \frac{2}{M}$$

$$Var[\hat{\alpha}] = \frac{(M-1)^2 \left((M\alpha+2)^2 + 4(M-2)(M\alpha+1)\right)}{M^2(M-2)^2(M-3)}.$$

$$(3.16)$$

It can be observed from Eq. (3.16) that the MML estimator is a biased estimator. The bias

value reduces as the value of M increases, making the ML estimator asymptotically

unbiased.

Assuming the noise process to be stationary, its variance can be computed by processing

the entire data set prior to C/N$_0$ estimation. In this situation, the noise variance can be

assumed to be a known constant. Under the assumption of known noise variance it can be

readily shown that the MML estimates are distributed according to a NCC distribution as

$$f_{\hat{A}}(\hat{\alpha}) = \frac{1}{M} \chi_2^2(\alpha M). \qquad (3.17)$$

Thus, the mean and variance of the MML estimator under the assumption of a known variance can be written as (Papoulis 1991)

$$E[\hat{\alpha}] = \left(\frac{2}{M} + \alpha \right)$$

$$Var[\hat{\alpha}] = \frac{4}{M} \left(\frac{1}{M} + \alpha \right).$$

(3.18)

It is shown in the subsequent sections that the NCC and NCF models are sufficiently close for carrier power levels lower than -150 dBm and for a total integration time T lower than 1 s. Any difference in these models has little practical significance.

3.5.3 CRLB

The Cramer-Rao Lower Bound (CRLB) determines a lower bound on an estimator's accuracy (Kay 1993). Table 3-1 summarizes the CRLB for SNR estimates under the assumption of known and unknown noise variances in both linear and logarithmic units for the data model given in Eq. (3.6). The CRLB expressions listed in Table 3-1 are well established in the literature (Alagha 2001, Muthuraman & Borio 2010) and hence their derivation is not considered in this work.

Table 3-1: CRLB expressed in linear and logarithmic units for known and unknown noise variances (Alagha 2001, Muthuraman & Borio 2010).

Scenario	CRLB of SNR (linear units)	CRLB of SNR (dB^2)
Known variance (KV)	$\dfrac{4\alpha}{M}$	$\left[\dfrac{10}{\alpha \ln(10)} \right]^2 \dfrac{4\alpha}{M}$
Unknown variance (UKV)	$\dfrac{4\alpha}{M} + \dfrac{\alpha^2}{M}$	$\left[\dfrac{10}{\ln(10)\alpha} \right]^2 \left(\dfrac{4\alpha}{M} + \dfrac{\alpha^2}{M} \right)$

It can be easily verified that, for large values of M, the theoretical variances of the MML estimator under the assumption of known and unknown variances (Eqs. (3.16) and (3.18)) approaches the CRLB bound as

$$Var\left[\hat{\alpha}_{UKV}\right] \approx \frac{4\alpha}{M} + \frac{\alpha^2}{M} \to CRLB_{UKV}$$

$$Var\left[\hat{\alpha}_{KV}\right] \approx \frac{4\alpha}{M} \to CRLB_{KV}$$

(3.19)

where subscripts UKV and KV represents unknown and known noise variance cases, respectively. Now, the theoretical variance of the transformed variable $\hat{\alpha}_{dB} = 10\log_{10}\left(\hat{\alpha}\right)$ can be approximated using the Taylor expansion as (Papoulis 1991)

$$Var[\hat{\alpha}_{dB}] = \left|\frac{\partial \hat{\alpha}_{dB}}{\partial \hat{\alpha}}\right|^2 Var(\hat{\alpha})$$

(3.20)

where $\dfrac{\partial \hat{\alpha}_{dB}}{\partial \hat{\alpha}} = \dfrac{10}{\alpha \ln(\alpha)}$. From Eq. (3.19) and Eq. (3.20) it can be seen that the theoretical variance of the transformed variable $\hat{\alpha}_{dB}$ matches that of the CRLB given in Table 3-1. Thus, the MML estimator approaches the CRLB values for large values of M making it an asymptotically efficient estimator. In the following section, errors associated with the MML estimator as a function of M are quantified. Thus, the appropriate choice of M (or T) can be made by limiting the absolute errors to a predefined design criteria.

3.5.4 Quantification of T

In this section the minimum total integration time, T, or equivalently M (the number of correlator outputs) required by the MML estimator to achieve a predefined level of accuracy given a defined confidence level is derived. As shown in Section 3.5.2, MML

estimates, $\hat{\alpha}$, follow a NCF distribution when the noise variance is unknown and a NCC distribution when the noise variance is known. Now the PDF of $\hat{\alpha}_{dB}$ can be determined from the PDF of $\hat{\alpha}$ using the transformation property of random variables (Papoulis 1991). Thus, PDF of $\hat{\alpha}_{dB}$ can be written as

$$
\begin{aligned}
f_{\hat{A}_{dB}}\left(\hat{\alpha}_{dB}\right) &= \left|\frac{\partial h(\hat{\alpha})}{\partial \hat{\alpha}}\right| f_{\hat{A}}\left[h(\hat{\alpha})\right] \\
&= Z\exp\left(Z\hat{\alpha}_{dB}\right) f_{\hat{A}}\left(\exp\left(Z\hat{\alpha}_{dB}\right)\right)
\end{aligned}
\tag{3.21}
$$

where $h(\hat{\alpha}) = \exp(Z\hat{\alpha}_{dB})$, $Z = \ln(10)/10$ and $f_{\hat{A}}(\bullet)$ is the PDF of $\hat{\alpha}$ given by Eq. (3.15) or Eq. (3.17). Figure 3-6 shows the PDF of $\hat{\alpha}_{dB}$ evaluated using the correlator outputs with $T_c = 1$ ms and $M = 200$ for four different input carrier power levels. In Figure 3-6, solid lines represent the PDFs of $\hat{\alpha}_{dB}$ assuming a known noise variance and dashed lines represents the PDFs of $\hat{\alpha}_{dB}$ under the hypothesis of unknown noise variance. It can be observed that the PDFs are nearly identical for power levels below -155 dBm. This shows that for carriers power levels below -155 dBm, the noise variance estimated from the correlator outputs are quite accurate. Thus, under low carrier power levels, the NCC distribution can be effectively used to predict the performance of the MML estimator. Figure 3-7 shows the PDFs of $\hat{\alpha}_{dB}$ for two different values of M. As expected, it can be observed that the PDFs of $\hat{\alpha}_{dB}$ becomes sharper for increased values of M. However, the PDFs under known and unknown noise variance scenarios are still nearly identical for a fixed value of M.
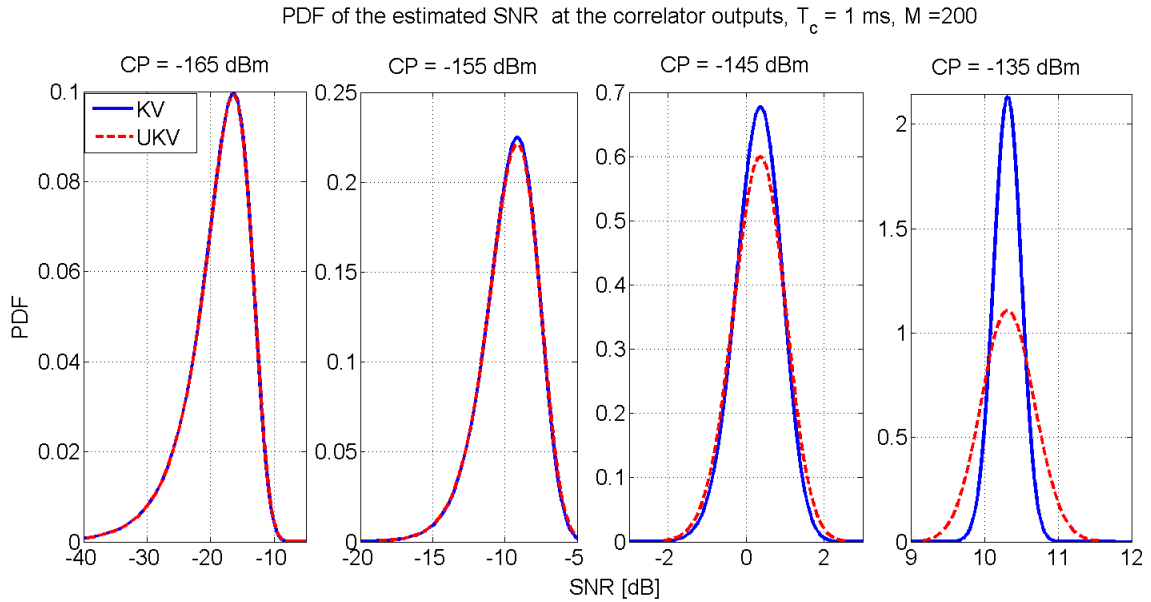
Figure 3-6: Comparison of PDFs of MML estimates under known and unknown noise variance conditions.
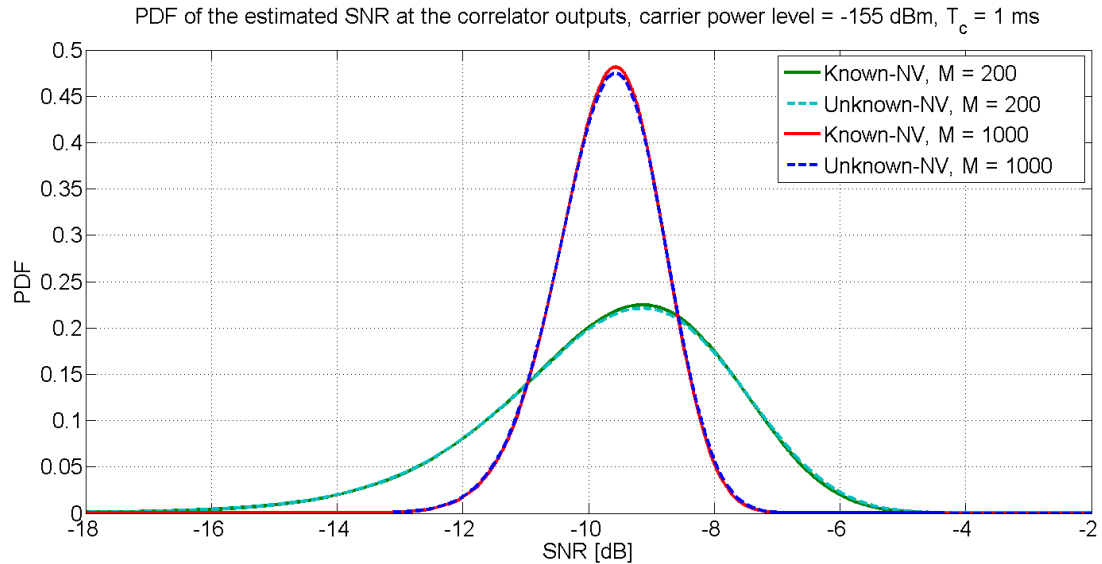
Figure 3-7: Comparison of the PDFs of the MML estimates under known and unknown noise variance hypotheses for two different values of integration time.

Now, the minimum value of T can be determined by constraining the bias and error envelope levels. The bias of the MML estimator in dB is defined as the difference

between the true and expected value of the estimator output as $\alpha_{dB,true} - E[\hat{\alpha}_{dB}]$ where

$\alpha_{dB,true}$ is the true value of the SNR and $E[\hat{\alpha}_{dB}]$ is the expected value of the SNR estimate

defined as (Papoulis 1991)

$$E[\hat{\alpha}_{dB}] = \int_{-\infty}^{\infty} \hat{\alpha}_{dB} f_{\hat{A}_{dB}}(\hat{\alpha}_{dB}) d\hat{\alpha}_{dB}. \tag{3.22}$$

On the other hand, error bounds determine the region around the expected value of an

estimator with a certain probability level (confidence). Figure 3-8 shows a sample PDF of

the estimated SNR for the values $\alpha_{dB} = -18\,dB$ and $M = 200$. In Figure 3-8, $\hat{\alpha}_{dB,L}$ and

$\hat{\alpha}_{dB,U}$ determines the lower and upper limiting values of the SNR defining a confidence

interval of $(1-\varepsilon)\%$ such that

$$\begin{aligned} f_{\hat{A}_{dB}}\left(\hat{\alpha}_{dB,L} < \hat{\alpha}_{dB} \leq \hat{\alpha}_{dB,U}\right) &= \int_{\hat{\alpha}_{dB,L}}^{\hat{\alpha}_{dB,U}} f_{\hat{A}_{dB}}(\hat{\alpha}_{dB}) d\hat{\alpha}_{dB} \\ &= F_{\hat{A}_{dB}}(\hat{\alpha}_{dB,U}) - F_{\hat{A}_{dB}}(\hat{\alpha}_{dB,L}) \\ &= \left(1 - \frac{\varepsilon}{2}\right) - \left(\frac{\varepsilon}{2}\right) \\ &= 1 - \varepsilon \end{aligned} \tag{3.23}$$

where $F_{\hat{A}_{dB}}(\cdot)$ is the CDF of $\hat{\alpha}_{dB}$. Thus, the values of $\hat{\alpha}_{dB,L}$ and $\hat{\alpha}_{dB,U}$ can be easily

computed by fixing ε to a predefined value according to the design criteria (e.g. 0.05 or

0.1) as

$$\begin{aligned} \hat{\alpha}_{dB,L} &= F_{A_{dB}}^{-1}\left(\frac{\varepsilon}{2}\right) \\ \hat{\alpha}_{dB,U} &= F_{A_{dB}}^{-1}\left(1 - \frac{\varepsilon}{2}\right) \end{aligned} \tag{3.24}$$

where $F_{A_{dB}}^{-1}(\cdot)$ is the inverse CDF of $\hat{\alpha}_{dB}$. As it can be seen from Figure 3-8, $\hat{\alpha}_{dB,L}$ and

$\hat{\alpha}_{dB,U}$ values are not equally distant from the expected value of the SNR estimate. This is

due to the fact that the PDF of the MML estimator is asymmetrical around its mean

value. Now, the upper and lower bound (UB and LB) of the MML estimates around its

expected value with a confidence level of $(1-\varepsilon)\%$ can be defined as

$$UB = \hat{\alpha}_{dB,U} - E[\hat{\alpha}_{dB}]$$
$$LB = \hat{\alpha}_{dB,L} - E[\hat{\alpha}_{dB}]$$

(3.25)

where $\hat{\alpha}_{dB,L}$ and $\hat{\alpha}_{dB,U}$ are given by Eq. (3.24) and $E[\hat{\alpha}_{dB}]$ is given by Eq. (3.22).
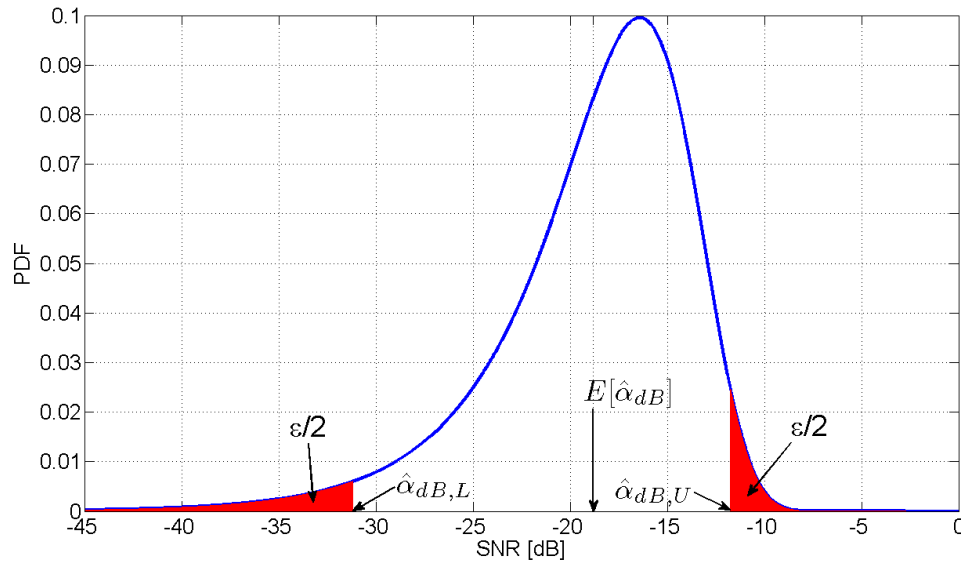
Figure 3-8: PDF of the estimated SNR showing the lower and upper limiting values for a confidence interval of 1-ε.

Even though it is not directly evident from Eqs. (3.23) to (3.25), the values of UB and

LB depend on the parameter T or equivalently M. Thus, the value of T can be

determined such that the estimated $\hat{\alpha}_{dB}$ resides within the desired error bounds with a

$(1-\varepsilon)\%$ confidence level.

Figure 3-9 (a) shows the bias of the estimated SNR values for different values of T. As

expected, the bias values decreases as T increases. Bias values are well within 0.1 dB for

values of T equal to 0.6 s and above. Figure 3-9 (b) shows the error bounds with a 95%

confidence level for various values of T. It can be observed that the error bounds are

asymmetrical around the expected value of SNR estimates. As expected, the size of the

uncertainty region increases as the value of T decreases.
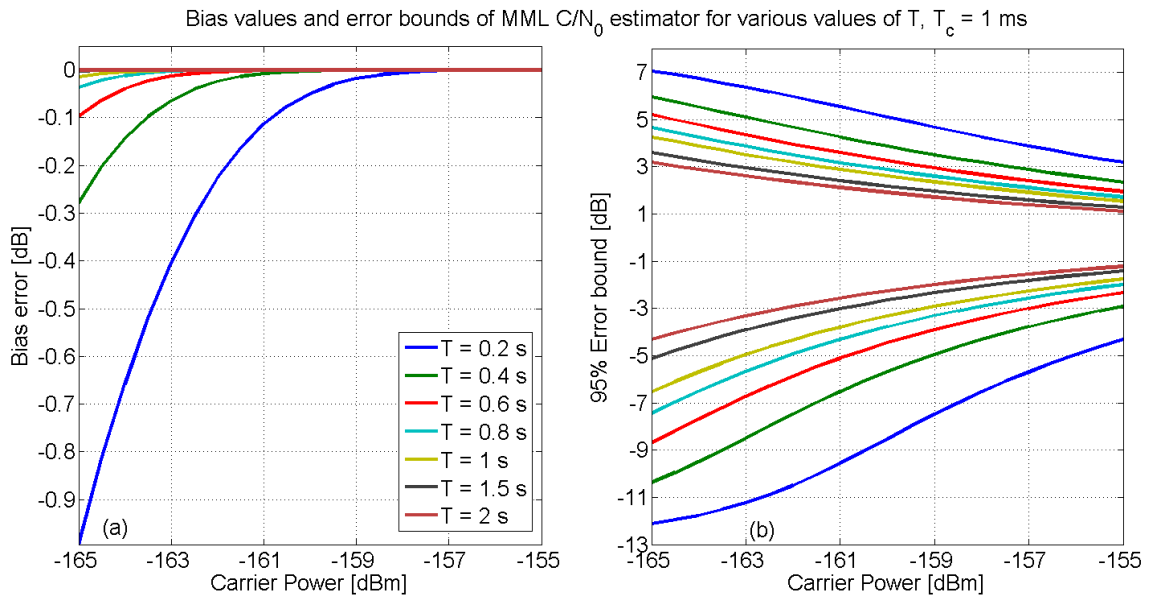
Figure 3-9: Bias values (a) and confidence intervals (b) of MML estimator for various values of *T* for a 95% confidence level.

Thus, in order to achieve an error bound of ±2 dB with a 95% confidence for an incoming

signal with carrier power level of -160 dBm, the required total integration time is about

two seconds. Table 3-2 lists the confidence levels for three different input carrier powers

for several values of T. Here, a design requirement of ±2 dB is chosen as the limiting

values for the upper and lower error bounds for analysis purposes. For example, with $T = 1$ s, the probability value with which the estimated carrier power levels are within ± 2 dB of their true values are 98.1%, 82.6% and 56.4% for an incoming signal with power levels -155 dBm, -160 dBm and -165 dBm, respectively. In this way, the value of T can be appropriately chosen depending on the desired level of confidence.

Table 3-2: Confidence levels for three different input carrier power levels with an upper and lower error bound of ±2 dB for various values of *T*.

	Probability level (%) for ± 2 dB error bound		
T (s)	-155 dBm	-160 dBm	-165 dBm
0.2	72.4	47.1	33.3
0.4	87.2	61.7	40.0
0.6	93.6	71.2	46.3
0.8	96.6	77.8	51.7
1	98.1	82.6	56.4
1.5	99.5	90.2	65.6
2	99.9	94.2	72.4

3.5.5 Simulation analysis

In this section, the theoretical results presented in Sections 3.5.2 and 3.5.4 are validated using software and hardware simulations. The distribution of the MML estimates has been at first evaluated using a MC technique (Kay 1993). Here, the correlator outputs were simulated according to Eq. (3.6) and provided as inputs to the SNR estimator. Later, the PDF of the SNR estimates was evaluated using 10000 MC simulation runs.

In the hardware simulation analysis, a Spirent GSS 7700 hardware simulator was used to generate a realistic GPS scenario with multiple satellites in view. Figure 3-10 shows the test setup adopted for validating the theoretical results using the hardware simulator. The Spirent GSS 7700 simulator was used in conjunction with the NI signal analyzer described above to collect synchronous digitized GPS IF samples and later processed using GSNRx-rr[TM] (Satyanarayana et al. 2010, Petovello et al. 2009).In Figure 3-10, the output of the front panel of the GSS 7700 simulator was used to obtain weak GPS signals with powers in the [-150 dBm, -160 dBm] range. The rear panel output (Mon/Cal port) of the GSS 7700 simulator was used to obtain GPS signals with powers approximately 60 dB stronger as compared to the front panel output (Spirent 2008). The signal from the rear panel of the simulator was used to aid the processing of the GPS weak signals coming out from the front panel by providing data bits, code phase and carrier Doppler aiding.
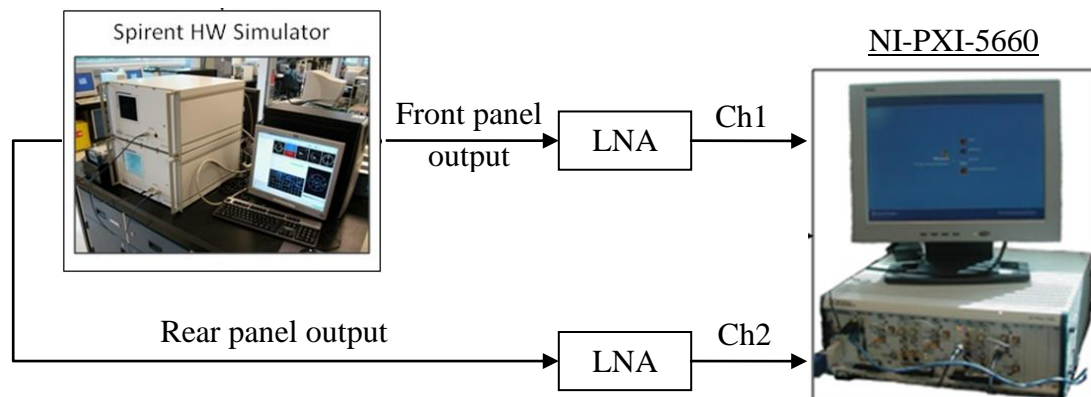
Figure 3-10: Test setup for collecting synchronized GPS L1 C/A weak signals (front port) and strong signals (rear Mon/Cal port) from the Spirent GSS 7700 GPS hardware simulator using a National Instruments multiple RF signal analyzer.

In this way, the synchronization errors while processing the GPS weak signals were minimized. The signals from the hardware simulator were passed through low noise amplifiers (LNA) before being provided to the NI signal analyzer.

The ability of the considered hardware setup to operate under a wide dynamic range of signal powers was initially verified using the following approach. The carrier power in the hardware simulator was varied from -125 dBm to -164 dBm in steps of 3 dB every one minute. Digitized IF samples obtained from the NI signal analyzer were processed using GSNRx-rr^{TM} to obtain correlator outputs. The correlator outputs obtained in this way were then provided as inputs to the SNR estimation algorithm. Finally, the estimated SNR values were mapped back to the simulator port to obtain absolute carrier power levels. The methodology adopted for calibrating the system and obtain absolute carrier power levels is detailed in Appendix A. Figure 3-11 shows the estimated carrier power levels for different values of T.
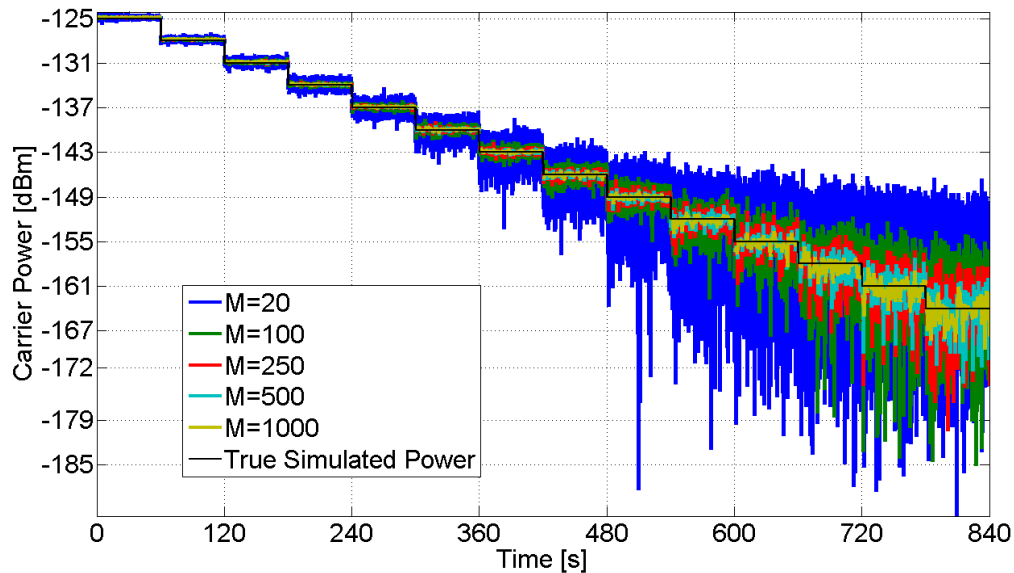
Figure 3-11: Estimated carrier power levels along with the true simulated power levels for different coherent integration times.

It can be observed that the estimated carrier power level values follow the simulated curve. As expected, the variance of the estimated values reduces for increased values of T. This validates the hardware measurement setup considered in this work and shows the effectiveness of the considered SNR estimator for the characterization of low signal powers.

In order to obtain reliable statistics of the SNR estimates, two different scenarios, each with eight satellites in view, were simulated for approximately five minutes with fixed carrier power levels. The power levels of all visible satellites were fixed to -152.5 dBm and 157.5 dBm in the first and second scenario, respectively. Finally, the PDFs of the SNR estimates were evaluated empirically using the SNR estimates obtained from all satellite measurements. The same PDFs were estimated using the MC approach described above. The PDFs of the SNR estimates obtained using the hardware simulator data and MC simulations are compared against the theoretical PDFs in Figure 3-12. Two different integration times (0.2 s and 1 s) were considered for the analysis. Approximately 24000 (for $T = 0.2$ s) and 4800 (for $T = 1$ s) independent SNR estimates were used for evaluating the PDFs from the hardware simulator data. A kernel density estimation technique (Wand & Jones 1995) with Gaussian kernel was adopted to estimate the PDF in both the hardware and MC approach. From Figure 3-12, it can be observed that the empirical PDFs are in good agreement with the theoretical ones. This supports the theoretical results described in the previous sections.

3.6 A note on real GNSS signals

Until now, it was assumed that the fading parameters remain invariant within one observation window of T seconds, however, they may vary over subsequent observation intervals. In practice, multipath parameters vary continuously over time and the rate of variation depends on the dynamics of the receiver.
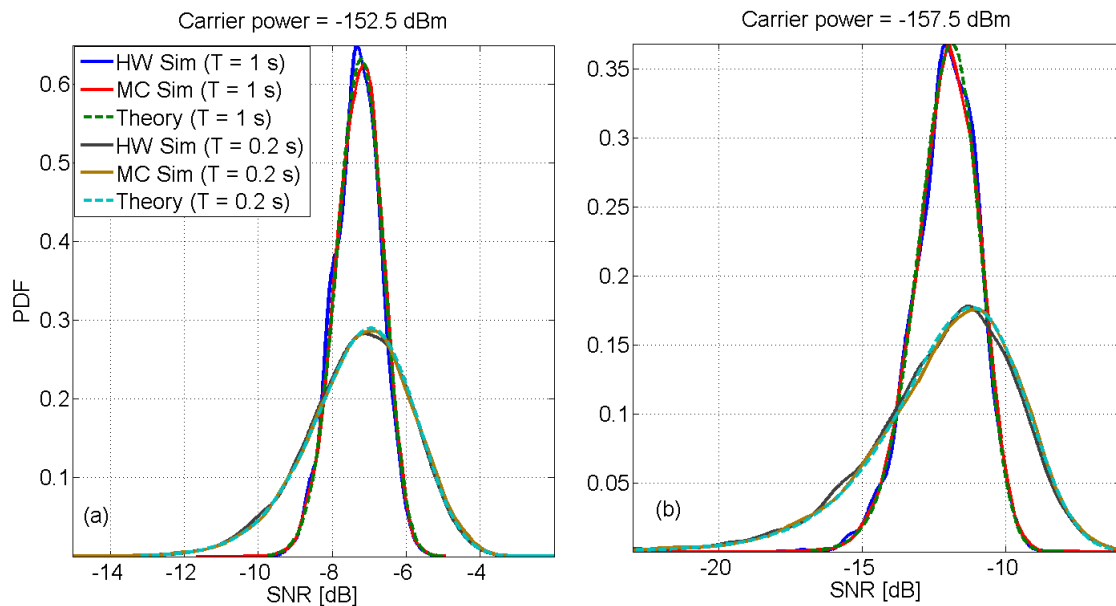
Figure 3-12: Comparison of the SNR distributions obtained using hardware simulator data, MC simulations and theoretical results for carrier power levels of -152.5 dBm (a) and -157.5 dBm (b).

In such scenarios, the receiver's observation window may be larger than the interval over which the signal parameters can be considered constant. If the signal integration time is too long, the signal variations within one observation window are averaged. In order to increase the observability of the signal variations due to multipath fading, C/N_0 estimators based on overlapping blocks can be considered. Figure 3-13 shows the concept of overlapping blocks for carrier power estimation for an overlapping factor equal to the 50% of the individual block duration. In Figure 3-13, the top row shows the situation

where non overlapping blocks of 1 second of data are used for C/N_0 estimation. Each

block contains $M = T/T_c$ complex correlator outputs. The bottom five rows show the

overlapping blocks that can be considered for C/N_0 estimation. The initial sample of each

block is separated by $T/Overlap\_factor$ seconds which in this case is 0.5 s.
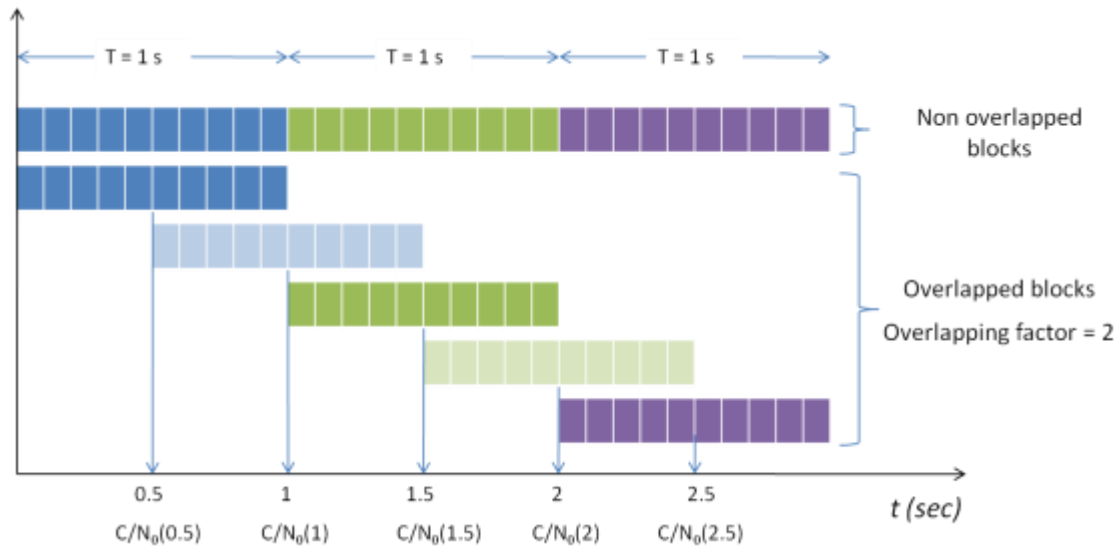
Figure 3-13: Conceptual diagram for the estimation of C/N_0 values using overlapping data blocks.

3.7 Summary

This chapter described the characterization approach adopted in this research work to

measure and analyze GNSS weak signals under harsh environment. It was shown that the

accurate characterization of weak signals is a joint problem of synchronization and

estimation. Towards this, a RR processing strategy was described to minimize the

synchronization losses and a comprehensive analysis of a modified ML C/N_0 estimator

was provided for the accurate estimation of carrier power levels under weak signal

conditions. It was shown that the minimum total integration time required to attain certain

predefined accuracy can be determined by constraining the estimator errors to lie in a

specified confidence interval with a certain probability level. It was shown that for a GPS signal with a carrier power level of -160 dBm, a total integration time of $1.5 - 2$ seconds is required to limit the estimator errors within ± 2 dB with a confidence level of $90 - 95\%$. In the subsequent chapters, the characterization methodology presented in this chapter is adopted to extract and analyze the GPS fading parameters under harsh environments.

Chapter Four: **FIRST ORDER CHARACTERIZATION OF GPS WEAK SIGNALS**

The first order characterization of a communication channel deals with statistics such as PDF and/or CDF of the received signal envelope. In general, the first order statistics also include the characterization of the multipath signal phase (Ibnkahla 2004). However, since the received signal phase is very sensitive to small changes in the path delays, it can be safely assumed that the signal phase is uniformly distributed between $-\pi$ and π (Hashemi 1993). For example, in case of GPS L1 C/A signals, from Eq. (2.16) it is clear that a path delay of 1 ns corresponds to approximately a 3π radians phase shift at the 1,575.42 MHz frequency. In practice, the multipath delays can vary between ten and hundreds of nanoseconds resulting in a signal phase randomly varying between $-\pi$ and π. Thus, the characterization of the signal amplitude alone is considered in this research work.

In this chapter, the weak signal measurement and processing strategies described in Chapter 2 and 3 are used to characterize the amplitude of real GPS signals in several harsh environments. More specifically, a methodology for extracting the fading parameters listed in Section 3.4 is at first described. The described methodology is used to extract fading parameters from real GPS signals collected in urban, sub-urban, foliage and indoor scenarios. Also, the various statistical models described in Section 2.6.1 have been validated using real GPS signals collected in the aforementioned scenarios. More emphasis is given to the indoor channel characterization.

4.1 Amplitude characterization

The complex nature of the signal propagation mechanism under multipath environment results in randomly varying signal amplitudes. Thus, the amplitude of the received signal can be viewed as a stochastic process whose characteristics highly depend on the nature of the propagation medium. In general, random processes are characterized based on their stationary or non-stationary behaviour. In a stationary process, the statistics of the process are assumed to be time invariant, and on the contrary, the random process that do not follow this assumption are classified as non-stationary processes. Various single/composite/mixture models described in Chapter 2 are based on whether the channel is stationary or non-stationary. Single state models such as Rayleigh or Rice are well suited for stationary channels. However, a typical GNSS channel is non-stationary in nature due to continuous motion of the satellites and shadowing effects caused by various signal blocking elements. In such situations, composite/mixture models are better suited for describing a non-stationary behaviour. A composite model such as Suzuki and Loo's described in Section 2.6.1.2 is well suited for scenarios where the shadow fading effects are relatively small and slow. On the other hand, multi state mixture models based on probabilistic transitions are well suited for scenarios where the variations due to shadowing are large and fast. Within each state of the multi state mixture models the channel is considered quasi-stationary and described using either single or composite models.

Thus, for an effective characterization of a GNSS communication channel, it is necessary to study the effects of slow and fast fading independently. In the following section, a procedure for isolating slow and fast fading components from the measured correlator

outputs is described. Once the slow and fast fading components are isolated, further analysis is performed on each of these components to extract fading parameters.

4.2 Signal analysis and parameter extraction

In this section, a procedure for extracting the fade statistics of the GNSS communication channel from empirical data is described. The described methodology is later used in the rest of the chapter to extract various fading parameters. In order to extract fading parameters from the measured correlator outputs, the following assumptions are made:

- Various fading phenomenon such as path loss, shadowing and multipath are multiplicative in nature (as described in Chapter 2) and can be transformed to additive relationship using a logarithmic transformation;

- Path loss, shadow fading and multipath fading components have different frequency content and thus can be separated through filtering. More specifically, path loss, shadow fading and multipath fading components have low, medium and high frequency contents, respectively;

- The reference signal used in the RR processing strategy is mainly affected by the path loss component.

In practice, the reference signals are also affected by slow fading component due to the ionosphere, troposphere, antenna gain pattern and any multipath signal arriving from a distant object. However, it is shown in subsequent sections that these slow variations are generally minimal and do not significantly affect characterization results.

The methodology for extracting fading parameters from empirical data is shown in Figure 4-1. Here, a two stage filtering has been applied on the estimated carrier power levels to isolate various fading effects.
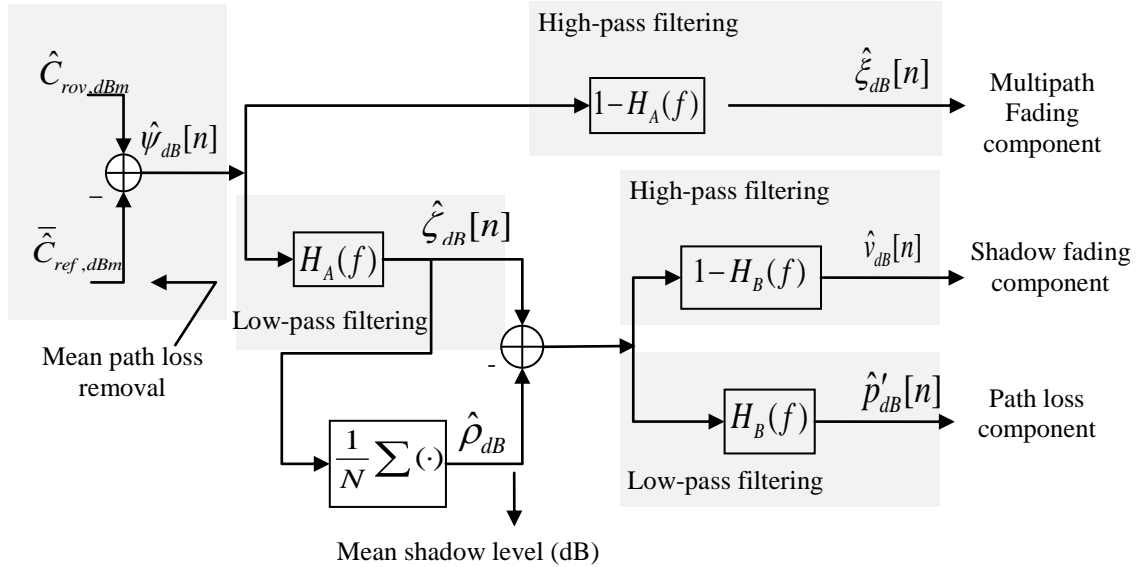
Figure 4-1: Block diagram showing the procedure used for extracting fading parameters from empirical data.

The C/N$_0$ of the reference and rover signals is at first estimated. The absolute carrier power levels of the reference signal, $\hat{C}_{ref,dBm}$, and rover signal, $\hat{C}_{rov,dBm}$, are then determined using the procedure described in Section 3.5. Using Eqs. (2.13) and (3.5), the estimated carrier power levels $\hat{C}_{ref}$ and $\hat{C}_{rov}$ can be expressed in dBm as

$$\hat{C}_{ref,dBm}[n] = C_{t,dBm} + p_{dB}[n]$$
$$\hat{C}_{rov,dBm}[n] = C_{t,dBm} + p_{dB}[n] + s_{dB}[n] + \xi_{dB}[n]$$

$$(4.1)$$

where $p_{dB}[n]$, $s_{dB}[n]$ and $\xi_{dB}[n]$ are obtained using the transformation $x_{dB} = 20\log_{10}(x)$.

In Eq. (4.1), the path loss component $p_{dB}[n]$ and slow fading component $s_{dB}[n]$ can be further expressed as

$$p_{dB}[n] = \bar{p}_{dB} + p'_{dB}[n]$$
$$s_{dB}[n] = \rho_{dB} + v_{dB}[n]$$

(4.2)

where

- $\bar{p}$ represents the mean path loss component;

- $p'_{dB}[n]$ is a zero mean deterministic component in the path loss variations which accounts for the satellite motion and antenna gain variations;

- ρ_{dB} is the mean shadow level which represents mean attenuation level of the signals at the rover antenna with respect to the reference antenna;

- $v_{dB}[n]$ represents the random variations associated with the slow fading effects.

$\xi_{dB}[n]$ represent the envelope variations due to multipath (fast fading component) and is assumed to be centered around the mean shadow level, ρ_{dB}. From Eqs. (4.1) and (4.2), the mean path loss component, $\bar{p}$, can be removed from the rover observation as

$$\hat{\psi}_{dB}[n] = \hat{C}_{rov,dBm}[n] - \bar{\hat{C}}_{ref,dBm}$$
$$= \hat{p}'_{dB}[n] + \hat{s}_{dB}[n] + \hat{\xi}_{dB}[n]$$

(4.3)

where $\bar{\hat{C}}_{ref,dBm}$ represents the mean carrier power level of the reference signal. A first stage of filtering is applied on $\hat{\psi}_{dB}[n]$ to isolate the fast fading effects due to multipath from the rest of the fading phenomena. The signal $\hat{\psi}_{dB}[n]$ is high-pass filtered to obtain

the fast fading signal power $\hat{\xi}_{dB}[n]$ and low-pass filtered to obtain the signal $\hat{\zeta}_{dB}[n]$ which contains both slow fading components due to shadowing and path loss and can be written as

$$\hat{\zeta}_{dB}[n] = \hat{p}'_{dB}[n] + \hat{s}_{dB}[n]. \tag{4.4}$$

$H_A(f)$ and $1 - H_A(f)$ are the transfer functions of the low-pass and high-pass filters, respectively ($H_A(f)$ is assumed to have unit gain at the zero frequency). Now, the envelope of the fast fading component $\hat{\xi}[n]$ can be obtained from $\hat{\xi}_{dB}[n]$ using an anti-logarithmic operation.

$\hat{\zeta}_{dB}[n]$ is further analyzed to extract the mean shadow level as

$$\hat{\rho}_{dB} = \frac{1}{N} \sum_{n=0}^{N-1} \hat{\zeta}_{dB}[n]. \tag{4.5}$$

A second stage of filtering is applied on the signal $\hat{\zeta}_{dB}[n] - \hat{\rho}_{dB}$ to isolate the deterministic variations due to path loss from the shadow fading effects as shown in Figure 4-1. The signal $\hat{\zeta}_{dB}[n] - \hat{\rho}_{dB}$ is high-pass filtered to obtain the slow fading signal power variations $\hat{v}_{dB}[n]$ and low-pass filtered to obtain the deterministic component of the path loss $\hat{p}'_{dB}[n]$. In Figure 4-1 $H_B(f)$ and $1 - H_B(f)$ denote the transfer functions of the second low-pass and high-pass filtering stage, respectively. In general, the deterministic variation in $\hat{\zeta}_{dB}[n] - \hat{\rho}_{dB}$ can be easily removed using standard curve fitting techniques. Finally, the envelope of the slow fading component $\hat{v}[n]$ can be obtained

from $\hat{v}_{dB}[n]$ using an anti-logarithmic operation. Table 4-1 summarizes the various symbols introduced in this section.

Table 4-1: List of symbols introduced for the analysis of indoor GPS signals.

Symbol	Description
$\hat{C}_{ref}$, $\hat{C}_{rov}$	Estimated reference and rover carrier powers
$\hat{\psi}_{dB}[n]$	Difference between $\hat{C}_{rov}$ and mean reference carrier power $\bar{\hat{C}}_{ref}$
$\hat{\xi}[n]$, $\hat{\xi}_{dB}[n]$	Estimated fast fading envelope in linear and dB units
$\hat{\zeta}_{dB}[n]$	Intermediate signal which contains both slow fading and deterministic path loss components
$\hat{s}_{dB}[n]$	Slow fading or shadow fading component
$\hat{v}[n]$, $\hat{v}_{dB}[n]$	Random variations associated to the slow fading component in linear and dB unit
$\hat{\rho}_{dB}$	Mean shadow level with respect to the outdoor scenario

The distribution of the fast and slow fading components are then estimated using $\hat{\xi}[n]$ and $\hat{v}[n]$ respectively. The empirical distributions of the slow and fast fading components are later compared against standard parametric models such as Rayleigh, Rice, Log-Normal distributions. The MSE criterion is used to determine the best fit among standard parametric models. The MSE is defined as

$$MSE = \frac{1}{N}\sum_{n=1}^{N}\left(f_{\hat{X}}(\hat{x}_n) - f_X(x_n)\right)^2 \tag{4.6}$$

where $f_{\hat{X}}(\cdot)$ and $f_X(\cdot)$ are the estimated and theoretical PDF, respectively. In this work, $f_{\hat{X}}(\cdot)$ is estimated using a non-parametric Kernel Density Estimation (KDE) technique (Wand & Jones 1995) as

$$\hat{f}_X(x) = \frac{1}{Nh} \sum_{i=0}^{N-1} K\left(\frac{z - Z_i}{h}\right) \tag{4.7}$$

where $K(\cdot)$ is called the kernel function satisfying the criteria $K(u) \geq 0, \int K(u)du = 1$, h is called the bandwidth or window width and it is a positive number. N is the total number of samples. The most widely used kernel is the Gaussian with zero mean and unit variance:

$$K(u) = \frac{1}{\sqrt{2\pi}} \exp\left(-\frac{u^2}{2}\right). \tag{4.8}$$

In this case, the estimated density function can be written as

$$\hat{f}_X(x) = \frac{1}{Nh\sqrt{2\pi}} \sum_{i=0}^{N-1} \exp\left(-\frac{(x - X_i)^2}{2h^2}\right). \tag{4.9}$$

It should be noted that the signal analysis scheme described in this section is general and can be applied to any scenarios to extract the fading parameters. In the rest of the chapter, the high frequency component, $\hat{\xi}_{dB}[n]$, is referred to as the fast fading component (attributed to multipath), the medium frequency component, $\hat{v}_{dB}[n]$ is referred to as the slow fading component (attributed to shadowing) and the very low frequency content, $\hat{p}'_{dB}[n]$, is referred to as path loss.

It should also be noted that the spectral characteristic of the analysis filters $H_A(f)$ and $H_B(f)$ are critical for isolating various fading effects. The choice of filters depend on factors such as scenario type (indoors, foliage, etc.), and user dynamics. In this work, a zero phase digital filtering technique is adopted (Oppenheim & Schafer 2010). In this

technique, the input time series is filtered in both forward and backward direction to minimize the phase distortion. The filter cut-off frequency is determined experimentally.

4.3 Data collection and scenarios

The various data collections performed as part of this research work are summarized in this section. Several data collections were performed in signal degraded conditions within the campus of the University of Calgary (UofC). The rover antenna was placed in several harsh environments such as in the middle of buildings, under foliage and indoors. Table 4-2 summarizes the scenarios that have been considered in this work. Pictures showing the actual environments tested will be shown later.

Multiple data collections were performed with/without user dynamics in the aforementioned scenarios. The following paragraphs summarize two different types of data collections that were performed:

- **Static data collection:** a single antenna was used to collect static GPS data for several minutes. In this case, it is possible to assume that signal amplitude variations are essentially due to temporal variations in the communication channel.

- **Dynamic data collection:** a single antenna was used to collect dynamic GPS data for several minutes. Here, the simulated dynamics were similar to a pedestrian navigation scenario with an approximate speed of 5-80 cm/s. Data were collected either by holding the antenna in the hand or by mounting the antenna on a moving cart.

Table 4-2: Description of the scenarios used for data collection to characterize the amplitude of GNSS signals.

Scenario	Description
Open Sky	Rooftop of the Calgary Centre for Innovative Technology (CCIT) building. The antenna was placed in order to minimize reflections from nearby buildings.
Open Sky with a strong reflector	In front of a glassy building. The parking lot in front of the west side of the CCIT building was selected in order to have reflections from the building.
Open Sky with multiple reflectors	Middle of a square surrounded by buildings. This was possible in the backyard of the engineering buildings at the UofC. The antenna was surrounded by buildings on three sides and tall trees on the fourth side.
Foliage	By the side of a pedestrian pathway with tall trees and bushes on either sides. The antenna was placed right next to the pathway in the middle of trees.
Indoors	Five different indoor scenarios have been considered namely: laboratory, conference room, wooden house main floor, basement and a shopping complex scenario. More details on each scenario and the corresponding data collections are provided in Section 4.4.5.1.

The default parameters used for all the data collections are summarized in Table 4-3. In most of the harsh environments considered in this work, the RR processing strategy described in Chapter 3 was adopted in conjunction with the NI signal analyzer to collect, store and process GPS weak signals. A coherent integration of 100-120 ms was used for outdoor scenarios and up to 1 s for indoor scenarios. The choice of 1 s coherent

integration was made based on the design criteria described in Chapter 3. Also, the receiver antenna gain variations are not considered for determining absolute carrier power levels. Further details on the data collections and the corresponding results are summarized in the following section.

Table 4-3: Default parameter values used for data collections under various scenarios.

Parameter	Value
Sampling Frequency	5 MHz
IF Frequency	0.42 MHz
Sampling type	Complex
Quantization bits	14 bits
Data collection duration	5-30 minutes
Antenna	NovAtel-GPS-702-GG

4.4 Results and analysis

In this section, the behavior of several amplitude time series obtained under different scenarios such as open sky, single reflector, multiple reflectors, foliage and indoors, is detailed. At first, a simplistic scenario under open sky conditions is considered.

4.4.1 Open sky environment

The signal analysis and fading parameter extraction methodology described in Section 4.2 requires the presence of a reference receiver. Thus, it becomes crucial to analyze the behaviour of the received signal from the reference antenna. For this reason, data collected under an open sky environment are considered first. As described in Table 4-2,

a data collection was performed in an open sky environment on the rooftop of the CCIT building.

Figure 4-2(a) shows the position and orientation of the receiver antenna on the roof top. Figure 4-2 (b) shows the sky plot of the satellites in view during the data collection period. The satellite constellation at the start and end of the data collection is shown in red and blue color respectively.
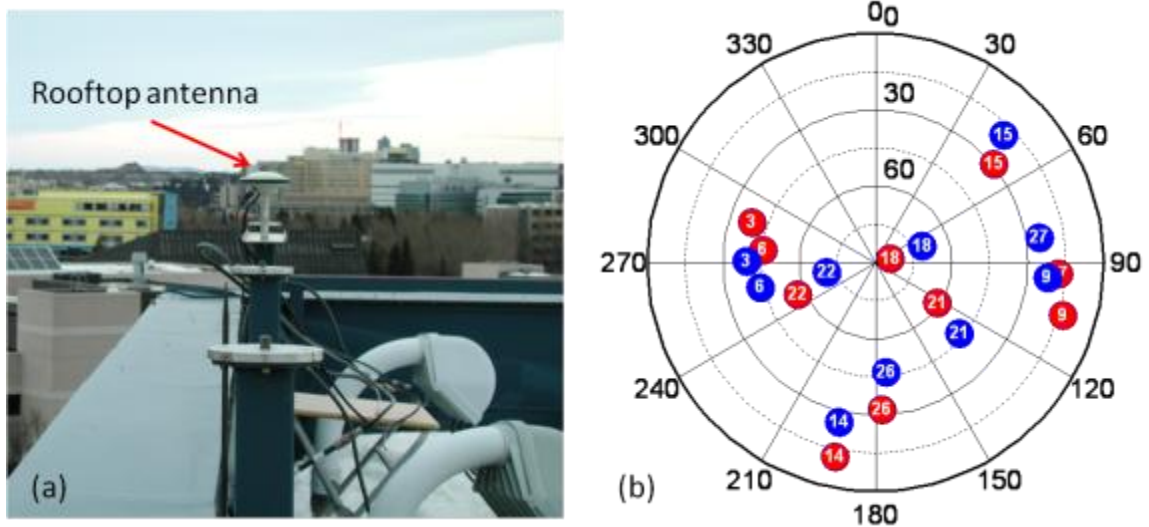
Figure 4-2: (a) Data collection setup on the rooftop of the CCIT building. (b) Sky plot of the satellites at the beginning (shown in red) and end (show in blue) of the data collection.

The collected GPS signals were processed using the standard version of the GSNRx^{TM} software receiver and the absolute carrier power values for all visible satellites were estimated using the procedure described in Appendix A. The estimated carrier powers were further processed according to the procedure described in Section 4.2 to extract fade statistics. In this case, since there is only one antenna observation, $\hat{C}_{rov,dBm}$ is replaced by

$\hat{C}_{ref,dBm}$. The implication of this is that the mean shadow level will be equal to 0 dB since the mean carrier power is removed from the observations.

A sample plot of the estimated carrier powers for three different satellites PRN21, PRN22 and PRN26 is shown in Figure 4-3(a). It can be clearly observed that receiver antenna gain variations and path loss are the major contribution to the maximum amplitude variation. As evident from Figure 4-2 (b), PRN22 and PRN26 are approaching towards the receiver antenna whereas PRN21 is heading away.
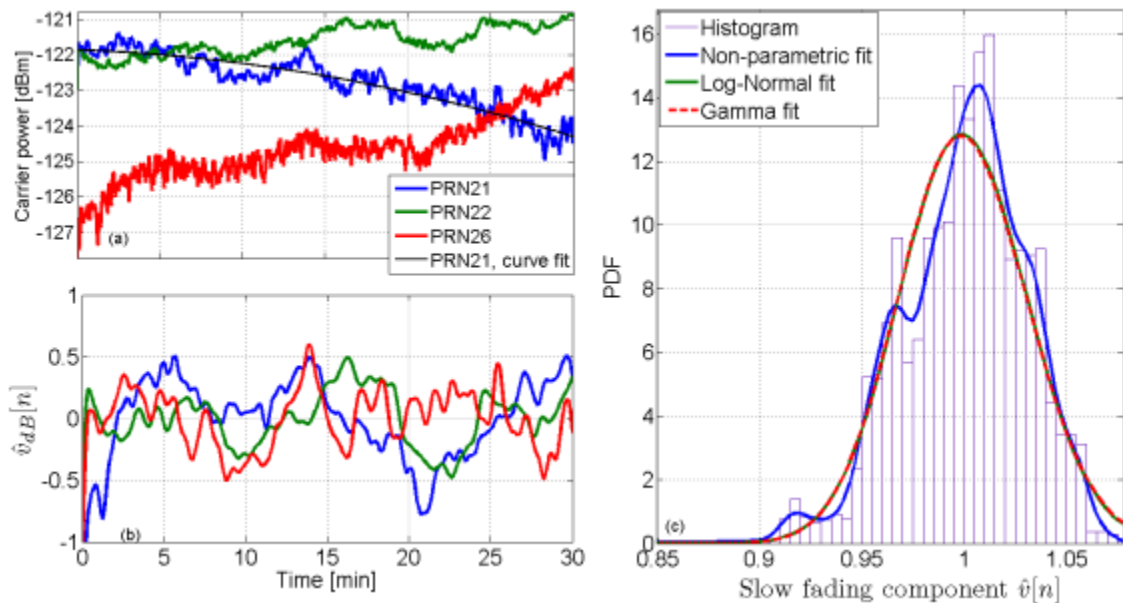
Figure 4-3: (a) Estimated carrier power levels at the output of the reference antenna for three different satellites. (b) Slow fading component obtained after removal of the path loss effect (c) Comparison of the empirical PDF of slow fading component with the parametric models.

Accordingly, the received carrier power for PRN22 and PRN26 is increasing as a function of time whereas it is decreasing for PRN21. This plot clearly highlights the fact that the channel is continuously changing due to the relative motion between satellite and receiver. It is also possible to observe from Figure 4-3(a) that the carrier power variation

has both deterministic and random components. Deterministic variations can be attributed to the path loss component whereas slowly varying random fluctuations can be attributed to the shadow fading phenomenon. As it is evident from Figure 4-3(a),the contribution from fast fading effects are minimal and hence neglected in the following. As described earlier in Section 4.2, the deterministic component, $\hat{p}'_{dB}[n]$, can be obtained by curve fitting using a first or second order polynomial. For example, the deterministic component for PRN21 obtained using second order curve fitting is shown in Figure 4-3(a). Here, the estimated $\hat{p}'_{dB}[n]$ is added to the mean carrier power level to bring it to the absolute scale (from Figure 4-1, $\hat{p}'_{dB}[n]$ is a zero mean signal). Now, the slow fading component, $\hat{v}_{dB}[n]$, can be obtained by subtracting $\hat{p}'_{dB}[n]$ from the signal $\hat{\zeta}_{dB}[n]$ (high pass filtering) as shown in Figure 4-3(b). These random variations are generally small and well within 0.5 to 1 dB around the deterministic component.

Figure 4-3(c) compares the PDF of $\hat{v}[n]$ with the standard Log-Normal and Gamma distributions. It can be observed that the empirical PDF is in good agreement with the standard parametric models. The corresponding Log-Normal parameters are estimated to be $\mu_s = \hat{\rho}_{dB} = 0$ and $\sigma_s^2 = 0.0735$. Since the variance of $\hat{v}[n]$ is very small, it can be safely assumed that under open sky conditions, amplitude variations are mainly due to free space propagation losses.

4.4.2 Open sky, single side reflector scenario

Figure 4-4 shows one of the data collections performed in front (West side) of the CCIT building at the UofC. Two different data collections were performed, one on 20 Feb 2009

at 7:00-7:30 pm and another on 29 May 2009 at 4:00-6:00 pm. Multiple datasets were collected on each day under both static and dynamic conditions. As it can be seen from Figure 4-4, the CCIT building acts as a strong reflector for those signals arriving from the west side of the building. Due to the high power of the received signals, only rover antennas were used.
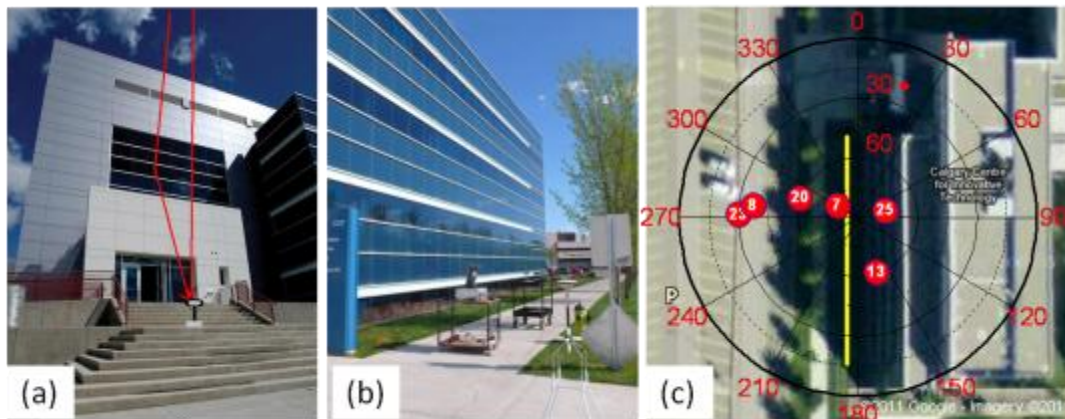
Figure 4-4: Data collection performed in front of a reflecting building (CCIT building). (a) Static placement of the antenna. (b) Data collection under dynamic conditions on a cart. (c) Top view of the CCIT building along with the sky plot of the visible satellites.

Figure 4-5 shows the estimated carrier power variations for two different satellites, PRN20 and PRN23 obtained from the static dataset. The absolute carrier powers were -125.8 dBm and -128.4 dBm for PRN20 and PRN30, respectively. Here, the procedure described in Section 4.2 is used to isolate the high and low frequency components from the measurements. It can be clearly observed that there exists a periodic nature in the received carrier power. These variations cannot be attributed to shadowing as there was no signal blocking elements during the entire data collection period. Also, the receiver antenna was static for the entire data collection interval. It is possible to show that under

limited number of multipath signals, the received signal envelope results in a standing wave pattern (Fontan & Espineira 2008). For example, considering a two ray multipath model, the received complex baseband signal can be written as

$$\tilde{r}(t) = a_0(t)\exp\left(j\phi_0(t)\right) + a_1(t)\exp\left(j\phi_1(t)\right) \tag{4.10}$$
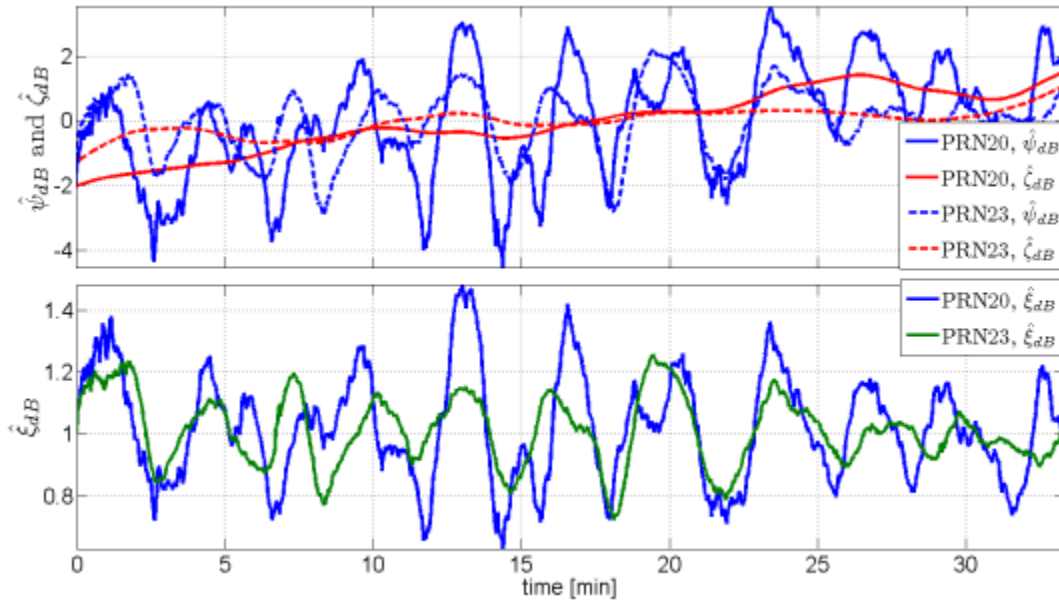
Figure 4-5: Estimated carrier profiles for PRN20 and PRN23 under static conditions.

Thus, the resulting envelope is given by

$$z(t) = \left|\tilde{r}(t)\right| = \sqrt{a_0^2(t) + a_1^2(t) + 2a_0^2(t)a_1^2(t)\cos\left(\phi_0(t) - \phi_1(t)\right)} \tag{4.11}$$

It is evident from (4.11) that the resulting envelope is oscillatory in nature and its period is proportional to the difference in Doppler values of the direct and the reflected signal. The magnitude of the variations depends on the amplitude of the LOS and reflected signal. In the current scenario, as the user antenna is static, the difference in Doppler values of the direct and multipath signal is purely due to the satellite motion. From this

observation, it is possible to conclude that, when considering a static scenario under the presence of a single reflector, the effect of fading can be simulated using a reduced number of sinusoidal functions with random phase values. On the basis of this observation, an effort was made towards reconstructing the slow variations in the signal envelope with few sinusoidal functions (Satyanarayana 2010). Here, the amplitude time series were passed through a low pass filter in order to remove the high frequency component. As an effect of this, only slow signal variations were retained. Fundamental frequency components were extracted using the Fast Fourier Transform (FFT). Only fundamental frequency components were retained by comparing the magnitude values against a predefined threshold. The amplitude series is then reconstructed using the Inverse FFT (IFFT) operation on the retained signal magnitudes. Figure 4-6 shows two such cases for different PRNs.
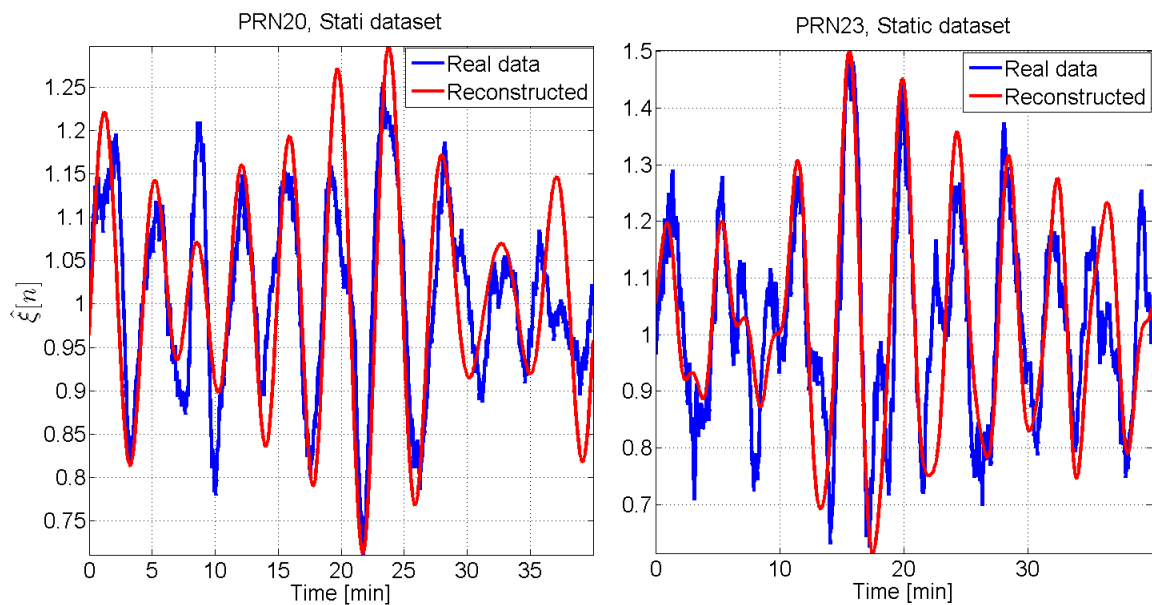
Figure 4-6: Amplitude profiles obtained from real GPS data along with the reconstructed signal using the first seven fundamental periodic components.

It can be clearly seen that the reconstructed signal almost matches real data suggesting its modelling through a Fourier series approach.

Figure 4-7 shows the estimated carrier profiles for four different satellites under dynamic conditions. Here the amplitude variations are much faster than those observed in the static scenario. This is due to the fact that as the receiver moves from one place to another, the delay associated with multipath rays varies. A small change in delay parameters results in a significant change of phase of multipath rays. This, in turn, causes rapid variations in the signal amplitude due to the constructive and destructive nature of the fading phenomena. It can be observed from Figure 4-4(c) and Figure 4-7 that the range of signal power variations is dependent on the elevation angle of the satellite and orientation of the reflecting surfaces. For example, PRN07 and PRN08 have larger signal power variations than those of PRN13 and PRN25.
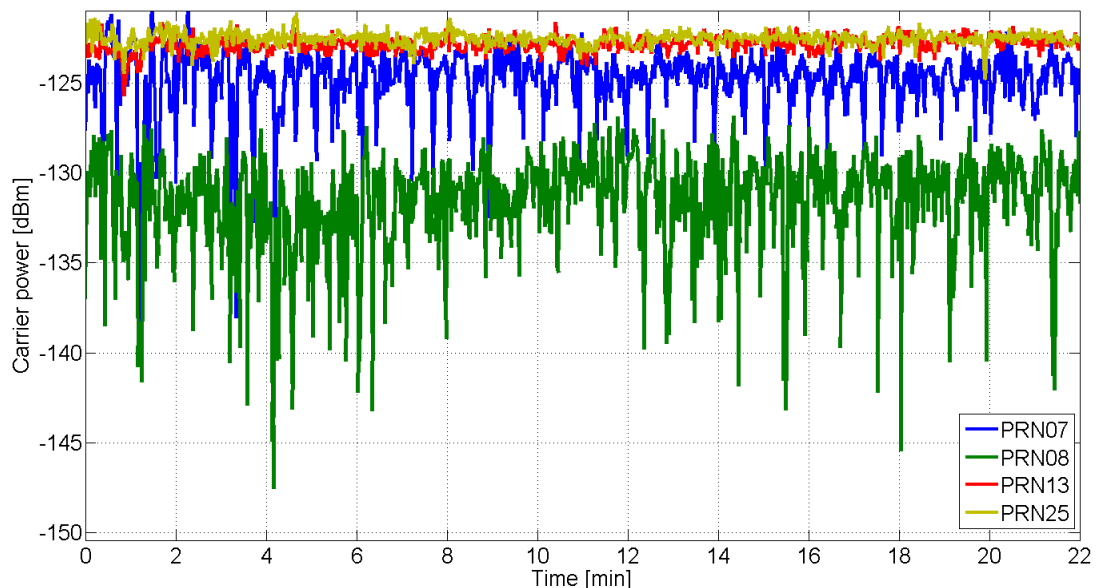
Figure 4-7: Estimated carrier powers of four different satellites from the dynamic dataset collected in front of the CCIT building.

This is due to the fact that the elevation angles of PRN07 and PRN08 are relatively low (sky plot not shown) and located exactly on the opposite side of the reflecting surface (low incident angles) whereas PRN13 and PRN25 are high elevation angle satellites and the reflecting surface lie almost in a plane parallel to the signal propagation.

From Figure 4-5 and Figure 4-7, it is clear that the signal variations due to slow fading effects are minimal and hence ignored from further analysis. Earlier in this section, fast fading variations were modeled as the sum of a limited number of sinusoids with random phases and different frequencies. This leads to an extremely time correlated amplitude profile that can also be modeled as a non-white random process (Pätzold 2002). For this reason, it is worth considering the empirical distribution of the extracted amplitude profile. Time correlation and second order statistics will be considered in Chapter 5.

Figure 4-8 compares the estimated PDFs of the fast fading component, $\hat{\xi}[n]$, due to multipath under both static and dynamic conditions against the standard parametric models. It can be observed that the empirical PDFs are in good agreement with the theoretical models. The Rician K factors under static and dynamic scenarios are 24.2 (13.8 dB) and 13.1 (11.2 dB), respectively and the corresponding Nakagami-m parameter can be obtained from the Rice factor K using the relationship provided in (Stüber 2002). As expected, the Rician K factor under static scenario is comparatively higher than the dynamic scenario. In a dynamic scenario, the signal variations are more unpredictable due to faster multipath phase changes resulting in a lower K factor value.
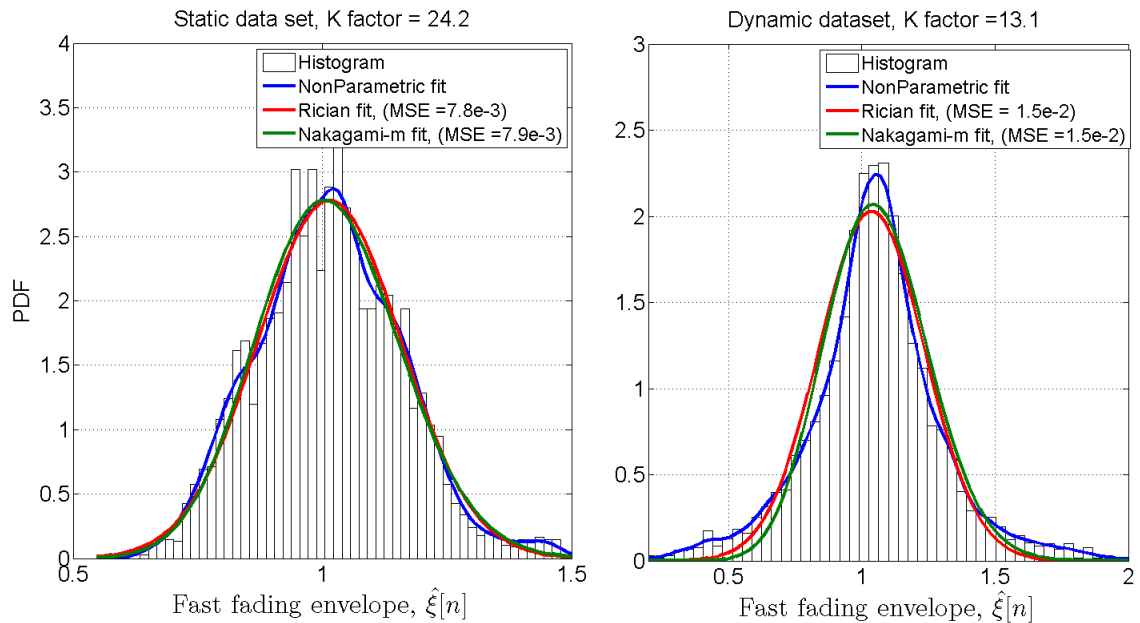
Figure 4-8: PDFs of the fast fading component under static (a) and dynamic (b) conditions.

4.4.3 Open sky, multiple reflectors scenario

Figure 4-9 illustrate the data collection that was performed on the (East side) of the CCIT building at the UofC. The data collection was performed on 12 Aug 2009 at 3:30-5:00 pm. Multiple data sets were collected under dynamic and static conditions. The red dot in Figure 4-9 shows the position of the static reference antenna whereas the yellow strip shows the approximate path followed during the dynamic data collection. The surrounding buildings consisted of different materials, leading to different reflection properties.

The sky map of the satellite constellation is superimposed on the top view of the data collection site. Figure 4-10 shows a sample plot of carrier power variations for PRN17 from the reference antenna placed in the middle of the data collection site. The overall carrier power level variation is limited to ±2 dB with respect to its mean value. Similar

results were found for the rest of the satellites and additional results can be found in

Appendix B.
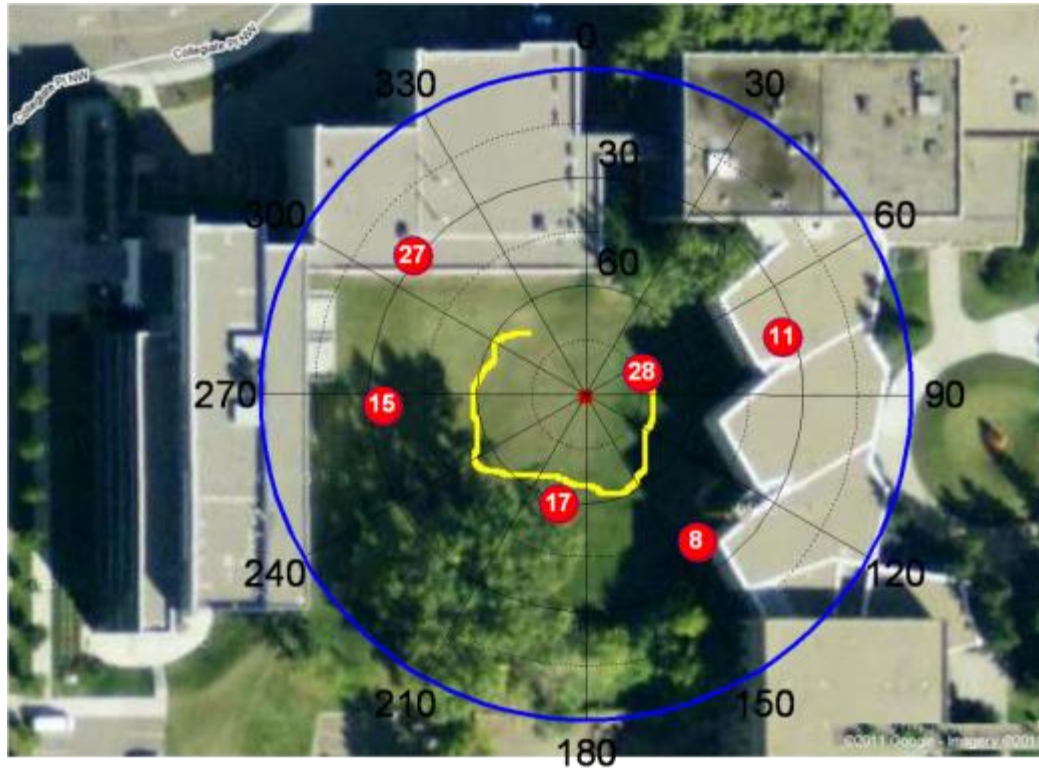
Figure 4-9: Data collection performed in an open sky environment surrounded by buildings. The position of the reference receiver is indicated by a red dot whereas the yellow line shows the approximate path taken by the user during the data collection.

In contrast to the single reflector scenario presented in Section 4.4.2, no dominant

periodic patterns were observed in the carrier power variations. This is due to the fact that

most of the satellites considered for analysis were high elevation and most of the

reflecting buildings were relatively far from the receiver. Figure 4-11 compares the

empirical density functions of fast and slow fading components obtained from the static

antenna with the standard parametric models. It can be observed that the empirical

density functions are in good agreement with the parametric models. The Rice factor K of the signals in this scenario is estimated to be 92.3 (19.7 dB).
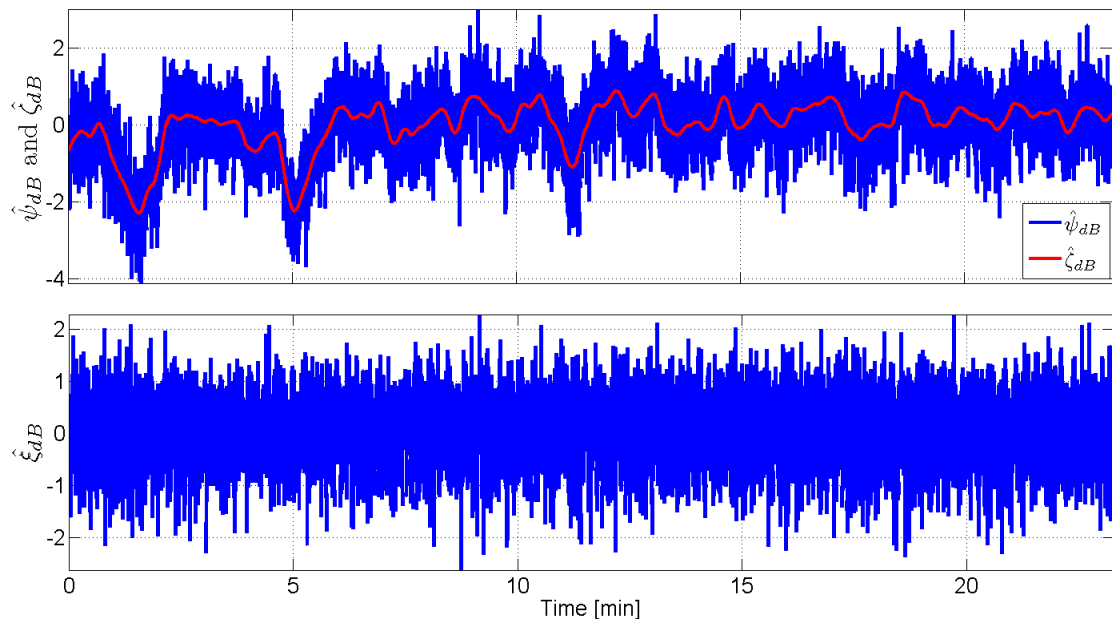
Figure 4-10: Carrier power variations for PRN17 from the static antenna.
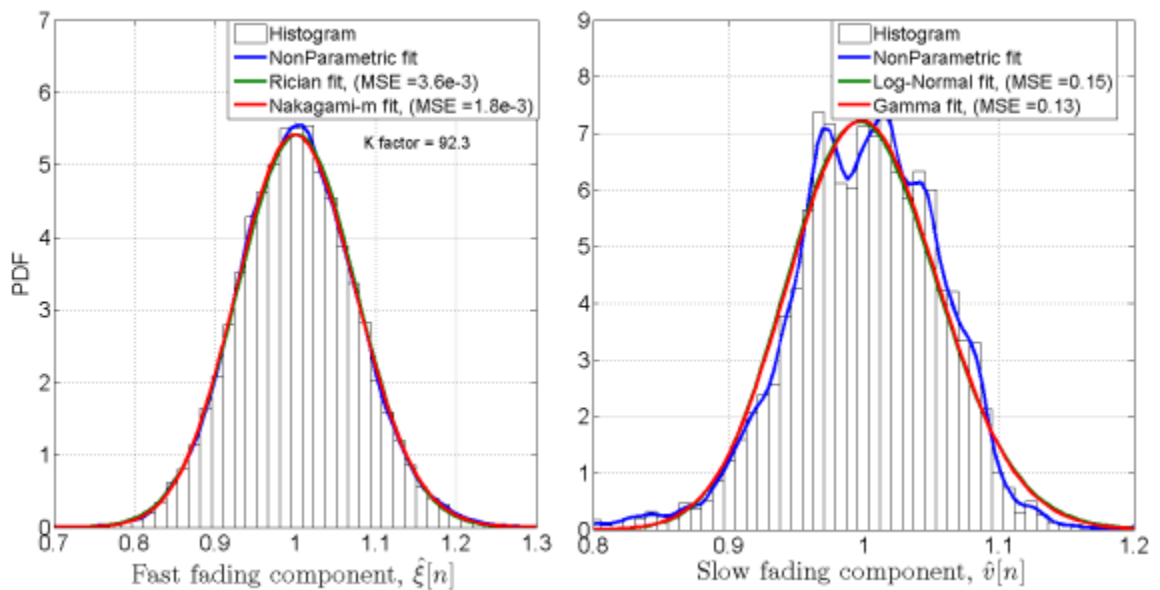
Figure 4-11: Comparison of the empirical PDF of the fast and slow fading components with the standard parametric models (static conditions).

Figure 4-12 shows the estimated carrier power levels for six different satellites from the dynamic dataset. It can be observed that each received signal has different characteristics. This difference in the received signal power is mainly due to the elevation angle of the satellite, structure of the buildings and the antenna displacement. For example, PRN15 and PRN08 have similar elevation angles (different azimuth angles) and both have LOS condition with respect to the receiver antenna. From Figure 4-12, it is clear that the carrier power variations for these two satellites are similar and hence have similar amplitude characteristics.

Figure 4-13 compares the estimated density functions of the fast and slow components obtained from combining the measurements of PRN15 and PRN08 with the standard parametric models.
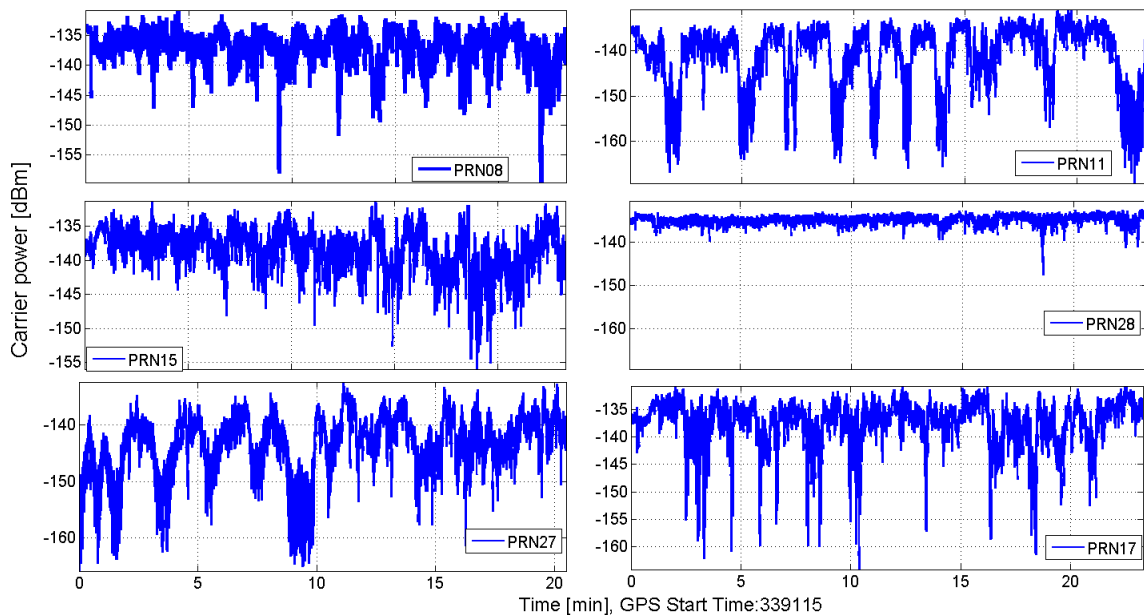
Figure 4-12: Estimated carrier power profiles for six different satellites from dynamic dataset.
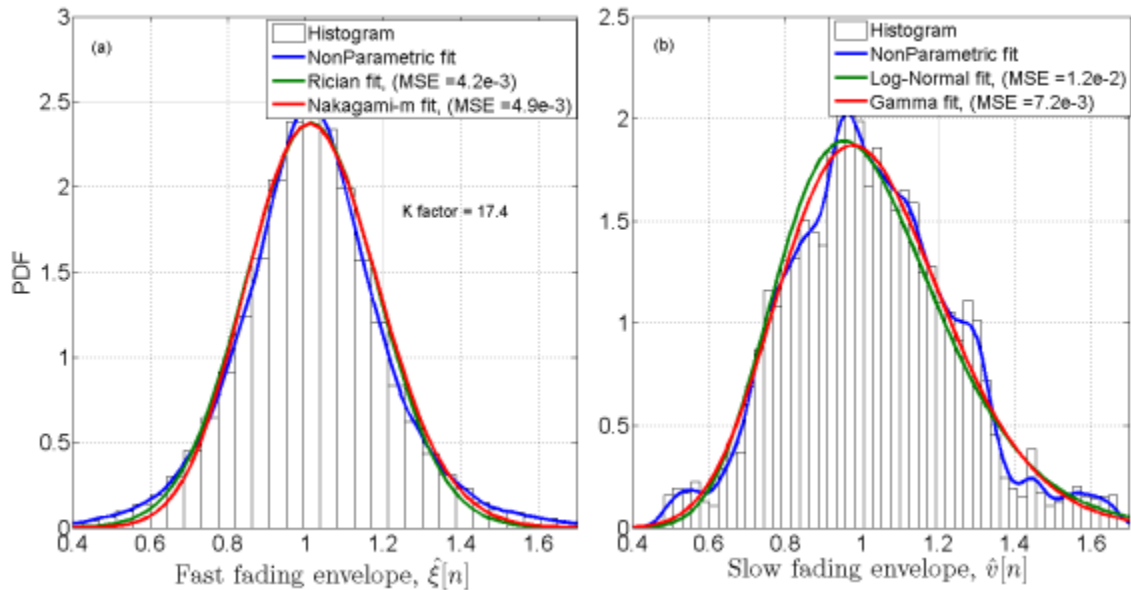
Figure 4-13: Comparison of empirical PDF with the standard parametric models.

It can be observed that a good agreement can be found between the empirical and standard models. The Rice factor K in this case is estimated to be 17.4 (12.4 dB). The carrier power variations of PRN28 were found similar to the case of PRN25 and PRN13 from the single reflector scenario presented in Section 4.4.2. The elevation angle of PRN28 was close to 85 degrees. As the satellite was at zenith, the multipath is mainly due to the reflections from the edges of the building and trees. It was shown in (Satyanarayana 2010) that the amplitude distribution of the PRN28 is in good agreement with the Rician model under both static and dynamic conditions.

Figure 4-14 shows the typical amplitude variation that can occur in an urban or semi-urban scenario. PRN11 was to the east side during the data collection period.
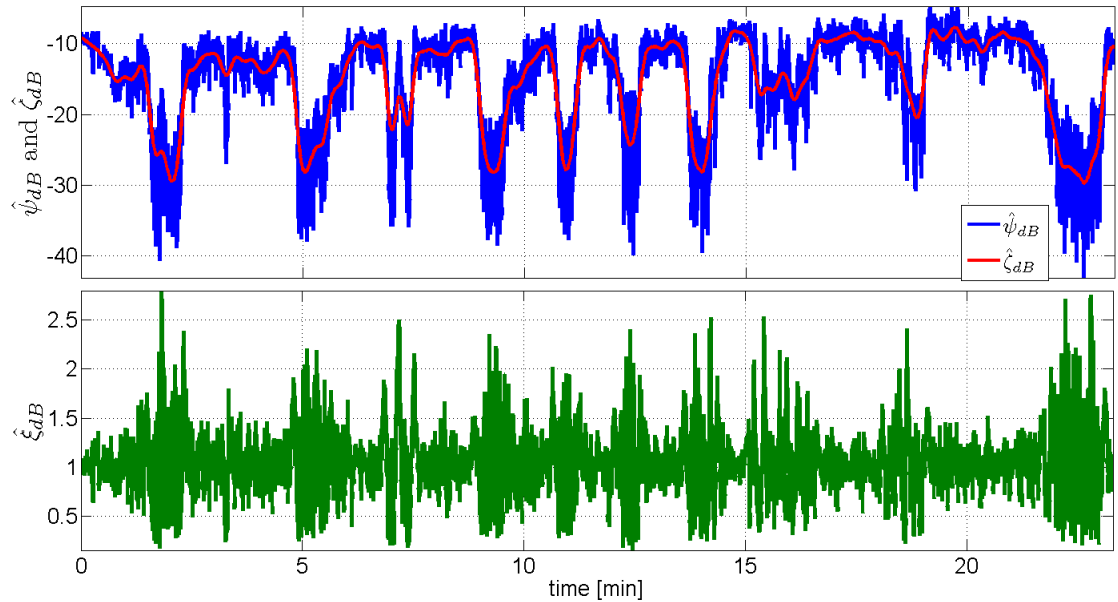
Figure 4-14: Amplitude profiles for PRN11 under dynamic conditions representing a typical urban/semi-urban scenario. The LOS signal is occasionally blocked by building and trees.

Due to the user motion, PRN11 was blocked as the user was moving close to the building on the east side. As the LOS component was blocked, the receiver antenna was receiving signal components due to reflections and diffraction caused by the nearby building resulting in a significant reduction of the signal strength. Here a single model such as the Rice or Log-Normal distribution cannot be used to capture large scale signal variations. Generally such channels are described using two/three state models. For example the two state GOOD/BAD model described in Section 2.6.1.3 is more suitable in these types of scenarios.

An interesting observation is that the variance of the fast fading components under GOOD and BAD states show different characteristics. As it can be observed from Figure 4-14, the variance of the fast fading component increases whenever the channel is in the BAD state and vice versa. Similar amplitude characteristics were found on PRN17 and

PRN27. PRN27 was blocked by the north side of the buildings whereas PRN17 was blocked by the trunks of large trees in the south side. As a result, the dwell time for PRN11 and PRN27 under bad state was found to be larger as compared to that of PRN17. The Satellite Availability (SA) in the present scenario as a function of absolute carrier power level (receiver sensitivity) and percentage of time is summarized in Figure 4-15. It can be observed that in these conditions, most of the satellites are available for a receiver sensitivity of -149 dBm.
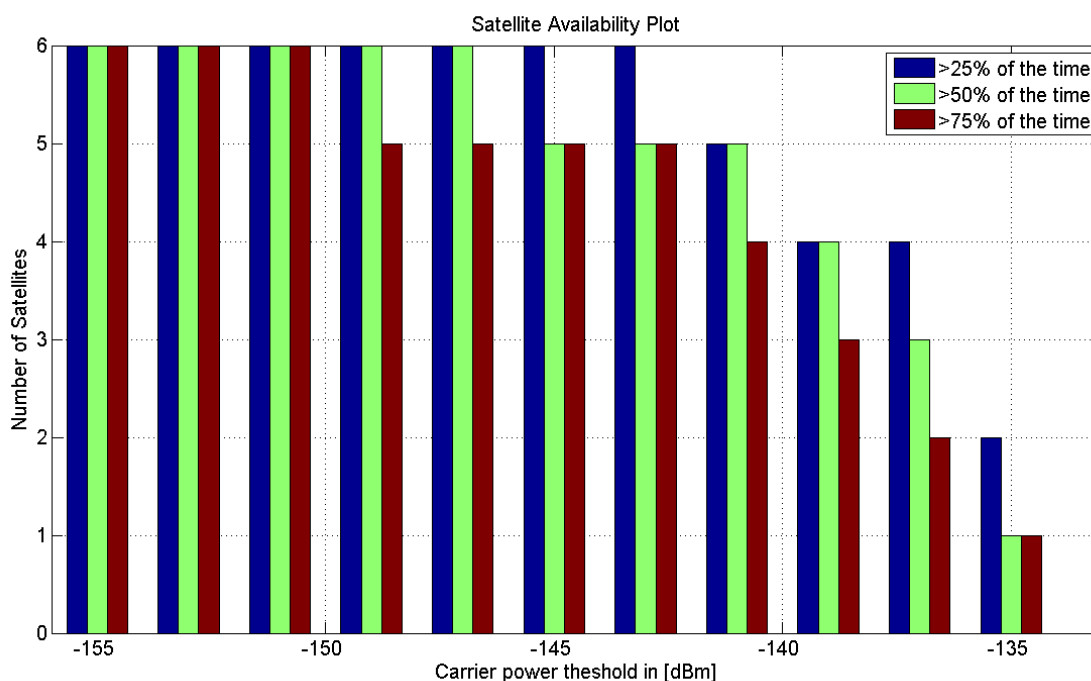
Figure 4-15: SA as a function of the power level in dBm and the percentage of time with respect to the total duration of the dynamic data collection.

4.4.4 Foliage scenario

Figure 4-16 shows the data collection performed in a parking lot in front of the CCIT building at the UofC. Data collection was performed on 19 Aug 2009 at 12:00-1:00 pm. The trees in the parking lot provided a very good foliage scenario resulting in a degraded

signal environment. The first data set included a dynamic test in which the user holding the antenna was randomly walking. In another test, the antenna was kept static in a pathway covered by trees on both sides. In both cases, only those satellite signals which were blocked by trees were considered for the analysis.
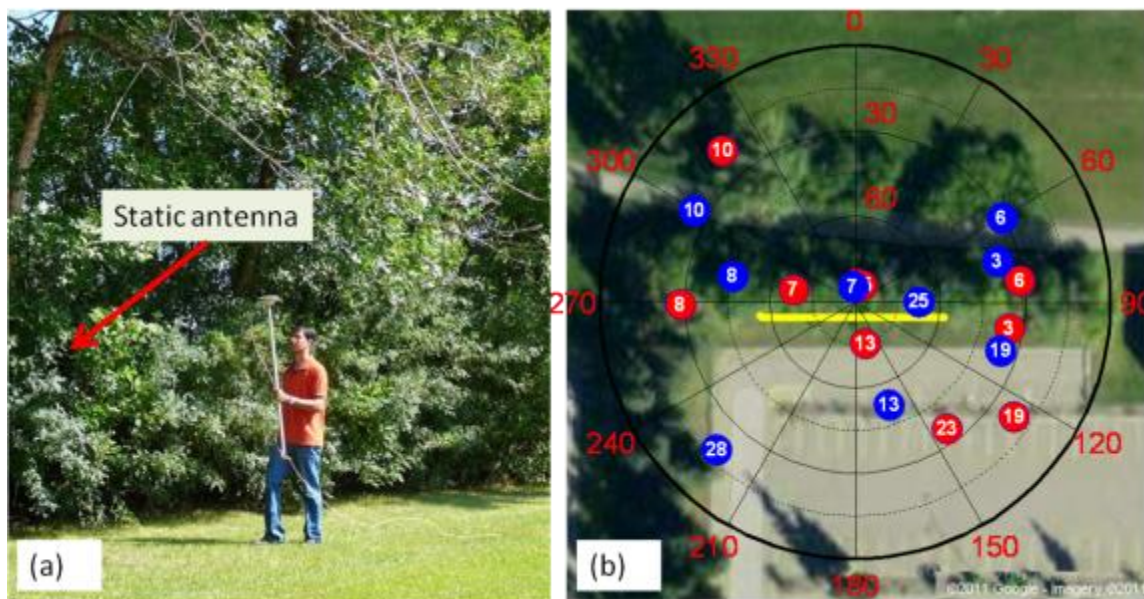
Figure 4-16: Data collection setup used for collecting raw samples under a foliage scenario. (a) The antenna was kept static in a pathway surrounded by bushes whereas for the dynamic case the user was walking close to the trees. (b) Skyplot of the data collection under foliage.

A sample plot of the slow and fast fading components for PRN19 obtained from the static dataset under foliage conditions are shown in Figure 4-17(a) and (b). As it can be seen from Figure 4-16 (b), PRN19 is a low elevation angle satellite (40 degrees) and is completely blocked by trees and their leaves. A major contribution for signal fading under static condition is the shadowing caused by the branches and leaves of the trees. As the satellites moves over time, the incoming signals are blocked by various branches resulting in a time varying shadow phenomena. From Figure 4-17(a) and (b), it can be

observed that the signal is attenuated by almost 10 dB as compared to the reference signal. Similar results were found for the other satellites as shown in Appendix B.
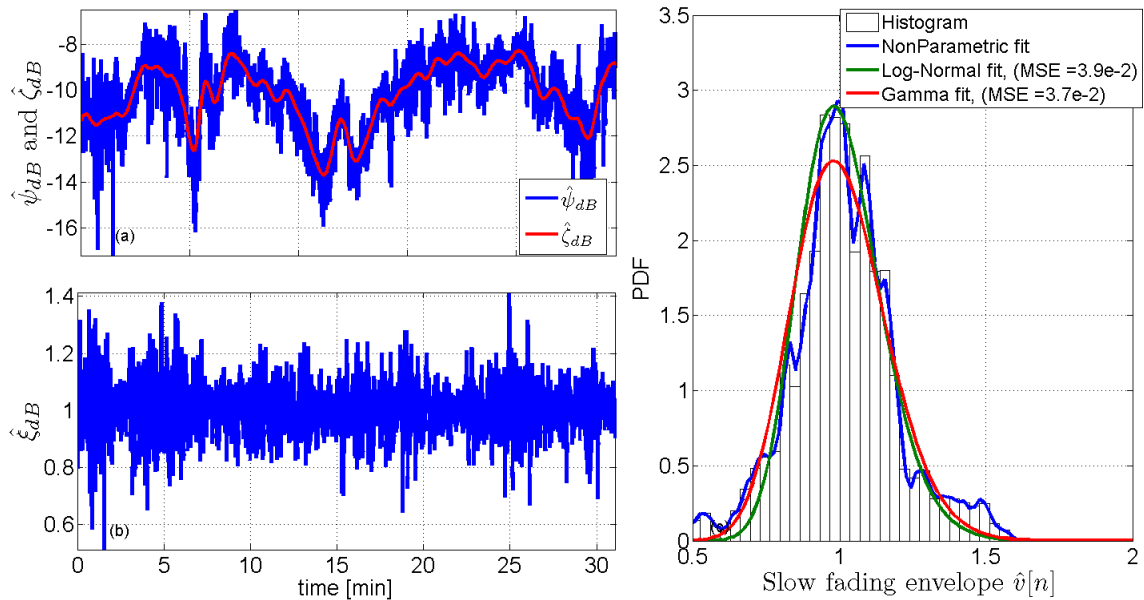
Figure 4-17: (a) Carrier power variations of PRN19 from static dataset (slow fading component is shown in red). (b) Fast fading component obtained after high pass filtering. (c) Comparison of empirical PDF of slow fading component with standard models.

A comparison of the empirical PDF of the slow fading component with standard models is shown in Figure 4-17(c) for the static dataset. It is found that Log-Normal and Gamma distributions closely approximate the shadowing phenomena.

Figure 4-18 shows the carrier power profiles for PRN06 under dynamic conditions. It can be clearly seen from the plot that the variations in the signal strength are much larger as compared to the static scenario. During dynamics, few static periods were simulated by keeping the receiver antenna under a tree. These intervals are shown in Figure 4-18 (top). It can be clearly seen that under the static intervals, signal variations are relatively small as compared to the dynamic scenario.
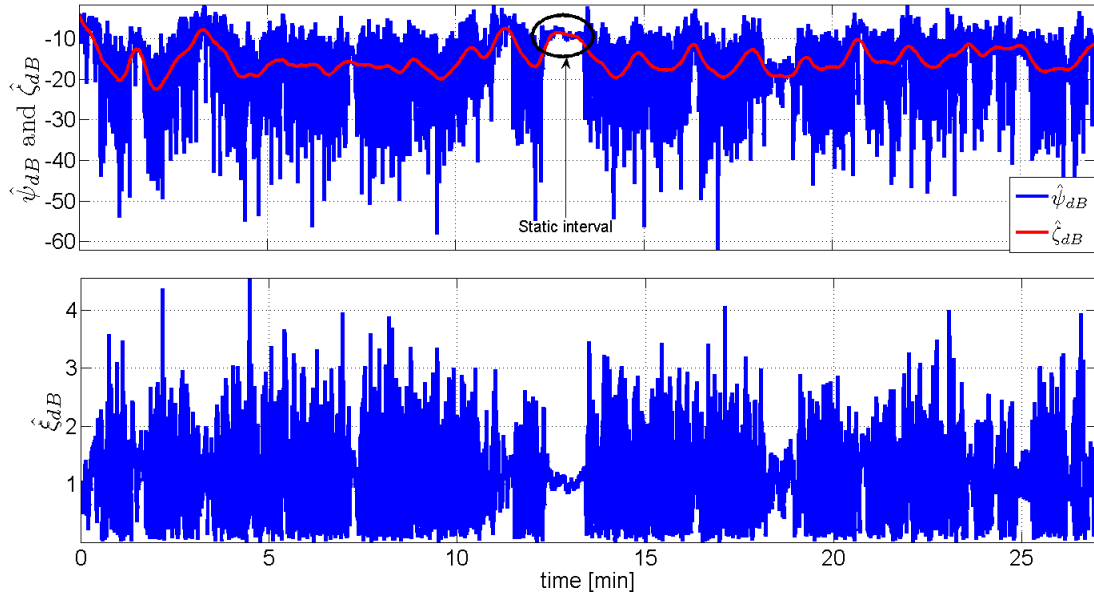
Figure 4-18: Carrier power variations of PRN06 from dynamic dataset (slow fading component is shown in red).

Figure 4-19 compares the empirical density functions of fast and slow fading components obtained from the dynamic antenna with standard parametric models. It can be observed that the empirical density functions are in good agreement with parametric models. The Rice factor K of the signals in this scenario is estimated to be 1.94 (2.83 dB). Thus a dynamic receiver under foliage condition almost experiences a Rayleigh fast fading phenomena.

SA in the foliage scenario as a function of absolute carrier power level (receiver sensitivity) and percentage of time is summarized in Figure 4-20. In these conditions most of the satellites are available for a receiver sensitivity of -152 dBm under dynamic conditions and -155 dBm under static conditions.
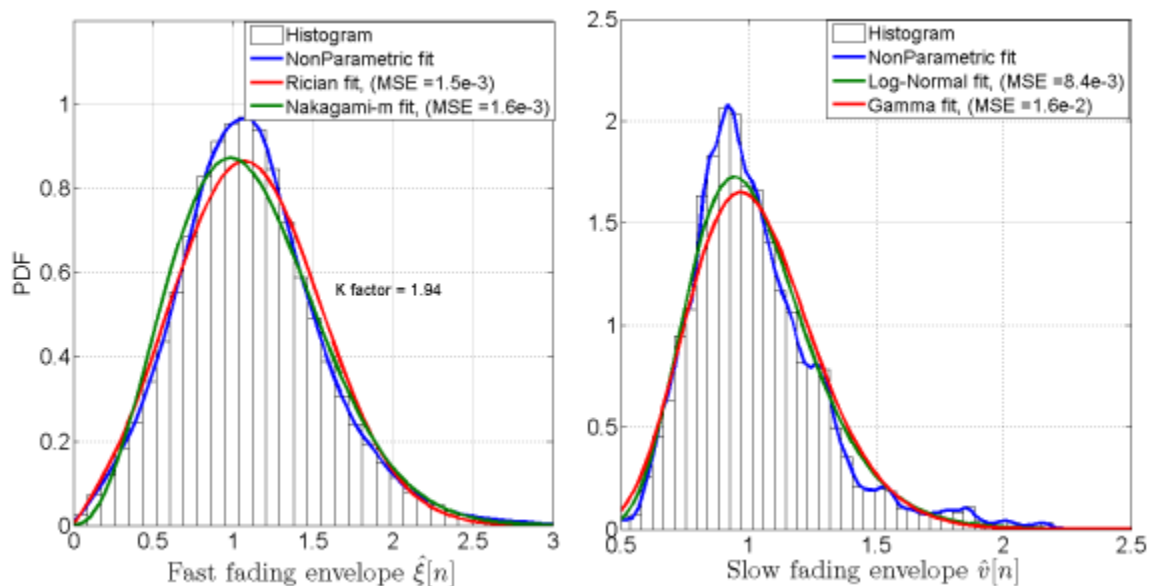
Figure 4-19: Comparison of empirical PDF with standard parametric models for a dynamic data set under foliage scenario.
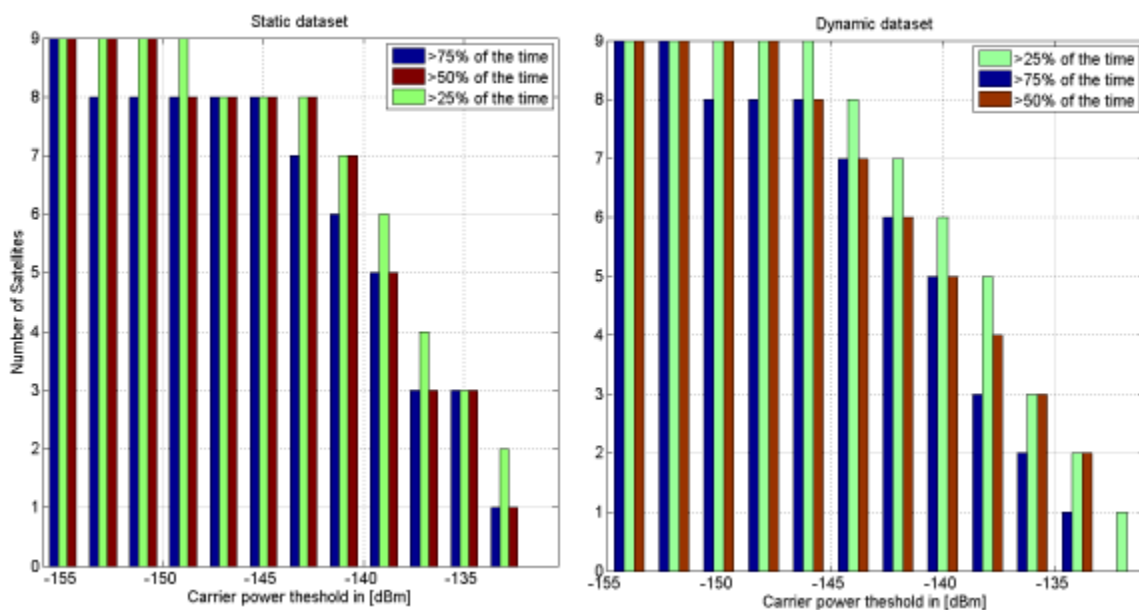
Figure 4-20: Satellite availability as a function of the power level in dBm and the percentage of time with respect to the total duration under both static and dynamic conditions in a foliage scenario.

It is interesting to note that even though the signal variations are large under dynamic conditions, the probability of satellite visibility is higher under dynamic conditions as compared to static. This could be because the recovery from a deep fade state is faster under dynamic conditions.

4.4.5 Indoor scenario

Results obtained for both static and dynamic tests conducted in several indoor environments are presented in this section. To begin with, a brief summary of the various data collections performed in order to characterize the GNSS indoor propagation channel is provided.

4.4.5.1 Data collection summary

Five different indoor scenarios have been considered for signal characterization. A list of all the indoor data collections along with their IDs is summarized in Table 4-4 and Table 4-5.

Table 4-4: Summary of indoor data collections.

Dataset ID	Scenario description
NL-DS1-S	Navigation Laboratory (NavLab) located in the third floor of the CCIT building, static experiment. The NavLab resembles a large office room made of concrete walls with coated windows on the east side
NL-DS1-D	NavLab, dynamic experiment
CR-DS1-S	Conference room located in the third floor of the CCIT building, static experiment. This conference room is surrounded by metallic coated windows on three sides and a wall on the other side.

Table 4-5: Summary of indoor data collections (Cont'd).

WH-DS1-S	Main floor of a wooden house, static experiment. This wooden house has two levels, main floor and basement with multi layered wooden rooftop.
WH-DS2-S	Basement of the wooden house, static experiment
WH-DS1-D	Wooden house, dynamic experiment covering both main floor and basement
ME-DS1-D	McEwan hall at the UofC, dynamic experiment. The McEwan hall resembles a typical shopping mall scenario having a vast empty area with food courts, furniture and glass rooftops
ME-DS2-D	McEwan hall at the UofC, dynamic experiment, dataset 2

More details on each of the experiments and results are provided in the following subsections. At first, the results corresponding to static experiments are described followed by the findings relative to the dynamic experiments.

4.4.5.2 Static scenarios

Figure 4-21 shows the data collection performed inside the NavLab (dataset NL-DS1-S) on 02 Feb 2010 at 02:15-02:45 pm. In this indoor scenario, the signal is strongly attenuated by the structure of the building.

Figure 4-22 (a) shows the estimated carrier power levels difference between reference and rover antennas, $\hat{\psi}_{dB}[n]$, and the low-pass filter signal, $\hat{\zeta}_{dB}[n]$, for two different satellites, namely PRN18 and PRN27. In this case, the recovered signals show variations of up to 30 dB with a mean attenuation level of approximately 27 dB with respect to the reference signal.
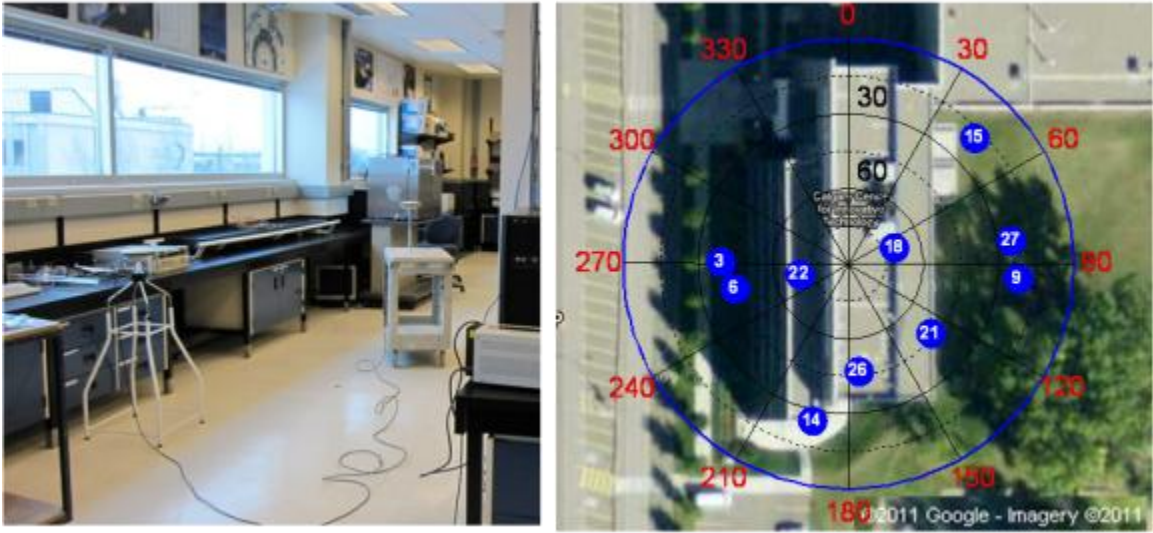
Figure 4-21: (a) Static and dynamic data collection setup inside the NavLab. (b) Sky plot of the satellite constellation superimposed on the top view of the CCIT building.
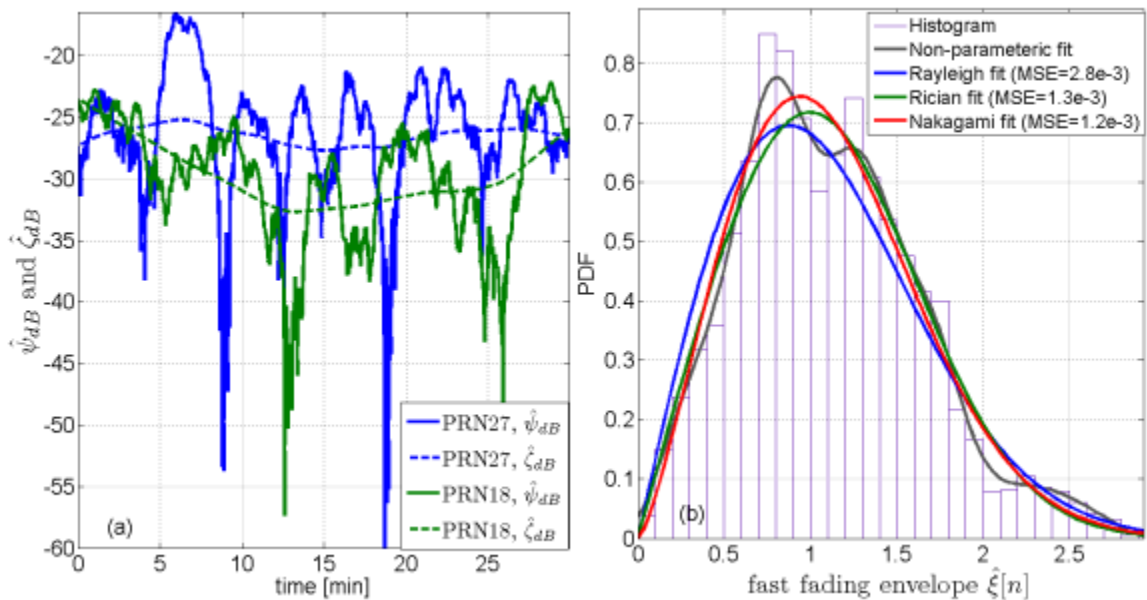
Figure 4-22: Static characterization results for NavLab data collection. (a) Carrier power levels of the indoor signals with respect to outdoor reference signals. (b) Comparison of the empirical PDF with standard models.

Figure 4-22 (b) shows the estimated density function of the fast fading component, $\hat{\xi}[n]$.

The estimated density function is compared against standard parametric models such as

Rayleigh, Rice and Nakagami-m distributions. It can be observed that the empirical data is in good agreement with the standard models. However, Rice and Nakagami-m distributions have lower MSE as compared to the Rayleigh model. The Rice factor K in this case is estimated to be 0.83.

Figure 4-23(a) shows the static data collection performed inside the conference room on 06 March 2009 at 2:30 pm (dataset CR-DS1-S). The static antenna was kept close to the metallic coated windows on the west side of the room. Figure 4-23(b) shows the sky plot of the satellite constellation during the data collection hour.
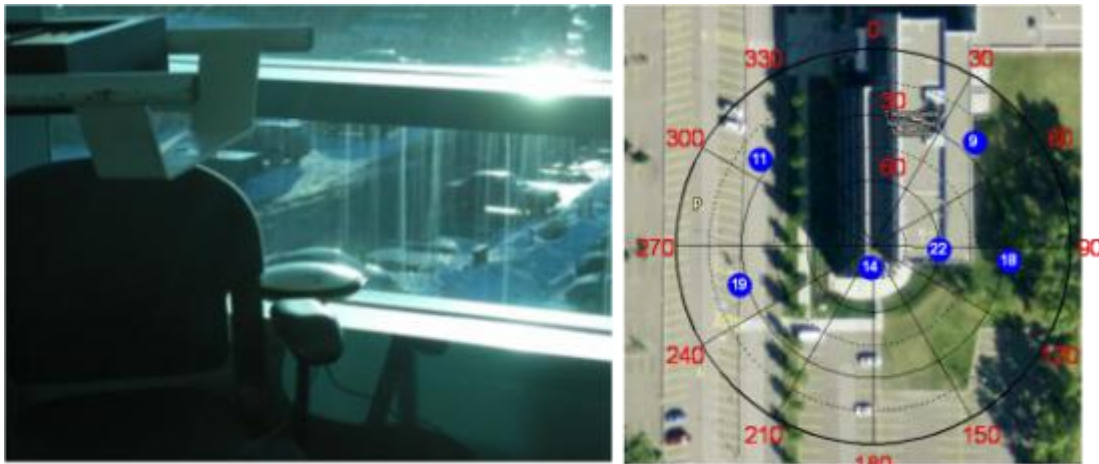
Figure 4-23: (a) Static data collection inside the conference room. The antenna was kept static next to the metallic coated windows. (b) Sky plot during the data collection period.

Slow and fast fading components for PRN19 are shown in Figure 4-24(a) and (b). It can be observed that the fast fading components exhibit periodicity in their variations. A similar behavior was observed for PRN11 which is also on the west side of the building and is shown in Appendix B. This scenario can be compared with the single reflector scenario presented in Section 4.4.2 except that the mean attenuation levels of the signals are in the order of 25 to 30 dBs.

Comparison of the empirical PDF of the fast fading components against the standard models is shown in Figure 4-24(c). In this case, a good match is obtained with the Rician model and the estimated Rician *K* factor is 3.8 dB. It should be noted that the Rician *K* factor is slightly higher than that of the NavLab scenarios due to the placement of the receiver antenna close to the window.
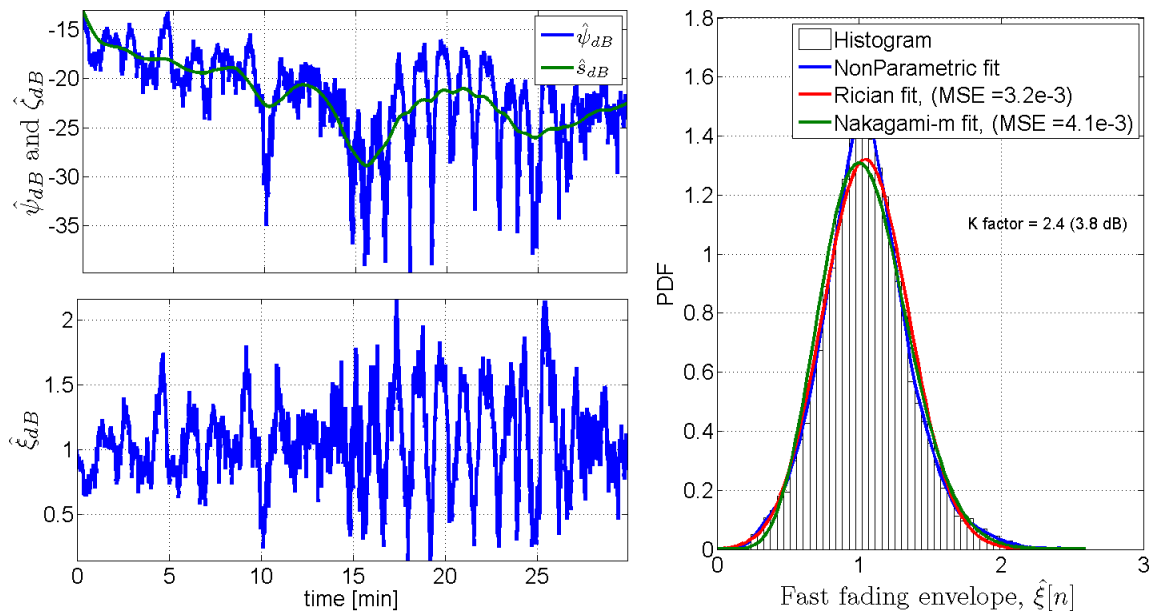
Figure 4-24: (a) Carrier power variations of PRN19 from static dataset (slow fading component is shown in green). (b) Fast fading component obtained after high pass filtering. (c) Comparison of empirical PDF of fast fading component with standard models.

Table 4-6 summarizes the estimated fade statistics for all the visible satellites available during the time of data collections NL-DS1-S and CR-DS1-S. It can be observed that GNSS signals received inside the NavLab are strongly attenuated and most of the satellites have mean carrier power levels below -150 dBm. The mean shadow levels experienced by the signals are in the range of 24-35 dB. It should be noted that indoor signals with power levels below -160 dBm are generally weak and require a coherent

integration time longer than one second to overcome the effect of noise. Similar levels of attenuation were experienced by the signals in the CR-DS1-S dataset. It can be observed that PRN09 has the lowest mean carrier power level. This is due to the fact that PRN09 is located in the North East side of the building and was totally blocked by the building walls.

Table 4-6: Summary of fade statistics obtained from the static experiment for all the visible satellites during NL-DS1-S and CR-DS1-S data collections.

NavLab (Dataset NL-DS1-S)			Conference room (Dataset CR-DS1-S)		
SV ID	Mean carrier power (dBm)	Mean shadow level $(\hat{\rho}_{dB})$	SV ID	Mean carrier power (dBm)	Mean shadow level $(\hat{\rho}_{dB})$
3	-165	-40.4	9	-168.2	-34.0
6	-162	-37.8	11	-158.0	-27.0
9	-160	-30.2	14	-157.7	-29.9
14	-165	-33.9	18	-161.0	-27.2
15	-160	-30.6	19	-155.1	-21.8
18	-154	-31.8	21	-156.3	-30.0
21	-158	-36.3	--	--	--
22	-145	-25.3	--	--	--
26	-160	-35.9	--	--	--
27	-159	-28.6	--	--	--

The test setup for the static data collection performed inside a typical North American wooden house is shown in Figure 4-25(a). Here, two different static data sets were collected in the main floor and basement of the building. The sky plot of the satellite constellation during the main floor (in red) and basement (in blue) data collection periods

is shown in Figure 4-25(b). The placement of the indoor antenna inside the house is indicated by a red circle.

A sample plot of the estimated carrier power levels for the main floor (WH-DS1-S) and basement datasets (WH-DS2-S) is shown in Figure 4-26. Here, satellite signals from four different elevation angles (1 high elevation, 1 medium elevation and 2 low elevations) are considered for the analysis.
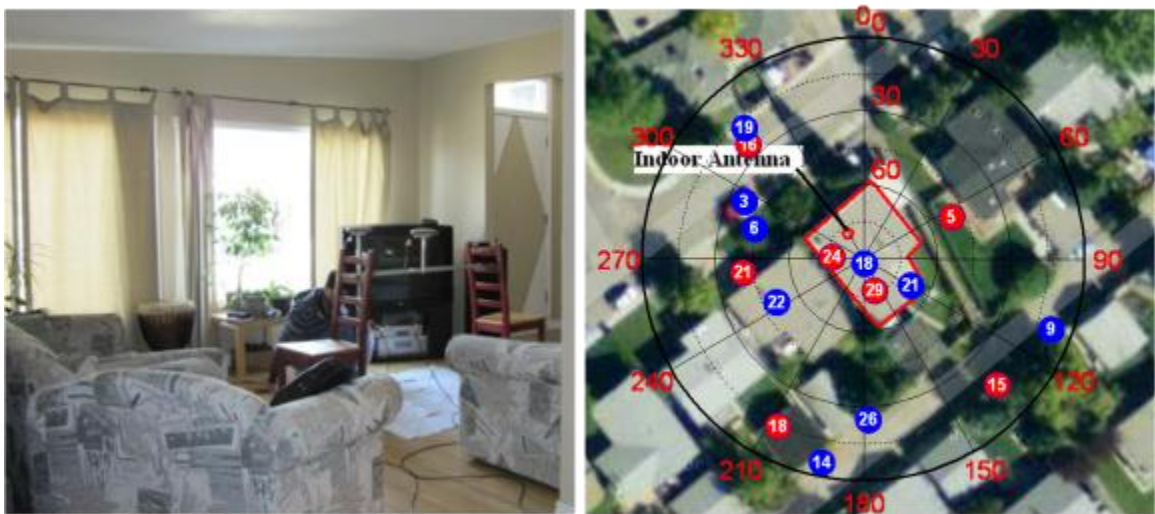
Figure 4-25 (a) Static data collection performed inside the wooden house. (b) Sky plot of the satellite constellation during the data collection on main floor (in red) and in the basement (in blue).

It can be observed that the signals collected in the main floor are characterized by stronger power (most of the signals have carrier power levels greater than -137 dBm) and minimal variations are observed. In this case, the signal amplitude does not significantly vary during the whole duration of the test (5 minutes). It can be safely assumed that the signal variations are mainly due to the path loss component. On the other hand, signal collected in the basement of the house also showed characteristics similar to those of the main floor except that the mean shadow levels were comparatively higher. Mean carrier

power levels and shadow levels for all the visible satellites from both main floor and basement datasets are summarized in Table 4-7. As expected, the mean carrier power levels from the main floor dataset are higher than those measured in the basement. In this latter case, 6-10 dBs of additional attenuation were experienced.
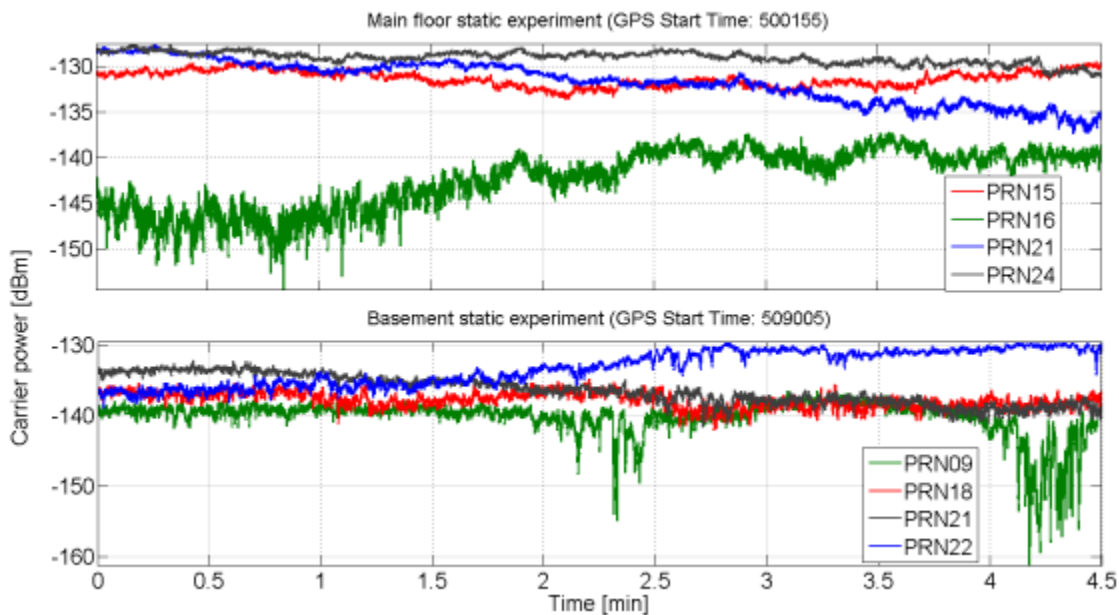
Figure 4-26: Carrier power levels estimated for the signals collected in the main floor of the wooden house (a) and in the basement (b).

The SA in the NavLab as a function of power level (receiver sensitivity) and percentage of time is summarized in Figure 4-27(a). In these conditions most of the satellites are available for a receiver sensitivity of -165 dBm. The power of all the available satellites is below -144 dBm. The same type of analysis has been repeated for the wooden house tests. Results for the main floor experiment are summarized in Figure 4-27(b). In this case, seven satellites are available for a receiver sensitivity lower than -145 dBm. Intermediate results are obtained for the basement experiments.

Table 4-7: Mean carrier power and shadow levels observed in the main floor and basement of a wooden house.

Wooden house, Main floor			Wooden house, Basement		
SV ID	Mean Carrier power [dBm]	Mean Shadow level [dB]	SV ID	Mean Carrier power [dBm]	Mean Shadow level [dB]
5	-137.2	-3.6	3	-141.4	-15.9
15	-131.2	-6.3	6	-145.6	-19.2
16	-142.1	-10.7	9	-140.2	-9.36
18	-135.5	-10.9	14	-144.8	-15.3
21	-132.0	-8.1	18	-137.6	-14.4
24	-129.2	-7.2	21	-136.4	-12.4
29	-133.6	-8.5	22	-133.5	-10.9
--	--	--	26	-144.1	-21.0
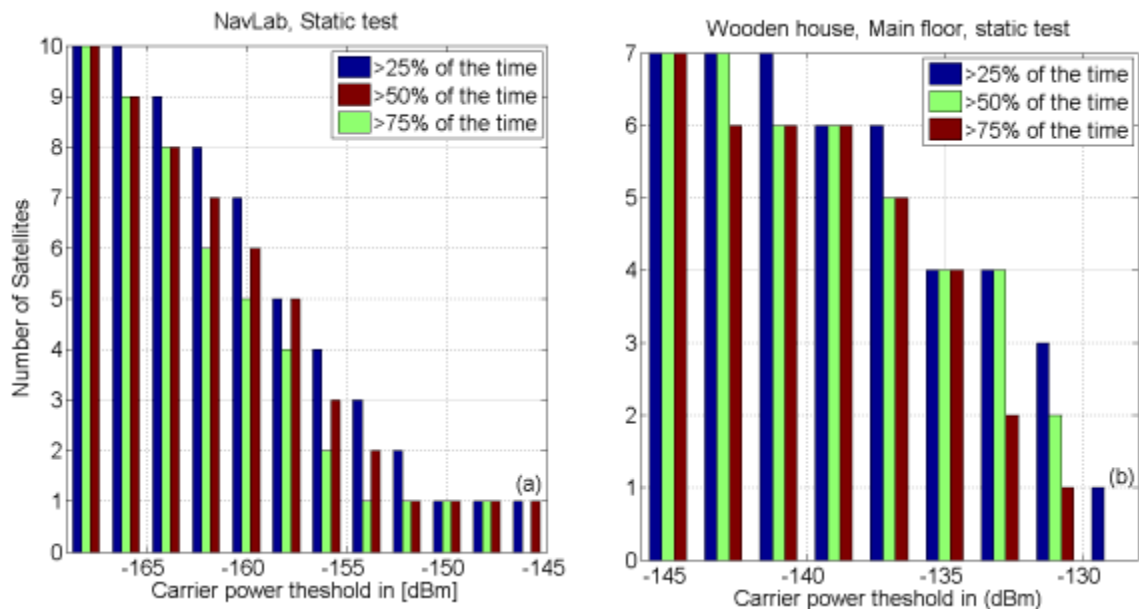
Figure 4-27: Comparison of the satellite availability for the NavLab and wooden house scenarios under statistic conditions.

From these results it can be concluded that a receiver can hardly have a position fix in an environment such as the NavLab. In this case, receiver sensitivity lower than -156 dBm would be required to successfully process at least four satellites. The wooden house is a

much more benign environment and four satellites are usually available for a receiver sensitivity of about -137 dBm. This implies that in the NavLab, a 20 dB additional attenuation is experienced by GPS signals with respect to the wooden house case.

4.4.5.3 Dynamic scenarios

Figure 4-28 shows a sample plot of the estimated carrier power variations for PRN18 under dynamic conditions for the NL-DS1-D dataset. Here, the signal variations are much more random as compared to the static case. It can be observed from Figure 4-28 that the mean shadow level of the signal under dynamic condition is consistent with the static case. Similar results were found on other satellites as shown in Appendix B.

Comparison of the estimated PDF of slow and fast components obtained under dynamic conditions against the standard models is shown in Figure 4-29. It can be observed that the fast fading components are in good agreement with the Rayleigh model. This means that, under such indoor scenarios, the LOS component is almost completely blocked by the building structures resulting in a received signal envelope following a Rayleigh model.

Figure 4-30 shows the approximate trajectory followed during the wooden house dynamic data collection (WH-DS1-D). The antenna was hand held during the whole experiment. Initially, the antenna was outdoors for 2-3 minutes. Then it was slowly moved inside the wooden house.
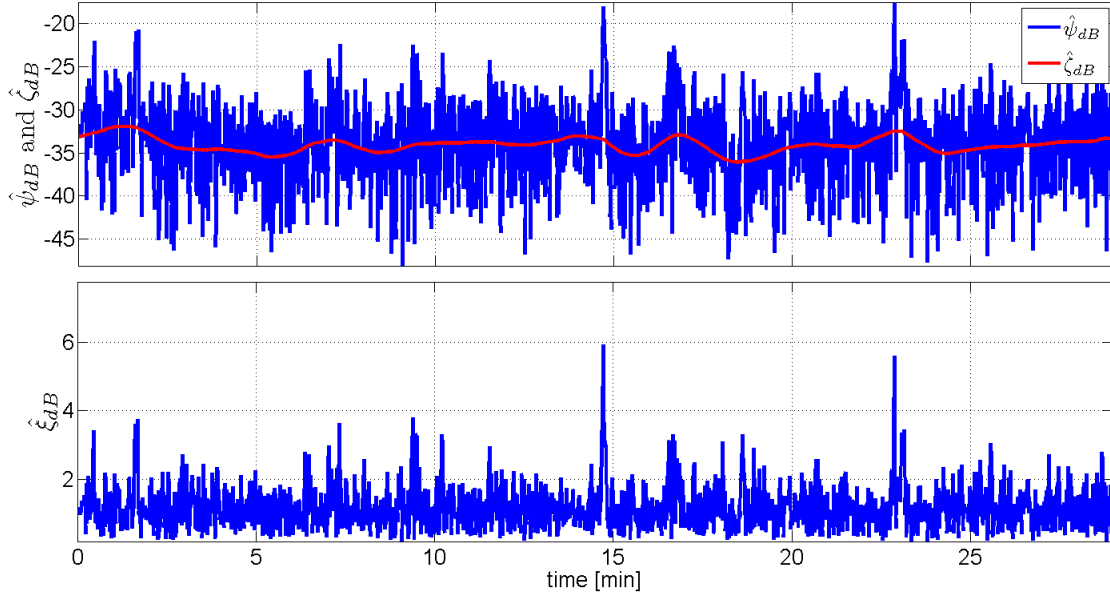
Figure 4-28: Carrier power variations of PRN18 from the dynamic dataset collected in the Navlab (NL-DS1-D).
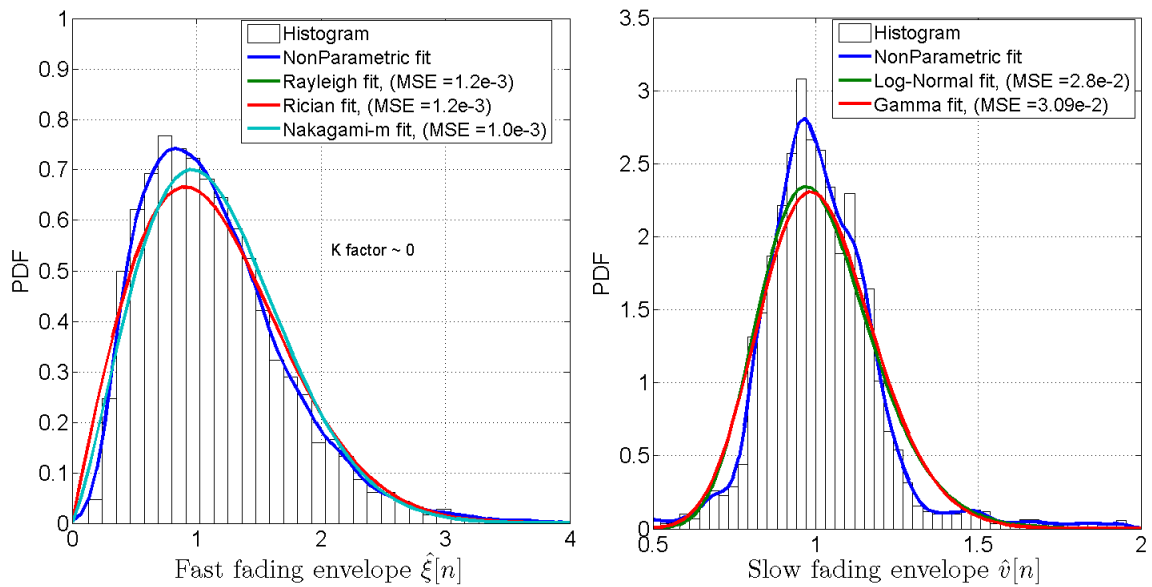
Figure 4-29: Comparison of empirical PDF with the standard parametric models.

Main floor

Basement
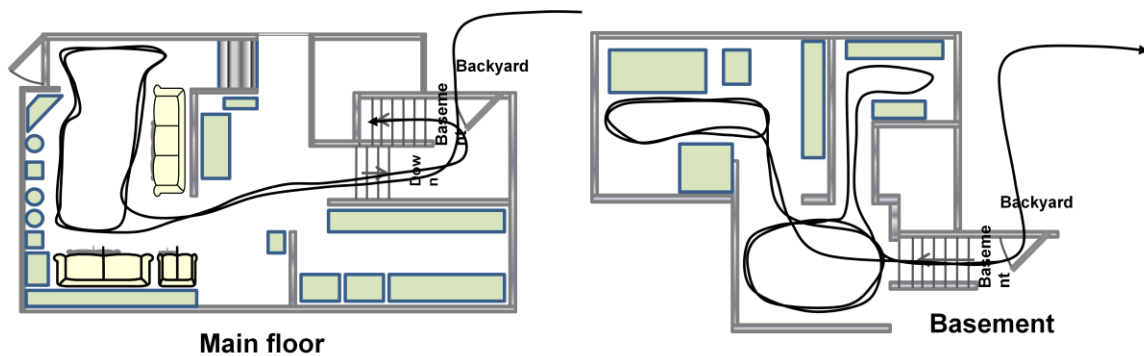
Figure 4-30: Schematic representation of the dynamic data collection performed during the wooden house experiment (WH-DS1-D).

Several approximately rectangular trajectories were followed in the living room area and then the antenna was taken to the basement. Similar trajectories were followed in the basement and finally the antenna was taken outside to an open sky environment. Figure 4-31(a) shows the slow fading components (mean signal variations) for all the satellites present during the data collection duration.

It can be seen that an attenuation of 10-12 dB was observed when the antenna was moving from open sky conditions to the main floor of the house. Then the signals were further attenuated by 8-12 dB while moving from the main floor to the basement. In Figure 4-31(b), the empirical PDF of the fast fading component is compared against standard models and it can be observed that the envelope almost follows a Rayleigh distribution. Here, only the amplitude values corresponding to the time duration where the receiver antenna was in the main floor and basement is considered for computing the empirical PDF.

SA in the NavLab as a function of carrier power level and percentage of time is summarized in Figure 4-32(a) for dynamic conditions. In these conditions most of the satellites are available for a receiver sensitivity of -165 dBm. The power of all the satellites is below -150

dBm. The SA in the wooden house scenario for the dynamic test is shown in Figure 4-32(b).

It can be observed that most of the satellites are above -155 dBm and most of the currently

available commercial GPS receivers can be used to obtain a position fix.
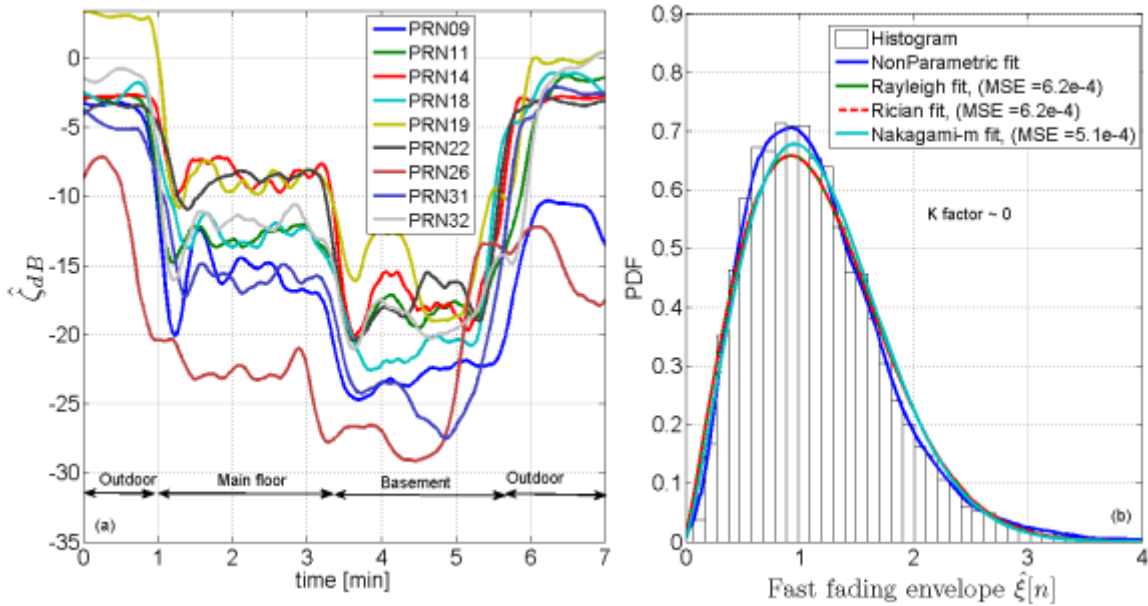
Figure 4-31: (a) Slow fading component for all the visible satellites from the dataset WH-DS1-D. (b) Comparison of the empirical density of the fast fading envelope with the standard models.

Two more data collections were performed inside the McEwan Hall at the UofC as

shown in Figure 4-33 (dataset ME-DS1-D and ME-DS2-D). The McEwan Hall resembles

a shopping mall with wide empty spaces, corridors and food courts. In ME-DS1-D, a

GPS antenna was mounted on a cart and the cart moved at a nominal speed of 5-10 cm/s

along a straight path of approximately 50 m as shown in Figure 4-33 (b) (paths are shown

in red colour). The reference antenna was placed outside the McEwan hall as shown in

Figure 4-33(a). ME-DS2-D was collected approximately one hour after the ME-DS1-D

along the same track with slightly higher speed. The corresponding results of these tow

data collections are discussed in the following paragraphs.
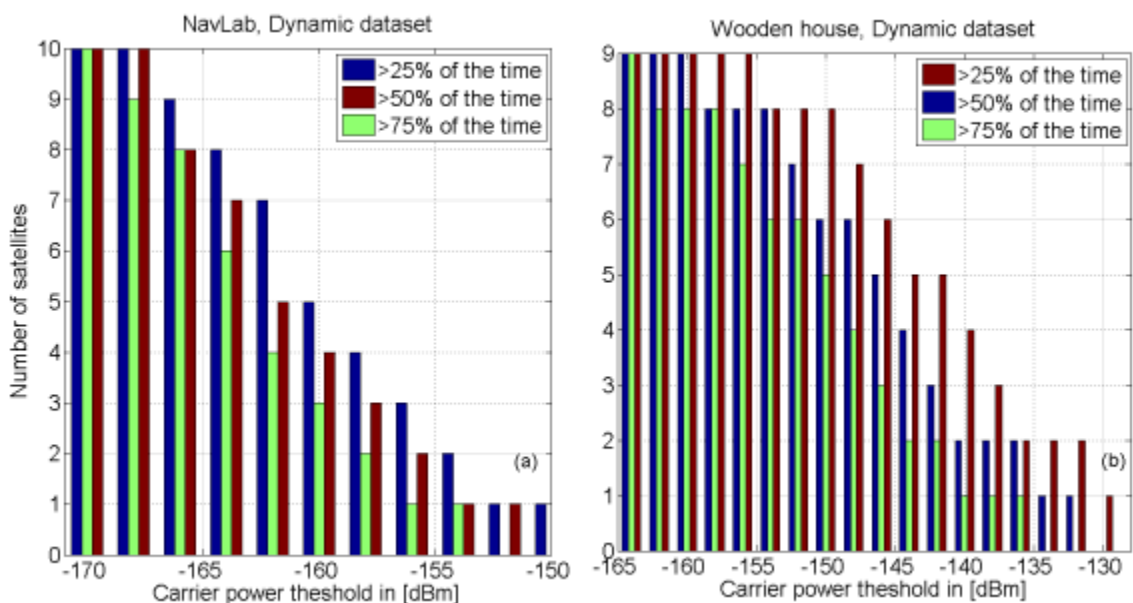
Figure 4-32: SA as a function of power level in dBm and the percentage of time with respect to the total duration under dynamic conditions.
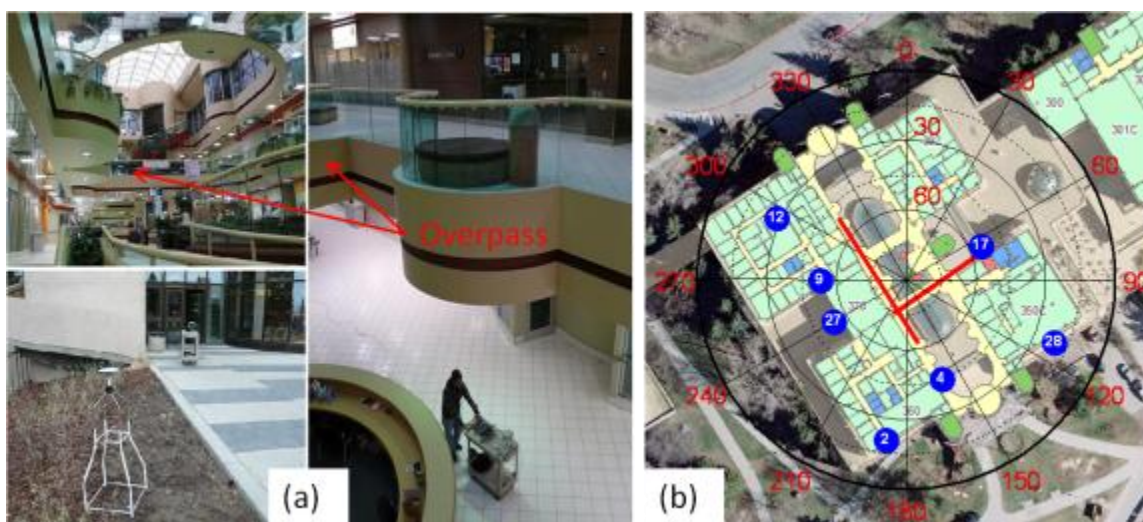
Figure 4-33: (a) Data collection performed inside the McEwan hall at UofC. (b) Sky map of the satellite constellation.

In the first experiment, the cart was moved from North East to South West covering a total distance of about 50 metres. This type of experiment is useful in analyzing the shadow fading effects over large physical areas. Figure 4-34(a) shows the slow fading

component for all the available satellites from the dataset ME-DS1-D. It can be observed that, in this scenario, the range of signal variations due to slow fading is approximately ±6 dB. It can also be observed that the slow fading components are correlated across satellites. This is due to the fact that the signals are simultaneously shadowed and unshadowed by the overpass structure as shown in Figure 4-33(a).
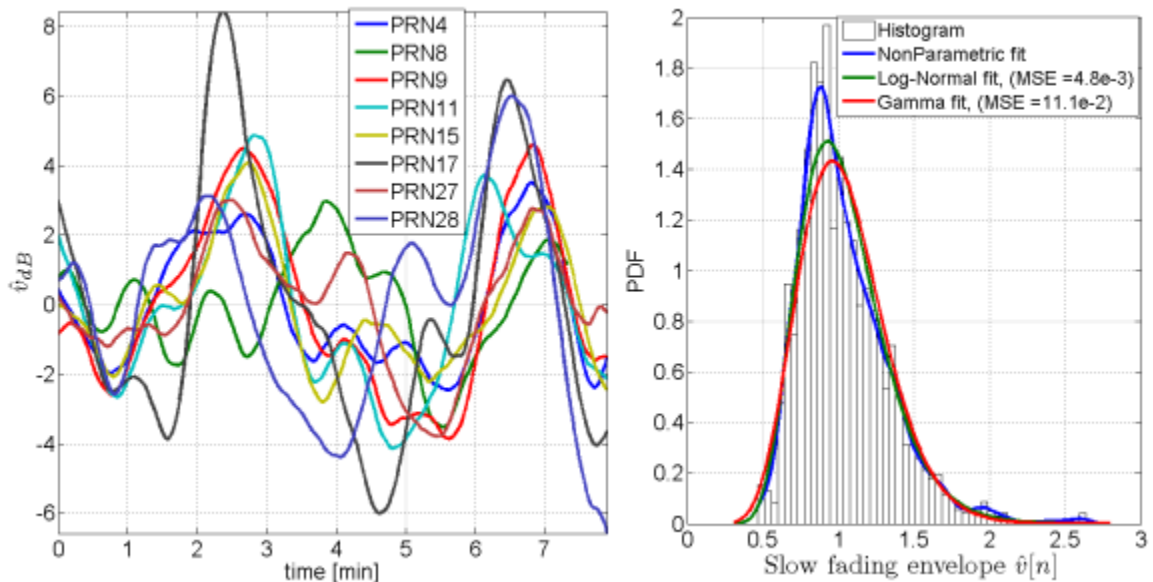
Figure 4-34: (a) Slow fading components for all the visible satellites after removing the path loss effect. (b) Comparison of the empirical density function of the slow fading components with the parametric models.

Comparison of the empirical density function of the slow fading components obtained from dataset ME-DS1-D against standard models is provided in Figure 4-34(b). A good agreement is obtained between empirical and standard models. In this scenario, the Log-Normal distribution has a slightly better match than the Gamma distribution. It was also observed that the fast fading components obtained under this scenario are in good agreement with the Rician model and more details can be found in Appendix B.

Figure 4-35 shows the estimated carrier power levels for five different satellites from the data set ME-DS2-D. An interesting observation from this dataset is the carrier power variation of PRN17. From Figure 4-35 it can be clearly seen that PRN17 has a wide dynamic range of about 40 dB (-125 dBm to -165 dBm). This is due to the fact that PRN17 was close to zenith as shown in Figure 4-33 and the receiver was able to occasionally establish LOS conditions through the glass rooftop.
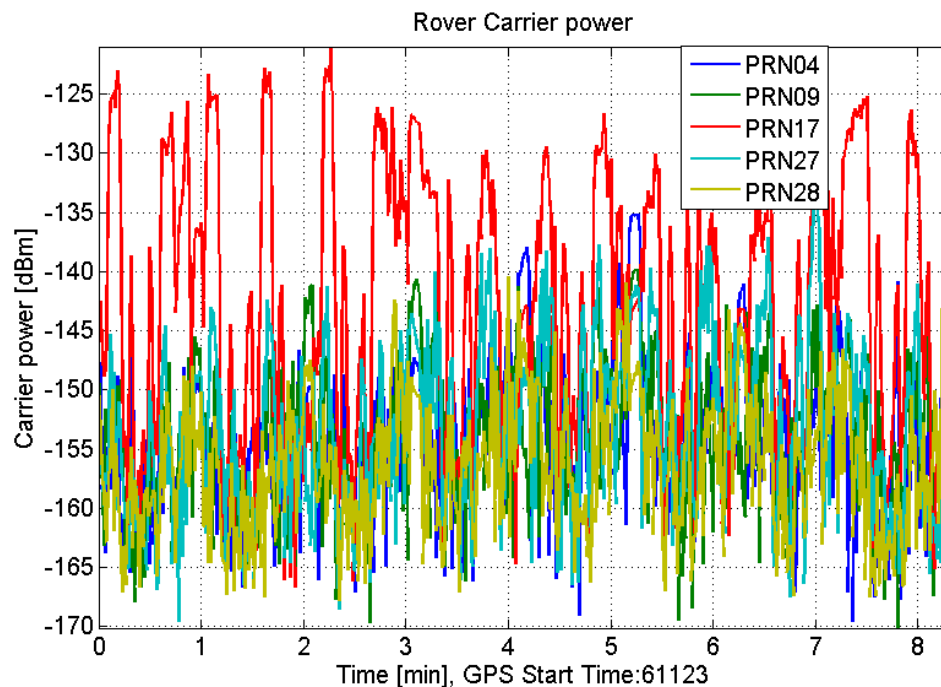
Figure 4-35: Carrier power levels estimated for the signals collected in McEwan Hall under dynamic conditions, Dataset ME-DS2-D.

Therefore, this scenario is a mixture of LOS and NLOS conditions which makes fading phenomena much more unpredictable. It is also important to note that under such scenarios (mixture of LOS and NLOS conditions), satellites with higher carrier power level will mask the satellites with lower carrier power level due to cross correlation effects (O'Driscoll 2007).

The SA in McEwan Hall as a function of carrier power level and percentage of time is summarized in Figure 4-36 for datasets ME-DS1-D and ME-DS2-D. In these conditions most of the satellites are available for a receiver sensitivity of -162 dBm. The power of all the satellites is below -140 dBm in ME-DS1. Due to the presence of the LOS component in ME-DS2, the maximum carrier power level is approximately -135 dBm.
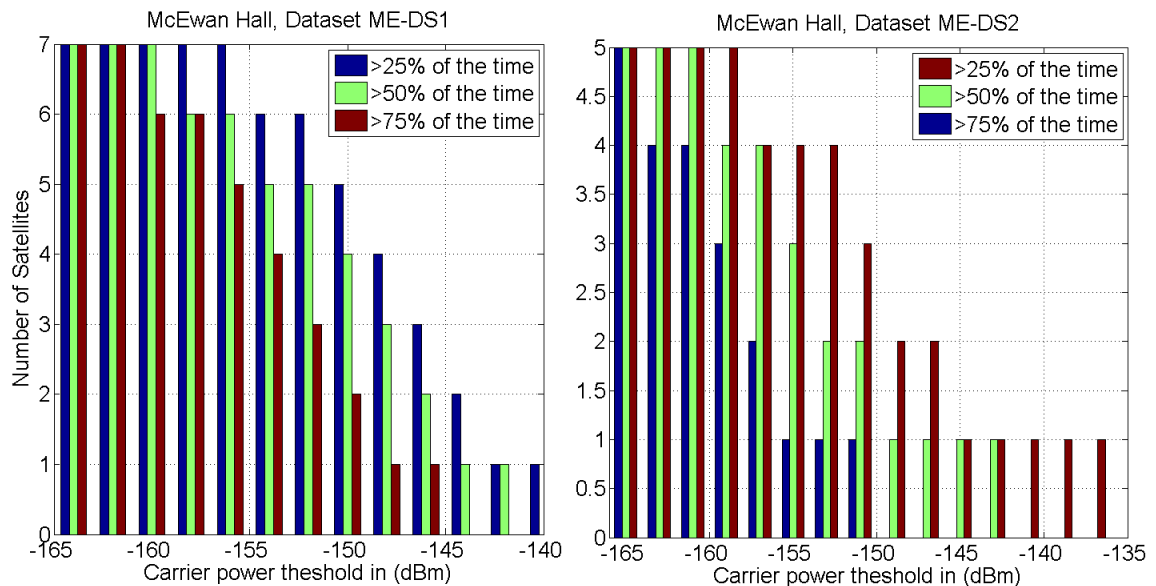
Figure 4-36: SA as a function of power level in dBm and the percentage of time with respect to the total duration for two different datasets ME-DS1-D and ME-DS2-D.

4.5 Summary

In this chapter, the characterization of GPS signals under several weak signal conditions was considered. More specifically, the amplitude of the received signal was analyzed under open sky, single/multiple reflector, foliage and indoor scenarios. It was shown that received GPS signals under the considered harsh environments are affected by path loss, slow and fast fading phenomena. However, the contribution of each component depends on the type of scenario and receiver dynamics. It was also shown that the received signal envelope can be effectively modelled by isolating and analyzing various fading

components, individually. Characterization results showed that, in most situations, a composite model is capable of capturing both slow and fast fading effects where the fast fading component is modelled using Rician or Nakagami-m distribution and the slow fading components using a Log-Normal or Gamma distribution. However, under certain circumstances, a rather simple model such as Rice or more complicated model such as Lutz (Lutz et al. 1991) is required to describe the fading phenomena. A brief summary of the findings of the characterization is provided in Table 4-8, Table 4-9 and Table 4-10.

Table 4-8: Summary of the amplitude characterization results under various weak signal conditions.

Scenario	Comments and description
Outdoor, strong single reflector, LOS, static	• When the receiver is placed close to a strong reflector, amplitude variations tend to be periodic in nature. Under such conditions, a sum of sinusoids model with up to 6 or 7 components can be used to reconstruct the signal amplitude. • Alternatively, the amplitude envelope can be modelled as a correlated Rician process with a typical K factor equal to 13.8 dB. • Effects of shadow fading are minimal and very slow in nature
Outdoor, strong single reflector, LOS, dynamic	• Envelope variations are generally fast and the range of variations depends on the elevation angle of the satellite and position of the receiver with respect to the reflecting surface. • The amplitude envelope tends to follow the Rician model and a typical value of the Rice factor is 11.2 dB. • Effects of shadow fading are minimal and can be modelled using a Log-Normal distribution
Outdoor, Multiple reflector, LOS, static	• The sinusoidal model can be used when the receiver is placed close to any of the reflectors • When strong specular components are absent, the received signal envelope tends to follow a composite Rice/Log-Normal (RLN) distribution with typical values of $K = 19.2$ dB and $\sigma_s^2 = 0.23$.

Table 4-9: Summary of the amplitude characterization results under various weak signal conditions (Cont'd).

Outdoor, Multiple reflector, dynamic	• Under LOS conditions, the received signal envelope tends to follow a composite RLN distribution with typical values of Rice K factor = 12.4 dB and $\sigma_s^2 = 3.52$. • Under a mixture of LOS and NLOS conditions, more complicated multistate models are required to describe the envelope behaviour. This is a typical scenario for a pedestrian walking in an urban environment with high surrounding buildings.
Foliage, static	• Shadowing is the major contributor of signal fading under static conditions. • The level of shadowing depends on the type and size of the tree and its branches. • In the considered scenario, mean attenuation levels of the order of 5-10 dB were observed. • Over sufficiently long duration, the received signal envelope tends to follow composite RLN distribution with typical values of Rice K factor = 17.1 dB, $\mu_s = -8.5$ and $\sigma_s^2 = 0.2$.
Foliage, dynamic	• Both shadowing and multipath affect signal under dynamic conditions. • It was observed that the Rician K factor estimated under foliage was considerably low, indicating the severity of the multipath. • Mean signal attenuation levels were slightly higher than the static scenarios • Under dynamic conditions, the received signal envelope tends to follow composite RLN distribution with typical values of Rice K factor = 2.83 dB, $\mu_s = -12.2$ and $\sigma_s^2 = 3.9$. • One can also model the received envelope using a multistate model with fast transition rates.

Table 4-10: Summary of the amplitude characterization results under various weak signal conditions (Cont'd).

Indoor, static	• The signal variations were slow with mean shadow levels in the rang of 10-35 dBs.
	• The mean shadow levels depend on the type of the scenario. For example, the mean shadow levels found in various scenarios are as follows
	  ○ A typical wooden house main floor : 6-10 dB
	  ○ A typical wooden house basement : 10-18 dB
	  ○ Shopping mall (McEwan hall) main floor : 15-25 dB
	  ○ Modern building (Navigation Laboratory) : 25-35 dB
	• Received signal envelope over sufficiently short time (less than few seconds) can be considered constant however, over sufficiently long duration (more than several minutes), envelope tends to follow Rayleigh distribution due to the increased attenuation levels. A typical value of the Rice K factor is -0.8 dB

Indoor, dynamic	• The received signal envelope tends to follow composite RLN distribution in indoor dynamic conditions. The estimated Rice K factor was almost close to zero, indicating very harsh environments for GNSS signal reception. • The mean shadow levels under dynamic conditions were consistent with the static results discussed above. • The slow fading components under NLOS condition tends to follow a Log-Normal process with typical parameter values of $\mu_s = \hat{\rho}_{dB}$ and $\sigma_s^2 = 1.4 - 2.3$ • It was also observed that, under certain indoor scenarios such as shopping complex, a mixture of LOS and NLOS instances could result in sudden increase or decrease of the received carrier power. Under such conditions, a multistate mixture model can be used to capture the amplitude behaviour.

Based on the results discussed in this chapter, it is clear that the received signal envelope can be modelled using a composite distribution such as RLN. The RLN distribution encapsulates several other distributions such as Loo, Suzuki, Rice, Log-Normal and

Rayleigh as its special cases and thus offers flexibility in modelling several scenarios. However, a mixture of LOS and NLOS conditions makes the amplitude much more unpredictable and require a complex multistate model to describe their behaviour. Thus, a multistate model can be viewed as a generalized model which can have several single/composite models as one of its states.

During the characterization process, it was observed that a standard commercially available high sensitivity receiver was able to acquire and track most of the satellites in the scenarios considered above except indoors. This is due to the fact that GPS signals indoors are relatively weak and the excess attenuation caused by walls, rooftops and various building materials strongly impacts the operation of a standard high sensitivity receiver. In order to further gain insight into the behaviour of indoor signals, a detailed analysis of the second order statistics of indoor GPS signals is considered in the next chapter. In Chapter 5, the temporal/spectral/spatial behaviour of indoor GPS signals are characterized under various indoor scenarios

Chapter Five: **SECOND ORDER CHARACTERIZATION AND SIMULATION OF GPS INDOOR SIGNALS**

Second order characterization deals with the analysis of temporal, spectral and spatial behaviour of the fading process (Ibnkahla 2004). AFD, LCR, temporal and spatial correlation are some of the standard metrics involved in the second order signal characterization. In a typical wireless communication system, metrics such as AFD and LCR are useful for the design and optimization of efficient coding schemes (such as convolution coding, interleaving, etc.) in order to reduce bit error rate (BER) (Abdi et al. 2000). In the case of GPS, second order statistics such as AFD and LCR have little importance from an coding design efficiency point of view since data rate, frame structure and coding schemes are all fixed. Also, with the current state of the art, high sensitivity GPS receivers obtain data bits through a mobile network (Network Assisted GPS or also known as AGPS) and thus do not depend on raw indoor signals for the navigation data bits.

AGPS not only provides navigation data bits (satellite ephemeris) but also reduce code and frequency uncertainty for signal acquisition (van Diggelen 2009). Thus, a GPS receiver operates on a reduced search space for acquisition and tracking of weak satellite signals. Once a minimum of four satellites is acquired and tracked, the GPS receiver generates range measurements which are then used for position computation. It should be noted that the ability to provide continuous position updates indoors still depends on the algorithms incorporated in the remote GPS receiver to sustain fading and remain locked to the satellite signals. As seen in the Chapter 4, fading results in random variations in the

received signal power causing the weak signal tracking algorithms to lose lock when the carrier power is below the receiver sensitivity.

Thus, a thorough understanding of the statistical properties of fading, such as the mean fade duration and the average time between deep fades, allows the proper integration of aiding technologies that can help a GNSS receiver to maintain lock during signal attenuation/blockage conditions. For example, if the mean fade duration were observed to be in the order of a few hundreds of milliseconds, a proper aiding source like an inertial measuring unit could be used in order to bridge time gaps when the signal is unavailable. Thus, the second order characterization becomes critical for designing new receiver systems and algorithms that can operate under weak signal environments.

In this chapter, temporal, spectral and spatial characteristics of indoor GPS signals are analyzed. Second order statistics such as AFD, LCR and MFD are extracted from the measured correlator outputs. Empirical curves are compared against standard parametric models. It is also shown that the spectra of the slow and fast fading components can be effectively modeled using a 4th order low-pass Butterworth filter. An extended analysis of the satellite availability statistics as a function of distance travelled is also provided. A simulation scheme is finally suggested for the generation of indoor GNSS signals. A brief description of the parameters of interest, signal analysis methodology and tools used for extracting the second order statistics from the measured correlator outputs are described in the following section.

5.1 Signal analysis and parameter extraction

The parameters of interest in this research work for the analysis of temporal/spectral characteristics of the received signal are:

- AFD, LCR, MFD statistics

- SA as a function of distance travelled

- Temporal/Spatial correlation of the fast and slow fading components

The AFD, LCR and MFD statistics of the received signal are analyzed as a function of absolute carrier power levels. From an indoor GPS receiver design point of view, these statistics provide useful information on the fade durations and/or fade distances and their frequency of occurrence as a function of the receiver sensitivity. Efforts are made to compare the empirical curves against parametric models. From Eq. (2.36) and Eq. (2.38), it is clear that the LCR and AFD statistics are dependent on the distribution of the received signal envelope. In the previous chapter, it was shown that under several NLOS indoor conditions, the fast fading component of the received signal envelope can be modeled using a Rician or Nakagami-m distribution. Thus, the AFD and LCR values of the fast fading components are compared against the standard Rician and Nakagami-m models. Under the assumption of ring of scatterers, LCR expressions of the Rice and Nakagami-m models are given by (Stüber 2002, Abdi et al. 2000):

$$
\begin{aligned}
L_{\xi,Rice}\left(\rho\right) &= \sqrt{2\pi(K+1)} f_{D,\max} \rho e^{-K-(K+1)\rho^2} I_0(2\rho\sqrt{K(K+1)}) \\
L_{\xi,Nak}\left(\rho\right) &= \sqrt{2\pi} f_{D,\max} \frac{m^{m-0.5}}{\Gamma(m)} \rho^{2m-1} e^{(-m\rho^2)}
\end{aligned}
\tag{5.1}
$$

where $f_{D,\max}$ is the maximum Doppler frequency, $\rho = \xi / \xi_{rms}$ is the normalized signal envelope and ξ_{rms} is the root mean square (rms) signal envelope. The corresponding AFD expressions can be obtained using Eq. (2.38).

An extended analysis of the satellite availability (SA) statistics is also conducted in this chapter. Here, the number of available satellites is analyzed as a function of the distance travelled for several values of the receiver sensitivity.

In order to characterize the temporal/spectral behavior of the fading phenomena, the ACF and PSD of the slow and fast fading components have also been evaluated. The ACF of the fast fading component were evaluated using the normalized correlator outputs as

$$\hat{R}_{uu}[m] = \frac{1}{N} \sum_{n=0}^{N-m+1} \tilde{u}_f[n]\tilde{u}_f^*[n+m]; \qquad m \geq 0 \tag{5.2}$$

where $\hat{R}_{uu}[m]$ is the ACF of the fast fading component referred to as fading correlation and $\tilde{u}_f[n] = \tilde{w}[n] / \hat{\zeta}[n]$ is the normalized complex correlator outputs representing the fast fading components. Here, the measured correlator outputs, $\tilde{w}[n]$, given by Eq. (3.5) are normalized by the signal $\hat{\zeta}[n]$ in order to remove the amplitude variations introduced by the slow fading component. The PSD of the fast fading component is estimated using the Welch method by averaging the periodogram of the signal as (John & Manolakis 1996):

$$\hat{S}_{uu}(f) = \frac{1}{N} \left| \sum_{i=0}^{N-1} \tilde{u}_f[n]h[n]\exp\left(-2\pi fnT_s\right) \right|^2 \tag{5.3}$$

where $\hat{S}_{uu}(f)$ is the PSD of the signal and $h[n]$ is a smoothing window (in this case a Hamming window). Similarly, the ACF and PSD of the slow fading component are

estimated using Eqs. (5.2) and (5.3) by replacing $\tilde{u}_f[n]$ with $\hat{v}[n]$. The empirical ACF and PSD of the slow and fast fading components obtained in this way are compared against the correlation and square magnitude of standard filter transfer functions.

5.2 Results and analysis

In this section, the second order characterization results of indoor GPS signals are provided. Results obtained under static conditions are described first followed by dynamic scenarios.

5.2.1 Static scenarios

AFDs as a function of the carrier power threshold and for different satellites are shown in Figure 5-1(a) for the case of the NavLab experiment (NL-DS1-S). As the power level threshold increases, the AFD increases as well. Signals suffering the same level of attenuation have similar fade durations. The signal from PRN 22 is characterized by a carrier power greater than -153 dBm hence it is not affected by fades occurring below this power level. LCRs as a function of the carrier power level are shown in Figure 5-1(b) for different satellites. The LCR curves assume a bell shape with a width between 15 and 20 dB. This provides an indication of the variations in power levels caused by the fading process. AFD and LCR of PRN 22 are shifted by approximately 10 dB with respect to the other signals. This 10 dB difference corresponds to the power difference between PRN 22 and the other signals.
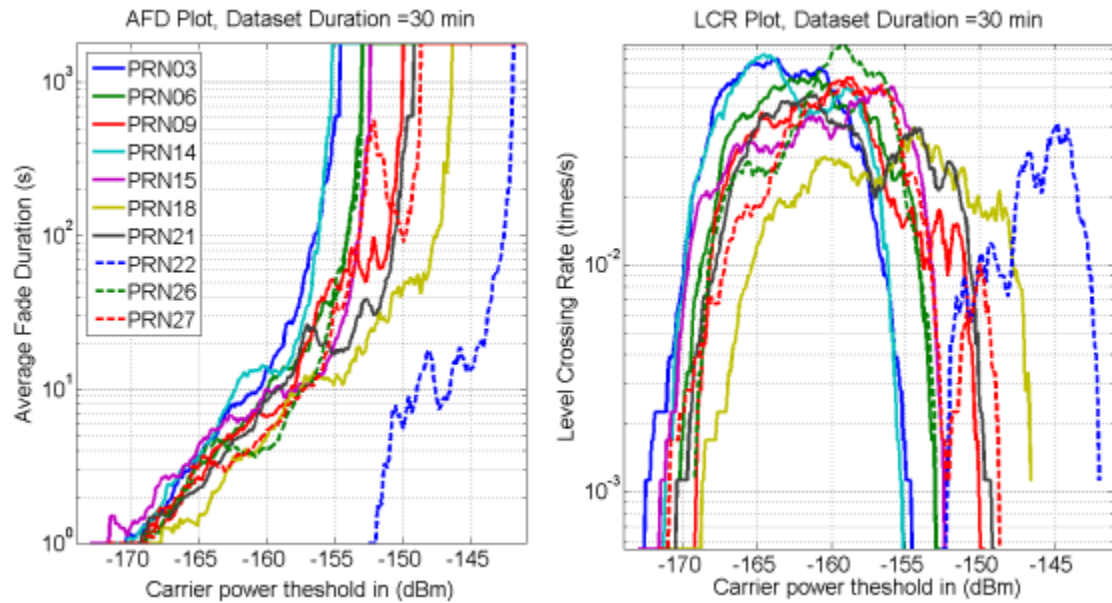
Figure 5-1: AFD and LCR as a function of the carrier power threshold in dBm, NavLab, static conditions, Dataset NL-DS1-S.

AFD and LCR results for the wooden house static experiments can be found in (Satyanarayana et al. 2010). Figure 5-2 compares the AFD and LCR value of the fast fading components obtained under NavLab and conference room conditions against the parametric models discussed in Section 5.1. It can be observed that even though the distributions of the envelope under NavLab and the conference room follow Rician distribution with similar K factor values, the second order statistics are quite different from each other. Signals in NavLab experience lower LCR and higher AFD values in contrast to the higher LCR and low AFD values experienced by the signals in the conference room. This means that the Doppler spread experienced by the signals in CR-DS1-S dataset is higher as compared to the NL-DS1-S data set [from Eq. (5.1) LCR is directly proportional to the maximum Doppler spread]. The empirical curves are in good agreement with the parametric models.
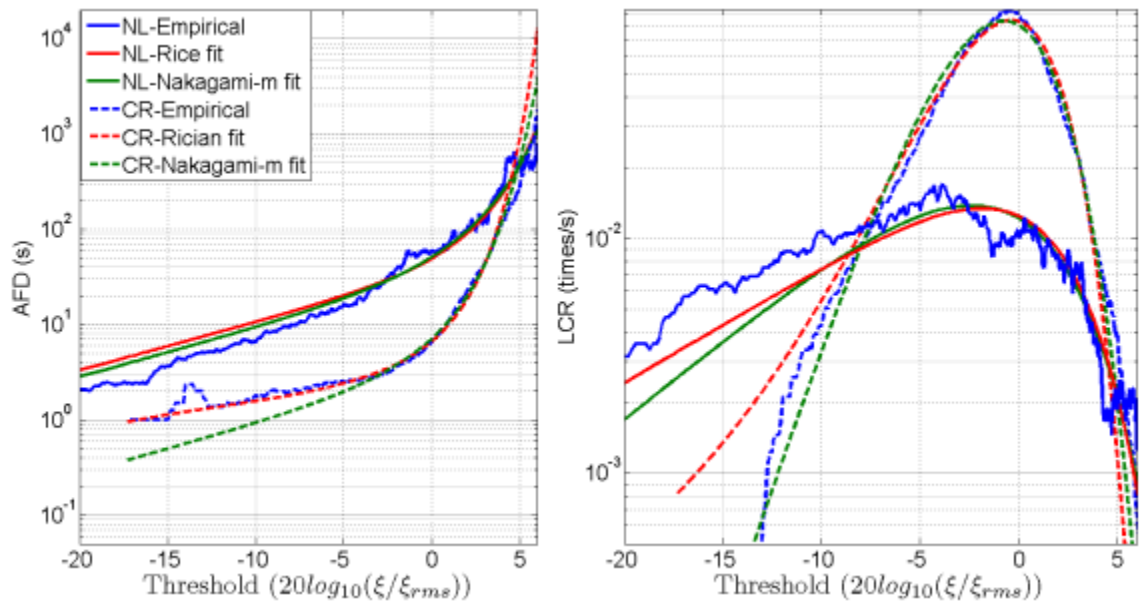
Figure 5-2: Comparison of AFD and LCR values fast fading components obtained from NL-DS1-S and CR-DS1-S datasets against the standard models.

In order to gain further knowledge of the fading phenomena, temporal/spectral characteristics of the fast fading components are further investigated. As it can be seen from Figure 4-22(a), the signal power varies slowly over time. The RR processing strategy explained in Section 3.3 ensures that the satellite motion induced Doppler effects on the indoor GNSS signals are removed using the measurements provided by the reference signal. Thus, any temporal variation present in the rover signal amplitude is mainly due to the local scattering and shadowing effects at the rover antenna. Figure 5-3 shows a sample PSD of the received rover signals for three different indoor scenarios. It can be observed that the PSD is very narrow and centered on the zero frequency. It can also be observed that the PSD of the signal under NavLab and the wooden house conditions has a single peak whereas multiple peaks were observed under conference room scenario. This means that in the NavLab and wooden house scenarios, no dominant

multipath was present. However, in the conference room scenario, multipath signals with slightly different Doppler frequency as compared to the LOS component were observed. This also explains the periodicity observed in the amplitude values as shown in Figure 4-24(a). A similar behavior was observed for PRN11 in the CR-DS1-S dataset.
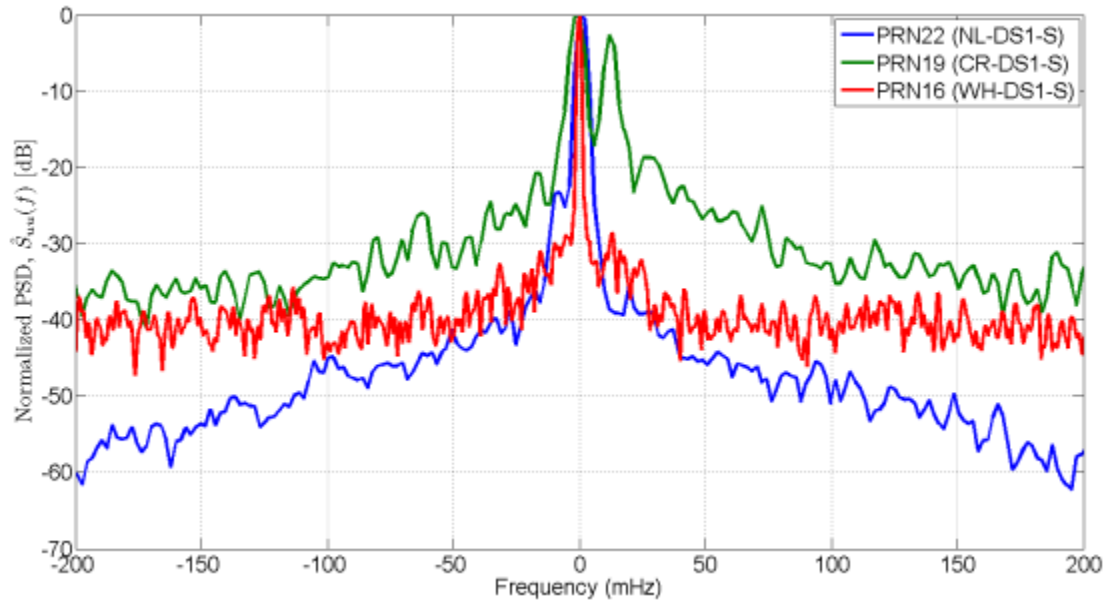
Figure 5-3: PSD of the fading process experienced by a static receiver in three different indoor environments.

However, the amplitude and phase of the received signal vary slowly over time due to the dynamic nature of the scattering environment and variations in the shadowing due to satellite displacement. Thus, signals tend to decorrelate slowly over time. The signal decorrelation time can be determined by computing the ACF. The ACF of the rover signal was computed using Eq. (5.2). The signal decorrelation time, τ_0, was computed as the time duration for which $\hat{R}_{uu}[\tau] = e^{-1}$. Table 5-1 summarizes the decorrelation time for all the visible satellites under three different scenarios. It can be observed that under static scenarios, the signals are approximately correlated for about one minute.

Table 5-1: Summary of the signal decorrelation times for signals under NavLab, conference room and wooden house scenarios.

Dataset NL-DS1-S		Dataset CR-DS1-S		Dataset WH-DS1-S	
SV ID	Decorrelation time (s)	SV ID	Decorrelation time (s)	SV ID	Decorrelation time (s)
3	29	9	6.4	5	54
6	32	11	36	15	32
9	56	14	46	16	56
14	81	18	37	18	62
15	27	19	22	21	20
18	27	22	118	24	15
21	83	--	--	29	33
22	39	--	--	--	--
26	77	--	--	--	--
27	64	--	--	--	--

5.2.2 Dynamic scenarios

In this section, second order characterization results for dynamic indoor scenarios are provided. Temporal/spatial and spectral characteristics of the fast and slow fading components are analyzed independently. For an effective temporal/spatial characterization of signals indoors additional data collection methodologies have been considered in this research work. In the following subsections, a description of the data methodologies is first provided followed by the fast and slow fading characterization results.

5.2.2.1 Data collection methodologies

In addition to the static and pedestrian motion experiments described in Chapter 2, several other data collection methodologies have been considered in this chapter for an effective characterization of indoor propagation channels. The basic idea behind these experiments is to obtain precise distance information of the antenna displacement during the data collection. A brief description of the two different methodologies considered in this work is summarized below.

- **Rotation table experiment**: Single/Multiple antennas were mounted on a rotating arm. The angular speed of the rotating arm was precisely controlled using a personal computer interfaced with the motor. In this way, the antenna took different positions in a period of time sufficiently short to consider the temporal variations of the channel negligible. In this way, the fast fading statistics of the GPS signals were estimated with precise spatial resolution. Due to the ability of the rotation table to capture the small scale fading effects with fine spatial resolution, this type of experiment was used for characterizing fast fading effects.

- **Instrumented cart experiment**: a cart was instrumented with a wheel speed sensor capable of measuring distance travelled along a straight path. The cart was moved along a straight trajectory and the displacement information measured by the wheel speed sensor was used to determine the slow fading statistics of indoor GPS signals. This type of approach is similar to the one adopted in (Spirent 2008) wherein the indoor antenna was mounted on a model train equipped with a rotary encoder capable of providing accurate distance measurements. In this research

work, experiments based on instrumented cart are considered for characterizing slow fading components indoors.

Thus, apart from the PDF and CDF of the received signal, characterization of GPS signals using a rotation table enables one to determine the temporal/spectral/spatial aspects of the communication channel. This type of characterization is capable of isolating the spatial variations of the channel from the temporal variations. On the other hand, the instrumented cart experiment is used to characterize GPS signals over large spatial distances/areas of 10 to 100 metres with a spatial resolution of the order of 5 to 50 centimetres. This type of characterization complements and validates the results obtained from the small scale analysis (rotation table experiments) by characterizing the received signals over large physical areas. Also, large scale characterization provides additional information on the mean signal power level variations due to path loss and shadowing.

Based on the data collection methodologies described above, several experiments were conducted in three different indoor environments, namely a NavLab, a look alike shopping mall (McEwan Hall) and a wooden house. Table 5-2 summarizes the experiments considered for the fast and slow fading characterization. Each experiment is identified by a unique ID code. Descriptions of each individual test along with their results and analysis are provided in the following sections.

Table 5-2: Summary of the data collections performed in three different indoor environments. Each data collection is identified by an ID code.

ID	Date/Time	Place/Type
NL-DS2-D	27 Jul 2010 4:20 pm	NavLab, rotation table experiment
WH-DS2-D	02 Feb 2010 11:15 am	Wooden house, main floor , rotation table experiment
WH-DS3-D	02 Feb 2010 3:15 am	Wooden house, basement, rotation table experiment
NL-DS3-D NL-DS4-D	18 Aug 2010 3:15 pm	NavLab, instrumented cart experiment. Two different locations.
ME-DS3-D	14 Nov 2010 10:16 am	McEwan hall , instrumented cart experiment

5.2.2.2 Fast fading characterization

This section provides the results on fast fading characterization of GPS signals using the rotation table approach with single/multiple antennas mounted on a rotating arm. In this way, the antenna takes different positions in a period of time sufficiently short to consider the temporal variations of the channel negligible. This type of approach can be used to characterize the spatial dependence of the fading process for different antenna separations.

With the rotation table approach, a turning table has been used to slowly displace the indoor antenna. The signal power levels are determined as a function of the angular displacement with respect to the initial position of the antenna. The distance of the antenna from the centre of the moving table is equal to D_R. The procedure adopted for the evaluation of the fade statistics is shown in Figure 5-4. A power threshold is used to determine the crossing points of the fading process as a function of the angular displacement. These points are then used to determine fade statistics such as average fade

distances. In Figure 5-4, the signal power level crosses the power threshold in two points separated by an angular distance, $\Delta\theta$. The fade distance is then computed as

$$D_f = 2D_R \sin\left(\min\left(\frac{\Delta\theta}{2}, 180 - \frac{\Delta\theta}{2}\right)\right).$$

(5.4)

Several experiments have been performed using this methodology both in the wooden house and in the NavLab.
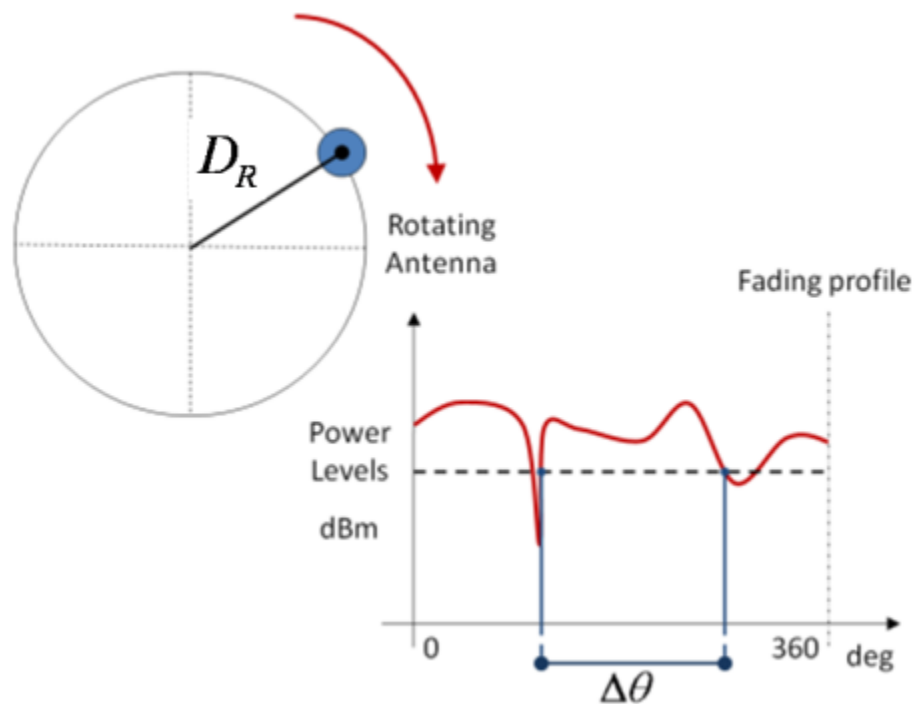
Figure 5-4: Procedure adopted for the evaluation of the fade statistics using a turning table. For each turn the fade profile is evaluated as a function of the angle measuring the antenna displacement with respect to its initial position.

Figure 5-5 (a) shows the data collection setup used to collect live GPS signals inside the NavLab (NL-DS2-D). In this experiment, two NovAtel 702-GG antennas were mounted on the rotating arm. The radius of the outer antenna (Ant1) and inner antenna (Ant2) were 85.7 cm and 40 cm, respectively. The spatial separation between the two antennas was

approximately 45 cm which is more than two wavelengths of the GPS L1C/A signal. A rotation speed of 0.25 rev/min was used during the data collection. Thus, the average speeds of the inner and outer antennas are 1.1 and 2.2 cm/s, respectively.
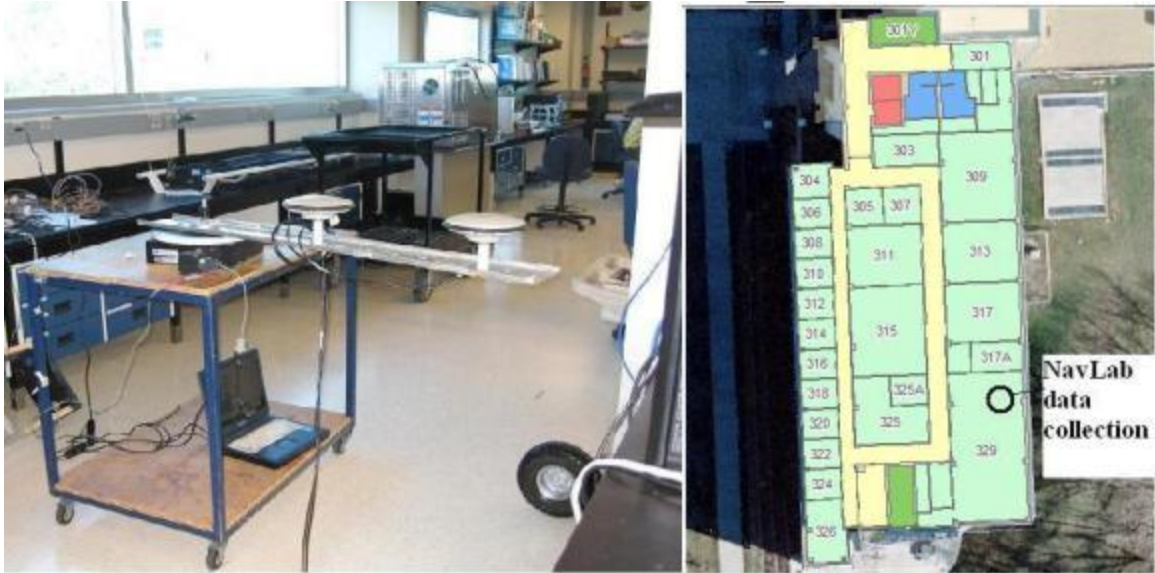
Figure 5-5: Data collection setup inside the NavLab. Rotation table experiment wherein two antennas are mounted on a rotating arm (left). Location of the data collection inside the NavLab (right).

The estimated carrier power difference between reference and rover antennas, $\hat{\psi}_{dB}[n]$, and the slow fading component, $\hat{s}_{dB}[n]$, of PRN08 from Ant1 and Ant2 are shown in Figure 5-6(a). The slow fading component is shown as dotted lines. It can be seen that the slow fading component contributes to a total signal power variation of 8-10 dB for PRN08. Fast fading components for PRN08 after removing the slow fading component are shown in Figure 5-6 (b). Signal variations of the order of 15-20 dB can be observed.
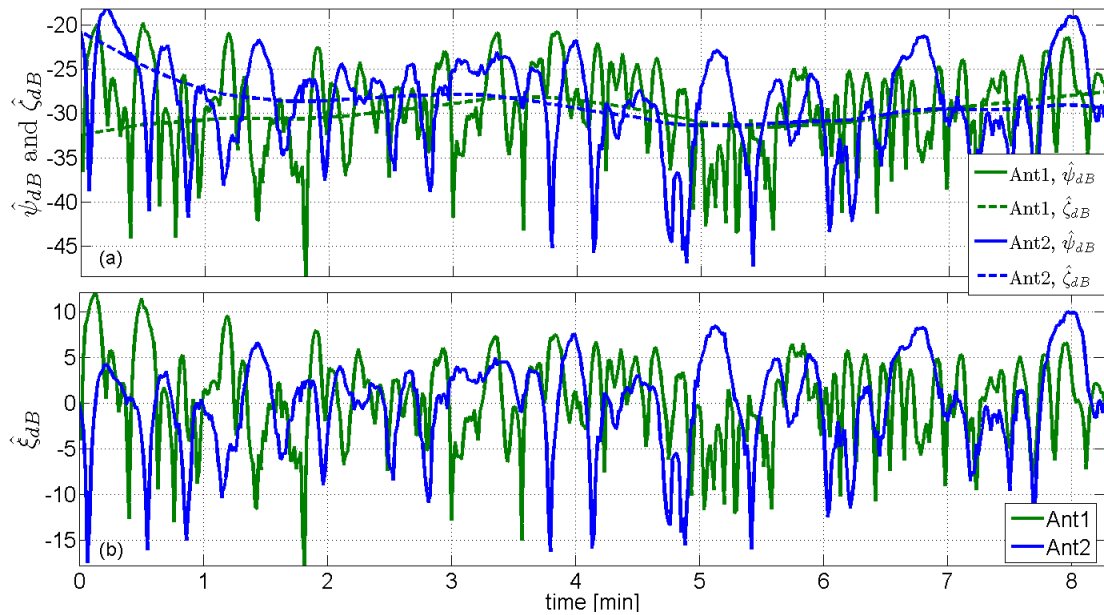
Figure 5-6: Carrier power variations for PRN08 from two antennas with respect to the outdoor reference antenna. Dotted lines represent the slow fading component obtained using a low-pass filter.

Figure 5-7 (a) compares the AFD values obtained from Ant1 and Ant2. It can be seen that the AFD values obtained from Ant2 (shown in dotted lines) are relatively higher as compared to AFD values obtained from Ant1. This means that signals from Ant1 experiences deep fades for shorter durations as compared to Ant2. This can also be readily observed from Figure 5-6(b) where the signal power rate of change is higher for Ant1 as compared to Ant2, which results in the increased LCR values for the Ant1 shown in Figure 5-7 (b). This can be explained from the fact that the velocity with which Ant1 is rotating is higher than that of Ant2. Thus the carrier Doppler variation experienced by Ant1 is higher as compared to Ant2, which results in an increased value of LCR and reduced AFD values.
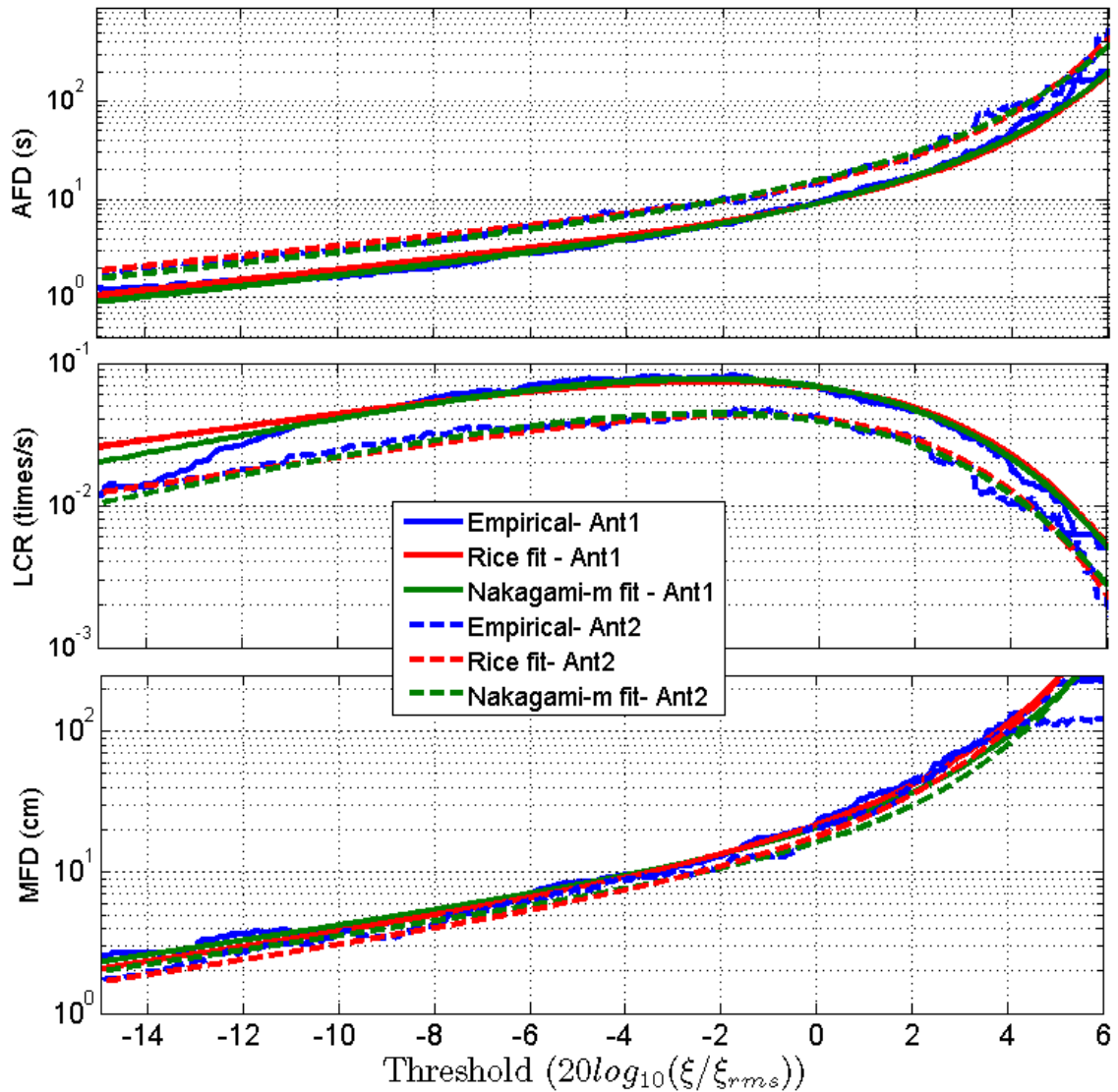
Figure 5-7: (a) AFD (b) LCR (c) MFD plot of the fast fading components from the dataset NL-DS2-D. Empirical values are fitted with standard parametric models.

This fact is further strengthened in Figure 5-7 (c) which compares MFD values from both antennas. The maximum values of the MFD are limited by the diameter of the rotating arm. Thus, the limiting MFD values for Ant1 and Ant2 are 171 cm and 80 cm respectively. It can be seen that MFD values from both antennas nearly overlap each other. This shows that the MFD values are independent of the antenna dynamics. Also, it

is evident from Figure 5-7 that the empirical values are in good agreement with the standard models. It should be noted that the Rician and Nakagami fit for the MFD values are obtained by multiplying the AFD values with the average speed of the antennas. Figure 5-7 supports the effectiveness of the characterization methodology adopted for the small scale analysis.

The rate of change of amplitude variations is higher for the rotation table experiment as compared to the static scenario, as explained in Chapter 4. This is due to the fact that the displacement of the antenna causes motion induced Doppler effects on the received signal. Thus, it becomes necessary to characterize the effect of receiver motion on the temporal/spectral characteristics of the received signal. In the following, the empirical ACF and PSD of the fading process are estimated and compared against some standard filter responses such as the Butterworth and Gaussian filters.

Figure 5-8 compares the ACF and PSD of the empirical fast fading component with the frequency responses of a standard Gaussian and 4th order Butterworth filter. The empirical ACF and PSD are computed according to Eq. (5.2) and Eq. (5.3), respectively. The squared magnitude of the Gaussian filter transfer function can be written as (Pätzold 2002)

$$|H_G(f)|^2 = \frac{1}{\sqrt{2\sigma_c^2}}\exp\left(-\frac{f^2}{2\sigma_c^2}\right) \tag{5.5}$$
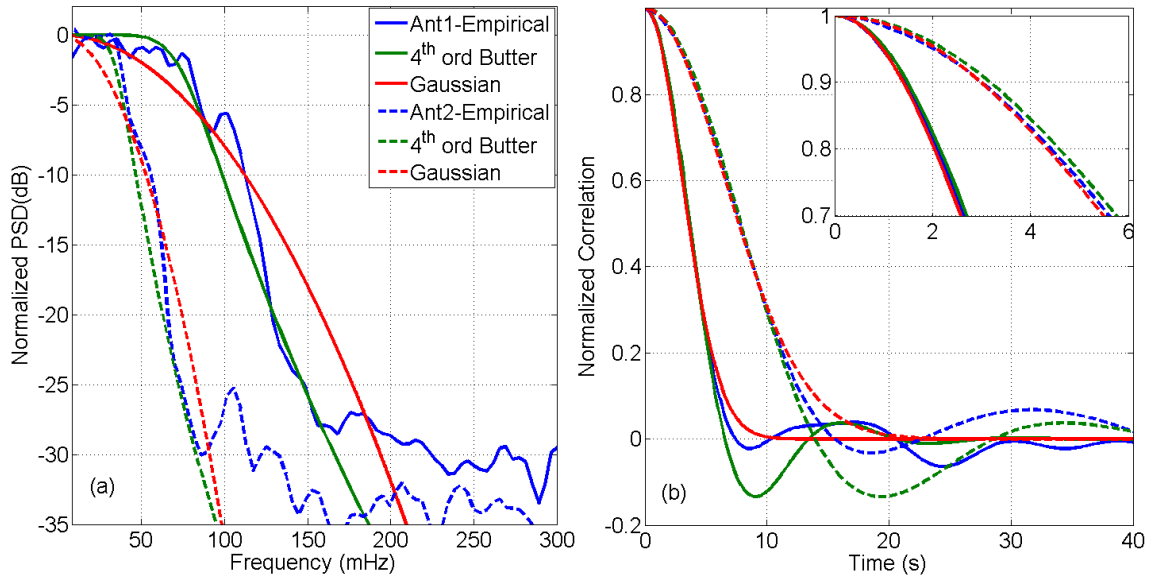
Figure 5-8: Comparison of empirical PSD and ACF of the fast fading process from Ant1 and Ant2 with that of the Gaussian and Butterworth filter responses.

where the variance σ_c is related to the 3 dB cut off frequency f_{3dB} by the relationship

$f_{3dB} = \sigma_c \sqrt{2\ln(2)}$. The ACF of the Gaussian filter is given by (Pätzold 2002)

$$R_G(\tau) = \exp\left[-\left(\tau/\tau_0\right)^2\right] \tag{5.6}$$

where τ_0 is the decorrelation time for which $R_G(\tau_0) = e^{-1}$. τ_0 is related to σ_c as

$$\sigma_c = 1/\left(\sqrt{2}\pi\tau_0\right)_. \tag{5.7}$$

On the other hand, the squared magnitude response of a 4th order Butterworth filter is given by (John & Manolakis 1996)

$$\left|H_B(f)\right|^2 = \frac{1}{1 + \left(f/f_{3dB}\right)^8} \tag{5.8}$$

where f_{3dB} is the 3 dB cut off frequency. The ACF of a 4th order Butterworth filter can

be obtained by computing the inverse Fourier transform of Eq. (5.8) and can be written as

$$R_B(\tau) = K \exp\left(-\frac{\beta\kappa}{\tau_0}|\tau|\right)\left[\alpha_1 \cos\left(\frac{\beta}{\tau_0}|\tau|\right) + \alpha_2 \sin\left(\frac{\beta}{\tau_0}|\tau|\right)\right] +$$
$$K \exp\left(-\frac{\beta}{\tau_0}|\tau|\right)\left[\alpha_2 \cos\left(\frac{\beta\kappa}{\tau_0}|\tau|\right) + \alpha_1 \sin\left(\frac{\beta\kappa}{\tau_0}|\tau|\right)\right]$$

(5.9)

where $\beta = 0.786362$, $\kappa = \sin(5\pi/8)/\sin(7\pi/8)$, $\alpha_1 = 0.231$, $\alpha_2 = 0.0957$ and

$K = (\alpha_1 + \alpha_2)^{-1}$. The value of β always ensures that $R_B(\tau_0) = e^{-1}$. The 3 dB cut off

frequency, f_{3dB}, of the Butterworth filter is related to the decorrelation time τ_0 by the

relationship

$$f_{3dB} = \frac{\beta}{2\pi \sin\left(\frac{7}{8}\pi\right)\tau_0}.$$

(5.10)

In Figure 5-8, the ACF and PSD of the empirical data obtained from the rotation table

experiment are compared to the standard filter responses as follows. The value of τ_0 is

computed from the empirical ACF as the time at which the ACF is equal to e^{-1}. The

value of τ_0, along with Eq. (5.7) and Eq. (5.10), is then used to determine the ACF and

magnitude squared responses of the Gaussian and 4th order Butterworth filter. From

Figure 5-8, it is clear that the empirical data from both Ant1 and Ant2 match closely the

Gaussian and Butterworth responses. However, the response of the Butterworth filter has

a better match as compared to the Gaussian response in terms of both ACF and PSD.

The average decorrelation time, τ_0, for the signals from Ant1 and Ant2 are 4.5 s and 8.52

s, respectively. It should be noted that the value τ_0 is directly proportional to the speed of

the receiver antenna. Thus, τ_0 when multiplied by the speed of the antenna provides a

measure of the decorrelation distance defined as $d_f = \tau_0 v_{avg}$ where d_f is the decorrelation distance and v_{avg} is the average speed of the antenna (Stüber 2002).

Figure 5-9 compares the estimated carrier power levels as a function of distance for PRN28 from dataset NL-DS2-D. A good agreement can be found between the carrier powers for two different rotations. A coherent integration time of 1 s has been used to minimize the noise effect on the estimated carrier power levels.
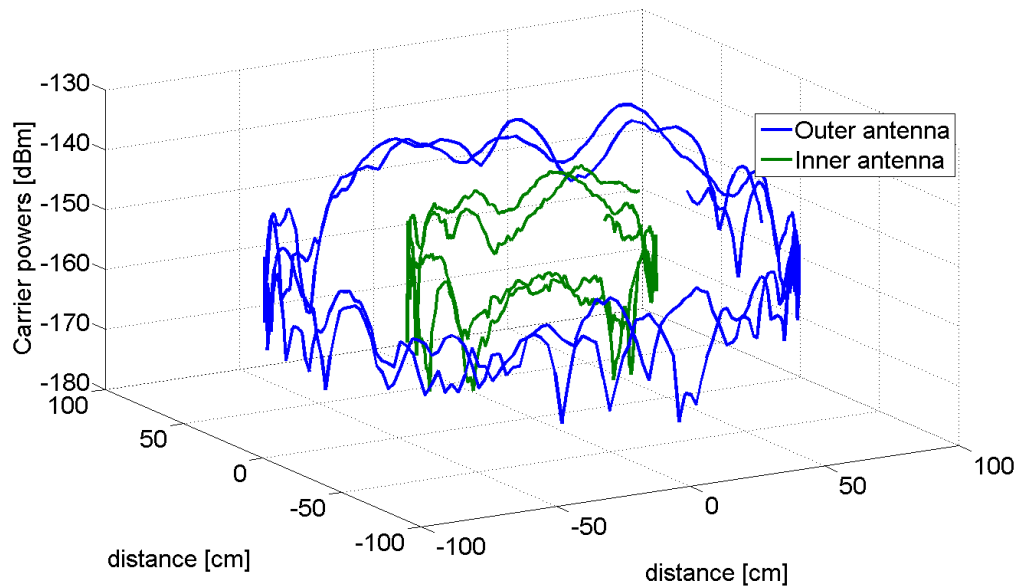
Figure 5-9: Carrier power profiles obtained using two GPS antennas mounted on the rotating arm of a turning table from dataset NL-DS2-D.

Thus, each point in Figure 5-9 represents an averaged signal power over 2.2 cm and 1.1 cm for Ant1 and Ant2, respectively. It can be seen that signal variations up to 10-15 dB can be observed for a small antenna displacement of the order of 7-10 cm.

Carrier power levels measured on the main floor of the wooden house are shown in Figure 5-10 for PRN05. In this case, signal power levels are plotted as a function of the antenna displacement. The antenna performs several turns and the power levels measured

at each turn are characterized by similar trends. This behaviour supports the hypothesis of time invariance of the communication channel. For this test, each point corresponds to 60 ms coherent integration. Since the radius of the turning table was 36 cm and a speed of 1 turn/min was used, the spatial sampling was therefore approximately every 0.2 cm. Note that the coherent integration effectively corresponds to a low pass filter in the spatial domain. This sampling scheme thereby avoids aliasing effects.

From Figure 5-10 (a), it appears that this spatial sampling is more than sufficient to observe the fading effect. Similar experiments were performed in the basement of the wooden house. A sample carrier profile for PRN06 from basement dataset WH-DS3-D is shown in Figure 5-10 (b). In this case a 51 cm radius and a speed equal to 4 turns/minutes have been used. It can be observed that the results are consistent with the main floor dataset, WH-DS2-D.

As described above, ACF and PSD for the wooden house experiments were estimated and the decorrelation distances of the signals from several PRNs were computed. Table 5-1 summarizes the decorrelation distances for four different satellites from the NavLab and wooden house experiments. Thus, the fast fading average decorrelation distance computed from the NavLab and wooden house experiments are approximately equal to half the GPS LIC/A carrier wavelength (9.8 cm).
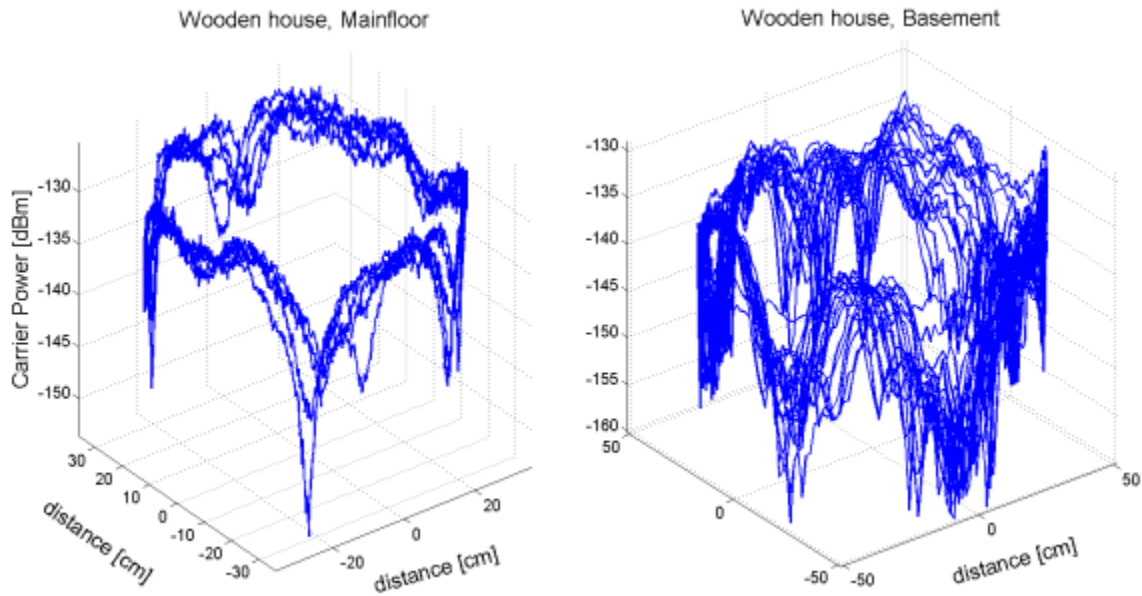
Figure 5-10: Carrier power profiles obtained using a single GPS antenna mounted on the rotating arm of a turning table from dataset WH-DS2-D (left) and WH-DS3-D (right).

Table 5-3: Summary of the fade statistics obtained from the rotation table experiment for high signal strength satellites during the data collection.

NL-DS2-D			WH-DS2-D		WH-DS3-D	
SV ID	Ant1, d_f (cm)	Ant2, d_f (cm)	SV ID	d_f (cm)	SV ID	d_f (cm)
8	7.7	8.6	6	7.6	5	5.8
11	8.8	9.2	18	9.9	18	7.3
17	9.9	9.3	21	8.7	21	13.9
21	12.9	10.4	26	10.3	29	8.0

5.2.2.3 Slow fading characterization

Second order slow fading characterization of GPS signals was carried out using an instrumented cart equipped with a wheel speed sensor. A high precision optical encoder capable of measuring an angular rotation of the order of $(2\prec)/1000$ radians was

interfaced with the shaft of the wheel. The estimated signal power levels were associated with the time tagged distance information provided by the wheel speed sensor. Data was collected along a straight path in the NavLab and McEwan Hall scenarios. Figure 5-11(a) shows the data collection setup used to collect live GPS signals in the NavLab using the instrumented cart (dataset NL-DS3-D and NL-DS4-D). Data was collected along a straight path. The instrumented cart was moved on parallel tracks of length approximately 9 metres long. The two tracks were separated by an approximate distance of 60 cm. A third dataset (in addition to ME-DS1-D and ME-DS2-D datasets described in Chapter 4) was collected using the instrumented cart in McEwan Hall as shown in Figure 5-11(b) (dataset ME-DS3-D). The cart was moved from west to east (50 m long) and then from east to west covering a total distance of 100 metres.

Figure 5-12 shows the speed and distance information obtained from the wheel speed sensor for the dataset NL-DS3-D and ME-DS3-D. It should be noted that the sign of the speed is reverted during the integration for the return path to make the absolute travelled distance equal to zero. In this way, the accuracy of the wheel speed sensors was also validated. It was observed that the distance error was lower than 2% of the total distance travelled during the data collection.

Figure 5-11: Data collection inside the NavLab (left) and McEwan Hall (right) using an instrumented cart.
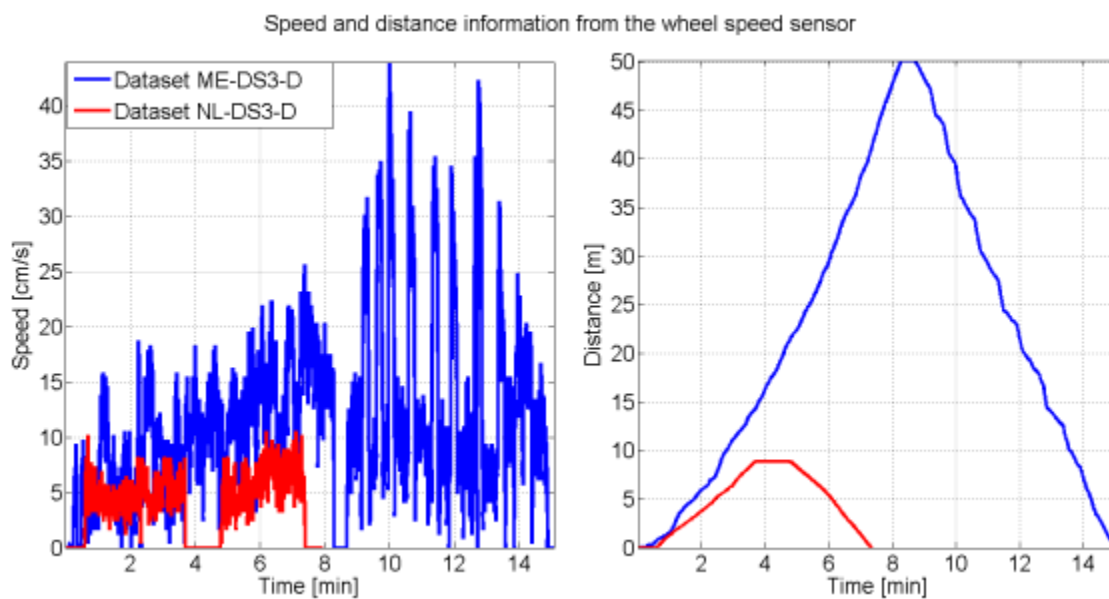
Figure 5-12: Speed and distance information obtained from the wheel speed sensor for the dataset NL-DS3-D and ME-DS3-D.

The estimated carrier power differences between reference and rover antennas, $\hat{\psi}_{dB}[n]$, and the low-passed signal, $\hat{\zeta}_{dB}[n]$, for two different satellites, namely PRN08 and PRN11, are shown in Figure 5-13. The rate of signal variations of the fast fading components is higher as compared to that of the rotation table experiment shown Figure 5-13. This is due to the higher antenna speed of the instrumented cart experiment (approximately 5-6 cm/s) as compared to that of the rotation table experiment (1.1 cm/s and 2.2 cm/s).
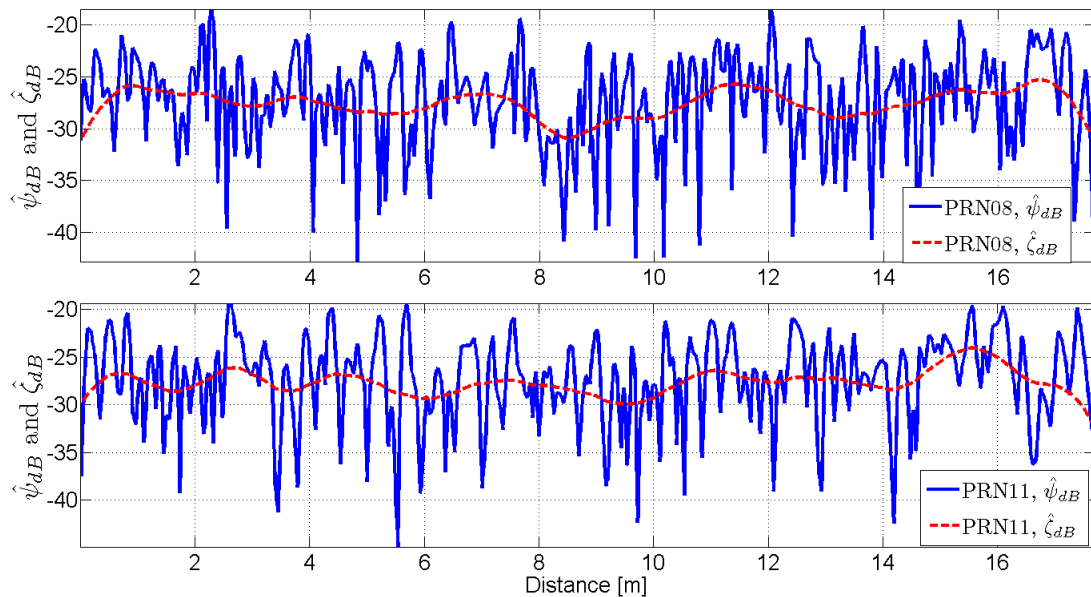
Figure 5-13: Carrier power variations for PRN08 and PRN11. Dotted lines represent the slow fading components obtained using a low-pass filter.

In Chapter 4, it was shown that the PDFs of the slow fading components, $\hat{s}[n]$, in the NavLab and McEwan Hall scenarios approximately follow a Log-Normal distribution. This means that the signal $\hat{s}_{dB}[n]$ follows a normal distribution. Thus, $\hat{s}_{dB}[n]$ can be modeled as a white Gaussian process whose statistical properties need to be

characterized. In the following, the signal $\hat{s}_{dB}[n]$ measured in the NavLab and McEwan Hall scenarios are analyzed and the corresponding temporal/spectral characteristics are extracted.

Figure 5-14 compares the ACF and PSD of the slow fading component, $\hat{s}_{dB}[n]$, against standard filter responses. As it can be observed from Figure 5-14, the response of the 4th order Butterworth filter is in good agreement with the empirical data. In this case, the average speed information obtained from the wheel speed sensor is used to determine the slow fading decorrelation distance, which was found to be approximately 78.5 cm.
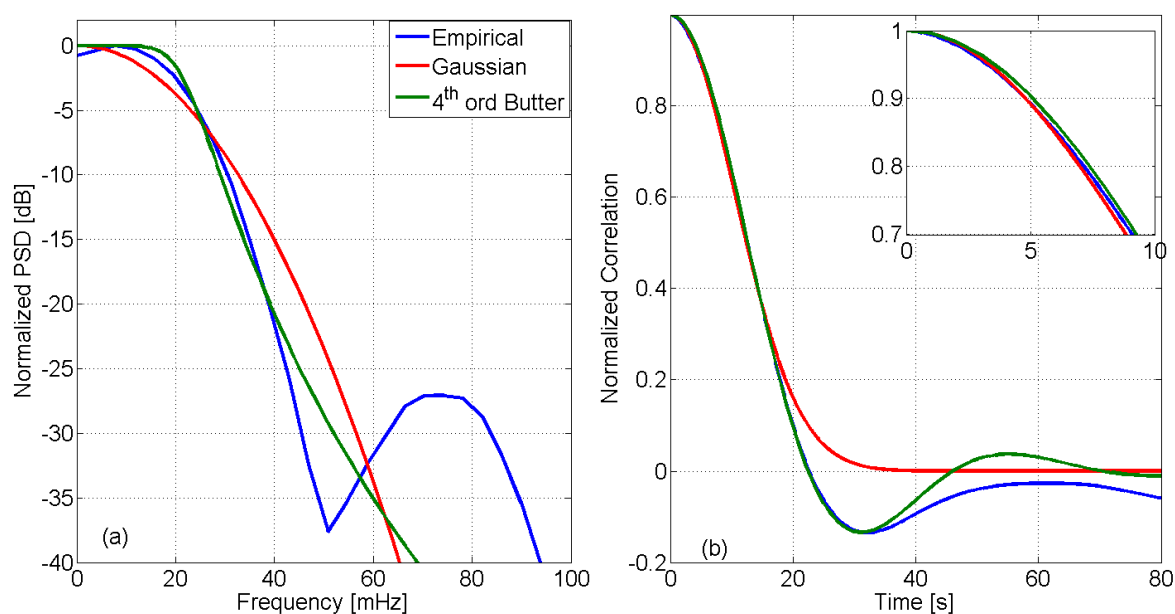
Figure 5-14: Comparison of empirical PSD and ACF of the slow fading process with that of the Gaussian and Butterworth filter responses for the NavLab scenario.

Similar analysis was performed on the slow fading components obtained from the McEwan Hall dataset and it was found out that the spectral and temporal characteristics were in good agreement with the response of a 4th order low-pass Butterworth filter. Table 5-4 summarizes the decorrelation distances for the slow fading components

measured in the NavLab and McEwan Hall experiments. It can be observed that the slow fading decorrelation distances found in the McEwan Hall experiments were significantly higher than the NavLab scenario. This is due to the fact that McEwan Hall is a relatively much wider area as compared to the NavLab and thus the signal blocking elements are spread apart and the receiver has to be displaced over longer distance in order to experience different shadowing effects.

Table 5-4: Statistics of slow fading components for high signal strength satellites from the instrumented cart experiment.

NL-DS3-D		NL-DS4-D		ME-DS1-D		ME-DS3-D	
SV ID	d_s (m)	SV ID	d_s (m)	SV ID	d_s (m)	SV ID	d_s (m)
8	0.75	8	0.78	4	3.12	4	7.5
11	0.61	11	0.75	9	3.8	9	5.0
17	0.68	17	0.68	17	2.9	17	4.6
28	0.74	28	0.65	28	3.0	28	7.1

Figure 5-15 compares the number of available satellites as a function of distance travelled for two different carrier power thresholds of -157 dBm and -160 dBm. Here, both NavLab and McEwan Hall scenarios are considered for the analysis. It can be clearly observed that for a carrier power threshold of -160 dBm, between 6 and 8 satellites are available in the McEwan Hall scenario as compared to 3 to 6 satellites in the NavLab. This is mainly due to the higher attenuation levels caused by the opaque NavLab rooftops, whereas, McEwan Hall's roof includes glass windows and rooftops that are more transparent to GNSS signals.
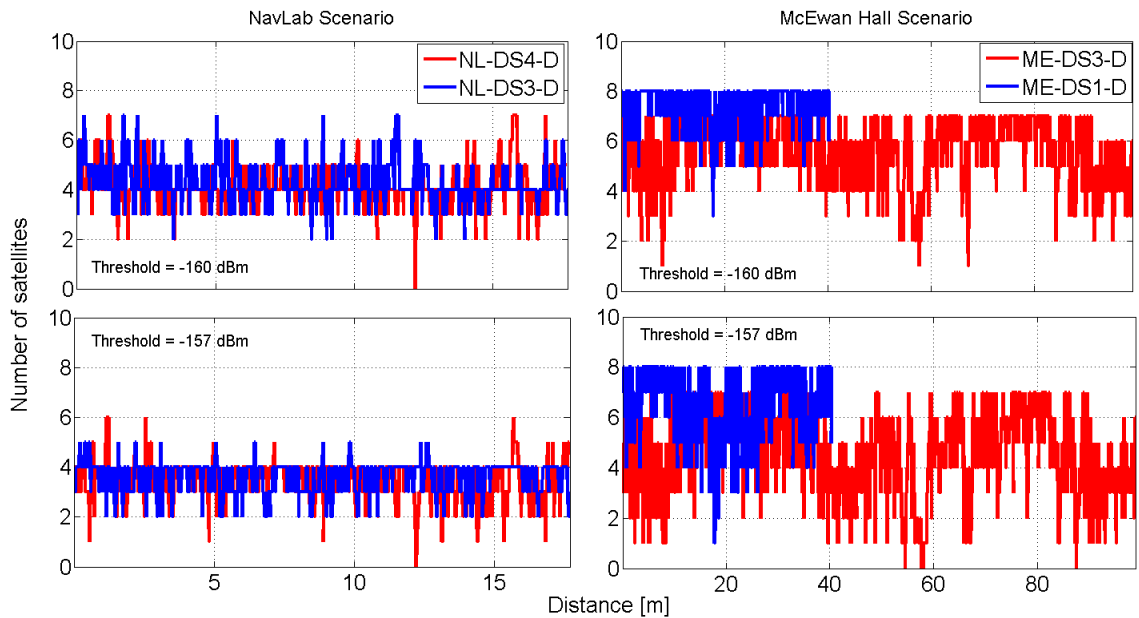
Figure 5-15: Number of satellites available as function of distance travelled in NavLab and McEwan Hall datasets.

Based on the results presented in this section it is clear that even under static conditions, the signal amplitude changes over time and has a correlation time of about 1 minute. Under dynamic conditions, the signal amplitude is affected by both shadowing and multipath phenomena. The effects due to shadowing are generally slow in nature and have a correlation distance of about 1-5 metres depending on the scenario. Effects on the signal amplitude due to multipath fading are generally fast and have a correlation distance of about half a GPS L1 C/A carrier wavelength. In the following section a simulation scheme for simulating GPS indoor signals under NLOS conditions is described.

5.3 Simulation Scheme

In this section, a simulation scheme based on the results obtained in Section 4.4.5 and 5.2 is suggested. The simulation of indoor GNSS signals under a controlled environment

provides the tool to perform repeated tests and thoroughly analyze the receiver performance. In Section 4.4.5, it was shown that the amplitude of the indoor GNSS signal can be modeled as a multiplicative process of the slow and fast fading components. The slow and fast fading amplitude components were shown to approximately follow Log-Normal and Rice distributions, respectively. In this section, the empirically derived parameters of the slow and fast fading processes are used to simulate indoor GNSS signals.

A simulation approach based on filtering a white Gaussian noise (WGN) process is considered (Stüber 2002, Pätzold 2002). Here, the WGN process is filtered using a standard filter. The filter transfer function, $H(f)$, is designed such that the PSD of the filtered output approximately matches the empirical PSD of the fading process. If $S_{xx}(f)$ is the PSD of the signal at the filter input, the PSD of the filtered output is given by (Pätzold 2002)

$$S_{yy}(f) = \left| H(f) \right|^2 S_{xx}(f).$$ (5.11)

Since the PSD of a WGN process is constant, the PSD of the filtered output is directly proportional to the squared magnitude of the filter transfer function. The ACF of the filter output is given by the inverse Fourier transform of the squared magnitude of the filter transfer function. Based on the temporal/spectral characterization results obtained in Section 5.2.2.2 and 5.2.2.3, a 4th order low-pass Butterworth filter is considered for simulating GNSS indoor signals. A block diagram representing the proposed simulation scheme for indoor GNSS signals is shown in Figure 5-16. Here, the output $\tilde{w}[n]$ represents the complex correlator outputs.
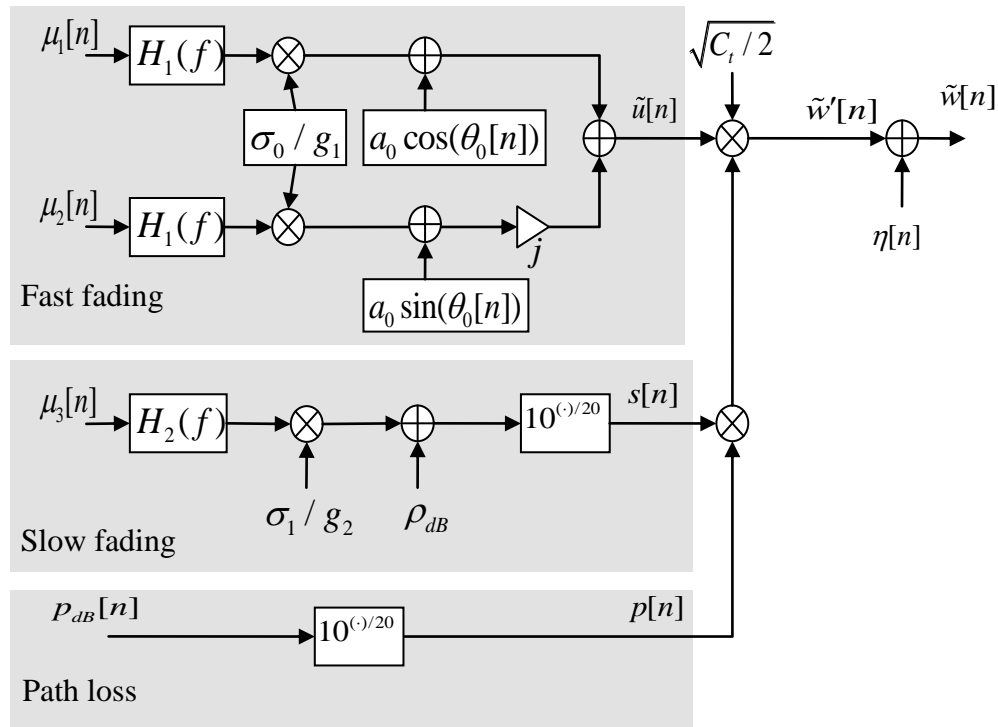
Figure 5-16: Block diagram of the indoor GNSS signal simulation.

In Figure 5-16, path loss, slow fading and fast fading components are simulated independently and multiplied together to produce the composite indoor GNSS signal. A standard Rice simulation scheme (Stüber 2002) is used to generate the fast fading component. Two independent standard WGN sequences ($\mathcal{N}(0,1)$) $\mu_1[n], \mu_2[n]$ are filtered using a 4$^{\text{th}}$ order Butterworth filter with transfer function $H_1(f)$. The filtered outputs are scaled by a factor σ_u / g_1 where g_1 is the overall gain of the filter given by $g_1 = \int_{-\infty}^{\infty} |H_1(f)| df$. Then the scaled filtered outputs are combined with the LOS component $a_0 \cos(\theta_0[n])$ and $a_0 \sin(\theta_0[n])$ to form a complex signal $\tilde{u}[n]$ whose magnitude follows a Rice distribution. Here, a_0 and $\theta_0[n]$ are the amplitude and phase variations associated with the LOS component as described in Chapter 2.

In order to generate a Log-Normal sequence, a third WGN $\mathcal{N}(0,1)$ sequence $\mu_3[n]$ is filtered using a 4th order Butterworth filter with transfer function $H_2(f)$. The filtered output is scaled by a factor σ_1/g_2 where σ_s is the standard deviation of the Normal process and g_2 is the overall gain of the filter given by $g_2 = \int_{-\infty}^{\infty}|H_2(f)|df$. Then the scaled filtered output is added to the mean shadow level ρ_{dB} to produce the signal $s_{dB}[n]$. Later, $s_{dB}[n]$ is transformed using an anti-logarithmic operation to produce the Log-Normal sequence $s[n]$.

The path loss sequence is generated using the standard Friis formula given by (Kaplan & Hegarty 2006)

$$p_{dB}[n] = 20\log_{10}\left(\frac{\lambda}{4\pi l[n]}\right) + \Phi[n] \qquad (5.12)$$

where λ is the GPS L1 C/A carrier wavelength, $l[n]$ is the true distance between the satellite and the receiver and $\Phi[n]$ accounts for any other losses such as rain, cloud, ionospheric, antenna gain variations etc. The signal $p_{dB}[n]$ is transformed using an anti-logarithmic operation to produce the path loss sequence, $p[n]$. The simulated sequences, $\tilde{u}[n]$, $s[n]$ and $p[n]$, are then multiplied together along with the transmitted carrier power $\sqrt{C_t/2}$ to produce the composite signal $\tilde{w}'[n]$. Finally, the composite signal $\tilde{w}'[n]$ is combined with additive WGN to produce the complex correlator output $\tilde{w}[n]$ as given by Eq. (3.5). An example of simulated signal using the parameters obtained from

the empirical data (NL-DS3-D) is shown in Figure 5-17. Here, a receiver antenna speed

of 5 cm/s and a coherent integration of 1 s are assumed.
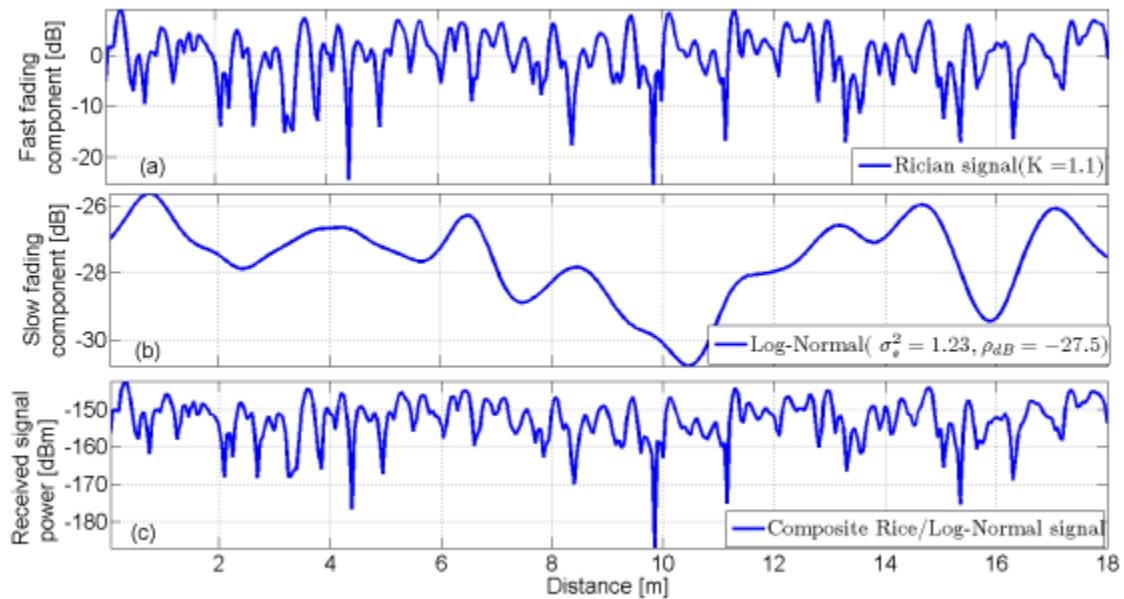
Figure 5-17: Simulated indoor GPS signal power levels using the parameters obtained from the empirical data.

The simulation parameters obtained from the empirical data are:

- Rice K factor = 1.1,

- Log-Normal parameters, $\rho_{dB} = -27.5$ dB and $\sigma_s^2 = 1.23$,

- Fast fading decorrelation distance = 9.7 cm and

- Slow fading decorrelation distance = 78.5 cm.

The simulated fast fading, slow fading and the composite RLN waveforms are as shown

in Figure 5-17(a), (b) and (c), respectively. It can be observed that the signal variations

are consistent with the real data results presented in Figure 5-13. It should be noted that

the simulation methodology presented in this section can also be used to simulate the

signals for a static scenario. For a static case, the cutoff frequencies of $H_1(f)$ and $H_2(f)$ in Figure 5-16 can be further narrowed down to obtain very slow signal variations.

Figure 5-18 compares the empirical density function of the received signal envelope from the dataset NL-DS3-D and ME-DS30D with the theoretical RLN and simulated PDFs.
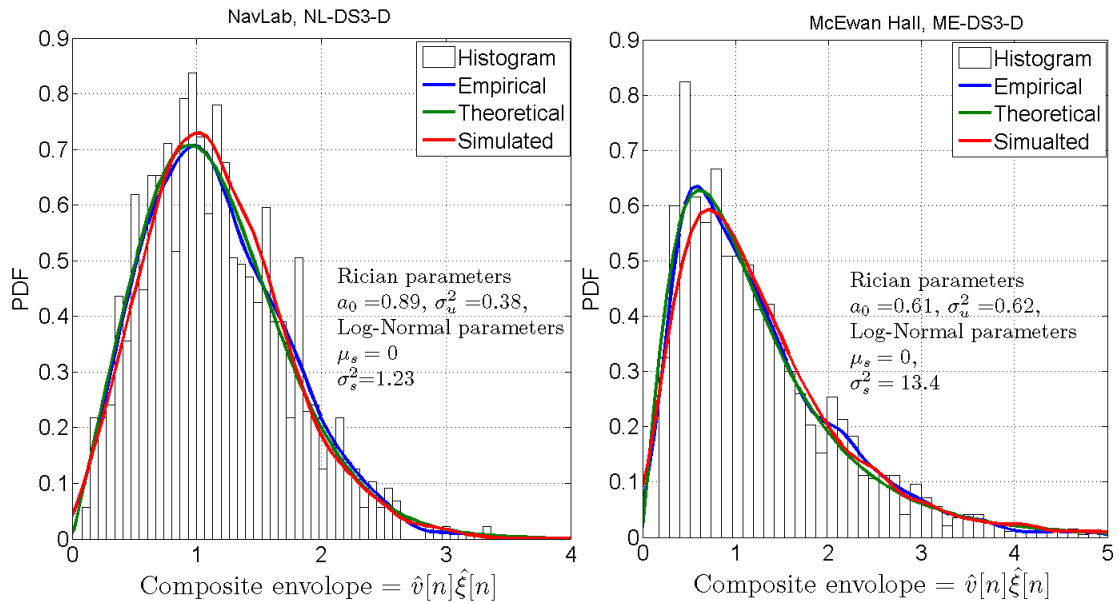
Figure 5-18: Comparison of the empirical, theoretical and simulated PDFs of the composite amplitude envelope under two different scenarios.

Here, the parameters of the Rice and Log-Normal distribution were estimated from the empirical data. The estimated parameters are used in the theoretical RLN PDF obtained using Eqs. (2.29) and (2.30). In addition, the estimated parameters are used in the simulation model described above to generate the correlator outputs. The simulated correlator outputs can then be analyzed in a similar way as the real GPS correlator outputs using the methodology described in Section 4.2. In this way, the density function of the simulated data is obtained. A good agreement was found between the empirical and simulated RLN PDFs. It should be noted that in Figure 5-18, signals from NL-DS3-D

are less affected by the slow fading phenomena as compared to the signals found in ME-DS3-D. This is because the variance of the Log-Normal process, σ_s^2, estimated from ME-DS3-D datasets are comparatively higher than NL-DS3-D dataset. Also, the Rician K factors found for the NavLab scenario are slightly higher than those of the McEwan datasets. Figure 5-18 shows that the RLN model is capable of simulating both conditions and thus it can be used for a wide range of scenarios.

Comparison of second order statistics of the fast fading components obtained from NL-DS2-D dataset (Ant2) with the simulated data is shown in Figure 5-19.
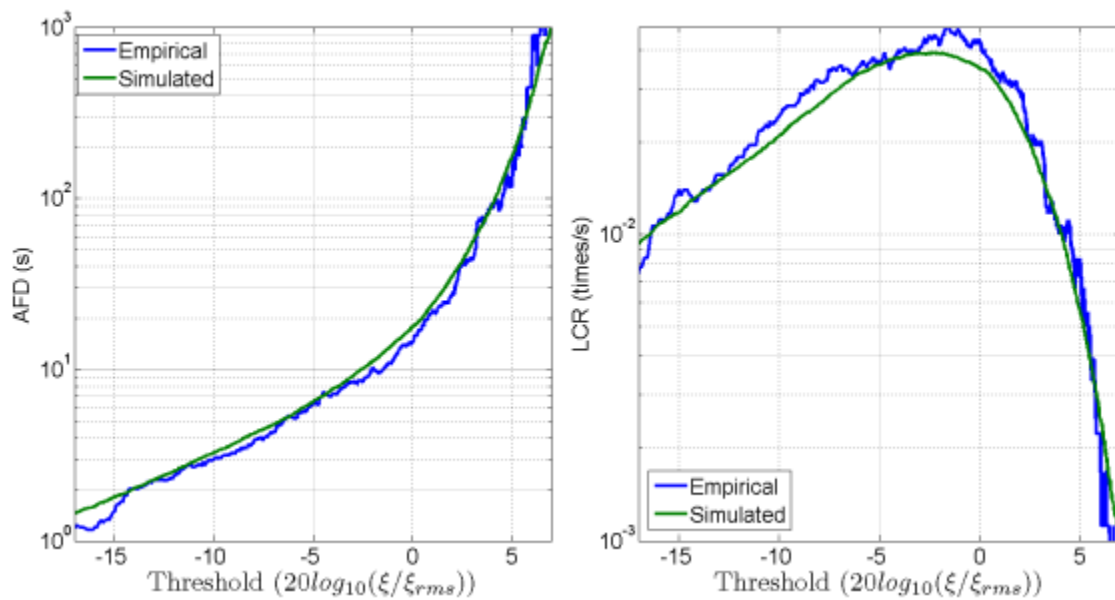
Figure 5-19: Comparison of the second order statistics of the empirical data (NL-DS2-D, Ant2) with the simulated data.

It can be observed that a good agreement is obtained between the theoretical and the simulated curves. This shows that the simulation model described in this section is an effective tool for simulating the indoor GPS signals in a wide range of scenarios. The

considered simulation model is capable of capturing both first and second order statistics of the indoor fading phenomenon.

5.4 Summary

An extended statistical characterization of the indoor GPS signals was considered in this chapter. More specifically, the second order statistics of the received signal envelopes were analyzed under several indoor environments. Two different methodologies were considered to characterize GPS signals over small and large physical areas. It was shown that experiments based on rotation tables are effective in capturing the fast fading phenomena with fine spatial resolution. A cart instrumented with a wheel speed sensor was used to effectively characterize slow fading over large physical areas. Slow and fast fading phenomena can thus be effectively captured using the proposed approaches.

The spectral characteristics of the fading process were also investigated. It was shown that the fast and slow fading processes can be generated by filtering WGN sequences using 4th order low-pass Butterworth filters. Finally, a simulation model for simulating indoor GNSS signals was described. It was also shown that the first and second order statistics of the simulated data are in good agreement with the empirical data.

Chapter Six: **ENHANCED SIGNAL PROCESSING FOR GNSS WEAK SIGNALS**

As shown in previous chapters, GNSS signals under harsh environments such as indoors are generally weak and experience fading phenomena which result in a time varying signal power. Traditional signal acquisition and tracking techniques used in a standard GNSS receiver may not be adequate to overcome the effects of excess attenuation and fading under such conditions. Thus, it becomes crucial to design and develop new signal acquisition and tracking techniques that are capable of detecting weak GNSS signals and maintain lock under deep fade conditions.

In this chapter, enhanced signal processing techniques have been considered for GPS weak signal acquisition and tracking for standalone receivers. A new detection scheme for weak signal acquisition is proposed. Performance of the new detection scheme is evaluated using simulations and compared against existing techniques. Finally, a new architecture for tracking GPS weak signals is described. Performance of the proposed tracking scheme is evaluated using both software and hardware simulations. The effectiveness of the proposed algorithm is shown by tracking GPS weak signals in several indoor environments under dynamic conditions.

6.1 Acquisition of GNSS weak signals

Acquisition is the first signal processing stage in a GNSS receiver wherein the presence or absence of a satellite signal is determined using statistical methods. In other words, the acquisition process can be viewed as a binary detection problem, wherein the incoming GNSS signal buried in noise is processed to derive a decision variable. This decision variable is compared against a threshold to determine the presence or absence of a given

satellite signal. In the case of GNSS, the presence or absence of a given satellite signal corresponds to two hypotheses namely (Borio 2008):

- *Null hypothesis* (H_0): signal is absent or misaligned with the local replica

- *Alternative hypothesis* (H_1): signal is present and aligned with the local replica.

In general, a *detector* can be defined as a signal processing block or an algorithm which operates on the incoming signals to generate a decision variable. The decision variable is then compared against a threshold to determine the presence or absence of the signal under test. The decision variable which is a random variable is also referred to as *test statistics*. In general, the detector exploits statistical properties of the incoming signal under H_0 and H_1 to derive the test statistics. In turn, the test statistics is completely characterized by its PDF under H_0 and H_1. In the case of GNSS, the performance of a given detector is analyzed by considering two probability functions, namely the probability of detection (P_d) and probability of false alarm (P_{fa}). More specifically, P_d and P_{fa} are given by (Kay 1998)

$$
\begin{aligned}
P_d(\gamma) &= P\big(T(\mathbf{x}) > \gamma \,|\, H_1\big) \\
P_{fa}(\gamma) &= P\big(T(\mathbf{x}) > \gamma \,|\, H_0\big)
\end{aligned}
\tag{6.1}
$$

where γ is the threshold value, $P(\cdot|\cdot)$ indicates conditional probability and $T(\mathbf{x})$ is the test statistics obtained by processing the incoming signal vector $\mathbf{x}$. The plot of P_d vs. P_{fa} is called the Receiver Operating Characteristics (ROC).

As described earlier in Chapter 3, in a typical GNSS receiver, incoming signals are correlated with the local code and carrier replicas and integrated over T_c seconds. The correlated outputs obtained in this way are given by Eq. (3.6). These correlator outputs are further processed by various detection algorithms to determine the signals presence or absence. The most common forms of detectors used in a GNSS receiver are the coherent, non-coherent (NC) and differential detectors. Since the correlator outputs are used by these detection techniques, they are also referred to as post-correlation detectors. A comprehensive analysis of these detection techniques can be found in (Borio 2008, O'Driscoll 2007, Shanmugam 2008). The test statistics obtained from coherent, non-coherent and differential schemes are summarized in Table 6-1 (Borio 2008, O'Driscoll 2007).

Table 6-1: Test statistics for coherent, non-coherent and differentially non-coherent detection techniques.

Detection scheme	Test statistics
Coherent	$T_{Coh}(\tilde{\mathbf{w}}) = \left\| \sum_{k=0}^{K-1} \tilde{w}[k] \right\|^2$
Non-coherent	$T_{NCoh}(\tilde{\mathbf{w}}) = \sum_{k=0}^{K-1} \left| \tilde{w}[k] \right|^2$
Differentially non-coherent (DNC)	$T_{DNCoh}(\tilde{\mathbf{w}}) = \left\| \sum_{k=1}^{K-1} \tilde{w}[k]\tilde{w}^*[k-l] \right\|^2$

As it can be seen from Table 6-1, a coherent detector, coherently integrates the incoming signal over KT_c seconds. Thus, a GPS receiver operating in standalone mode (without data bit aiding) can only coherently integrate L1 C/A code based measurements over 20

ms ($K = 20$) due to the data modulation. A NC detector removes the phase dependence (data bit effect) by summing the absolute square value of the correlator outputs. It should be noted that the absolute square operation also increases the noise effect reducing the overall effectiveness of the post correlation averaging. This increase in the noise effect can be reduced to a certain extent by adopting the differential detection scheme (Borio 2008). It should be noted that there exist several variants of differential detectors. Only the non-coherent form (DNC) of the differential detectors is shown in Table 6-1. In the DNC test statistics expression, l represents the delay element. In the following section, a new detector referred to as *squaring detector (SD)* is derived under the presence of data bit modulation. It is shown that under certain conditions SD has a superior performance over the NC and differential detectors considered in Table 6-1.

6.1.1 Squaring detector

In this subsection a new detector for acquiring GPS weak signals under the presence of the data bit modulation is derived. Using Eq. (3.6), the correlator outputs under the presence of data modulation can be written as

$$
\begin{aligned}
w_k &= I_k + jQ_k \\
&= Ad_k \exp\{j\varphi\} + \tilde{\eta}'_k
\end{aligned}
\tag{6.2}
$$

where $A = \sqrt{C/2}$. Here, the amplitude A and phase φ are assumed to be deterministic and unknown constants. Assuming the data bits uniformly distributed between ± 1, the PDF of the signal w_k can be written as (Borio & Lachapelle 2009)

$$f(\tilde{w}_k; A, \varphi) = \sum p(d_k) f(w_k | d_k)$$

$$= \frac{1}{2\pi\sigma^2} \exp\left[-\frac{1}{2\sigma^2}\left(I_k^2 + Q_k^2 + A^2\right)\right] \cosh\left[\frac{A}{2\sigma^2}\left(I_k \cos\varphi + Q_k \sin\varphi\right)\right]. \quad (6.3)$$

For K independent observations, the joint PDF of w_k under H_1 can be written as

$$f(\tilde{\mathbf{w}} | H_1; A, \varphi) = \frac{1}{\left(2\pi\sigma^2\right)^K} \exp\left[-\sum_{k=0}^{K-1} \frac{1}{2\sigma^2}\left(I_k^2 + Q_k^2 + A^2\right)\right] \cdot$$

$$\prod_{k=0}^{K-1} \cosh\left[\frac{A}{2\sigma^2}\left(I_k \cos\varphi + Q_k \sin\varphi\right)\right]. \quad (6.4)$$

The PDF of w_k under H_0 can be obtained by substituting $A = 0$ in Eq. (6.4) and thus can be written as

$$f(\tilde{\mathbf{w}} | H_0) = \frac{1}{\left(2\pi\sigma^2\right)^K} \exp\left[-\sum_{k=0}^{K-1} \frac{1}{2\sigma^2}\left(I_k^2 + Q_k^2\right)\right]. \quad (6.5)$$

Now, the optimal detector using the Neyman-Pearson approach (Kay 1998) is given by the Generalized Likelihood Ratio Test (GLRT) which maximizes P_d for a given P_{fa} and decides H_1 if

$$L(\tilde{\mathbf{w}}) = \frac{\max_{A, \varphi} \hat{f}\left(\tilde{\mathbf{w}} | H_1, A, \varphi\right)}{f\left(\tilde{\mathbf{w}} | H_0\right)} > \gamma \quad (6.6)$$

where $L(\tilde{\mathbf{w}})$ is the likelihood ratio. From Eq. (6.6), it is noted that the GLRT computes the ratio of the maxima of the likelihood function under H_1 and H_0 respectively. Now, substituting Eqs. (6.4) and (6.5) in Eq. (6.6), the test (6.6) can be rewritten as

$$L'(\tilde{\mathbf{w}}) = \prod_{k=0}^{K-1} \cosh\left[\frac{\hat{A}}{2\sigma^2}\left(I_k \cos\hat{\varphi} + Q_k \sin\hat{\varphi}\right)\right] > \gamma'. \quad (6.7)$$

where γ' is a new threshold incorporating the constant terms removed from $L(\tilde{\mathbf{w}})$.

Taking the logarithm of each sides, Eq. (6.7) can be further expressed as

$$\sum_{k=0}^{K-1} \ln\left(\cosh\left[\frac{\hat{A}}{2\sigma^2} \left(I_k \cos\hat{\varphi} + Q_k \sin\hat{\varphi} \right) \right] \right) > \ln(\gamma'). \tag{6.8}$$

Now, by approximating $\ln(\cosh(x)) = x^2$ for small values of x, Eq. (6.8) can be simplified as

$$\sum_{k=0}^{K-1} \left(I_k \cos\hat{\varphi} + Q_k \sin\hat{\varphi} \right)^2 > \gamma''. \tag{6.9}$$

Thus, using Eq. (6.9), the test statistics for the SD detector can be written as

$$\begin{aligned} T_{SD}(\tilde{\mathbf{w}}) &= \sum_{k=0}^{K-1} \left(I_k \cos\hat{\varphi} + Q_k \sin\hat{\varphi} \right)^2 \\ &= \sum_{k=0}^{K-1} (I_k^2 + Q_k^2 + (I_k^2 - Q_k^2)\cos 2\hat{\varphi} + 2I_k Q_k \sin 2\hat{\varphi}). \end{aligned} \tag{6.10}$$

In the above expressions, $\hat{\varphi}$ represents the ML estimate of φ and is given by (Borio & Lachapelle 2009)

$$\hat{\varphi} = \frac{1}{2}\arctan 2\left(\frac{\sum_{k=0}^{K-1} 2I_k Q_k}{\sum_{k=0}^{K-1} (I_k^2 - Q_k^2)} \right). \tag{6.11}$$

Substituting Eq. (6.11) in Eq. (6.10) and further simplifying, the test statistics for the SD, $T(\tilde{\mathbf{w}})$, can be written as

$$\begin{aligned} T_{SD}(\tilde{\mathbf{w}}) &= \sum_{k=1}^{K-1} \left(I_k^2 + Q_k^2 \right) + \sqrt{\left(\sum_{k=0}^{K-1} (I_k^2 - Q_k^2) \right)^2 + \left(\sum_{k=0}^{K-1} 2I_k Q_k \right)^2} \\ &= \underbrace{\sum_{k=1}^{K-1} |w_k|^2}_{T_{SD,1}(\tilde{\mathbf{w}})} + \underbrace{\left| \sum_{k=1}^{K-1} w_k^2 \right|}_{T_{SD,2}(\tilde{\mathbf{w}})}. \end{aligned} \tag{6.12}$$

It can be observed from Eq. (6.12) that the $T_{SD}(\tilde{\mathbf{w}})$ contains two parts. The first part is identical with the test statistics of the NC detector listed in Table 6-1 whereas the second part is obtained by summing the squared values of the complex signal $\tilde{w}_k$ and hence referred to as *squaring detector*. A similar kind of test statistic which is a combination of non-coherent and differential test statistics was derived in (Corazza & Pedone 2007). It was shown that the performance of the combined detector was superior compared to that of the individual detectors. As explained above, in order to evaluate the P_d and P_{fa} associated with the SD, it is necessary to compute the PDF of $T_{SD}(\tilde{\mathbf{w}})$ under H_0 and H_1. However, it should be noted from Eq. (6.12) that $T_{SD}(\tilde{\mathbf{w}})$ is a summation of two non independent random variables, $T_{SD,1}(\tilde{\mathbf{w}})$ and $T_{SD,2}(\tilde{\mathbf{w}})$. Thus, the PDF of $T_{SD}(\tilde{\mathbf{w}})$ under H_0 and H_1 cannot be easily determined. P_d and P_{fa} are thus evaluated using MC simulations. The analytical characterization of the theoretical P_d and P_{fa} are left as future work. MC simulation results are compared against the performance of the detectors listed in Table 6-1.

6.1.2 Performance analysis

In the following, ROC curves for the SD are evaluated using MC simulations. Here, the correlator outputs were simulated according to Eq. (6.2). The simulated correlator outputs were then used as inputs to the various detectors discussed in the previous section. P_d and P_{fa} values are then computed numerically using various threshold values. The

results shown in this section are generated using 100,000 MC simulation runs; zero frequency and code phase errors are assumed.

For the simulations, it is assumed that the GPS receiver has a prior knowledge of the data bit boundaries (for example re-acquisition scenario). Under such condition, the receiver can coherently integrate the signal up to 20 ms and non-coherently process over multiple data periods. Figure 6-1 compare the ROC curves for two different values of K for an incoming signal with C/N$_0$ = 18 dB-Hz and $T_c = 20$ ms. For differential detectors, a value of one was considered for the delay element, l. In Figure 6-1, the P_{fa} axis is shown on a logarithmic scale whereas P_d is shown on a linear scale. As expected, the coherent detector, computed in the absence of data bits, sets the upper bound for the detection probability.
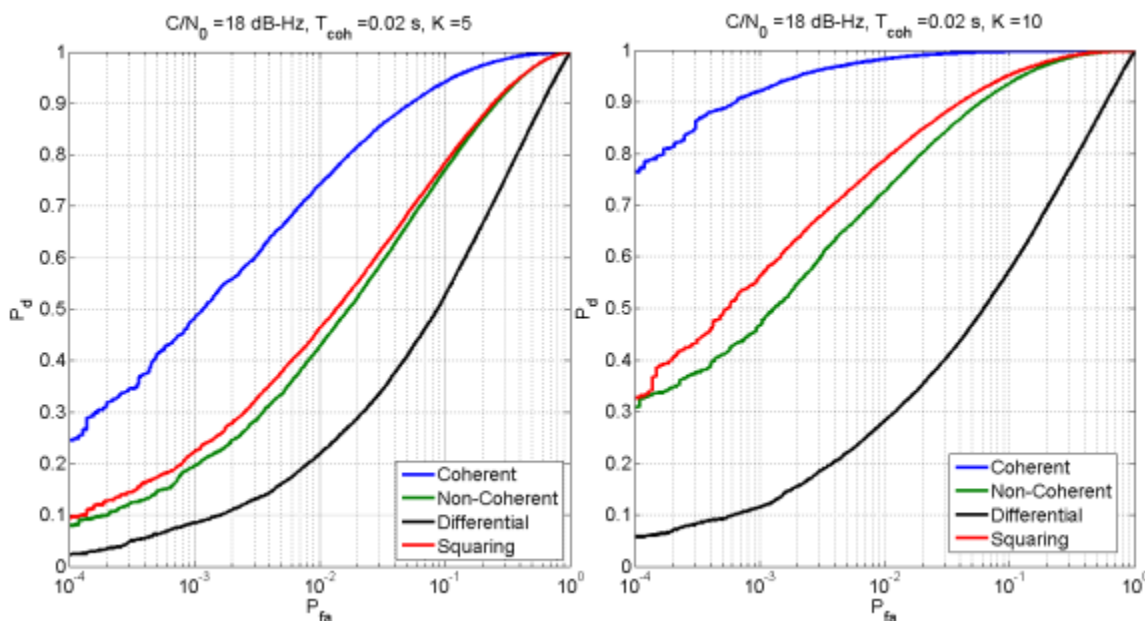
Figure 6-1: ROC curve comparison of the SD against traditional detectors for two different K values at a C/N$_0$ of 18 dB-Hz.

It can be observed that the SD has a superior performance as compared to the NC and DNC detectors. Here, the differential detectors have low P_d values as compared to the other detectors. This is due to fact that the 180° phase shift introduced by the data bits significantly reduces the accumulated signal power. However, the differential detector have poor performance due to the presence of data bits. Better performance is expected under the absence of data bits (such as for pilot channels).

The SD derived in the previous section provides an improved signal detection performance under the presence of data bit modulation. In the following section, tracking of GPS weak signals based on the squaring principle is considered.

6.2 Tracking of GNSS weak signals

A brief introduction to various existing weak signal tracking techniques was provided in Chapter 1. In this section, a new carrier frequency tracking structure for a standalone receiver operating in a harsh environment is described. More specifically, a hybrid NC tracking structure (Borio & Lachapelle 2009) with the block processing (Uijt de Haag 1999, Graas et al. 2005) technique is considered. In this method, it is assumed that the initial synchronization parameters such as fine code phase, carrier Doppler and bit boundaries are known to the receiver. This can be achieved by initializing the receiver in a good/medium environment such as in the case of a pedestrian walking from outdoors to indoors.

6.2.1 NC block processing tracking architecture

The block diagram of the proposed hybrid non-coherent block processing (NCBP) architecture for weak signal frequency tracking is shown in Figure 6-2. This architecture

exploits the ML estimate of the carrier phase under the presence of data bit modulation to track the carrier Doppler frequency. In Figure 6-2, the incoming digitized samples are correlated with the local replica of the code and carrier samples and integrated over one data bit period ($T_c = 20$ ms). The correlator outputs are then squared to remove the data bit effect. Here, the squaring operations remove the data bit modulation effect but retain the original incoming carrier phase. The squaring operation is a nonlinear operation and thus increases the noise level. To further reduce the noise effect, the squared correlator outputs are averaged over K samples to obtain the signal $\tilde{w}_s$.
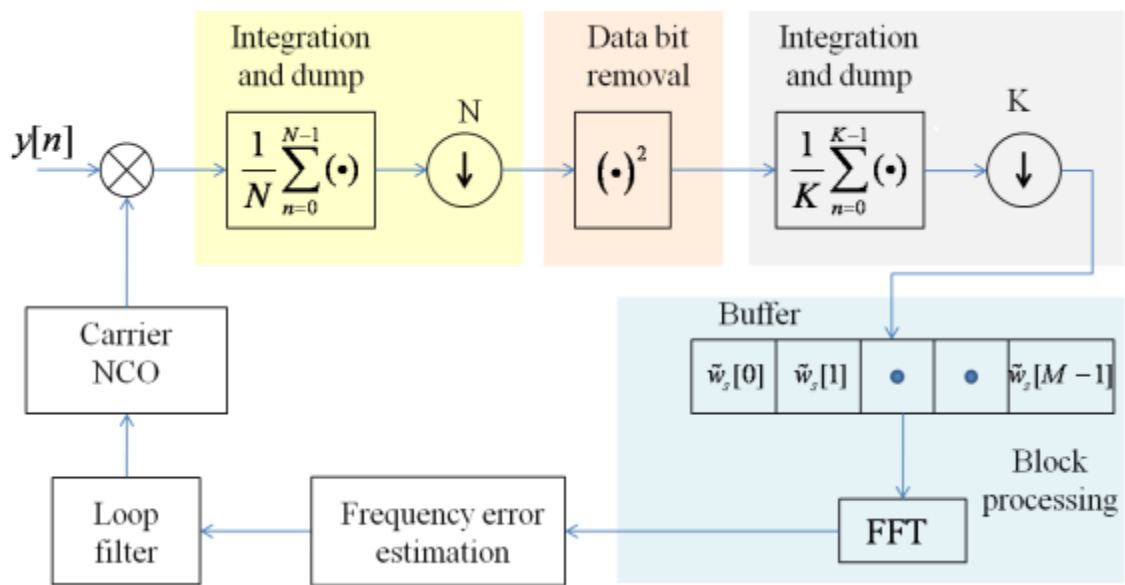
Figure 6-2: Block diagram of the GNSS weak signal frequency tracking architecture under the presence of data modulation.

The averaged squared correlator outputs, $\tilde{w}_s$, obtained in this way are stored in a buffer of size M where $M = T/(KT_c)$ and T is the update rate of the loop. This block of correlator outputs is utilized by code and carrier tracking loops to extract the code phase and carrier Doppler information. More specifically, a block processing technique based

on FFT is applied on the stored correlator outputs to extract the residual carrier Doppler frequency. The estimated residual frequency error from the FFT block is passed through the loop filter. Finally, the loop filter output is used to update the carrier NCO that closes the loop. From Figure 6-2, it is clear that the frequency resolution of the FFT output is limited to $1/T$ Hz. For example, for value of $T = 1.2$ s, the accuracy of the frequency error estimate is limited to ± 0.42 Hz. However, a finer resolution of the frequency error estimate can be obtained by simple zero padding of the FFT input signal vector, $\tilde{\mathbf{w}}_s$ (John & Manolakis 1996). Alternatively, an interpolation technique can be adopted to determine the frequency index corresponding to the peak value of the FFT output (Lyons 2004). In this research work, the technique based on the zero padding is adopted to increase the frequency resolution.

6.2.2 Results and analysis

In this section, the performance of the NCBP architecture is analyzed using three different approaches. More specifically, software simulations, hardware simulations and real GPS indoor dynamic data are used to evaluate the frequency tracking performance of the proposed technique. The default processing parameters were set to $T_c = 20$ ms and $T = 1.2$ s. Software simulation results are first presented.

6.2.2.1 Software simulation results

Software simulations provide an ideal environment to analyze and evaluate the performance of any new algorithm. In this section, the sensitivity of the NCBP architecture is quantified by simulating progressively attenuated carrier wave signals at the IF level. The code effect was ignored in order to analyze the performance of the

carrier tracking loop alone. The simulated IF signal, $y[n]$, was provided as input to the tracking algorithm shown in Figure 6-2. The C/N$_0$ value at which the estimated carrier frequency begins to deviate significantly from its true value is declared as the tracking sensitivity of the algorithm. More specifically, the following condition is adopted for obtaining the tracking sensitivity:

$$\left| \hat{f} - f_{true} \right| > \frac{\alpha_{th}}{2T_c K} \tag{6.13}$$

where $\hat{f}$ and f_{true} represent the estimated and true carrier frequency and α_{th} determines the admissible relative frequency error. For further analysis, α_{th} is set to 0.3 (30 %).

A sample plot of the estimated carrier Doppler values and the corresponding sensitivity is shown in Figure 6-3. Here, a carrier signal with a constant Doppler frequency was simulated with progressively decreasing signal strength (0.5 dB/6 seconds) as shown in Figure 6-3(b). In Figure 6-3(a), the differences between estimated and true Doppler values are shown for three different values of K, the number of non-coherent integrations. As expected, the sensitivity of the algorithm improves for increased values of K.

It can be observed that for values of $K = 1, 2$ and 4, the sensitivity of the algorithm is approximately 14.5 dB-Hz, 13.5 dB-Hz and 11.5 dB-Hz, respectively. It should be noted that, for the simulation results presented in this section the effect of code was completely ignored. Thus, in order to accurately evaluate the performance of the NCBP architecture under GPS scenarios, a more realistic simulation approach based on the hardware simulator described in Section 3.5.5 is considered in the following section.
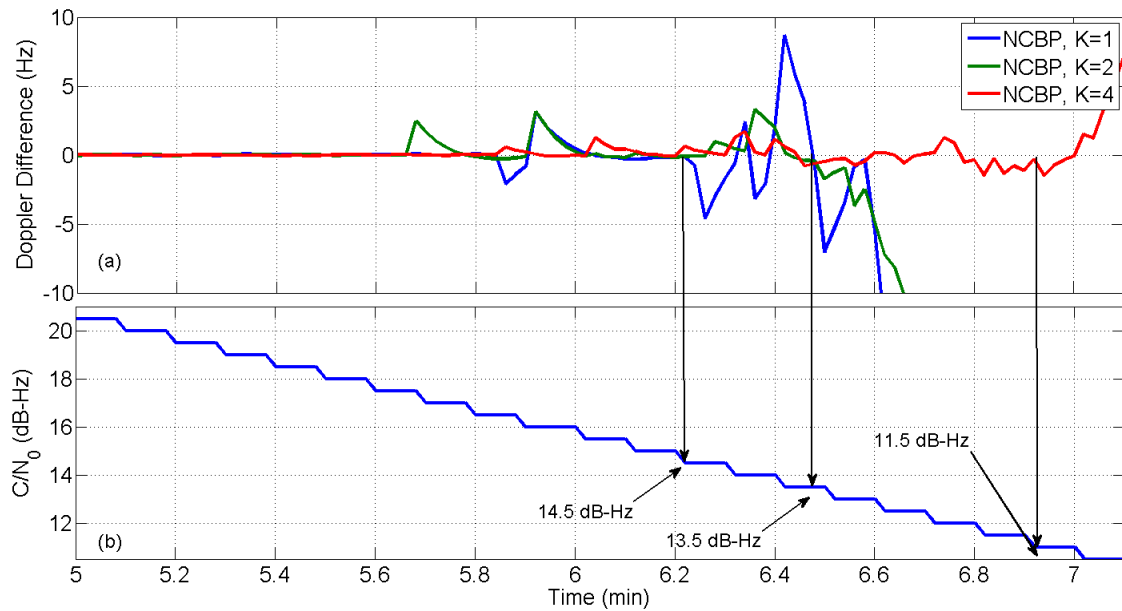
Figure 6-3: (a) Difference between estimated and true carrier Doppler values for various values of _K_ for IF simulated data. (b) Simulated C/N$_0$ values as a function of time.

6.2.2.2 Hardware simulation results

As described in Chapter 3, the Spirent GSS7700 hardware simulators provide a controlled environment to simulate GPS signals with desired parameters. A hardware test setup similar to that described in Section 3.5.5 is used to validate the weak signal tracking algorithm described above. In this case, a static GPS scenario with multiple satellites in view was simulated. The carrier power levels were progressively decreased from -154 dBm to -164 dBm with a step of 1 dB every two minutes. Initially, the attenuated signal was tracked using the RR processing strategy to extract accurate estimates of the C/N$_0$ and carrier Doppler values that were used to initialize the NCBP scheme. After initialization, the attenuated signals were tracked using the NCBP scheme. The obtained results are compared against the reference carrier Doppler values to determine the algorithm sensitivity.

The estimated carrier Doppler values using the NCBP architecture for two different satellite IDs, namely PRN15 and PRN11, are shown in Figure 6-4. In Figure 6-4(a), the estimated carrier Doppler values for three different values of K are shown for PRN15. As expected, the track times corresponding to $K = 2$ and 4 are higher as compared to $K = 1.$ However, the estimated Doppler values corresponding to $K = 2$ and 4 begins to deviate from the nominal trajectory almost at the same instant. This could be due to the fact that the C/N$_0$ of the incoming signal is fluctuating between 12-16 dB-Hz during that particular time interval, corresponding to the sensitivity region of the algorithm as shown in Figure 6-3.
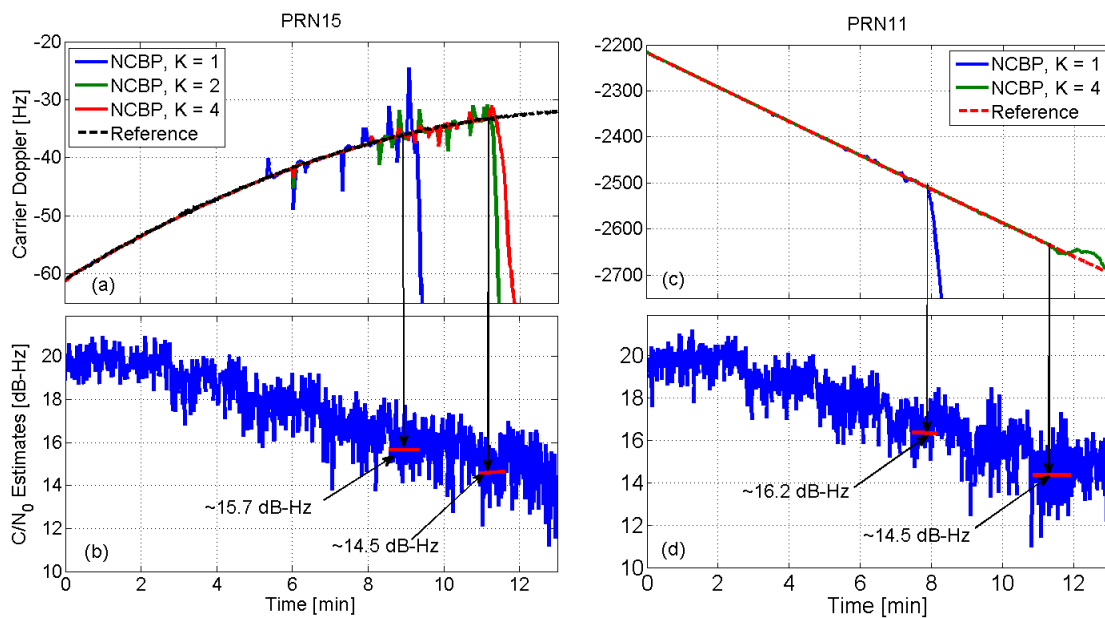
Figure 6-4: (a) Estimated carrier Doppler values for various values of K for hardware simulator data, PRN15. (b) C/N$_0$ values obtained from RR processing.

Thus, the sensitivity of the algorithm using hardware simulator data was estimated by averaging the C/N$_0$ values obtained from the different satellites in the loss of lock region. As shown in Figure 6-4(b), the sensitivity of the algorithm corresponding to $K = 1$ and 4

are 15.7 and 14.5 dB-Hz respectively. As expected, the sensitivity values are slightly higher as compared to the software simulation results presented in the previous section. This is due to the fact that, in hardware simulations, the effect of code processing, i.e., the impact of the DLL, is also included.

As it can be seen from Figure 6-4(a), occasional outbursts in the estimated carrier Doppler were observed. However, the tracking loop was able to sustain and recover from those instants in the successive time intervals. This also highlights the robustness of the NCBP architecture with respect to occasional outliers in the frequency estimates. This is due to the use of the DFT that provides a wide frequency pull-in region.

The tracking results corresponding to PRN11 are shown in Figure 6-4(c) and (d). As it can be seen, the Doppler rate for PRN11 (approx 0.7 Hz/s) is comparatively high as compared to PRN15 (approx 0.04 Hz/s). The NCPB algorithm is able to correctly process signal PRN11 and the tracking sensitivity values are in good agreement with that of PRN15. In the following, tracking results obtained from real GPS data collected indoors are described.

6.2.2.3 Real data results

During the course of the signal characterization in previous chapters, it was observed that a commercial high-sensitivity receiver was able to successfully track weak signals in the wooden house scenario. Hence datasets corresponding to NavLab and McEwan Hall experiments where the high sensitivity receivers provided poorer performance are considered here. In the following, the dynamic datasets, namely ME-DS3-D and NL-DS2-D described in Chapter 5, are considered for the analysis.

Figure 6-5(a) compares the estimated carrier Doppler using the NCBP scheme for PRN09 from dataset ME-DS3-D with the reference Doppler values obtained using the RR strategy. It can be observed that, the NCBP technique was able to track and maintain the signal locked for the entire duration of the experiment (travelled distance ~100 m).

The estimated Doppler values are in good agreement with reference Doppler values. Here, it should be noted that the value of $K = 1$ was sufficient to track the indoor signal over the entire duration. In Figure 6-5(b) a comparison between the estimated C/N$_0$ values obtained using the RR strategy and the NCBP estimates is shown. The RR strategy uses the MML estimator given by Eq. (3.12) to estimate the C/N$_0$ values. However, a GPS receiver operating under standalone mode cannot use the MML estimator as it requires data bits to be removed before C/N$_0$ computation.

Thus in Figure 6-5(b), NCBP C/N$_0$ estimates are computed by first estimating the SNR of the signal as (Muthuraman & Borio 2010)

$$\hat{\alpha} = \frac{\hat{C}}{2\hat{\sigma}^2} = \frac{\left(\dfrac{1}{M} \sum_{m=1}^{M} |\tilde{w}_m| \right)^2}{\dfrac{1}{2(M-1)} \sum_{m=1}^{M} \left| |\tilde{w}_{ext,m}| - \dfrac{1}{M} \sum_{k=1}^{M} |\tilde{w}_{ext,k}| \right|^2} \tag{6.14}$$

where $\tilde{w}_m$ is the 20 ms correlator output and $\tilde{w}_{ext,m}$ is the 20 ms correlator outputs obtained by correlating the incoming signal with a non-existing PRN code as explained in Chapter 3.
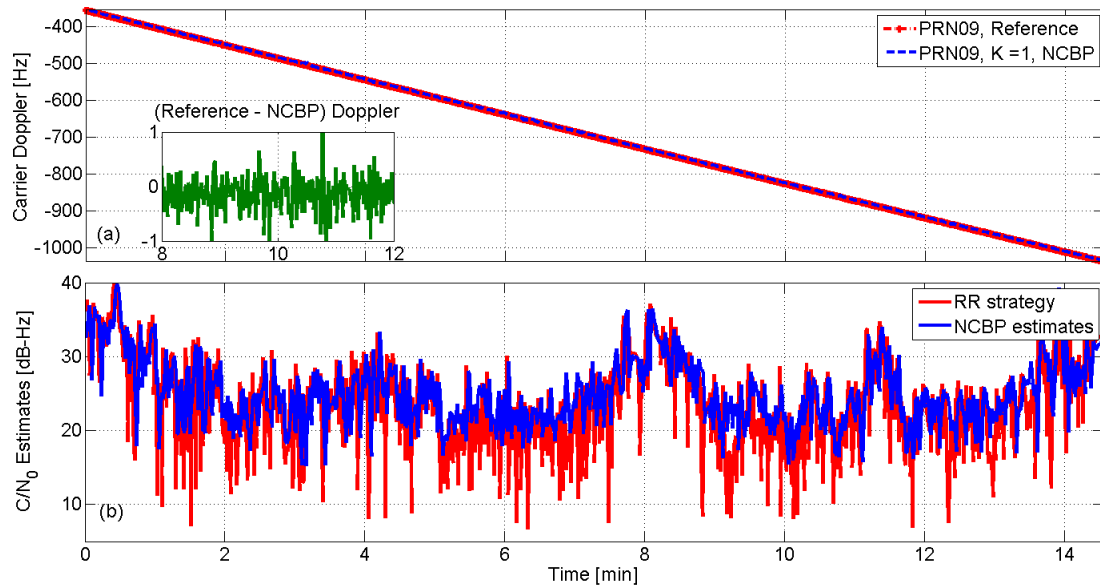
Figure 6-5: (a) Estimated carrier Doppler values for PRN09 from ME-DS3-D dataset. In the small box: zoom of the frequency difference between reference and estimated values. (b) Estimated C/N$_0$ values abstained from RR processing and NCBP estimates.

The SNR values obtained in this way are used in Eq. (3.8) to obtain the C/N$_0$ values. It can be observed that a good agreement is obtained between the C/N$_0$ values. However, the estimates obtained from the NCBP saturate at 16 dB-Hz due to the high bias arising at low C/N$_0$ conditions as described in (Muthuraman & Borio 2010).

Frequency tracking results for PRN17 from both inner and outer antennas obtained from the rotation table experiment NL-DS2-D is shown in Figure 6-6 (a-d). It can be observed that the NCBP architecture was able to successfully track the signals under dynamic conditions. Again, a value of $K = 1$ was sufficient to track the indoor signal for the entire duration of the data collection. Here, it should be noted that the indoor signals have mean shadow levels of approximately 27 dB with respect to the outdoor scenario and an additional 20-25 dB variations due to fading.
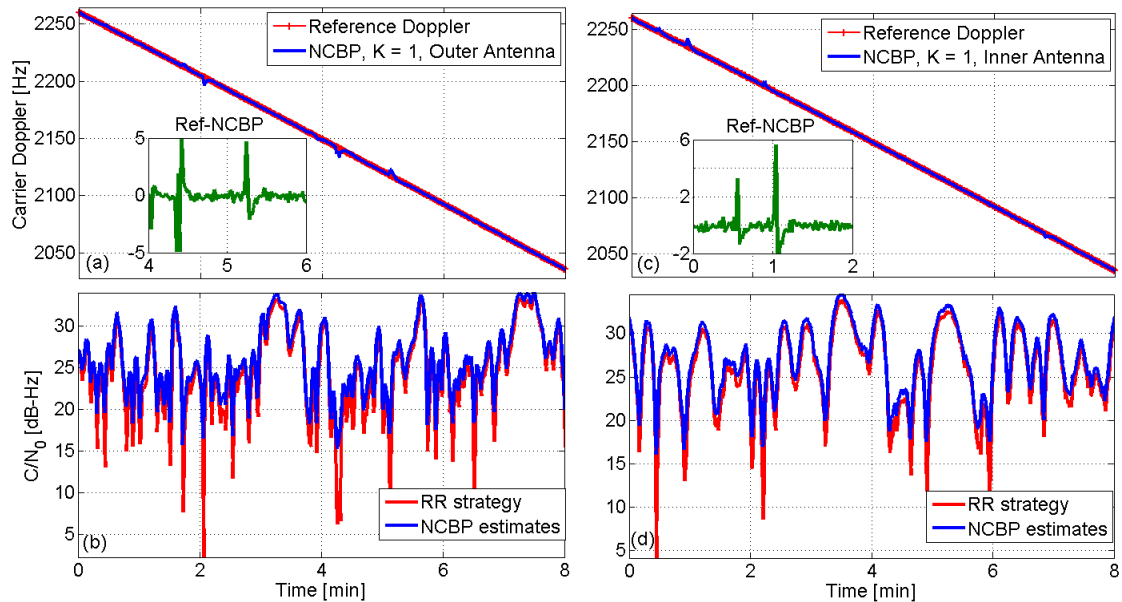
Figure 6-6: (a) Estimated carrier Doppler values for PRN17 from NL-DS2-D dataset. In the small box: zoom of the frequency difference between reference and estimated values. (b) Estimated C/N$_0$ values obtained from RR processing and NCBP estimates.

It can also be observed from Figure 6-6(b) and (d) that the C/N$_0$ values dropped below 10 dB-Hz several times which is well below the sensitivity of the algorithm as discussed in the previous section. This is due to the ability of the algorithm to recover from estimation outliers. Small outliers in the estimated carrier Doppler values can be seen at those instants when the C/N$_0$ values dropped below 10 dB-Hz, however, the NCBP architecture was able to successfully recover from the deep fade instants and provide continuous frequency measurements.

These results show the effectiveness of the proposed algorithm and its ability to process signals in the presence of fading and other impairments.

6.3 Summary

In this chapter, advanced signal processing techniques for the acquisition and tracking of weak GNSS signals were described. Towards this, a new detector for weak signal acquisition under the presence of data bit transitions was derived. It was shown that the performance of the new detector is superior to existing detection techniques under certain conditions. A new architecture for GPS weak signal frequency tracking was also proposed. It was shown that, the new architecture is able to track signals with a C/N_0 as low as 14.5 dB-Hz under static conditions. It was also shown that the new tracking scheme is able to withstand occasional deep signal fades well below 10 dB-Hz and provide continuous tracking measurements under dynamic indoor scenarios.

Chapter Seven: **CONCLUSIONS AND RECOMMENDATIONS**

This chapter provides the conclusions of this thesis towards the characterization of GNSS weak signals and development of new weak signal acquisition and tracking. Recommendations for possible future work that can complement the presented results are provided.

7.1 Conclusions

Based on the results and analysis presented in the earlier chapters, this section lists the conclusions drawn from GNSS channel characterization and enhanced weak signal processing techniques.

7.1.1 GNSS channel characterization

With respect to GNSS channel characterization, the following conclusions are drawn:

1. Accurate characterization of real GNSS weak signals is a problem of both synchronization and estimation. Thus, special care has to be taken in order to reduce synchronization errors between incoming and locally generated signals.

2. The RR data collection and processing strategy were proven to be an effective approach to characterize GNSS weak signals. RR processing helps in reducing the synchronization errors along with providing the navigation data bits which enables long coherent integration. This allows one to isolate the useful signal component from the noise.

3. The analytical characterization of the MML SNR estimator showed that for an accurate characterization of received signal power levels on the order of -160 dBm, a coherent integration time of $1.5 - 2$ seconds is required to limit the

estimator errors within ±2 dB with a $90 - 95\%$ confidence level. Also, it was shown that the variance of the MML estimator approaches the CRLB values for long integration times making it an asymptotically efficient estimator.

4. The first order characterization of GPS weak signals under several signal degraded environments revealed that composite and/or mixed models are necessary for describing the behaviour of the received signal amplitude. Composite models are well suited for situations where the LOS component is present or absent for the entire observation window. On the other hand, mixed models are well suited in scenarios where the receiver antenna experiences a mixture of LOS and NLOS conditions such as in the case of urban outdoor scenarios.

5. The RLN distribution encapsulates several other distributions such as Loo's, Suzuki's, Rice's, Log-Normal and Rayleigh's as its special cases and thus offered flexibility in modelling several scenarios. It was shown that a composite RLN model was able to describe the received signal envelope under several outdoor and indoor scenarios efficiently.

6. The proposed experimental strategies based on the rotation table and instrumented cart experiments were able to effectively capture the fast and slow fading effects as a function of both time and space. Experiments using a rotation table were effective to capture the amplitude of the received signal envelope over fine spatial resolution helping in characterizing fast fading effects. The experimental strategy based on an instrumented cart was effective to characterize slow fading components over large physical areas.

7. The temporal/spectral characterization of indoor GPS signals showed that the ACF and PSD of the incoming signal amplitudes can be approximated using a 4th order low-pass Butterworth filter response. It was shown that under static conditions, the received signals are correlated over several seconds (30-100 seconds). However, as the antenna is displaced, the signal quickly decorrelates and the rate of decorrelation is proportional to the antenna speed. Accordingly, the PSD of the received signals are narrower for the static case as compared to dynamic scenarios. Second order statistics such as AFD, LCR and MFD of the fast fading components were in good agreement with standard parametric models.

8. The spatial analysis of indoor GPS signals revealed that fast fading components due to multipath tend to decorrelate over distances of approximately half a wavelength of GPS L1 C/A carrier wave (9.5 cm).

9. The spatial analysis of the slow fading component performed using an instrumented cart showed that decorrelation distances of the slow fading component highly depends on the scenario type and various rooftop materials. For example, in a laboratory scenario the slow fading components were approximately correlated over 1 m, whereas slow fading components were correlated over several metres in a shopping complex type of scenario.

10. Based on the characterization results, a simulation strategy for simulating GPS indoor signals based on the RLN model was proposed and analyzed. The simulation results showed that the first and second order statistics obtained from the simulated signals are in good agreement with the empirical values.

7.1.2 Enhanced weak signal processing

In this subsection, conclusions relative to the acquisition and tracking of GPS weak signals are provided.

1. A new signal detection scheme called a squaring detector was developed for the case when data bit modulation is present. The test statistics of the new detector is a combination of two individual test statistics. It was shown that the squaring detector has superior performance with respect to standard techniques such as non-coherent and differential non-coherent detectors.

2. A hybrid frequency tracking architecture based on the combination of NC and block processing architectures was proposed and analyzed. The NCBP architecture exploits the ML estimate of the incoming signal phase along with the advantages of block processing techniques to estimate the frequency of GPS weak signals.

3. Through hardware simulations, it was shown that the new NCBP architecture is able to track weak signals as low as 14.5 dB-Hz under static conditions. The results obtained by tracking real indoor GPS signals showed that the NCBP tracking scheme is able to withstand occasional deep signal fades well below 10 dB-Hz and provide continuous tracking measurements under dynamic conditions.

4. The proposed algorithm is effective in maintaining continuous code and carrier frequency lock for the entire data collection duration (10-14 minutes in this case) without any external aiding. Thus, the NCBP architecture is capable of tracking GPS signals indoors with moderate dynamics. In addition, smaller FFT size and low update rate (1-2 s) allows for an easy realization on modern Field

Programmable Gate Arrays (FPGAs) or Digital Signal Processors (DSPs) making this architecture a good candidate for high sensitivity GNSS receiver design. The proposed algorithms are effective tool for the characterization of indoor signals and should be used when reference data are not available.

7.2 Recommendations

Recommendations for future work are summarized below:

1. In this research work, the area over which the signal characterization can be performed is limited by the measurement setup as RR processing strategy requires both reference and rover antennas to be physically connected to the NI system. In order to overcome this limitation, a measurement setup based on an inertial navigation system (INS) as described in (Aminian et al. 2010) could be adopted. This approach could be used for extending the analysis performed in this thesis.

2. The proposed simulation model can be further extended to include mixed/multi-state models. In this way, it will be possible to account for non-stationary channels and account for time-variant LOS components.

3. The performance of the squaring detector described in Section 6.1.1 was evaluated using numerical techniques. This is due to the fact that the PDF of the test statistics under H_0 and H_1 assume complex forms and thus the analytical characterization of P_{fa} and P_d is rather difficult. A Gaussian approximation of the tail probabilities should be investigated to obtain threshold values.

4. In the NCBP architecture presented in Section 6.2.1, the index corresponding to the peak magnitude value of FFT output was used to estimate the frequency error.

However, under weak signal conditions, the peak magnitude value of the FFT output can be significantly different from the true frequency index due to the increased level of noise. Thus, advanced algorithms to detect and isolate outliers could be investigated to further improve the tracking sensitivity.

5. As seen from the frequency tracking results presented in Section 6.2.2, the estimated carrier Doppler values are in good agreement with the reference values even under low C/N_0 values. A more thorough analysis of the proposed algorithm should be performed for instance to determine the variance of the Doppler frequency estimates as a function of input C/N_0.

References

Abdi, A. and M. Kaveh (1999) "On the utility of gamma PDF in modeling shadow fading (slow fading)," in *Proceedings of the IEEE Trasaction on Vehicular Technology*, 16-20 May, Houston, TX, pp. 2308

Abdi, A., W. C. Lau, M. S. Alouini, and M. Kaveh (2003) "A New Simple Model for Land Mobile Satellite Channels-First and Second order statistics," in *IEEE Transaction on Wireless Communication*, Vol. 2, Issue 3, pp. 519-528

Abdi, A., K. Wills, H.A. Barger, M.S. Alouini, and M. Kaveh (2000) "Comparison of the level crossing rate and average fade duration of Rayleigh, Rice and Nakagami fading models with mobile channel data," in *Proceedings of the IEEE VTS-Fall VTC 2000 52nd*, , pp. 1850-1857

Alagha, N. S. (2001) "Cramer-Rao bounds for SNR estimates for BPSK and. QPSK modulated signals," in *Commun. Lett.*, Vol. 5, Jan, pp. 10–12

Aminian, B., V. Renaudin, D. Borio, and G. Lachapelle (2010) "Indoor Doppler Measurements and Velocity Characterization Using a Reference-Rover Software Receiver," in *Proceedings of the ION GNSS*, , Portland

Anyaegbu, E. (2006) "A Frequency Domain Quasi-Open Loop Tracking Loop for GNSS Receivers," in *Proceedings of the ION GNSS*, 26 - 29 Sept, Fort Worth, TX, pp. 790 - 798

Blunck, H., M.B. Kjaergaard, T. Godsk, T. Toftkjaer, D.L. Christensen, and K. Grønbaek (2009) "Empirical Analysis and Characterization of Indoor GPS Signal Fading and Multipath Conditions," in *Proceedings of the ION-GNSS*, , Savannah, GA , pp. 2362 - 2371

Borio, D. and G. Lachapelle (2009) "A non-coherent architecture for GNSS digital tracking loops," in *Annals of Telecommunications*, Vol. 64, Issue 9-10, pp. 601-614

Borio, D., S. Fazio, and G. Lachapelle (2009) "Multirate Signal Processing: a Solution for Wide-band GNSS Signal Recovery," in *Proceedings of the European Navigation Conference 2009 (ENC09)*, 3-6 May, Naples, Italy

Borio, D., N. Sokolova, and G. Lachapelle (2009) "Memory Discriminators for Non-Coherent Integration in GNSS Tracking Loops," in *Proceedings of the European Navigation Conference*, , Naples, Italy

Borio, D. (2008) *A Statistical Theory for GNSS Signal Acquisition*, Doctoral Thesis, Dipartimento di Elettronica, Politecnico di Torino

Brown, A. K. and P. Olson (2005) "Urban/Indoor Navigation Using Network Assisted GPS," in *Proceedings of the Proceedings of the 61st Annual Meeting of The Institute of Navigation*, , Cambridge, MA, pp. 1131 - 1136

Cioni, S., G.E. Corazza, and M. Bousquet (2005) "An Analytical Characterization of Maximum Likelihood Signal-to-Noise Ratio Estimation," in *Proceedings of the International Symposium on Wireless Communication Systems*, Sept, Siena , pp. 827 - 830

Corazza, G.E. and R. Pedone (2007) "Generalized and Average Likelihood Ratio Testing for Post Detection Integration," in *IEEE Transactions on Communications*, Vol. 55, Issue 11, pp. 2159 - 2171

Corazza, G. E. and F. Vatalaro (1994) "A statistical model for land mobile satellite channels and its application to nongeostationary orbit systems," in *IEEE Transaction on Vehicular Technology*, Vol. 43, pp. 738-742

Coulson, A.J., A.G. Williamson, and R.G. Vaughan (1998) "Improved fading distribution for mobile radio," in *IEE Communications*, Vol. 145, Issue 3, pp. 197 - 202

Fontan, F. P. and P.M. Espineira (2008) *Modeling the Wireless Propagation Channel: A Simulation Approach with MATLAB*, John Wiley & Sons Ltd

Fontan, F. P., M. A.V. Castro, J. Kunisch, J. Pamp, E. Zollinger, S. Buonomo, P. Baptista, and B. Arbesser (1997) "A Versatile Framework For A Narrow- and Wide-Band Statistical Propagation Model for the LMS Channel," in *IEEE Transaction on Broadcasting*, Vol. 43, Issue 4, Dec, pp. 431-458

Fontán, P. F., B. Sanmartín, A. Steingass, A. Lehner, J. Selva, E. Kubista, and B. A. Rastburg (2004) "Measurements and Modeling of the Satellite-to-Indoor Channel for Galileo," in *Proceedings of the ION-NTM*, , San Diego, CA, pp. 190-202

GPS ICD (2010) *Navstar GPS Space Segment/Navigation User Interfaces, Interface Specification, IS-GPS-200E*, Rev E, http://www.gps.gov/technical/icwg/IS-GPS-200E.pdf

Graas, v. F., A. Soloviev, U. d.M. Haag, S. Gunawardena, and M. Braasch (2005) "Comparison of Two Approaches for GNSS Receiver Algorithms: Batch Processing and Sequential Processing Considerations," in *Proceedings of the ION-GNSS*, , Long Beach, CA , pp. 200 - 211

Griffiths, J. and J.P. McGeehan (1982) "Interrelationship between some statistical distributions used in radio-wave propagation," in *IEE Communications, Radar and Signal Processing* , Vol. 129, Issue 6, pp. 411

Groves, P. D. (2005) "GPS Signal to Noise Measurement in Weak Signal and High Interference Environments," in *Proceedings of the Proceedings of ION GNSS*, 3-16 September, Long Beach, CA, pp. 643-658

Hashemi, H. (1993) "The indoor propagation channel," in *Proceedings of the IEEE*, Vol. 81, Issue 7, pp. 943 – 968

Haykin, S. (2001) *Communication Systems*, John Wiley & Sons, Inc., New York

Ibnkahla, M. (2004) *Signal Processing for Mobile Communications Handbook*, CRC press

Islam, A.K.M. N., E. S. Lohan, and M. Renfors (2008) "Moment based CNR estimators for BOC/BPSK modulated signal for Galileo/GPS," in *Proceedings of the 5Th Workshop On Positioning, Navigation And Communication*, , pp. 129-136

John, G. P. and K. D. Manolakis (1996) *Digital Signal Processing: Principles, Algorithms and Applications*, Prentice-Hall Publications, New Jersy, US

Jost, T. and W. Wang (2009) "Satellite-to-indoor broadband channel measurements at 1.51 GHz," in *Proceedings of the ION GNSS International Technical Meeting*, 26-28 Jan , Anaheim, CA, pp. 777-783

Kaplan, E. D. and C. Hegarty (2006) *Understanding GPS Principles and Applications*, Artech House, Boston

Kay, S. M. (1993) *Fundamentals of Statistical Signal Processing, Volume I: Estimation Theory*, Prentice-Hall, Inc

Kay, S. M. (1998) *Fundamentals of Statistical Signal Processing, Volume II: Detection Theory*, Prentice-Hall, Inc, New Jersey

Kazemi, P. L. (2008) "Optimum Digital Filters for GNSS Tracking Loops," in *Proceedings of the ION GNSS*, 16-19 Sep, Savannah, GA, pp. 2304 - 2313

Klukas, R., G. Lachapelle, C. Ma, and G. Jee (2003) "GPS Signal Fading Model for Urban Centers," in *IEE-Microwaves, Antennas and Propagation*, Vol. 150, Issue 4, pp. 245-252

Lakhzouri, A., E. S. Lohan, I. Saastamoinen, and M. Renfors (2005b) "On Second Order Statistics of the Satellite-to-Indoor Channel Based on FieldMeasurements," in *Proceedings of the IEEE 16th International Symposium on Personal, Indoor and Mobile Radio Communications*, , pp. 2632-2636

Lakhzouri, A., E. S. Lohan, I. Saastamoinen, and M. Renfors (2005) "Interference and Indoor Channel Propagation Modeling Based on GPS Satellite," in *Proceedings of the ION GNSS*, 13-16 Sept, Long Beach, CA, pp. 896 - 901

Langley, B. R. (1997) "GPS Receiver System Noise," *GPS World*, June, pp. 40-45

Lashley, M. and D. M. Bevly (2007) "Comparison of Traditional Tracking Loops and Vector Based Tracking Loops for Weak GPS Signals," in *Proceedings of the ION GNSS*, 25 - 28 Sept, Fort Worth, TX , pp. 789 - 795

Lashley, M. and D. Bevly (2009) "What About Vector Tracking Loops?," *Inside GNSS*, May/June, pp. 16-21

Lehner, A. and A. Steingass (2005) "A Novel Channel Model for Land Mobile Satellite Navigation," in *Proceedings of the ION GNSS*, , Long Beach, CA, pp. 2132-2138

Loo, C. (1985) "A statistical model for a land mobile satellite link," in *IEEE Transaction on Vehicular Technology*, Vol. 34, Issue 3, Aug, pp. 122–127

Lutz, E., D. Cygan, M. Dippold, F. Dolainsky, and W. Papke (1991) "The land mobile satellite communication channel-recording, statistics, and channel model," in *IEEE Transactions on Vehicular Technology*, Vol. 40, Issue 2, pp. 375 - 386

Lyons, R. G. (2004) *Understanding Digital Signal Processing* , Prentice Hall

Misra, P. and P. Enge (2001) *Global Positioning System: Signals, Measurements and Performance*, Ganga-Jamuna Press Lincoln, USA

Mitelman, A., P. Normark, M. Reidevall, and J. Thor (2006) "The Nordnav Indoor GNSS Reference Receiver," in *Proceedings of the ION GNSS 19th ITM*, , Fort Worth, TX

Muthuraman, K. and D. Borio (2010) "C/N0 Estimation for Modernized GNSS Signals: Theoretical Bounds and a Novel Iterative Estimator," in *NAVIGATION*, Vol. 57, Issue 4, Winter, pp. 309 - 323

National Instruments (2006) *2.7 GHz RF Vector Signal Analyzer with Digital Downconversion*, http://www.ni.com/pdf/products/us/cat_vectorsignalanalyzer.pdf, last accessed December 8, 2010

O'Driscoll, C. (2007) *Performance Analysis of the Parallel Acquisition of Weak GPS Signals*, Phd Thesis, Department of Electrical and Electronic Engineering, The National University of Ireland

Oppenheim, A.V. and R.W. Schafer (2010) *Discrete-Time Signal Processing*, Prentice-Hall

Paonni, M., V. Kropp, A. Teuber, and G.W. Hein (2008) "A new statistical model of the indoor propagation channel for satellite navigation," in *Proceedings of the ION GNSS*, , Savannah, GA, pp. 1748–1757

Papoulis, A. (1991) *Probability, Random Variables and Stochastic Processes*, McGraw Hill, New York

Parkinson, B. W. and J. J. Spilker (1996) *Global Positioning System: Theory and Applications*, American Institute of Aeronautics and Ast (AIAA)

Pätzold, M. (2002) *Mobile Fading Channels*, John Wiley & Sons, Ltd, Chichester, West Sussex

Pauluzzi, D. R. and N. C. Beaulieu (2000) "A Comparison of SNR Estimation Techniques for the AWGN Channel," in *IEEE Transactions On Communications*, Vol. 48, Issue 10, pp. 1681-1691

Peterson, B., D. Bruckner, and S. Heye (1997) "Measuring gps signals indoors," in *Proceedings of the ION/GNSS*, 16-19 Sep, Kansas City, MO, pp. 615–624

Petovello, M.G., C. O'Driscoll, and G. Lachapelle (2008) "Weak Signal Carrier Tracking Using Extended Coherent Integration with an Ultra-Tight GNSS/IMU Receiver," in *Proceedings of the Proceedings of European Navigation Conference*, 23-25 April, Toulouse

Petovello, M.G., C. O'Driscoll, G. Lachapelle, D. Borio, and H. Murtaza (2009) "Architecture and Benefits of an Advanced GNSS Software Receiver," in *Positioning*, Vol. 1, pp. 66-78

Psiaki, M. L. and H. Jung (2002) "Extended Kalman Filter Methods for Tracking Weak GPS Signals," in *Proceedings of the Proceedings of ION GNSS*, September, Portland, OR, pp. 2539 - 2553

Rappaport, T. (2001) *Wireless Communications: Principles and Practice*, Prentice Hall PTR

Satyanarayana, S., D. Borio, and G. Lachapelle (2010) "Power Levels and Second Order Statistics for Indoor Fading Using a Calibrated A-GPS Software Receiver," in *Proceedings of the ION GNSS*, 21-24 Sep, Portland

Satyanarayana, S. (2010) "Stationary, Cyclostationary and Nonstationary Analysis of GNSS Signal Propagation Channel," in *Proceedings of the ION GNSS 2010*, , Portland, OR, pp. 476 - 488

Saunders, S. R. and A. Aragón-Zavala (2007) *Antennas and Propagation for Wireless Communication Systems*, JohnWiley & Sons Ltd, England

Schubert, F. M., A. Lehner, A. Steingass, P. Robertson, B. H. Fleury, and R. Prieto-Cerdeira (2009) "Modeling the GNSS Rural Radio Channel: Wave Propagation Effects Caused by Trees and Alleys," in *Proceedings of the ION GNSS*, , Savannah, GA, pp. 2372-2377

Shanmugam, S. (2008) *New Enhanced Sensitivity Detection Techniques for GPS L1 C/A and Modernized Signal Acquisition*, Technical Report No. No. 20264, Phd Thesis, Department of Geomatics Engineering, University of Calgary, Canada

Simon, M. K. (2002) *Probability Distributions Involving Gaussian Random Variables: A Handbook for Engineers and Scientists*, Kluwer Academic Publishers, Boston, US

Spilker, J. J. (1996) *Global Positioning System: Theory and Applications, Volume I*, American Institute of Aeronautics and Astronautics, Inc, Cambridge, Massachusetts

Spirent (2008) *SimGEN User Manual*, Software For The Spirent Range Of Satellite Navigation Simulator Products, published as Report No Issue 1-28

Spirent (2008) *SimGEN User Manual*, Software For The Spirent Range Of Satellite Navigation Simulator Products, published as Report No Issue 1-28

Steingass, A. and A. Lehner (2003) "Land Mobile Satellite Navigation -Characteristics of the Multipath Channel," in *Proceedings of the ION GNSS*, , Portland, OR, pp. 1016-1022

Steingass, A. and A. Lehner (2004) "Measuring the Navigation Multipath Channel-A Statistical Analysis," in *Proceedings of the ION GNSS*, , Long Beach, CA, pp. 1157-1164

Steingass, A. and A. Lehner (2006) "New Findings on Land Mobile Satellite Multipath Navigation Performance," in *Proceedings of the ION GNSS*, , Fort Worth, TX, pp. 1687-1695

Steingass, A. and A. Lehner (2007) "A Model for the Suburban Multipath Channel," in *Proceedings of the ION GNSS*, , Fort Worth,TX, pp. 1699-1705

Steingass, A. and A. Lehner (2008) "Differences in Multipath Propagation between Urban and Suburban Environments," in *Proceedings of the ION GNSS*, , Savannah, GA, pp. 602-611

Steingass, A., A. Lehner, and F. Schubert (2009) "A Location and Movement Dependent GNSS Multipath Error Model for Pedestrian Applications," in *Proceedings of the ION-GNSS*, , Savannah,GA, pp. 2284-2296

Stüber, G. L. (2002) *Principles of Mobile Communication*, Kluwer academic publisher, New York

Teuber, A., M. Paonni, V. Kropp, and G. W. Hein (2008) "Galileo signal fading in an indoor environment," in *Proceedings of the ION GNSS*, , Savannah, pp. 952–960

Uijt de Haag, M. (1999) *An Investigation into the Application of Block Processing Techniques for the Global Positioning System*, Ph.D. Thesis, Ohio University

van Diggelen, F. (2009) *A-GPS: Assisted GPS, GNSS, and SBAS*, Artech House

Vatalaro, F. (1995) "Generalised Rice-lognormal channel model for wireless communications," in *Electronics Letters*, Vol. 31, Issue 22, pp. 1899 - 1900

Wand, M. P. and M. C. Jones (1995) *Kernel Smoothing*, Chapman & Hall, Londin, UK

Watson, J. R.A. (2005) *High-Sensitivity GPS L1 Signal Analysis for Indoor Channel Modelling*, Technical Report No. UCGE Number 20215, M.Sc Thesis, The Univeristy of Calgary

Wireless 911 Services (2010) *FCC Consumer Facts*, http://www.fcc.gov/cgb/consumerfacts/wireless911srvc.html, last accessed May 5, 2010

Yang, C. and S. Han (2007) "Tracking of Weak GPS Signal with BACIX," in *Proceedings of the ION GNSS*, 25 - 28 Sept, Fort Worth, TX, pp. 2797 - 2807

Ye, Z. and H. Satorius (2003) "Channel modeling and simulation for mobile user objective system (MUOS)--part 1: flat scintillation and fading," in *IEEE Communications*, Vol. 5, pp. 3503 - 3510

APPENDIX A: CALIBRATION OF MEASUREMENT SETUP

In this appendix, the procedure adopted for calibrating the NI data collection system available in the PLAN Group is described.

Any electronic device acts as a noise source leading to a degradation of the SNR of signals transiting through the device. The noise figure is the metric used to quantify the degradation of SNR when the signal transits through a given device and it is defined as (Haykin 2001)

$$F = \left(\frac{C}{N}\right)_{input} \bigg/ \left(\frac{C}{N}\right)_{output}$$

(A.1)

where C and N denote the signal and noise powers, respectively. Thus, the noise figure is the ratio between the SNRs at the input and output of the device. If the noise power at the input and output of the device are considered with respect to a common reference bandwidth, the noise figure can be rewritten in terms of input and output C/N_0 values:

$$F = \left(\frac{C}{N_0 B}\right)_{input} \bigg/ \left(\frac{C}{N_0 B}\right)_{output} = \left(\frac{C}{N_0}\right)_{input} \bigg/ \left(\frac{C}{N_0}\right)_{output}$$

(A.2)

The noise figure of a cascaded system is given by the Friis formula:

$$F_{total} = F_1 + \frac{F_2 - 1}{G_1} + \frac{F_3 - 1}{G_1 G_2} + ... + \frac{F_N - 1}{G_1 G_2 ... G_{N-1}}$$

(A.3)

where G_i and F_i are the gain and the noise figure of the ith device in the chain.

Using (A.2) and (A.3), the following procedure can be used for the determination of the noise figure of a data collection system.

Step 1

In the first step, a signal generator, in this case a Spirent GSS 7700 GPS signal simulator, is directly connected to the data collection system as shown in Figure A-1. More specifically, the Spirent GSS 7700 hardware simulator and an NI RF front-end are connected using a short cable whose attenuation and noise figure has been measured using an Agilent E4402B spectrum analyzer. In this case, the noise figure of the transmission chain is given by

$$F_1 = F_{c1} + \frac{F_{NI} - 1}{G_{c1}} \tag{A.4}$$

where F_1 is the noise figure of the chain, F_{c1} and G_{c1} are the noise figure and gain of the cable and F_{NI} is the noise figure of the NI system.
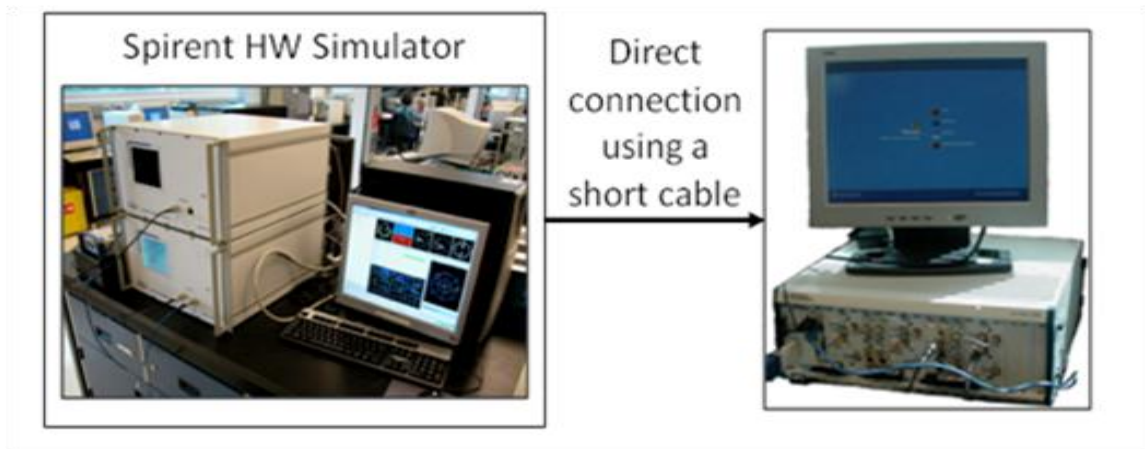

Figure A-1: Calibration procedure, step 1. The Spirent Hardware Simulator and the National Instrument front-end are directly connected using a short cable.

Using Eq. (A.2), Eq. (A.4) can be rewritten as

$$\left(\frac{C}{N_0}\right)_{input} \Big/ \left(\frac{C}{N_0}\right)_{output,1} = F_{c1} + \frac{F_{NI} - 1}{G_{c1}} \tag{A.5}$$

where $\left(C/N_0 \right)_{input}$ is the C/N_0 of the signal at the output of the Spirent signal generator

and $\left(C/N_0 \right)_{output,1}$ is the C/N_0 of the signal collected by the NI system. It is noted that

the only two unknown terms in (A.5) are F_{NI} and $\left(C/N_0 \right)_{input}$, since the Spirent

Simulator allows one to set the signal power but not the C/N_0. $\left(C/N_0 \right)_{output,1}$ is easily

measured using the PLAN group software receiver (GSNRx^{TM}-rr) whereas all the other

parameters in (A.5) have been determined using the spectrum analyzer. Since two

unknowns are present in (A.5), a second condition is required for determining F_{NI} and

$\left(C/N_0 \right)_{input}$.

Step 2

In order to obtain a second condition for determining F_{NI} a second test has been

performed. More specifically, the setup shown in Figure A-2 has been adopted. In this

case, an additional Low Noise Amplifier (LNA) has been inserted in the transmission

chain between the Spirent Simulator and the NI front-end. The noise figure and the gain

of the amplifier were known from the device specifications and have been verified using

the spectrum analyzer.

The characteristics of the cables used for connecting the three devices have also been

determined using the spectrum analyzer. In this case, the total noise figure of the

transmission chain becomes

$$
\begin{aligned}
F_2 &= \left(\frac{C}{N_0} \right)_{input} \bigg/ \left(\frac{C}{N_0} \right)_{output,2} \\
&= F_{c2} + \frac{F_{LNA}-1}{G_{c2}} + \frac{F_{c1}-1}{G_{c2}G_{LNA}} + \frac{F_{NI}-1}{G_{c2}G_{LNA}G_{c1}}
\end{aligned}
\tag{A.6}
$$

where F_{LNA} and G_{LNA} are the noise figure and gain of the LNA and F_{c2} and G_{c2} are the parameters characterizing the second cable used for the connection.
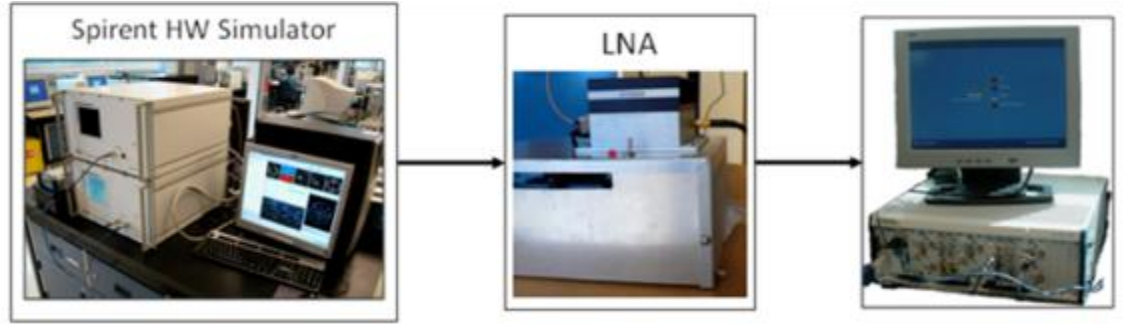

Figure A-2: Calibration procedure, step 2. An additional Low Noise Amplifier (LNA) is added in the transmission chain between the hardware simulator and the NI front-end.

In (A.6) the only unknown parameters are the noise figure of the NI front-end and the C/N_0 at the output of the Spirent Simulator. Since the same settings for the Spirent simulator have been used in the two tests, the generated signals are supposed to be characterized by the same $\left(C/N_0\right)_{input}$. $\left(C/N_0\right)_{output,2}$ has been measured using the GSNRx^{TM} software.

Eqs. (A.5) and (A.6) provides two independent conditions for two unknowns and thus can be used for determining F_{NI}. More specifically, by dividing (A.5) by (A.6) the following condition is found:

$$F_{c1} + \frac{F_{NI}-1}{G_{c1}} = \left(\frac{C}{N_0}\right)_{output_2} \bigg/ \left(\frac{C}{N_0}\right)_{output1} \cdot \left[F_{c2} + \frac{F_{LNA}-1}{G_{c2}} + \frac{F_{c1}-1}{G_{c2}G_{LNA}} + \frac{F_{NI}-1}{G_{c2}G_{LNA}G_{c1}}\right] \text{(A.7)}$$

that is a linear equation in one unknown. In this way, F_{NI} can be easily determined. Eq. (A.5) can be then used for determining the C/N_0 at the output of the Spirent Simulator.

From this C/N_0 and the carrier power level set in the simulator, it is possible to compute N_0 that in this case was found to be approximately -174 dBm/Hz.

In order to validate the adopted calibration procedure and the experimental setup, several experiments based on a signal generator and the Spirent hardware GPS signal simulator have been performed for different input signal powers. Different cables with different loss factors were used to test the applicability of the adopted calibration procedure.

The Spirent simulator was used to generate signals at different power levels. For example, in one of the tests, a static scenario with nine satellites was simulated. All the satellites were characterized by an initial carrier power of -125 dBm. The signal power was progressively decreased by 3 dB each 15 seconds. The simulated data were collected using the NI front-end and processed using the GSNRx^{TM}. The signal power was finally estimated using the NI noise figure. The mean difference between reference and empirical results was around 1 dB.

In the second type of experiments, an Agilent E4431B signal generator was used to obtain signals from a different source other than the simulator that was already used to compute the noise figure of the NI system. The signal generator was programmed to have an initial carrier power of -120 dBm. The power was progressively attenuated by 3 dB each 15 seconds. A Matlab script was used for estimating the signal C/N_0 that was later converted into the signal power.

Figure A-3 shows some sample results relative to the comparison between reference and estimated signal powers. The two curves match with a mean difference of 0.3 dB. These results show the validity of the calibration procedure adopted for the NI system.
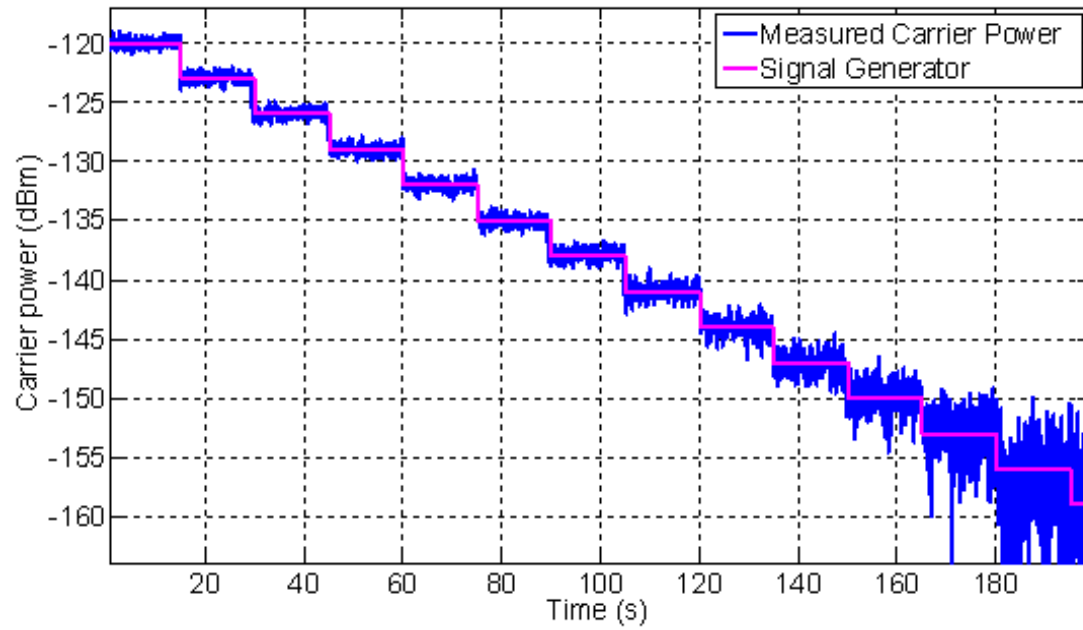
Figure A-3: Comparison between reference and estimated signal powers for the signal provided by the Agilent signal generator.

APPENDIX B: FIRST ORDER CHARACTERIZATION, ADDITIONAL

RESULTS

In this appendix, additional results for the first order characterization of GPS signals under harsh environments considered in Chapter 4 are presented. Characterization results for several satellites other than the one considered in Chapter 4 are summarized in the following sections.

B.1. Open sky, multiple reflectors scenario

Figure B-1 shows carrier power variations for four different satellites from the static antenna placed in the middle of the data collection site as shown in Figure 4-9. The carrier power variations are consistent with the results discussed in Section 4.4.3.
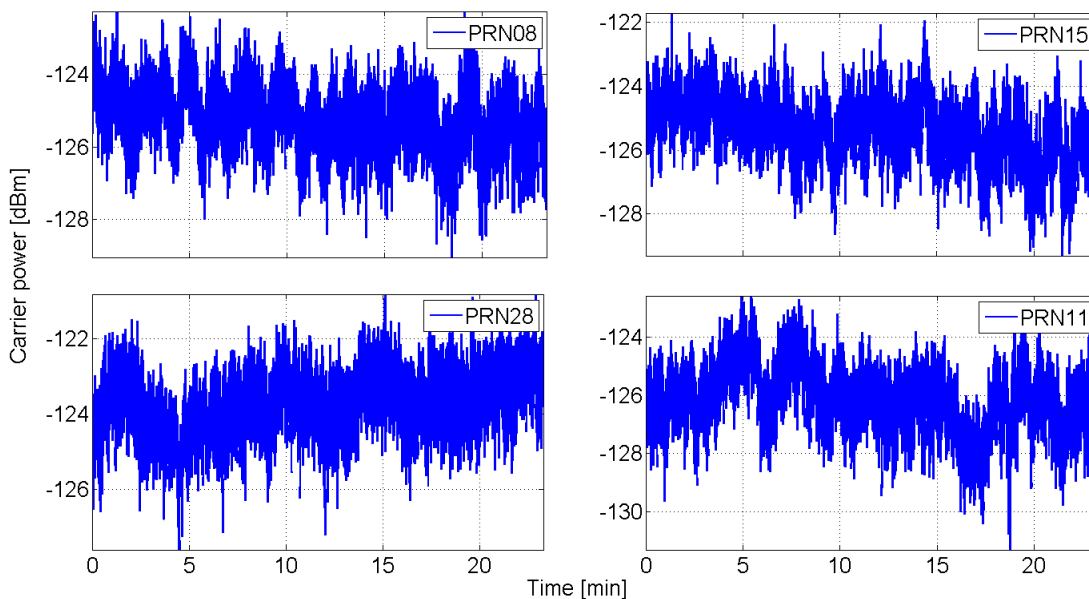

Figure B-1: Carrier power variations for four different satellites from the static antenna.

B.2. Foliage scenario

Slow and fast fading components for PRN03 and PRN28 obtained from the static dataset under foliage conditions are shown in Figure B-2. It can be observed that the carrier power variations are consistent with the results shown in Section 4.4.4.
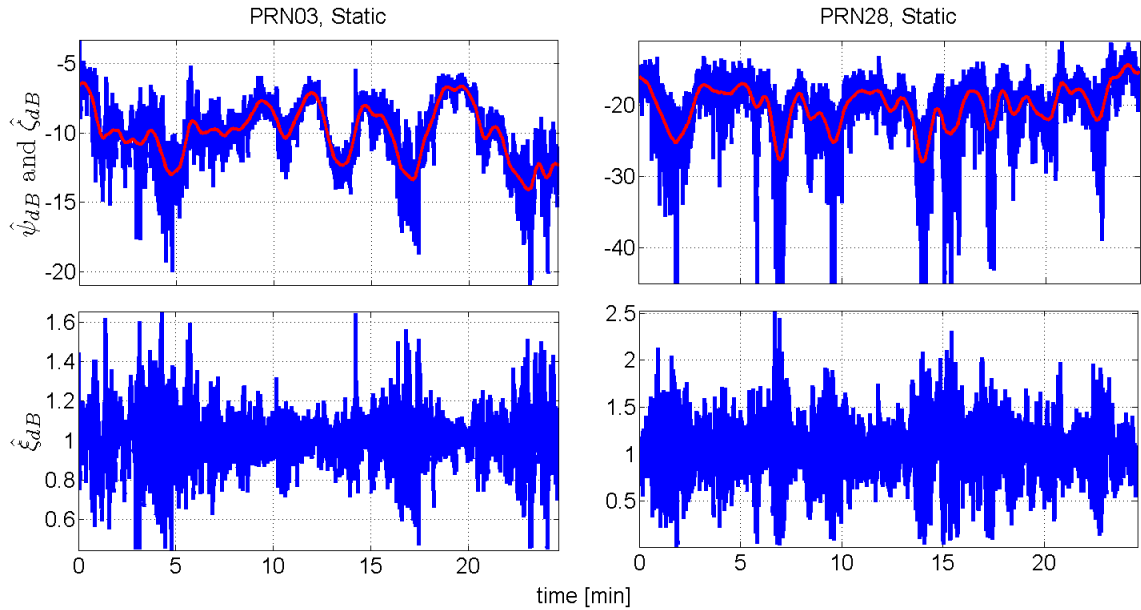

Figure B-2: (a) Carrier power variations of PRN03 and PRN28 from a static dataset (slow fading component is shown in red), upper row. (b) Fast fading component obtained after high pass filtering, bottom row.

B.3. Indoor scenario

Slow and fast fading components for PRN11 are shown in Figure B-3. It can be observed that the fast fading components exhibit periodicity in their variations. As seen from Figure 4-23(b), PRN11 is arriving on the west side of the conference room similarly to PRN19 with a similar elevation angle and different azimuth angle.

Figure B-4 shows the carrier power variations for PRN22 and PRN26 from the dynamic dataset NL-DS1-D. It can be observed that the variations are consistent with the results discussed in Section 4.4.5.3.

The comparison of the empirical PDF of the fast fading components against standard models for the McEwan Hall dynamic dataset, ME-DS1-D is shown in Figure B-5. In this case, a good match is obtained with the Rician model and the estimated Rician *K* factor is -7.5 dB.
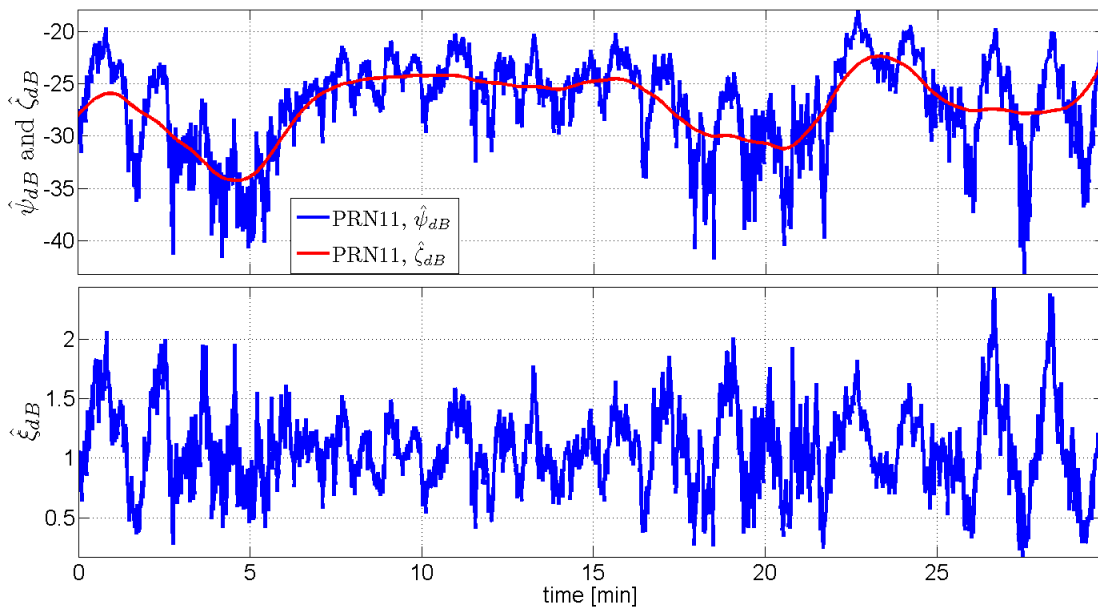

Figure B-3: (a) Carrier power variations of PRN11 in static dataset CR-DS1-S (slow fading component is shown in red). (b) Fast fading component obtained after high pass filtering.
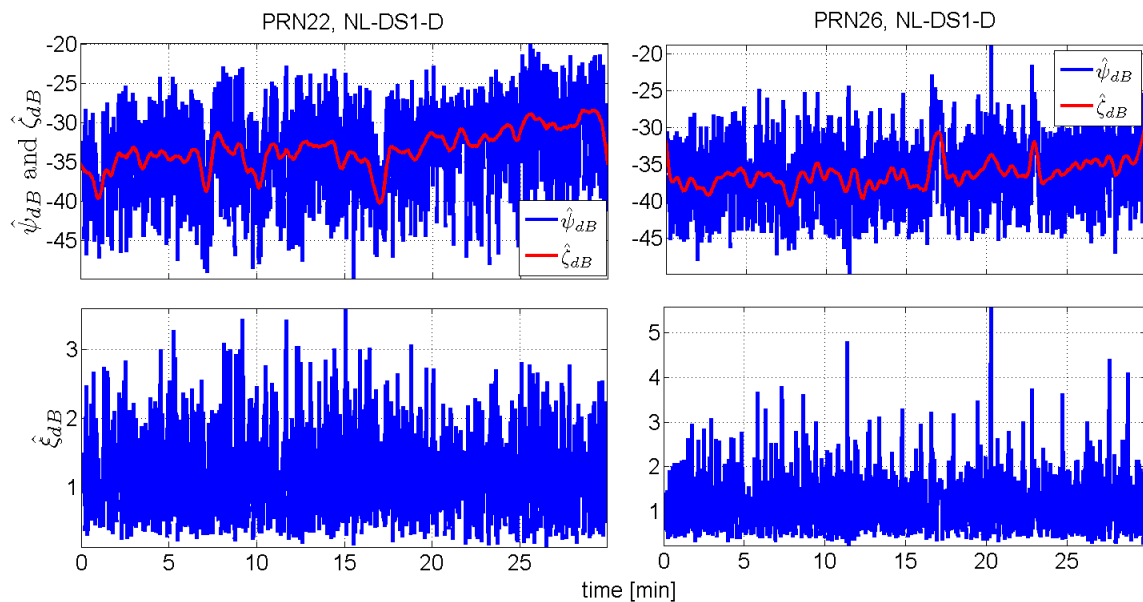
Figure B-4: Carrier power variations of PRN22 and PRN26 from the dynamic dataset collected in the Navlab (NL-DS1-D).
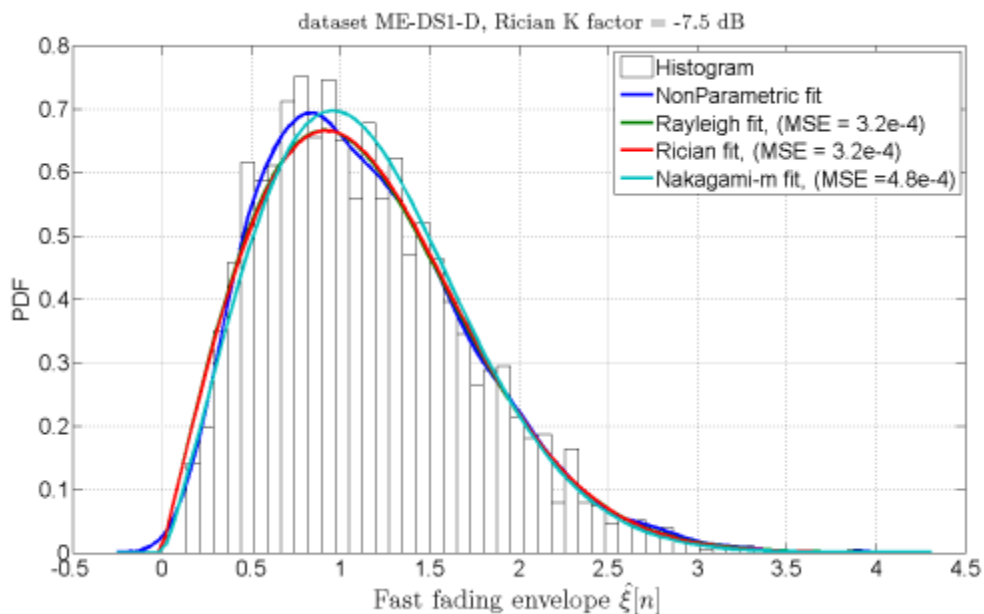

Figure B-5: Comparison of the density function of the fast fading components obtained from McEwan Hall dynamic dataset (ME-DS1-D).